LEABHARLANN CHOLÁISTE NA TRÍONÓIDE, BAILE ÁTHA CLIATH | TRINITY COLLEGE LIBRARY DUBLIN
Ollscoil Átha Cliath | The University of Dublin

Terms and Conditions of Use of Digitised Theses from Trinity College Library Dublin

Copyright statement

All material supplied by Trinity College Library is protected by copyright (under the Copyright and Related Rights Act, 2000 as amended) and other relevant Intellectual Property Rights. By accessing and using a Digitised Thesis from Trinity College Library you acknowledge that all Intellectual Property Rights in any Works supplied are the sole and exclusive property of the copyright and/or other IPR holder. Specific copyright holders may not be explicitly identified. Use of materials from other sources within a thesis should not be construed as a claim over them.

A non-exclusive, non-transferable licence is hereby granted to those using or reproducing, in whole or in part, the material for valid purposes, providing the copyright owners are acknowledged using the normal conventions. Where specific permission to use material is required, this is identified and such permission must be sought from the copyright holder or agency cited.

Liability statement

By using a Digitised Thesis, I accept that Trinity College Dublin bears no legal responsibility for the accuracy, legality or comprehensiveness of materials contained within the thesis, and that Trinity College Dublin accepts no liability for indirect, consequential, or incidental, damages or losses arising from use of the thesis for whatever reason. Information located in a thesis may be subject to specific use constraints, details of which may not be explicitly described. It is the responsibility of potential and actual users to be aware of such constraints and to abide by them. By making use of material from a digitised thesis, you accept these copyright and disclaimer provisions. Where it is brought to the attention of Trinity College Library that there may be a breach of copyright or other restraint, it is the policy to withdraw or take down access to a thesis while the issue is being resolved.

Access Agreement

By using a Digitised Thesis from Trinity College Library you are bound by the following Terms & Conditions. Please read them carefully.

I have read and I understand the following statement: All material supplied via a Digitised Thesis from Trinity College Library is protected by copyright and other intellectual property rights, and duplication or sale of all or part of any of a thesis is not permitted, except that material may be duplicated by you for your research use or for educational purposes in electronic or print form providing the copyright owners are acknowledged using the normal conventions. You must obtain permission for any other use. Electronic or print copies may not be offered, whether for sale or otherwise to anyone. This copy has been supplied on the understanding that it is copyright material and that no quotation from the thesis may be published without proper acknowledgement.

Magnetization Processes and Low Frequency Fluctuations in Micromagnetic Structures

A thesis submitted to the University of Dublin, Trinity College

in application for the degree of Doctor of Philosophy

by

Zhu Diao

School of Physics

Trinity College Dublin

Jan 2010

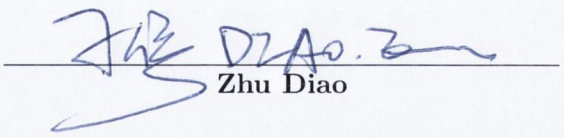
TRINITY COLLEGE
10 APR 2012
LIBRARY DUBLIN

9429

Declaration

I, the undersigned, declare that this work has not previously been submitted to this or any other University, and that unless otherwise stated, it is entirely my own work.

I, the undersigned, agree that Trinity College Library may lend or copy this thesis upon request.



Zhu Diao

Dated: Jan 2010

To Papa and Mama

We are always kids in the eyes of our parents.

Summary:

The study presented in this thesis is concerned with low frequency fluctuations in magnetic systems. Three different systems were investigated.

The first system is $(CoFe/Pt)_n$ multilayers patterned into micrometer scale Hall bars. Low frequency magnetic fluctuations in the active volume were probed by anomalous Hall effect. Magnetic noise was only observed during magnetization switching. It was shown that $1/f^{\alpha}$ noise spectrum, with $\alpha \sim 2$, dominates when at the macroscopic nucleation field, and close to negative saturation when domains annihilate. This is attributed to the irreversible magnetization switching and Barkhausen jumps. While in the slanted region of the hysteresis curve, a stationary $1/f$ noise spectrum was observed. This fluctuation is identified as the result of superposition a large number of reversible excursions of domain wall segments, which are roughly a hundred nanometers in length. First-order reversal curves have also been measured for the same samples. They show two dominant sets of 'hysterons', which coincide with the nucleation field and the negative saturation field, while the magnetization switching in between has high reversibility. These observations largely agree with the anomalous Hall voltage noise data.

The second system studied in this work is yoke-shaped spin-valve devices for sensing applications. The focus here is to understand the fundamental fluctuating entity, and its lateral length scale in a ferromagnetic material.

The technique we used here is to measure the spatial correlation and the high-order statistics of the $1/f$ noise. No enhancement in the spatial correlation above its statistical error has been found for electrode pairs spacing down to 300 nm apart, while the low frequency excess noise is still of mainly $1/f$ nature. This suggests that the volume of fundamental fluctuating entities in spin-valve stacks is much less than a single domain. Low frequency magnetic $1/f$ noise is not generated by a macroscopic magnetization process. However, it was also observed that below a length scale of a few hundred nanometers, local inhomogeneity in an otherwise homogeneous system becomes identifiable. There exist noisier segments in a macroscopically homogeneous yoke spin-valve device, whose noise dominate the measured spectrum. This leads to a violation of Hooge's volume scaling law, in which $1/f$ noise is inversely proportional to the sample volume. A high non-Gaussian component in the noise spectrum was often observed together with the appearance of the noisier segments. An enhanced spatial coherence function can also be observed when domain wall hopping across a large sample area takes place, however, this process often involves very few two-level fluctuators, and the noise spectrum deviates strongly from $1/f$.

The third system investigated was an electrochemical cell with paramagnetic platinum as working and counter electrodes. Two different low frequency electrochemical noise spectra types have been observed. Applying a magnetic field was shown to either suppress (for Type I spectrum), or enhance (for Type II spectrum) the low frequency noise plateau. We discuss the possible explanations for the two spectra types, and the mechanisms which lead to different magnetic field effects in terms of coalescence growth of hydrogen bubbles.

Acknowledgements

A PhD thesis is expected to be the candidate's own work, however, it for sure contains contributions from everyone he/she works or has worked with. In scientific research it is too common that we learn from our colleagues, sometimes even without our noticing. This makes the acknowledgements usually very vulnerable to some real 'scientific mistakes'. I hereby try my best to give a thorough account of everybody, whom I'm indebted to over the last five years as a PhD student in Dublin. If there is still any missing names, for sure I believe there will be, I sincerely hope that the relevant person will try to forget my mistake as I managed to forget his/her name.

I would like to thank Prof. Coey (commonly known as Mike), for giving me the opportunity to work in his group, and his supervision in the last five years. I'm deeply impressed by his motivation and enthusiasm towards research. Though I still have not made up my mind to be a scientist for life, at least I have continued for five more years, and most likely will continue for another while. I'm also in great debt to our 'noisy' professor, Ed Nowak, from University of Delaware, for him bringing us his long-time experience and insight in fluctuation measurements during his stay in our lab. Things got much easier for me since he came. I also learnt from him that a professor still has to be a hands-on man, and be able to show students how things are working (or most of the time not working). I will definitely remember

it if one day I unfortunately join the professor community. Another important figure (by important, I mean professors) to which I'm indebted to is Prof. Giovanni Zangari from University of Virginia, with whom part of the electrochemistry experiment was carried out.

I would also like to express my sincerest thanks to Tarek from whom I learnt nearly everything on how samples probed in this study are made, but also for showing me that there is a much broader world outside the university. Having him as both my personal ski trainer and driving tutor, I for sure learnt much more than only science from him (though I'm not sure if I'm good at either skiing or driving). I'm also in large debt to Plamen, who gave various little little helps to me during the last five years, and always tried to point out how naïve I am in both science and life. Chairman Mao said that it was easy to make a single good deed but difficult to continue it for life. I show great respect to Plamen as a person who always tries to contribute to others work without expecting returns. His ideas and suggestions bear fruit throughout this thesis. I also have to say many thanks to Mohamed, from whom I learnt various small things in research. He was also the one who tried hard to motivate me, a person always lacking of motivation, into research. Another sincere thank goes to Peter, with whom I carried out the electrochemistry experiment, the person who always helps me on modern highly advanced computer technology, e.g. how to convert an eps image to pdf. Yes, we did spend some days outside Dublin together as well. I was quite surprised that he did not end up beating me up during those days.

In relation to the work in this thesis, I have to express my dear thanks to Gen, Dr. Chun, Jiafeng, Junyang, and Ciáran, all my sample donors. It would be impossible for a person like me to complete this work, as I

have never grown any samples on my own for the last three years. I would also like to thank Cathy, Peter, Ciáran (this name shows up too much, but thanks a lot for checking the most important part of the thesis, the acknowledgements, for me), Karsten, Colm, and Jiafeng, who went through parts of this thesis in its very primitive form, and helped me to find my way in the black woods of English words and scientific plottings. Many thanks to Venky for SQUID measurement now and then, plus various practical issues related to living in Dublin, and surviving in the college. I have also to say thank you to two of my summer students, Nicolas and Pramey. You guys will for sure find your contributions in this work. They might not believe it but I did learn a lot from them, though the knowledge transfer was supposed to be in the opposite direction.

I have to mention the staff and related persons in the CRANN microscopy centre, Markus, Colm, Warren, and Hongzhou, for them kindly giving me full access to the equipment during my PhD work, also for various supports from time to time. Some old members of the group needs my special attention, Robbie (also known as the polar bear), Eoin (the powerful one), Fernando (now officially on the way towards professorship), Oscar (in the same track as Fernando), Lucio (sometimes his name is also Oscar), Cathy (I mentioned her already. Let's do it again then), Richard (sadly Chelsea did not win the Champions league in 2008. Where did we watch the game? Yes, in Manchester), Martin, Greg, Matt, Emma, Karl, and Ciara, for making this group a good place to work in. Many thanks to Marita, Jon, Simone. You guys did bring some extra to the normal lab life.

Living in a foreign country is not only about work. I sincerely thank my 'xxxx' flatmate Boris of the last three years, for bringing me so much fun now and then. Many thanks to the Trinity Hall lads plus their related

community, Mark, Matt, Laura, Thomas (many of them), Bredan, Yuni, Alex, Leo, Jill (this was a big mistake in the first version of this thesis), Daisy. Unfortunately, I'm going to be the last among you guys to finish his/her degree. Also many thanks to the small Chinese community I got involved in, Xue Li, Yongheng Liu, Hanchun Wu, Baomei Wen, Yaou Li, Yu Cui, Ze Zhou, Tianxing Wang, and Qinli Ma. It is always nice that there is a chance to speak your native language from time to time. Also thanks to several old friends of mine who lived or are still living on this little island, or the island next to it. In the last few years, I was really lucky to have them that close to me. Wallace, Lux, Crystal, Dawson, they gave me much more than they ever expect.

Also a thank you to everybody who was and who is now in the group. It was a long trip for me to come to Dublin five years ago. The completion of this thesis means that I will probably be on another long trip soon. I sincerely hope for all those mentioned above, our paths do not cross only once in our life.

I'm lost in picking up words to express my thanks to my parents, Qingji Diao and Zhou Li, for their never ending support and patience. I deeply understand that it is difficult for most parents to let their kids go free, and I feel very lucky that my parents did. Their hard working spirit, and nearly Utopian ideology in bringing fairness and equal opportunity to everyone, make me now, and ever, a person standing on the left, which I am always proud to admit. Though they might not be able to understand a single word in this thesis, it is dedicated to them.

My last sincere thank goes to my girlfriend, Jie Sun, for her kind understanding and continued support. It was probably only purely by chance that the draft of this thesis finished in the 20th year that we got to know

each other, and right after her birthday. Twenty years is a long time, five years, too. I already owe her a lot and am highly likely to owe more. The only thing I can do is try my best to make her happy for life. I don't know if she realizes, she is the one for whom I see the best things inside my heart.

Zhu Diao

University of Dublin, Trinity College

Jan 2010

List of abbreviations:

AFM - Atomic Force Microscopy

AHE - Anomalous Hall Effect

CIP - Current in Plane

CMR - Colossal Magnetoresistance CPP - Current Perpendicular to Plane

DAQ - Data Acquisition

DFT - Discrete Fourier Transform

DW - Domain Wall

ECC - Electrochemical Cell

EBL - Electron Beam Lithography

FIB - Focused Ion Beam

FM - Ferromagnetic

FORC - First Order Reversal Curve

GMR - Giant Magnetoresistance

HL - Hysteresis Loop

MFM - Magnetic Force Microscopy

MHL - Minor Hysteresis Loop

MPMS - Magnetic Properties Measurement System

MR - Magnetoresistance

MRAM - Magnetoresistive Random Access Memory

MTJ - Magnetic Tunnel Junction

PMA - Perpendicular Magnetic Anisotropy

PSD - Power Spectral Density

RA - Resistance per unit Area

RTN - Random Telegraph Noise

SEM - Scanning Electron Microscope

SFM - Scanning Force Microscopy

SVs - Spin-valves

TMR - Tunneling Magnetoresistance

TLF - Two-Level Fluctuations

Contents

Chapter 1 Introduction **1**

References 8

Chapter 2 Low Frequency Electrical Noise in Magnetic Materials and Microstructures **15**

2.1 Basic principles 15

2.2 Low frequency electrical noise 17

2.2.1 Thermal (Johnson) noise 17

2.2.2 Shot Noise 18

2.2.3 Random Telegraph Noise 19

2.2.4 $1/f$ noise 21

2.3 Low frequency electrical noise in magnetic systems 27

2.3.1 Magnetic metals and alloys 29

2.3.2 Magnetic mutilayers 32

2.3.3 Magnetic Oxides 41

References 46

Chapter 3 Experiment Methods **59**

3.1 Sample Fabrication 59

3.1.1 Photolithography 59

3.1.2 Electron Beam Lithography 61

3.1.3 Lift-off 64
3.1.4 Argon Ion Milling 66
3.2 Sample Characterization 67
3.2.1 Transport and Noise Measurement Set-up 67
3.2.2 Magnetic Force Microscopy 74
References 78

Chapter 4 Magnetization Switching and Fluctuations in $(CoFe/Pt)_n$ Multilayers with Perpendicular Magnetic Anisotropy 81
4.1 Introduction 82
4.1.1 Perpendicular Magnetic Anisotropy Media 82
4.1.2 Anomalous Hall Effect 86
4.1.3 Preisach Model and First Order Reversal Curves . . . 88
4.2 Materials and Methods 90
4.3 Results 92
4.3.1 Domain Structure and Anomalous Hall Effect 92
4.3.2 Anomalous Hall Voltage Noise 95
4.3.3 First Order Reversal Curves 104
4.4 Discussion 106
4.4.1 Anomalous Hall Voltage Noise 106
4.4.2 First Order Reversal Curves 112
4.4.3 The Existence of In-plane Magnetic Components . . 114
4.5 Conclusion 120
References 121

Chapter 5 Spatial Correlation and Statistics of 1/f Noise in Yoke-Shaped Spin Valves 127
5.1 Introduction 128

5.2 Sample Preparations 131
5.3 Results and Discussion 140
5.3.1 Micrometer-scale Yoke Sensors 140
5.3.2 Sub-micron-scale Yoke Patterns 146
5.4 Conclusion 163
References 164

Chapter 6 Electrochemical Noise Analysis of Hydrogen Bubble Evolution on Platinum Cathode **169**
6.1 Introduction 169
6.2 Materials and Methods 171
6.3 Results and Discussion 172
6.4 Conclusion 189
References 192

Chapter 7 Future Work **197**
References 201

Appendix A Theoretical Aspects **203**
A.1 Basic Statistical Mechanics 203
A.2 Fluctuation-Dissipation Theorem 204
A.3 Parseval's Theorem 208
A.4 Wiener-Khintchine Theorem 209
A.5 Kramers-Kronig Relation 210
A.6 The Stoner-Wohlfarth Model 211
A.7 The Draaisma-de Jonge Model 213
A.8 Verification of Contact Noise 216
References 218

Appendix B Lithography Recipes **221**

B.1 Photoresists 221

B.1.1 Shipley Microposit S1813 221

B.1.2 AZ nLOF 2070 222

B.2 Electron beam resists 223

B.2.1 Polymethyl Methacrylate (PMMA) 223

B.2.2 ma-N 2403 225

B.2.3 Hydrogen Silsesquioxane (HSQ) 225

References 227

List of Figures

2.1 (a) The experimentally measured $1/f^{\alpha}$ slope α compared with the prediction of the DDH model; (b) Hooge parameter γ as a function of temperature for a nickel thin film. . . 28

2.2 A diagram showing a spin-valve structure (a) and its MR curve (b) (courtesy of Dr. Gen Feng). 35

2.3 A diagram showing a MTJ stack (a) and its MR curve (b) (courtesy of Dr. Gen Feng). 36

3.1 Simplied diagram of a scanning electron beam writing system. 63

3.2 A schematic diagram of the lift-off process. 65

3.3 A schematic diagram of the lift-off process with lift-off resist creating the undercut. 66

3.4 SIMS readout during argon ion milling of a spin-valve stack on the Millatron. 67

3.5 Circuit diagram of the noise and transport measurement set-up. 68

3.6 The input noise equivalent circuit diagram of an amplifier. . 69

3.7 Power spectral density of magnetic field generated by the electromagnet in our set-up. The slope is due to the increase of the impedance of the pickup coil at low frequencies. . . . 72

3.8 Power spectral density measured on three thin film resistors of 100 Ω, 1 kΩ, and 10 kΩ using SR552 preamplifier with our set-up. Also shown is the amplifier input equivalent voltage and current noise. The blue dashed line is the voltage noise level of SR552 quoted in the specifications. Dashed lines in other colours indicate the respective theoretical estimate of the noise level for each resistor. The lower of the two green dashed lines is a theoretical estimate without taking account of the input current noise, whereas the higher one also has it counted. 73

3.9 A diagram showing a magnetic force microscopy system with active Q-control feedback loop. 77

4.1 Domains patterns observed in a typical magnetic thin film with $Q \sim 1$ during magnetization switching. (a) Stripe domains, (b) reverse stripes broadening while the normal stripes narrowing, (c) bubble domains. 85

4.2 A diagram showing a non-interacting hysteron (left) and a hysteron with an interaction field H_u. 89

4.3 SEM images of $(CoFe/Pt)_n$ Hall crosses fabricated by photolithography. (a) Hall crosses of a $(CoFe/Pt)_{10}$ sample with additional Au contacts; (b) Hall crosses of a $(CoFe/Pt)_{50}$ sample without additional Au contacts. 91

4.4 Magnetic hysteresis loops of three ($Co_{90}Fe_{10}$/Pt) multilayer stacks, with different numbers n of bilayer repeats. Hysteresis loops are deduced from the anomalous Hall effect. MFM images (5 μm $\times$ 5 μm) show the domain structure in the virgin state of each sample. In the $n = 20$ case, the magnetization curve is compared with one determined by SQUID magnetometry on an unpatterned film. 93

4.5 Magnetization curves measured by sweeping the applied magnetic field step by step with a rate of 1 - 2 mT·s^{-1}, and measured by boosting the magnetic field between positive and negative saturation within 5 s. 95

4.6 Anomalous Hall voltage and octave noise power (centred at 4.8 Hz) against magnetic field for three samples with different n. The bias current for AHE has been normalized to 1.2 mA. 97

4.7 Anomalous Hall votage and octave noise power in the lowest 3 octaves against magnetic field for a sample with $n = 10$. The bias current is 2.4 mA 98

4.8 Three minor hysteresis loops of anomalous Hall voltage and octave noise power (centred at 4.8 Hz) against magnetic field measured on a $n = 20$ sample. The reversal field H_R are -50 mT, -100 mT and -150 mT, respectively. The bias current is 1.2 mA. 99

4.9 Anomalous Hall voltage and octave noise power (centred at 4.8 Hz) against magnetic field on a sample with $n = 20$. Noise data were taken 5 min after each field setpoint was reached. The bias current is $\sim$ 3.2 mA. 100

4.10 Noise spectra at three different magnetic fields for the sample of Fig. 4.6. The field was swept from positive saturation to the setpoint at a rate of 2 $mT \cdot s^{-1}$. The background has been subtracted from the spectra except for the one taken in the second 5 min at -175 mT. The dashed line is the background, consisting of the amplifier noise and the thermal background noise of the sample. 101

4.11 Power spectrum density at 4 Hz and 10 Hz for a $n = 20$ sample with different current biases. 102

4.12 Time sequence measured on a n =10 sample with different setpoint fields. (a) -10 mT, (b) -20 mT, and (c) -250 mT. Points A, B and C refer to those labelled in Fig. 4.4a. The bias current is 1.2 mA. 103

4.13 FORCs measured on a $(CoFe/Pt)_{10}$ sample. 105

4.14 FORCs measured on a $(CoFe/Pt)_{20}$ sample. 106

4.15 FORCs measured on a $(CoFe/Pt)_{50}$ sample. 107

4.16 FORCs diagrams for samples with n = (a) 10, (b) 20, and (c) 50. 108

4.17 A diagram showing the proposed domain wall fluctuation mechanism as the $1/f$ noise source. 110

4.18 Anomalous Hall voltage and octave noise power for 3 consecutive octaves measured with the magnetic field in-plane for an $n = 20$ sample. 115

4.19 Out-of-plane and in-plane magnetization curves obtained by Hall effect measurement. Units in the figure do not represent the real ratio between the out-of-plane and in-plane magnetization. 118

5.1 A diagram showing the free layer and the pinned layer magnetization on the arm of the yoke. The applied magnetic field is perpendicular to the arm. 132

5.2 (a) Spin-valve stacks from which the yoke sensors are patterned; and (b) its MR curve (courtesy of B.-S. Chun). . . . 133

5.3 Optical microscope images showing the lithographic steps in patterning the yoke sensor. (a) Defining the yoke sensor; (b) UV lithography to define the contacts; (c) After contact lift-off (coutesy of B.-S. Chun). 133

5.4 MR curves of the unpatterned spin-valve stack with $Co_{40}Fe_{40}B_{20}$ as ferromagnetic electrodes, and a yoke sample with w = 600 nm patterned from the same spin-valve stack, measured across e1e6. 135

5.5 Pattern design for a $w = 2$ μm yoke sample with corresponding dimensions and labels for electrodes. 137

5.6 SEM images of (a) a 2 μm width yoke sample, (b) a 600 nm width yoke sample with copper contacts. 137

5.7 GMR vs. applied field for an unpatterned spin-valve stack used to pattern the yokes in sample set c). 138

5.8 SEM images of a yoke spin-valve structure with 2 μm width patterned by single step EBL. 139

5.9 SEM images of a yoke spin-valve structure with 600 nm width patterned by single step EBL. 139

5.10 Two MR curves measured across different electrode pairs on a yoke spin-valve biomagsensor. 140

5.11 PSD measured across e2e3 on a micro-scale yoke sensor. . . 141

5.12 $fS_V(f)/V^2$ against applied magnetic field for a yoke biomagsensor measured across e2e3. $fS_V(f)/V^2$ has been averaged between 18 - 22 Hz. 143

5.13 Coherence data between different electrode pairs on a yoke spin-valve sensor. The coherence between a frequency range of 18 to 46 Hz was averaged to avoid power line pick-up and the error bars are the standard deviations. 144

5.14 Averaged coherence function $\langle \eta^2(f) \rangle$ for e2e3 on a micrometer-scale yoke sensor. The green dashed line shows the predicted coherence function for a 1 kohm resistor (which is similar to the two-probe resistance of the sample) connected in both channels. Voltage noise from the amplifiers significantly decreases the coherence function at high frequencies. Some spurious power line pick-ups are removed during data processing. 145

5.15 MR curves of a $w = 2$ μm yoke (type I) measured across different electrode pairs. 146

5.16 (a) Noise summed across three consecutive octaves against magnetic field in a $w = 2$ μm yoke sample (type I); (b) Hooge parameter γ during magnetization switching in the same sample plotted against $dR/d\mu_0 H$. The black line is a guide to the eyes. 148

5.17 Ensemble averaged coherence function $\langle \eta^2 \rangle$ for a $w = 600$ nm yoke pattern and its MR curves measured across corresponding electrode pairs. 149

5.18 Ensemble averaged coherence function against applied magnetic field, and a MR curve measured between electrode 1 and 2, on a $w = 2$ μm yoke sample, with the easy-axis of the free layer and the pinned layer both along the yoke arm. . . 151

5.19 Noise spectra across five electrode pairs at 9 mT, where the coherence function increases significantly. The black line depicts the $1/f^2$ slope. For the lower two spectra (e4e5 and e5e6), bumps and deviations from pure $1/f$ slope are clearly visible. The sample is the same as that shown in Fig. 5.18. . 153

5.20 MR curves, and coherence function recorded at different magnetic field for four electrode pairs on a $w = 600$ nm yoke sample (type II). 155

5.21 α parameter obtained by fitting measured noise spectra at different magnetic field values with a $1/f^{\alpha}$ function. Sample is a $w = 600$ nm sub-micron-scale yoke pattern (type II). . . 156

5.22 Power spectral density measured across different electrode pairs at -25 mT on a $w = 600$ nm yoke sample (type II). The background thermal plus amplifier noise has been subtracted. 157

5.23 $fS_V(f)/V^2$ plotted against $1/d$ for different electrode pairs at -25 mT, for a $w = 600$ nm yoke sample (type II), with d the spacing between two electrodes. $fS_V(f)/V^2$ is averaged between 18 - 42 Hz. 158

6.1 Schematic diagram of the electrochemical noise analysis set-up. 173

6.2 Examples of noise spectra obtained using the spectrum analyser in the absence of an applied field. The black line shows the $1/f^2$ power spectrum. 174

6.3 (a) Power spectral density of type I spectra and (b) corresponding time sequence under applied magnetic field. Note how the amplitude of the voltage fluctuations and the overpotential decrease with applied field. 176

6.4 (a) Power spectral density of type II spectra and (b) corresponding time sequence (b) under applied magnetic field. Note that how the noise amplitude increases above a threshold field < 1 T. 177

6.5 Power spectral density of type II spectra measured with the applied magnetic field parallel and perpendicular to the electrochemical current. 178

6.6 Power spectral density of type II spectra measured within 3 days. For each applied magnetic field level, 4 spectra were recorded at different times, twice on the 1st day (straight line and dashed line), once the 2nd day (dotted line) and once the 3rd day (dashed dotted line), respectively. The spectra, and the magnetic field effect are stable and reproducible in time. 179

6.7 Magnetic field effect on the type II spectra measured by a DAQ board. 180

6.8 The threshold effect of the applied magnetic field on the low frequency plateau of type II spectrum. Each data point is averaged across the PSD in Fig. 6.7 between 0.1 Hz and 1 Hz. The dashed red line is a guide to the eyes. 181

6.9 A time sequence of the bubble evolution reaction under zero magnetic field. Applied current is -10 mA. 182

6.10 Electrochemical impedance spectra of 0.5 M Na_2SO_4 under different applied magnetic fields. The applied current is -10 mA. 183

6.11 Power spectra of hydrogen and deuteron evolution in H_2O and D_2O under applied magnetic field. 186

6.12 Time sequences and power spectra of hydrogen evolution during copper electrodeposition under zero and 1.5 T applied magnetic field. 190

7.1 A diagram showing the seven-terminal Hall noise measurement method. 198

A.1 A diagram of a Stoner-Wohlfarth particle. 212

A.2 A sketch depicts the sample geometry considered in the Draaisma-de Jonge model. 214

A.3 Circuit diagram in analysing the effect of contact noise. Other noise sources except those shown in the diagram are omitted for clarity. 216

A.4 Power spectral density across electrode 2 and electrode 3 in a $w = 2$ μm yoke measured with two different ballast resistors. The bias current was 120 μA. 218

List of Tables

3.1 Specifications of SR552 and SR550 preamplifiers. 70

5.1 List of spin-valve samples measured in Chapter 5. For spin-valve stacks, only the two ferromagnetic layers together with the spacers from the bottom of the stack to the top, are listed for simplicity. The exchange-bias is obtained by depositing 10 nm IrMn directly on the top ferromagnetic layer for all the samples (top-pinned structure). Yoke structures are always patterned with their arms perpendicular to the pinned direction to achieve the cross-anisotropy unless otherwise specified. w denotes the width of the yoke arm, l is the length of the whole yoke structure, and m is the transverse dimension of the yoke. The electrodes in the micrometer-scale yoke sensors are labelled from e1 to e7, in which e1 and e7 are used to pass the bias current, while e2 - e5 are used to probe the voltage. The current contacts in sample set (b) are (c) are not labelled. Hence, the six voltage contacts are labelled e1 to e6. The spacings between adjacent electrical contacts are given in μm. 134

5.2 Covariance matrix of octave noise power measured on electrode pair e3e4 at -102 mT. The sample probed is a $w = 600$ nm yoke pattern (type II). 159

5.3 Covariance matrix of octave noise power measured on electrode pair e3e4 at -25 mT. The sample probed is a $w = 600$ nm yoke pattern (type II). 159

5.4 Covariance matrix of octave noise power measured on electrode pair e2e5 at -25 mT. The sample probed is a $w = 600$ nm yoke pattern (type II). 160

A.1 Some important relations between the partition function and thermodynamic quantities. 205

Chapter 1

Introduction

Hysteresis is the defining property of a ferromagnet. The irreversible, nonlinear and time-dependent response of the magnetization to an external magnetic field is traced as a time- or frequency-dependent open loop, which represents the sequence of metastable states occupied by the magnet as it adapts its domain configuration to the external field. Magnetization processes of ferromagnets have been known for a long time and have been attracting the attention of physicists for an equally long time.

Magnetism is one of the oldest scientific disciplines, but also stands at the forefront of modern nanoscience and nanotechnology [1]. Recent progress in microfabrication and micromagnetic simulation in the last few decades open up a new era in magnetism research, magnetic micro- and nanostructures. These are ultra-small magnetic entities of nanometers to micrometers in at least one of their three dimensions (for reviews see ref.[2, 3, 4, 5]). As the lateral size of a system approaches different fundamental magnetic length scales, lateral confinement due to shape or size effects, and inter-magnet coupling become dominant. The response characteristics, thermodynamic properties, and other key aspects of magnetism may differ significantly from

what was found in bulk materials.

To determine the hysteresis behaviour of a ferromagnet, the essential starting point is the micromagnetic energy function [6, 7].

$$E = \int \{A[\nabla(\frac{\boldsymbol{M}}{\boldsymbol{M}_s})]^2 - K_1 \frac{(\boldsymbol{n}\cdot\boldsymbol{M})^2}{\boldsymbol{M}_s^2} - \mu_0 \boldsymbol{M}\cdot\boldsymbol{H} - \frac{\mu_0}{2}\boldsymbol{M}\cdot\boldsymbol{H}_d(\boldsymbol{M})\}\, dV \quad (1.1)$$

in which A is the exchange stiffness measured in J/m^3, K_1 is the anisotropy constant, $\boldsymbol{M}$ is the magnetization of the sample, $\boldsymbol{M}_s$ is the saturation magnetization, $\boldsymbol{H}$ is the applied magnetic field, $\boldsymbol{n}$ is the unit vector of the local anisotropy direction, and $\boldsymbol{H}_d$ is the demagnetizing field, given by

$$\boldsymbol{H}_d(\boldsymbol{r}) = \frac{1}{4\pi}\int \frac{3(\boldsymbol{r}-\boldsymbol{r}')(\boldsymbol{r}-\boldsymbol{r}')\cdot\boldsymbol{M}(\boldsymbol{r}') - |\,\boldsymbol{r}-\boldsymbol{r}'\,|^2\;\boldsymbol{M}(\boldsymbol{r}')}{|\,\boldsymbol{r}-\boldsymbol{r}'\,|^5}\, dV' \quad (1.2)$$

An analysis of Eqn. (1.1) gives two fundamental length scales for magnetic micro- and nanostructures, the domain wall width parameter [8, 9]

$$\delta_0 = \sqrt{\frac{A}{K_1}} \quad (1.3)$$

and the exchange length

$$l_{ex} = \sqrt{\frac{A}{\mu_0 M_s^2}} \quad (1.4)$$

The domain wall width parameter defines the thickness of the domain wall separating two magnetic domains with different magnetization orientations by $\delta_w = \pi\delta_0$ for a Bloch wall. The domain wall width parameter goes from about 1 nm in extremely hard magnets to a few hundred nm in soft magnets. This means that the domain wall width in typical magnetic

materials is much larger than the lattice spacing but much smaller than the domain size. The exchange length is the length scale below which the exchange interaction between lateral lattice sites dominants. Below this length scale, the exchange interaction is larger than the magnetostatic interaction, hence, the magnetization tends to become aligned. The exchange length is about 2 - 5 nm in conventional magnetic materials. The energy cost to generate non-uniform magnetization below this length scale is so large that a magnetic thin film with its thickness less than the exchange length retains uniform magnetization in its surface normal. The exchange length also determines the transition from a coherent rotation reversal mode to curling mode, and the grain size limit below which the hysteresis loop of a two-phase magnet behaves like that for single-phase magnet (exchange stiffening) [8, 9].

Magnetic micro- and nanostructures are created by two different approaches. The first is a bottom-up strategy, in which sub-micrometer magnetic arrays and particles are either template synthesized or grown by self-organized assembly [10, 11, 12, 13, 14]. This approach is cost effective, leading to a large number of similar micro- or nano-magnets in a single run. However, the drawback of this approach is also obvious. As template synthesis and self-assembly are both techniques offering little control to the processing parameters concerning a single object, a large particle-to-particle, even run-to-run difference is often measured. Measurement on template-synthesized or self-assembled magnetic entities usually only shows their averaged properties. The second is a top-down strategy, in which magnetic structures are patterned from bulk or thin-film material by different lithographic processes [15, 16, 17, 18, 19, 20]. Though this is a low yield and time-consuming approach, it still, however, has the great potential for

revealing the fundamental properties of a single tiny magnet.

The top-down approach raises serious questions about how magnetic properties of such small magnetic entities can be probed. Magnetization switching processes are conventionally measured by some sort of magnetometer, e.g. a vibrating sample magnetometer (VSM), an alternating gradient magnetometer (AGM), or a superconducting quantum interference device (SQUID) [21, 22]. However, most magnetometers are designed for bulk materials. For a single magnetic entity in the low micrometer size range, these macroscale magnetometers are usually not sensitive enough. Other technqiues to characterize magnetic micro- and nanostructures have been developed in the last few decades. These can be roughly summarized into three categories. The first category includes minimized microscale magnetometers. With the improvement of microfabrication technology, a few concepts utilized in macroscopic magnetometers have been adopted to the micro-meter scale, including micro-SQUID [23, 24], micro Hall magnetometers to detect stray field [25, 26, 27], and micro torque magnetometers [28]. These very sensitive devices, however, normally have critical requirements for their operating conditions, e.g. cryogenic temperature and high vacuum. The second category is beam-related techniques. An electron, x-ray or laser beam is sent towards the specimen, and either the transmitted beam (as in Lorentz microscopy [29, 30]), the reflected beam (as in Magneto-optic Kerr effect [31]), or secondary particles generated by the beam (as in scanning electron microscopy with polarization analysis [32]) are detected. This category includes a large number of very different approaches. Some of them have very high time resolution, and are able to characterize the specimen on an ultrafast dynamic timescale [33, 34, 35]. Others have refined spatial resolution, and magnetic structures of 10 nm lateral size can be resolved

[29, 32]. But these technqiues are usually expensive, time comsuming, and require sophisticated experiment set-ups. The third category is a combination of magnetic sensing with scanning probe microscopy, such as magnetic force microscopy [36, 37] and spin-polarized scanning tunnelling microscopy [38, 39]. These are high spatial resolution technqiues, which are also not very difficult to perform. However, due to the complicated nature of different interactions at the surface on a sub-nanometer scale, the interpretation of data collected by these techniques is always non-trivial [40].

An alternative approach to the problem, which has been widely adopted, is instead of measuring magnetic properties of the specimen directly, the magnetically dependent electrical resistance of the sample is sensed by contacting it with electrical leads. With a group of various magnetoresistance (MR) effects and Hall effects, the magnetic properties of the micro- or nano-entity can be deduced [41, 42]. For example, the Anomalous Hall effect has long been utilized in research and industry to characterize ultra-thin magnetic films [43]. The anisotropic magnetoresistance (AMR) has also been used to study the magnetization reversal in magnetic nanoparticles [44, 45, 46]. These measurements are relatively easy to perform. Magnetic microstructures can be integrated into the measurement scheme with only a few additional lithographic steps.

Low frequency fluctuations, or noise — random deviations of a physical quantity from its mean value — have long been recognized to contain important information on kinetic processes in the system [47]. Probing the low frequency electrical noise in micromagnetic structures thus becomes a method to characterize their dynamic properties, and it is very often much more sensitive than measuring the mean quantities [48, 49, 50, 51, 52]. In this work, we explore the low frequency 'fluctuation spectroscopy' as an al-

ternative method in charactering magnetic micro- and nanostructures. The scope of this work has two aspects. One is to utilise low frequency electrical noise measurements and related novel techniques to further characterise magnetization processes in microfabricated magnetic structures and devices. The other is to understand some less explored aspects of low frequency noise in magnetic systems, e.g. spatial correlations and statistical properties. These issues have been investigated in great detail on non-magnetic metallic and semiconducting thin films in the late 70s to early 90s [53, 54, 55, 56, 57, 58]. However, they have been neglected in magnetic systems. Besides its great scientific importance, a better understanding of low frequency noise in micromagnetic structures will also help to improve the design and fabrication of next generation magnetic field sensing devices.

The thesis is organized as follows. In Chapter 2 a short review of previous studies of low frequency electrical noise in magnetic structures has been given, with a brief introduction to the mathematics and physics for electrical noise analysis. We try to give a thorough account of low frequency noise studies on magnetic metals and multilayers over the last 30 years, while giving only a very brief summary on magnetic oxides, as most of the thesis work is related to the former. Chapter 3 introduces the main experimental techniques utilised in this work, summarized as sample fabrication procedures and measurement schemes. Chapter 4 concentrates on the low frequency Anomalous Hall effect noise and first order reversal curve diagrams measured on $(CoFe/Pt)_n$ multilayers with perpendicular magnetic anisotropy. It shows that anomalous Hall effect can be utilised to measure the magnetic fluctuations in a tiny magnetic sample area ($< 10^{-11}$ m^2). Together with the first order reversal curves, we pinpoint two different regions during the magnetization switching of $(CoFe/Pt)_n$ multilayers, namely a fast relax-

ation region due to either the avalanche of the nucleated reversal domains, or the strip out of bubble domains, and a quasi-equilibrium region in between due to the fluctuations of domain walls and creep growth of magnetic domains. In Chapter 5, the spatial correlation and statistical properties of low frequency noise in spin-valve sensors are discussed. We show that the $1/f$ noise in these micromagnetic devices is not spatially correlated down to a lateral distance of 300 - 400 nm, which further confirms the well-accepted understanding that $1/f$ noise is made of local fluctuators which have no spatial correlation. However, macroscopic domain wall motion can create excess noise, most of which has a random telegraphic nature. Here there is much higher spatial correlation and the noise spectrum clearly deviates from an ideal $1/f$ slope. It suggests that a better design of the ferromagnetic layer in magnetic sensors can effectively eliminate telegraphic switches due to random domain motion, especially during magnetization switching, at which point the sensor is at its active region. However, the normal $1/f$ noise is of another source, and is not directly related to macroscopic domain structure. In Chapter 6, we utilise the above developed low frequency noise measurement method to investigate a different problem — the effect of an applied magnetic field on an electrochemical system, the hydrogen bubble evolution on platinum electrodes at high overpotential. We suggest that by looking at the electrochemical noise signal under different applied magnetic fields, more insight into the magnetic field effect can be drawn, and more quantitative analysis will be made possible. In the last chapter, Chapter 7, we summarize the work and suggest a few future possibilities.

References

[1] S. D. Bader. *Rev. Mod. Phys.*, 78:1, 2006.

[2] H. Kronmüller, R. Fischer, M. Seeger, and A. Zern. *J. Phys. D: Appl. Phys.*, 29:2274, 1996.

[3] S. D. Bader. *Surf. Sci.*, 500:172, 2002.

[4] J. F. Bobo, L. Gabillet, and M. Bibes. *J. Phys.: Condens. Matter*, 16:S471, 2004.

[5] K. M. Krishnan, A. B. Pakhomov, Y. Bao, P. Blomqvist, Y. Chun, M. Gonzales, K. Griffin, X. Ji, and B. K. Roberts. *J. Mater. Sci.*, 41:793, 2006.

[6] R. Skomski and J. M. D. Coey. *Permanent Magnetism.* Institute of Physics Publishing, 1999.

[7] R. Skomski. *Spin Electronics*, chapter 10, page 204. Springer-Verlag, 2001.

[8] R. Skomski. *J. Phys.: Condens. Matter*, 15:R841, 2003.

[9] R. Skomski. *J. Magn. Magn. Mater.*, 272-276:1476, 2004.

[10] T. M. Whitney, J. S. Jiang, P. C. Searson, and C. L. Chien. *Science*, 261:1316, 1993.

[11] A. Fert and L. Piraux. *J. Magn. Magn. Mater.*, 200:338, 1999.

[12] P. Gambardella, A. Dallmeyer, K. Maiti, M. C. Malagoli, W. Eberhardt, K. Kern, and C. Carbone. *Nature*, 416:301, 2002.

[13] J. Y. Cheng, W. Jung, and C. A. Ross. *Phys. Rev. B*, 70:064417, 2004.

[14] A. A. Zhukov, A. V. Goncharov, P. A. J. de Groot, M. A. Ghanem, P. N. Bartlett, R. Boardman, and H. Fangohr. *Appl. Phys. Lett.*, 88:062511, 2006.

[15] O. Fruchart, J. P. Nozières, B. Kevorkian, J. C. Toussaint, D. Givord, F. Rousseaux, D. Decanini, and F. Carcenac. *Phys. Rev. B*, 57:2596, 1998.

[16] R. P. Cowburn, D. K. Koltsov, A. O. Adeyeye, M. E. Welland, and D. M. Tricker. *Phys. Rev. Lett.*, 83:1042, 1999.

[17] S. McVitie, G. S. White, J. Scott, P. Warin, and J. N. Chapman. *J. Appl. Phys.*, 90:5220, 2001.

[18] D. Atkinson, D. A. Allwood, G. Xiong, M. D. Cooke, C. C. Faulkner, and R. P. Cowburn. *Nature Mater.*, 2:85, 2003.

[19] J. Sort, B. Dieny, M. Fraune, C. Koenig, F. Lunnebach, B. Beschoten, and G. Güntherodt. *Appl. Phys. Lett.*, 84:3696, 2004.

[20] D. A. Allwood, G. Xiong, C. C. Faulkner, D. Atkinson, D. Petit, and R. P. Cowburn. *Science*, 309:1688, 2005.

[21] D. C. Jiles. *Introduction to Magnetism and Magnetic Materials.* CRC, 2nd edition, 1998.

[22] A. Hubert and R. Schäfer. *Magnetic Domains: The Analysis of Magnetic Microstructures.* Springer-Verlag, 1st edition, 1998.

[23] W. Wernsdorfer, B. Doudin, D. Mailly, K. Hasselbach, A. Benoit, J. Meier, J. Ph. Ansermet, and B. Barbara. *Phys. Rev. Lett.*, 77:1873, 1996.

[24] W. Wernsdorfer, E. Bonet Orozco, K. Hasselbach, A. Benoit, B. Barbara, N. Demoncy, A. Loiseau, D. Doivin, H. Pascard, and D. Mailly. *Phys. Rev. Lett.*, 78:1791, 1997.

[25] M. Rahm, M. Schneider, J. Biberger, R. Pulwey, J. Zweck, D. Weiss, and V. Umansky. *Appl. Phys. Lett.*, 82:4110, 2003.

[26] Y.Q. Li, P. Xiong, S. von Molnár, Y. Ohno, and H. Ohno. *Phys. Rev. B*, 71:214425, 2005.

[27] G. Mihajlović, K. Aledealat, P. Xiong, S. von Molnár, M. Field, and G. J. Sullivan. *Appl. Phys. Lett.*, 91:172518, 2007.

[28] J. Hofer, K. Conder, T. Sasagawa, G. M. Zhao, M. Willemin, H. Keller, and K. Kishio. *Phys. Rev. Lett.*, 84:4192, 2000.

[29] K. J. Kirk, J. N. Chapman, and C. D. W. Wilkinson. *J. Appl. Phys.*, 85:5237, 1999.

[30] A. K. Petford-Long and J. N. Chapman. *Magnetic Microscopy of Nanostructures*, chapter 10. Springer-Verlag, 2004.

[31] D. A. Allwood, G. Xiong, M. D. Cooke, and R. P. Cowburn. *J. Phys. D: Appl. Phys.*, 36:2175, 2003.

[32] M. R. Scheinfein, J. Unguris, M. H. Kelley, D. T. Pierce, and R. J. Celotta. *Rev. Sci. Instrum.*, 61:2501, 1990.

[33] M. R. Freeman and B. C. Choi. *Science*, 294:1484, 2001.

[34] B. C. Choi and M. R. Freeman. *Magnetic Microscopy of Nanostructures*, chapter 3. Springer-Verlag, 2004.

[35] B. C. Choi, J. Ho, G. Arnup, and M. R. Freeman. *Phys. Rev. Lett.*, 95:237211, 2005.

[36] M. R. Koblischka and U. Hartmann. *Ultramicroscopy*, 97:103, 2003.

[37] X. B. Zhu and P. Grütter. *MRS Bulletin*, 29:457, 2004.

[38] I. V. Shvets, R. Wiesendanger, D. Bürgler, G. Tarrach, H. J. Güntherodt, and J. M. D. Coey. *J. Appl. Phys.*, 71:5489, 1992.

[39] O. Pietzsch, A. Kubetzka, M. Bode, and R. Wiesendanger. *Appl. Phys. A*, 78:781, 2004.

[40] H. J. Hug, B. Stiefel, P. J. A. van Schendel, A. Moser, R. Hofer, S. Martin, H. J. Güntherodt, S. Porthun, L. Abelmann, J. C. Lodder, G. Bochi, and R. C. O'Handley. *J. Appl. Phys.*, 83:5609, 1998.

[41] C. Shearwood, S. J. Blundell, M. J. Baird, J. A. C. Bland, M. Gester, H. Ahmed, and H. P. Hughes. *J. Appl. Phys.*, 75:5249, 1994.

[42] C. A. Ross, F. J. Castaño, D. Morecroft, W. Jung, H. I. Smith, T. A. Moore, T. J. Hayward, J. A. C. Bland, T. J. Bromwich, and A. K. Petford-Long. *J. Appl. Phys.*, 99:08S501, 2006.

[43] J. Moritz, B. Rodmacq, S. Auffret, and B. Dieny. *J. Phys. D: Appl. Phys.*, 41:135001, 2008.

[44] J. E. Wegrowe, D. Kelly, A. Franck, S. E. Gilbert, and J. Ph. Ansermet. *Phys. Rev. Lett.*, 82:3681, 1999.

[45] Y. Jaccard, Ph. Guittienne, D. Kelly, J. E. Wegrowe, and J. Ph. Ansermet. *Phys. Rev. B*, 62:1141, 2000.

[46] S. Pignard, G. Goglio, A. Radulescu, L. Piraux, S. Dubois, A. Declémy, and J. L. Duvail. *J. Appl. Phys.*, 87:824, 2000.

[47] Sh. Kogan. *Electronic Noise and Fluctuations in Solids.* Cambridge University Press, 1996.

[48] M. A. M. Gijs, J. B. Giesbers, J. W. van Est, J. Briaire, L. K. J. Vandamme, and P. Beliën. *J. Appl. Phys.*, 80:2539, 1996.

[49] H. T. Hardner, M. B. Weissman, M. B. Salamon, and S. S. P. Parkin. *Phys. Rev. B*, 48:16156, 1993.

[50] B. Raquet, J. M. D. Coey, S. Wirth, and S. von Molnár. *Phys. Rev. B*, 59:12435, 1999.

[51] U. Chandni, A. Ghosh, H. S. Vijaya, and S. Mohan. *Applied Physics Letters*, 92:112110, 2008.

[52] A. Ozbay, A. Gokce, T. Flanagan, R. A. Stearrett, E. R. Nowak, and C. Nordman. *Appl. Phys. Lett.*, 94:202506, 2009.

[53] J. H. Scofield, D. H. Darling, and W. W. Webb. *Phys. Rev. B*, 24:7450, 1981.

[54] R. D. Black, M. B. Weissman, and F. M. Fliegel. *Phys. Rev. B*, 24:7454, 1981.

[55] P. J. Restle, M. B. Weissman, G. A. Garfunkel, P. Pearah, and H. Morkoç. *Phys. Rev. B*, 34:4419, 1986.

[56] G. B. Alers, M. B. Weissman, A. Kinzig, and N. Israeloff. *Phys. Rev. B*, 36:8429, 1987.

[57] C. E. Parman, N. E. Israeloff, and J. Kakalios. *Phys. Rev. B*, 47:12578, 1993.

[58] G. B. Alers, S. Martin, R. A. Hamm, A. Feygenson, and R. D. Yadvish. *Appl. Phys. Lett.*, 66:198, 1995.

Chapter 2

Low Frequency Electrical Noise in Magnetic Materials and Microstructures

In this chapter, we first discuss some fundamental issues and mathematical tools concerning noise analysis. Then different kinds of low frequency electrical noise, based on its spectrum characteristics are discussed. The last section is a short literature review of low frequency noise studies in different magnetic systems, e.g. metals and alloys, multilayered structures (GMR stacks, spin valves and tunnel junctions), and oxides.

2.1 Basic principles

We define the mean of a fluctuating quantity in the time domain as

$$\langle X(t) \rangle = \lim_{T \to \infty} \frac{1}{T} \int_{-T/2}^{+T/2} X(t)\, dt \tag{2.1}$$

which is the average of $X(t)$ across a measuring period T. If $X(t)$ represents the voltage across a resistor, the mean of $X(t)$ is simply the voltage V measured using a voltmeter, with T as its integration time. We can also define the variance, σ^2, of $X(t)$ as

$$\sigma^2 = \langle (X(t) - \langle X(t) \rangle)^2 \rangle = \lim_{T \to \infty} \frac{1}{T} \int_{-T/2}^{+T/2} (X(t) - \langle X(t) \rangle)^2 dt \tag{2.2}$$

If this fluctuating quantity is stationary, its autocorrelation function is defined as

$$C(\tau) = \lim_{T \to \infty} (\frac{1}{T}) \int_{-T/2}^{+T/2} X(t+\tau) X(t)\, dt \tag{2.3}$$

It shows the connection of the signal between consecutive time instants [1]. We can also define the power spectrum density (PSD) of $X(t)$ in the frequency domain as the amplitude squared of the Fourier transformed signal

$$S(f) = \lim_{T \to \infty} \frac{1}{T} | \int_{-T/2}^{+T/2} X(t) \exp(-i2\pi f t)\, dt\, |^2 \tag{2.4}$$

The PSD describes the distribution of the power in a signal across different frequencies [2]. $C(\tau)$ and $S(f)$ are related by the Wiener-Khintchine theorem, which says that the power spectrum is the Fourier transform of the autocorrelation function [3].

$$S(f) = \lim_{T \to \infty} \frac{1}{T} \int_{-T/2}^{+T/2} C(\tau) \exp(-i2\pi f \tau)\, d\tau \tag{2.5}$$

2.2 Low frequency electrical noise

Electrical noise in solids originates from different sources, e.g. defect motion, magnetic domain and local spin fluctuations, charge carriers crossing an energy barrier, electron traps or current redistribution in fluctuating inhomogeneous materials [2]. Despite its large number of different origins, electrical noise can be classified according to its power spectrum characteristic.

2.2.1 Thermal (Johnson) noise

The most frequent cause of noise in a conductor is probably the random movement of electrons due to their thermal energy. This random movement of electrons creates a noise power across the conductor. This noise is called thermal noise, or Johnson noise, first observed by Johnson in 1927 [4], later thoeretically derived by Nyquist from thermodynamics [5]. The power spectrum of thermal noise is described by

$$S_V(f) = 4k_BTR \tag{2.6}$$

with k_B the Boltzmann constant ($k_B = 1.38 \times 10^{-23}$ J K^{-1}), T the absolute temperature in Kelvin, and R the resistance of the conductor. This noise gives a flat and frequency independent spectrum, so it is also called 'white' noise. As the autocorrelation function at $\tau = 0$ is simply the variance of the signal, we have

$$\langle V^2 \rangle = 4k_BTBR \tag{2.7}$$

where B is the bandwidth in which the voltage noise is measured. This noise is only related to the resistance of the conductor, and has no magnetic

origin. However, in magnetoresistive systems, whose resistance depends on their magnetic states, the thermal noise level is also related to the magnetic states of the system. This phenomenon can be understood in general by the two-current model suggested by Mott [6, 7]. Thermal noise sets the absolute noise floor for a measurement, as we will see in the next few chapters.

2.2.2 Shot Noise

In an electronic component where flows of carriers cross potential barriers independently of each other, shot noise is observed due to the discrete nature of charge carriers. In the absence of any correlations, Poissonian shot noise, like thermal noise, is frequency independent and has a power spectrum density

$$S_I(f) = 2eI \tag{2.8}$$

where e is the electron charge and I is the current going through the sample. This is also known as *Schottky's theorem* [8]. It has been observed in various electronic components, such as p-n junctions, transistors, metal-semiconductor contacts, and vacuum tubes [9]. The Fano factor $F = S/2eI$ is defined as the ratio of measured shot noise against its ideal Poissonian value, and can be taken as the unit of transferred charge [10]. Electron-electron interactions can either enhance or suppress the Fano factor [11]. For example, in a tunnel junction between a normal metal and a superconductor, the Fano factor F is 2, because charge is added to the superconductor in Cooper pairs [12]. In magnetic materials and devices, shot noise is normally far less than the thermal noise, so not often observed. However, in certain conditions, e.g. in magnetic tunnel devices at low temperatures, shot noise can be much larger and eventually sets the noise floor. It has

been used to characterize electron-electron interactions during the tunneling process in magnetic tunnel junctions [11, 13].

Recent development in mesoscopic physics has drawn great attention to quantum shot noise. In a quantum conductor in which the cross-section is comparable to the Fermi wavelength, λ_F, the conductance G is quantized and can be related to the transmission probability of each channel, T_n, by the Landauer's formula [14, 15]

$$G = \frac{2e^2}{h} \sum_{n=1}^{N} T_n \tag{2.9}$$

where h is Planck's constant. So the quantum shot noise at zero temperature is

$$S = 2e \frac{2e^2}{h} V \sum_{n=1}^{N} T_n (1 - T_n) \tag{2.10}$$

with the factor $(1 - T_n)$ coming from the Fermi statistics [10]. Quantum shot noise was first measured in quantum point contacts independently by M. Reznikov's group in the Weizmann Institute [16] and C. Glattli's group in Saclay [17], in which they showed the vanishing of quantum shot noise when the conductance is quantized, as predicted by Eqn. (2.10).

2.2.3 Random Telegraph Noise

The generation of two-level random telegraph noise (RTN) can generally be traced to the action of two-level fluctuators [18]. The fluctuator switches back and forth between two states, which are local energy minimums separated by an energy barrier. The fluctuator itself can be either of electrical or magnetic origin [2]. The fluctuator undergoes thermally activated or tunnel transitions between these two energy states. As each state

is coupled differently to charge carriers, so it contributes differently to the sample resistance. The sample resistance thus also undergoes a two-state switching.

The two-level random telegraph noise can be considered as a discrete two-state Markov process. The lifetime of each state is a random variable and the resistance value of each state is fixed. It can be shown that the PSD of a single two-level fluctuator is a Debye-Lorentzian spectrum [19].

$$S_{D-L}(f) = 4\Delta V^2 \frac{(\tau_{up}\tau_{dn})^2}{(\tau_{up}+\tau_{dn})^3} \frac{1}{1+4\pi^2 f^2/f_c^2} \tag{2.11}$$

in which τ_{up} and τ_{dn} are the average lifetimes in the 'up' and 'down' states, respectively, and f_c is the corner roll-off frequency $f_c = \tau_{up}^{-1} + \tau_{dn}^{-1}$. It can be seen that the Debye-Lorentzian spectrum is invariant with the mutual replacement of the up and down states. The only information it contains is the corner frequency f_c and the intensity of the fluctuation at zero frequency. For symmetric random telegraph noise, e.g. $\tau_{up} = \tau_{dn}$, the corner frequency can be approximated as $f_c = \tau_{up}^{-1} + \tau_{dn}^{-1} = \tau^{-1}$, and the Debye-Lorentzian spectrum is reduced to the more familiar form [18]

$$S_{D-L}(f) = \frac{\Delta V^2 \tau}{1+(2\pi f\tau)^2} \tag{2.12}$$

In the strongly asymmetric case, e.g. $\tau_{up} \gg \tau_{dn}$, the spectrum is shot noise like, with one of the two states occupied for a very small fraction of time.

If the two-level fluctuation is thermally activated, the characteristic lifetime τ can be expressed by the Arrhenius relation

$$\tau = \tau_0 \exp(E/k_B T) \tag{2.13}$$

Random telegraph noise has been observed in a large variety of systems, such as metallic nanobridges [20], low temperature Josephson junctions [21, 22], superconducting quantum interference devices (SQUIDs) [23], two-dimensional electron gas, single electron devices [24], giant magnetoresistance spin-valves, and magnetic tunnel junctions. It is shown in the next section that a large number of two-level random telegraph systems can be taken as elemental fluctuators, which together form a $1/f$ spectrum.

2.2.4 $1/f$ noise

$1/f$ noise, also called 'flicker noise' or pink noise, is the kind of voltage fluctuation with a power spectrum density inversely proportional to frequency [25]. Nearly all resistors and amplifiers exhibit $1/f$ noise at low frequency, which merges into the thermal noise background at higher frequencies. In reality, the observed flicker noise spectrum is very variable, with a $1/f^{\alpha}$ behaviour, having the exponent α between 0.5 and 1.5, and extending over a few frequency decades [26]. This noise was first measured by J.B. Johnson in his attempt to capture the shot noise spectrum from a 'thermionic tube' [27] and was given its first theoretical explanation shortly after by W. Schottky [28] (though an intuitive but not very successful one).

It did not take long before people started realising how universal the $1/f$ noise spectrum is in nature, sometimes unexpectedly, for totally different phenomena. In a review paper by J.L. Tandon and H.R. Bilger, the authors gave a few very interesting examples of $1/f$ noise in other systems, e.g. the angular fluctuation spectrum in the earth's rotation and the voltage fluctuation spectrum across resting membrane of myelinated nerve fibers [29]. The signal of radio stations also has a $1/f$ spectrum [30]. In our following discussion, we restrict ourselves to the electrical $1/f$ noise.

The principal feature of $1/f$ noise is that its power spectrum $S_V(f)$ increases continuously as the frequency f goes down to the lowest frequency one can measure. No levelling off of the spectrum $S_V(f)$ is observed. The $1/f$ resistance noise has been measured in a careful experiment down to about 0.5 μHz by Caloyannides [31] and further extended to 10^{-7} Hz by R.A. Dukelow [32]. Such experiments lasted for months and it is very difficult from a technical point-of-view to avoid long-term drift in the measurement. This makes some authors believe that $1/f$ noise is, in fact, not a stationary process, since if it is, based on the Wiener-Khintchine theorem, an infinite power is contained in the fluctuations after integration across the whole frequency range. However, in everyday measurement, this does not become a major issue, since every measurement has a limited time window.

Two other widely accepted facts about $1/f$ have been summarized by Dutta and Horn in their highly recognized review paper as follows [33].

(1) $S_V \propto V^2$. This implies that the bias current through the sample does not generate the fluctuation but merely makes the resistance fluctuations detectable based on Ohm's law.

(2) In any given material, it has been shown that the $1/f$ noise level is inversely proportional to the sample volume. This has been taken as the evidence that the noise is a bulk rather than a surface effect. It has to be pointed out that exceptions are observed in different systems, in which all or part of the $1/f$ noise spectrum can be attributed to surface effects. For example, McWhorter has shown that $1/f$ noise in certain metal-oxide semiconductor field effect transistors (MOSFETs) is due to surface traps [34].

The most widely adopted description of flicker noise is probably the

formula, which was introduced by F.N. Hooge in the late 1960s [35].

$$\frac{S_V}{V^{2+\beta}} = \frac{\gamma}{N_c f^{\alpha}} \tag{2.14}$$

Here α, β, and γ are constants, N_c is the number of charge carriers in the sample. For an ideal $1/f$ noise with α=1 and β=0, γ is dimensionless. This is a purely empirical formula. Though some attempts to give physical explanations to it have been pursued, none of them led to less disagreement than others. In Hooge's early publications, the Hooge parameter γ was set to be a physical constant of 2×10^{-3}, but this was soon modified to fit in a larger set of data. An even more drastic modification of the Hooge's formula has been introduced by some authors, e.g. by Giordano and coworkers, based on their results on $1/f$ noise in metallic thin films [36].

It has long been under debate whether there exists any underlying universal explanation of the $1/f$ phenomenon, which does not depend on a particular materials system, though it has been more or less agreed that a more general approach, trying to summarize all $1/f$ noise under a single framework, is highly unlikely to succeed. The first influential theory of this kind is the temperature fluctuation model suggested by Voss and Clarke [37]. This model treats the $1/f$ resistance noise spectrum as a result of temperature fluctuation across the sample, which leads to a resistance fluctuation through the resistance temperature coefficient, dR/dT. It has been successful in explaining the $1/f$ noise in a few particular systems, e.g. noise in a superconductor close to its critical temperature [38]. A direct result of the temperature fluctuation model is that there exists a large spatial correlation of $1/f$ noise, which depends on the material's thermal diffusion coefficient. However, some well-defined experiments attempting to observe this spatial correlation on the millimetre scale failed [39, 40]. It has later

been widely accepted that the spatial correlation of $1/f$ noise observed in some earlier studies is caused by the thermal heating under a high bias current ($\sim 10^7$ A/cm^2). J.W. Eberhard and P.M. Horn carried out temperature dependent measurement of $1/f$ noise on Cu, Ag, and Ni thin films. They all showed completely different noise - temperature dependence from the prediction of the VC model [41, 42]. Moreover, some other parts of the original evidence in favour of this model has also been discounted by further studies. For example, a series of experiments carried out by Fleetwood and Giordano have shown that the difference in $1/f$ noise in thin metallic films deposited on different substrates can be well attributed to different strain levels created during the metallisation process instead of the differences in thermal conductivity of the substrates, which people originally took to be the reason [43, 44].

Nowadays the best model for $1/f$ noise is probably the construction of a $1/f$ spectrum from superposition of independent two-level fluctuators. The idea of this approach dates back to Schottky's first attempt in finding a physical explanation for $1/f$ noise [28] and was further developed by du Pré in his 1950 paper [45]. The obvious way to 'construct' a $1/f$ noise spectrum is probably to superimpose a large number of two-level fluctuations, mentioned in 2.2.3, with a distribution of the corner frequency $D(f_c) \propto 1/f_c$, in which $D(f_c)\Delta f_c$ is the net variance contributed from a Debye-Lorentzian spectrum with corner frequency from f_c to $f_c + \Delta f_c$ [25]. The validity of this approach has been supported by the work of C.T. Rogers and R.A. Buhrman [46], in which they studied the low frequency noise in metal-insulator-metal junctions with very small cross-sectional areas, $5\times 10^{-10} < A < 10^{-8}$ cm^2 under low temperatures. They have found that the measured spectra at $T \leq$ 80K for all their samples could be resolved into fewer than 5 distinct Debye-

Lorentzian spectra. This experiment proves at least in the case of tunnel junctions, the low frequency $1/f$ noise can be attributed to superposition of a large number of two-level fluctuators.

The first well-accepted model of this kind was suggested by McWhorter [34], which is utilized to explain the observed $1/f$ noise spectrum in MOSFETs. Charge traps form at the semiconductor-oxide interface. The author supposed simple quantum tunnelling from the bulk semiconductor to the charge traps as the rate determined process in the trapping-detrapping process. Hence, the corner frequency distribution $D(f_c)$ can be deduced from the distance l from the traps to the interface.

$$D(f_c) \propto \mid \frac{\partial l}{\partial f_c} \mid D(l) \propto \frac{lD(l)}{f_c} \tag{2.15}$$

since in a quantum tunneling event, we have

$$f_c = f_0 exp(-l/l_0) \tag{2.16}$$

Hence, uniformly distributed charge traps lead to a constant $D(l)$, so $D(f_c) \propto f_c^{-1}$. Superposition of a large number of trapping-detrapping fluctuators with $D(f_c)$ gives a $1/f$ spectrum.

Dutta, Dimon, Horn (DDH) proposed another model to explain results mainly on $1/f$ noise in metallic thin films [47, 33]. This so-called DDH model, was later proved to probably be the most successful $1/f$ noise model ever proposed. This model is based on the fact that in many observations the $1/f^\alpha$ noise has an α value not exactly 1. So the distribution of corner frequencies $D(f_c)$ can not be inversely proportional to f_c. The other important experimental observation is that a $D(f_c) \propto f_c^{-1}$ relation implies a uniform distribution of activation energies, $D(E)$, in a thermally acti-

vated process (Eqn.(2.13)) and this means a $S_V(f)$ directly proportional to temperature, T. This prediction contradicts lots of observations on the temperature dependence of $S_V(f)$. Instead in the DDH model, a strongly peaked $D(E)$ is proposed. The four assumptions the DDH model is based on have been summarized by Giordano and co-workers as follows [48],

(1) The low frequency excess noise is due to the superposition of random processes having thermally activated characteristic lifetimes.

$$S(f) \propto \int S_{D-L}(f)\, D(E)\, dE \tag{2.17}$$

(2) The distribution of activation energies $D(E)$ varies slowly over any interval, when $\Delta E \backsimeq k_B T$.

(3) The process is characterized by an attempt frequency, $f_0 = 1/\tau_0$, that is much larger than the frequency window of the measurement.

(4) The number of fluctuators and the coupling constant between the random processes and the resistance is independent of temperature.

These lead to the important results of the DDH model, which relate the activation energy distribution to the power spectrum under a certain temperature and the temperature dependence of $1/f^{\alpha}$ exponent α.

$$D(E_0) \backsim \frac{2\pi f S_V(f,T)}{k_B T} \tag{2.18}$$

where $E_0 = -k_B T ln(2\pi f \tau_0)$ is the peak activation energy and

$$\alpha(f,T) = 1 - \frac{1}{ln(2\pi f \tau_0)}\left(\frac{\partial ln S_V(f,T)}{\partial ln T} - 1\right) \tag{2.19}$$

with the second equation giving an important test for the DDH model. Various experiments on the temperature dependence of α have been carried out so far, most of them show reasonable, at least qualitative agreement with

the prediction of DDH model, especially in metallic thin films [25, 42]. It has been widely accepted that a DDH-like model can explain the $1/f$ noise property in a large number of different systems. Fig. 2.1(a) shows a measurement carried out by Giordano and co-workers on two carbon resistors [48]. However, occasional contradictions are also found. It is assumption (4) which receives most criticism as there is no reason to believe that the number of the fluctuators or the coupling constant should not change with temperature. For example, Giordano has proposed a modification of Eqn. (2.19) to take account of these two factors.

$$\alpha(f,T) = 1 - \frac{1}{ln(2\pi f \tau_0)}\left(\frac{\partial ln S_V(f,T)}{\partial ln T} - 1 - \frac{\partial ln\, n_f}{\partial ln T} - \frac{\partial ln\, c_f}{\partial ln T}\right) \qquad (2.20)$$

with n_f the number of fluctuators and c_f their coupling coefficient. Another good comment that has been made by several authors, is that it is not clear in the model whether resistance noise averaged by Ohm's law, $S_V(f)/V^2$, or the resistance noise itself, $S_V(f)/I^2$, should be plotted against temperature, especially in materials which have a large resistance-temperature coefficient [48]. The difference in these two cases is small when comparing them with Eqn. (2.19) for a few materials, but can not be neglected in many materials.

2.3 Low frequency electrical noise in magnetic systems

In magnetic materials and devices, noise can originate from magnetic domain and spin fluctuations. A physical coupling process is required to correlate these local 'fluctuators' to the charge carrier, inducing noise which is measurable electrically [2]. In the following sections, we review previous

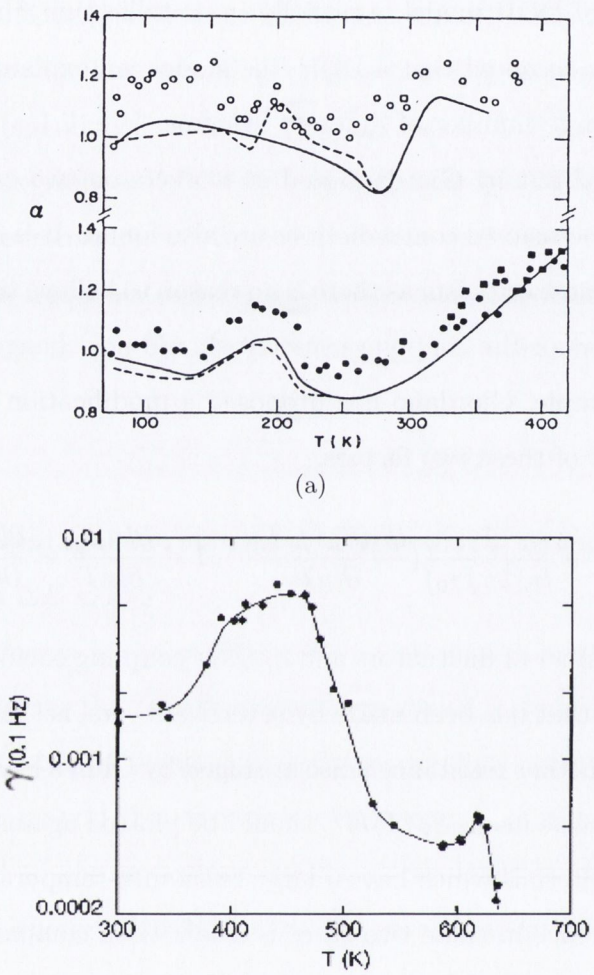


Fig. 2.1: (a) The experimentally measured $1/f^{\alpha}$ slope α compared with the prediction of the DDH model [48]; (b) Hooge parameter γ as a function of temperature for a nickel thin film [49].

studies on electrical noise in three different types of magnetic systems, each with its own coupling mechanism.

2.3.1 Magnetic metals and alloys

The most widely studied noise in magnetic metals and alloys is no doubt the Barkhausen noise [50, 51]. It was discovered by Heinrich Barkhausen in 1919, when he was trying to detect irreversible domain wall movement in nickel wires via the emf generated in a pickup coil by the flux jumps [52]. Nowadays, Barkhausen noise provides the basis for a method of non-destructive testing of steel parts under AC excitation [53]. It has also been used to study correlations in magnetization reversal cascades by recording the jumps with a magneto-optical microscope magnetometer [54, 55]. However, electrical excess noise in magnetic materials is very different from Barkhausen noise. It consists of fluctuations near the equilibrium state of the sample, while Barkhausen noise is the discrete changes of size or rotation of ferromagnetic domains during a magnetization process, which is irreversible [2].

Low frequency (less than a few kHz) electrical noise in magnetic metals and alloys is a subject which had been long ignored. Early studies either suggested that there was no excess low frequency noise in magnetic metals or alloys above the level of a non-magnetic system [56], or simply treated them as having no differences against other non-magnetic materials [57, 42].

In conventional non-magnetic metallic films, low frequency noise mainly originates from grain boundaries and defects [58, 59]. However, in magnetic materials, two other possible coupling mechanisms exist between magnetization or local spin fluctuaions and resistance. One is the anisotropic magnetoresistance (AMR) effect [60].The resistivity of a ferromagnetic sample depends on the angle α between current and the magnetization.

$$\rho = \rho_{\perp} + (\rho_{\parallel} - \rho_{\perp}) cos^2 \alpha \tag{2.21}$$

where $\rho_\perp$ and $\rho_\parallel$ are the resistivity for $\alpha = 90^0$ and $\alpha = 0^0$ respectively. This effect is related to the spin-orbital coupling and d-band splitting in a ferromagnetic material.

The other is domain wall magnetoresistance (DWMR) [61]. It has long been theoretically predicted that magnetic domain walls can create an intrinsic extra contribution to the sample resistance, either by a spin-scattering process [62, 63] or by mis-tracking of electron spin against local magnetization when an electron is passing through the wall [64, 65]. Although the conditions these theories require are sometimes not easy to fulfill and there is still an unsettled debate on the sign of this extra resistance due to the fact that intrinsic domain wall resistance is usually difficult to separate from AMR [66], series of plausible measurements have been realized which lead to the observation of DWMR in various ferromagnetic materials [67, 68, 69, 70, 71, 72, 73]. However, both of these mechanisms are comparably small. AMR ratio is normally about 1%, though much larger values are occasionally observed [60], whereas a typical DWMR value averaged across the whole ferromagnetic film is of the order 0.5%. So the coupling between fluctuators of magnetic origin and the resistance is weak. This probably helps explain why magnetic related low frequency noise in ferromagnetic materials was largely ignored in the literature.

Giordano is probably the first to link low frequency electrical noise in ferromagnetic thin films to their magnetic nature. In his pioneering study [49], which was mostly in search of support or violation of the DDH model, he measured the $1/f$ noise spectrum in nickel thin films from 300 K to above its Curie temperature T_C. Two maxima in $1/f$ noise magnitude, one at T_C and one at 450 K, are observed (Fig. 2.1(b)). The author attributes the maximum at 450 K to microscopic changes in the fluctuating processes.

While, well below this temperature the spins fluctuate nearly independently from their neighbours and the magnetic correlation length is of the lattice parameter scale, an increase in temperature induces a higher correlation of the fluctuating spins. Fluctuators at higher temperature are effectively spin clusters.

A later study on low frequency noise in ferromagnetic materials utilising the AMR effect was carried out by J. Briaire [74]. The author measured the $1/f$ noise and the out-of-phase resistance susceptibility of permalloy ($Ni_{80}Fe_{20}$) under different dc bias field, and concluded that there was a part of the low frequency noise, which could not be accounted for by the fluctuation-dissipation theorem. More recently, E.R. Nowak and co-workers measured the low frequency noise in a zigzag-shaped bridged AMR sensor also made of permalloy [75]. They observed both $1/f$ noise under saturation, and random telegraph noise during the magnetization switching. The Hooge parameter γ was also shown to have a linear relationship against the sensor sensitivity $1/R(dR/dH)$.

There is one report by Raquet et al. [76] in which the low frequency noise in nanostructured nickel Hall crosses and atomic point contacts, made by mechanically controllable break junction method [77], are measured. A non-Gaussian, Lorentzien-like spectrum was observed on top of conventional $1/f$ noise in Hall crosses, which demonstrates the highly inhomogeneous nature of electrical noise in nanometric scale magnetic samples. A correlation length of less than 600 nm was deduced from a spatial correlation measurement conducted simultaneously across two Hall crosses on the same sample. Nickel atomic contacts showed huge random telegraph switchings under 17 K. Another work carried out by Cespedes et al. reported low frequency noise in nickel nanoconstrictions, which were fabricated by electron beam

lithography [78]. These ferromagnetic constrictions, a few tens of nanometers in width, were once believed to have huge magnetoresistance responses due to a highly compressed domain wall pinned at the constriction [79, 80]. The authors observed a random telegraph noise together with $1/f$ noise in the low frequency range. The $1/f$ noise slope increases when a small magnetic field of several mT is applied.

More recently, two groups have reported measurements on low frequency noise in electrodeposited nickel nanowires embedded in alumina or polycarbonate membranes [81, 82]. Though different in details, they both observed an excess low frequency noise, which was strongly correlated with the applied magnetic field, and attributed it to a domain wall scattering process.

It needs to be stated that other much stronger coupling mechanisms also exist in magnetic materials, which lead to a more pronounced low frequency magnetic noise. For example, low frequency noise in antiferromagneic chromium, has been well characterized by Weissman and coworkers [83]. They measured tensor properties of resistance fluctuations in chromium films and concluded that there was strong evidence to relate the observed $1/f$ noise to rotations of the linear polarization of domains in the transverse spin-density-wave structure.

2.3.2 Magnetic mutilayers

Magnetic multilayers, namely giant magnetoresistance (GMR) stacks, spin-valves (SVs) and magnetic tunnel junctions (MTJs), have become the focus of the magnetics community for the last decade, partly due to their use as test beds for new spin-related physics and also partly due to their applications in sensors, magnetic read heads and magnetic random access memory (MRAM). Low frequency noise in GMR and TMR structures also

attracts great attention. Understanding low frequency noise in these magnetic multilayers, is a key for designing and fabricating magnetic sensors and read heads with lower noise background.

Giant magnetoresistance was first discovered independently by the groups of A. Fert [84] and P. Grünberg [85] in Fe/Cr multilayers. The resistance change of the multilayer stack under magnetic field is one or two orders of magnitude larger than the conventional AMR effect. The magnetoresistance ratio is defined as

$$\frac{\Delta R}{R} = \frac{R_{AP} - R_P}{R_P} \tag{2.22}$$

in which R_P and R_{AP} are the resistances of the sample when alternated ferromagnetic layers are aligned in parallel and antiparallel respectively. The giant magnetoresistance is a spin-related effect. Electrons with spin-up and spin-down are scattered differently with respect to the direction of the magnetization, giving R_P and R_{AP} [86].

Low frequency noise in GMR stacks was measured in Co/Cu multilayers shortly after the discovery of the GMR effect [87, 88]. The authors deduced a fluctuation-dissipation theorem for magnetic multilayers and showed that the low frequency noise in GMR stacks can be accurately predicted from the out-of-phase resistance susceptibility, except in the vicinity of zero applied field, where noise is an order of magnitude larger than the predicted value. Low frequency noise against field in patterned $Ni_{80}Fe_{20}$/Cu multilayers has also been measured by Gijs et al. [56]. In the same work they also compared it with the low frequency noise in permalloy films.

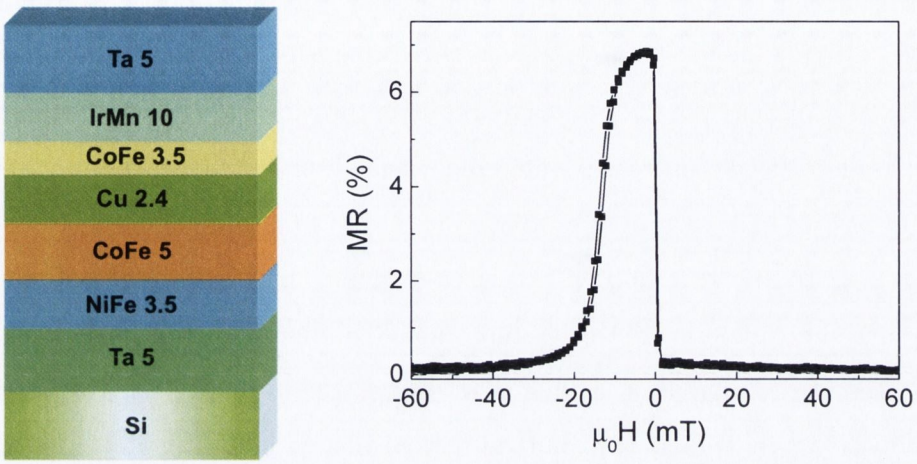
Another study carried out by S.E. Russsek [89] and co-workers has shown that besides the conventional $1/f$ noise, random telegraph noise also dominates during the magnetization switching in a $Ni_{82}Fe_{18}$/Ag multilayer stack.

The up state and down state lifetimes can be well described by a thermal activation process governed by the Arrhenius characteristic rates.

A recent study on low frequency noise in GMR stacks was conducted by Aliev and coworkers [90], in which they measured domain-wall magnetoresistance and noise in $[Fe/Cr]_{10}$ antiferromagnetically coupled multilayers under different current bias. A suppression of the low frequency noise during the magnetization switching was observed under a current bias of about 2×10^5 A/cm^2. They attributed the effect to a reduction of local magnetic disorder by large domain wall movement under spin polarized current.

Spin-valves are also based on the giant magnetoresistance effect. A basic spin-valve consists of two ferromagnetic layers separated by a non-magnetic spacer. The two ferromagnetic layers are engineered to be able to switch independently, so parallel and antiparallel alignments of them can be achieved in the device. Two common methods are utilized to realize the independent switching of the ferromagnetic layers. The easiest way is to use two ferromagnets with different coercive fields, e.g. a hard and a soft magnet. This forms a pseudo spin-valve. The other way, which is more effective, is to use the exchange bias (EB) between an antiferromagnet and a ferromagnet to pin the magnetization of the adjacent ferromagnetic layer to a certain direction [91]. Fig. 2.2 shows a diagram of a spin-valve structure grown by the Shamrock sputtering tool in our laboratory and its MR curve.

The first comprehensive study on low frequency noise in spin-valves was carried out by Gijs and coworkers [92], in which they fabricated yoke-shaped spin-valve magnetic elements and studied their noise - field response. It was reported that low frequency noise reaches its maximum during the alignment of the two ferromagnetic layers switching between parallel and antiparallel where dR/dH peaks. Similar noise levels have been observed when the



(a) (b)

Fig. 2.2: A diagram showing a spin-valve structure (a) and its MR curve (b) (courtesy of Dr. Gen Feng).

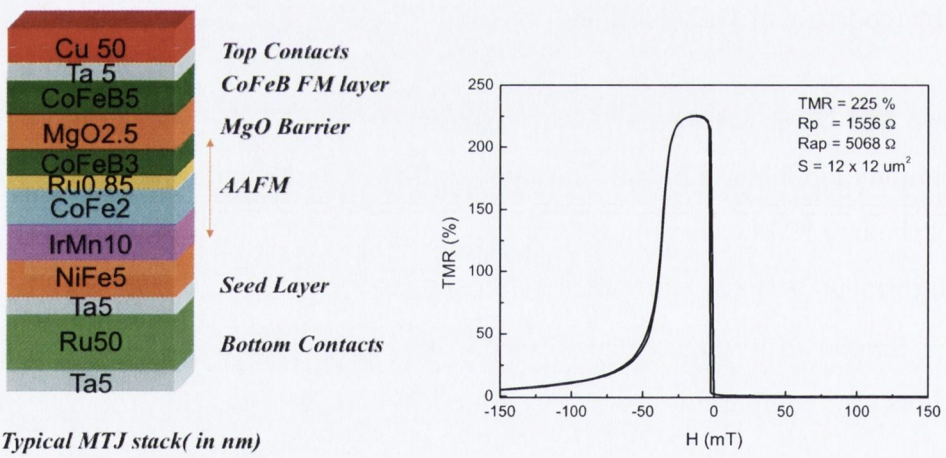
two FM layers are aligned either parallel or antiparallel to each other. A simple model based on calculating the effect of small variances in the angle of the free FM layer using Boltzmann statistics was introduced. Qualitative agreement between experiments and the model has been shown.

Similar experiments have been carried out by a number of different authors and comparable results are found [93, 94, 95, 96]. In a recent study, Nowak and co-workers showed that the low frequency noise in spin-valves also closely obeys the fluctuation-dissipation relation [97]. They also relate the Hooge's parameter to the sensitivity of a spin-valve sensor $(1/R)dR/dH$.

$$\gamma_{mag} = \frac{\Omega f S^{mag}}{V^2} = \varepsilon(f,H)\frac{k_B T}{\pi \mu_0 M_s}\frac{\Delta R}{R}\left(\frac{1}{R}\frac{dR}{dH}\right) \tag{2.23}$$

in which Ω is the volume of the sample, $\varepsilon(f,H) \approx \chi_R^{"}/\chi_R^{'}$ is the ratio of out-of-phase resistance susceptibility against its in-phase counterpart.

A magnetic tunnel junction is made by replacing the non-magnetic spacer layer in a spin-valve with a thin insulating tunnel barrier, normally AlO_x or MgO [98]. Electron preserves its spin during tunnelling and a mismatch of the spin-dependent band structure in the two ferromagnetic electrodes due to their relative alignment leads to large MR ratios. In 2007, MgO-based MTJ with room temperature TMR of more than 500% has been demonstrated by H. Ohno and co-workers [99]. The MTJ's high MR ratio under room temperature makes them ideal candidates for next-generation high-sensitivity magnetic field sensors. Fig. 2.3 illustrates an MTJ stack produced in the Shamrock sputtering tool in our laboratory and its MR response.



(a) (b)

Fig. 2.3: A diagram showing a MTJ stack (a) and its MR curve (b) (courtesy of Dr. Gen Feng).

The first low frequency noise study on MTJs was carried out by E.R. Nowak and M.B. Weissman [100] in 1998 on samples with AlO_x as tunnel barriers. Other studies on AlO_x-based MTJs are followed since then [101,

102, 103, 104, 105, 106, 107, 108]. It was found that the low frequency noise in MTJs is dominated by the tunnel barrier, most likely due to a charge-trapping process, and can not be effectively suppressed even under a high magnetic field. Two-level fluctuations due to large domain wall movement has also been observed. This suggests that the magnetic stability is a crucial factor for reducing the low frequency noise in MTJs, especially during the magnetization switching. In magnetic tunnel junctions, the Hooge formula is recast to reveal the fact that the low frequency noise is closely related to the area of the tunnel junctions.

$$\frac{S_V(f)}{V^2} = \frac{\gamma}{Af^\alpha} \tag{2.24}$$

with A the area of the tunnel junction, so the Hooge's parameter γ has the units of μm^2.

Later, electrical noise in MgO-based MTJs with CoFeB as ferromagnetic electrodes was also measured by several groups. These MTJs normally have much higher TMR ratio than those with AlO_x as tunnel barriers. Similar noise - field dependence has been observed as that in AlO_x-based MTJs. These studies also focused on how a low Hooge parameter γ could be achieved by either optimizing the tunnel barrier, or stabilising the FM electrodes. It has turned out that most of these MTJs have a very large resistance area product (RA) of 1 $M\Omega\mu m^2$ and an γ between 10^{-9} to $10^{-7}\mu m^2$, as summarized by Gokce et al. [109]. Though having a much larger MR effect, MTJs suffer high $1/f$ noise levels, which limits their use in magnetic field sensing applications. For pT magnetic field sensors, it is required that the Hooge parameter γ be further reduced by about two orders of magnitude to $< 10^{-10}$ μm^2. Besides this general agreement on noise levels, several issues are still under serious debate. For example, Fermon and co-workers

have shown that annealing has little influence on the noise level in MgO-based tunnel junctions [110], however a more recent study by Russek and co-workers suggests that hydrogen annealing under high magnetic fields can significantly alter the shape of the noise spectra, thus a reduction in low frequency noise can be expected [111].

Fermon and Freitas very recently studied the possibility of using an array up to 3000 MTJs connecting in series or in parallel for sensing applications [112]. The idea behind can be understood in a simple calculation. The detectivity D in $T/Hz^{1/2}$ of a magnetic field sensor is defined as

$$D = \frac{S_V}{\Delta V/\Delta H} \tag{2.25}$$

with $\Delta V/\Delta H$ the derivative of the transfer curve of the sensor. For a single MTJ, the voltage noise across the junction can be described as

$$S_V(f) = 2eIr^2 coth(\frac{eV}{2k_BT}) + \frac{\gamma V^2}{A}\frac{1}{f} \tag{2.26}$$

with r the resistance of a single MTJ. The first term covers both the thermal noise and the shot noise. For N MTJs connected in series, each having a resistance r, it can be shown that

$$D = \frac{1}{\varepsilon}\sqrt{\frac{4Rk_BT}{V_{tot}^2} + \frac{\gamma}{NA}\frac{1}{f}} \tag{2.27}$$

in which R is the resistance of the whole MTJ network, and $\varepsilon = (\Delta R/(R\Delta H)$ is the TMR ratio per unit field change. In this case, the $1/f$ noise in the junctions have been reduced to $1/\sqrt{N}$ of its original value. However, the thermal noise background increases with a factor of $\sqrt{N}$ as the total resistance of the network increases. Hence, it is not possible to stack thousands of MTJs together, since the resistance will become impractically large to

handle. An improved scheme consists of M parallel legs of N MTJs in series. The detectivity of this MTJs network is

$$D = \frac{1}{\varepsilon}\sqrt{\frac{4Rk_BT}{V_{tot}^2} + \frac{\gamma}{MNA}\frac{1}{f}} \tag{2.28}$$

in which R is still the resistance of the network and now can be adjusted by M and N. The $1/f$ of the MTJs network can be seen as $1/f$ noise in a single MTJ having an effective area of MNA. Their experiments also confirmed the above theoretical model [112].

Aliev and co-workers characterized the low frequency noise in single crystalline MTJs grown by molecular beam epitaxy (MBE), with MgO (111) as the tunnel barrier and Fe (110) as FM electrodes [113]. These junctions have a TMR ratio of only 15 - 20 % and a large Hooge parameter between 10^{-6} to 10^{-4} μm^2, which is more than an order of magnitude higher than what was observed in polycrystalline MgO-based MTJs with CoFeB as FM electrodes having similar RA values. This suggests that the Hooge parameter in magnetic tunnel junctions is very weakly dependent on whether the barrier and the electrodes are single crystalline. They also observed a magnetic field dependent of Hooge parameter γ in their large 20 μm $\times$ 20 μm junctions, and attributed it to the magnetoelastic constriction in the soft Fe layer.

Shot noise in magnetic tunnel junctions has also been characterised by several authors. In the original report by Nowak et al. [102], they found a full Poissonian shot noise with the Fano factor $F \approx 1$ in AlO_x-based MTJs with AP alignment of the FM electrodes. This was followed by another report by the same group, in which strong suppression of the Fano factor down to about 0.45 was observed [13]. Aliev and co-workers also measured shot noise in AlO_x-based MTJs, either with or without Cr doping at the

barrier layer. They reported a Fano factor of approximately 0.65 in the junctions without Cr doping, however, the Fano factor is restored to 1 in the Cr-doped ones. Two simple models have been developed in the same paper, utilising sequential tunneling through an island inside the tunnel barrier, to explain the observed suppression of Fano factor in the undoped junctions. In a later report, the same authors also measured the shot noise in epitaxial MTJs with MgO (001) tunnel barrier and Fe (001) as FM electrodes. These tunnel junctions have large TMR ratio at low bias voltages due to the fully spin polarized Δ_1 bulk electrons in Fe(001), which are reflected for the AP state and well transmitted for the P state. They measured a full Fano factor in these junctions, both under P and AP states of the FM electrodes. It has to be admitted at this stage that the origin of the suppression of Fano factors in some of the MTJs is still not well understood and more experimental and theoretical work is needed to elucidate the problem.

It is worth mentioning two other approaches in eliminating the influence of low frequency $1/f$ noise to the sensitivity of GMR- and TMR- based magnetic sensors. The first one is to integrate spin-valves and MTJs into microelectromechanical systems (MEMS). This approach is independently pursued by Edelstein and co-workers in the U.S. Army Research Laboratory [114, 115], and Freitas' group in INESC-MN, Lisbon [116, 117]. The idea is to microfabricate magnetic flux guides which can be electrostatically driven at a working frequency much higher than the $1/f$ knee of the sensor noise spectrum, where only white noise contributes. This method shifts the operating frequency of the sensor to high frequencies and gives about two orders of magnitude gain in the sensor detection limit, as the detection limit at low frequencies of a conventional magnetic field sensor is set ultimately by the $1/f$ noise. Edelstein's group has fabricated flux concentrators deposited

on electrostatic comb drives with a resonant frequency of about 10 kHz. Low frequency magnetic field signal shows up in their device as side bands, when the comb drives are driven at their resonance. They have shown that magnetic field with frequency as low as ~1 Hz could be demodulated by a lock-in amplifier, so the bandwidth of the drive does not set the detection frequency limit. Detectivity increase of a factor of 10 at 1 Hz is expected with their device [118]. Freitas' group succeeded in fabricating flux guides deposited on a cantilever, which is suspended on top of a GMR sensor. The vibration of the cantilever thus converts a dc field into an ac field. However, in their first device, the field modulation efficiency is very low (0.11%). So the lowest detectable field of their MEMS-GMR sensor is only 2.7 μT [116]. In later work [117], they replaced the cantilever flux guide with a MEMS 'torsionator'. This increases the field modulation efficiency to about two orders of magnitude, and gives a detectivity of 40 nT/Hz$^{1/2}$. The other approach was innovated by Fermon's group in CEA, Saclay [119, 120]. They fabricated GMR or MTJ sensors on top of a constricted superconducting loop serving as flux-to-field transformer. These devices are named mixed sensors. It has been demonstrated that it is capable of measuring a magnetic field as tiny as 32 fT at low temperature [119].

2.3.3 Magnetic Oxides

We can roughly divide magnetic oxides discussed in this section into two categories, half-metallic oxides and mixed-valence magnetic perovskites exhibiting colossal magnetoresistance (CMR).

Half-metals are ferromagnets with only one type of conduction electrons, either spin-up or spin-down. They are interesting materials for spintronics applications as fully polarized spin sources or analysts. It is of fundamen-

tal interest to study whether their electrical noise is related to the half-metallicity. Large $1/f$ noise, several orders of magnitude higher than normally found in metals, was measured in CrO_2, Fe_3O_4, and $La_{2/3}Sr_{1/3}MnO_3$ (also a mixed-valence perovskite), all proposed half-metallic oxides [121]. In CrO_2 films part of the $1/f$ noise has been shown to have magnetic origin, which can be suppressed by applying a high magnetic field of 4 T. However, the resistance fluctuation still remains very high even compared with some other oxides ($\gamma \approx 2000$). Whereas in Fe_3O_4, a ferrimagnetic half-metal, $1/f$ noise having a Hooge parameter $\gamma \approx 80$ at room temperature, shows no dependence on the applied magnetic field but it is strongly dependent on temperature. This temperature dependence has been attributed to the variation of the density of carriers in the conduction network. In $La_{2/3}Sr_{1/3}MnO_3$, an applied magnetic field of 12 T has been shown to suppress the $1/f$ noise to one quarter of its zero field level. The temperature dependence of the $1/f$ noise shows reasonable agreement with the DDH model.

Mixed-valence manganese oxides $(R_{1-x}A_x)MnO_3$, where R is a rare-earth cation and A is an alkali or alkaline earth cation, having a perovskite structure have received great attention since 1990s due to the colossal magnetoresistance (CMR) effect observed near their T_C [122]. It is generally understood that the manganese oxide is in a paramagnetic semiconducting phase at high temperatures, and in a ferromagnetic metallic phase at a low temperature. The transition between these two phases is called 'metal-insulator transition'. The CMR effect develops from the fact that this transition temperature can be shifted by an applied magnetic field, normally of several tesla. Based on the intensive research in the last two decades, unfortunately it turns out that the magnetic field required for CMR effect

is far too large for magnetic sensing applications. However, mixed-valence manganese still remains as an interesting system, where many materials physics concepts can be probed, e.g. percolation phase segregation [123]. For a recent review of noise studies on perovskite oxides we refer to section II of Méchin et al. [124].

In the paramagnetic semiconducting phase of manganese perovskite, the hopping conductivity depends strongly on the oxygen stoichiometry and defects [2]. Hence oxygen diffusion may introduce large low frequency noise in the sample, which is not of magnetic origin. This was used as an non-destructive method to characterize the quality of manganite thin films [125]. A Hooge parameter as low as 8×10^{-2} was reported in epitaxial $La_{2/3}Ca_{1/3}MnO_3$ (LCMO) thin flims on lattice-matched single crystal $NdGaO_3$ substrates [126]. The authors also showed that the low frequency noise in LCMO thin films decreases when less strain is introduced between the substrate and the thin film. It has been observed that there is an increase of the noise level of a few orders of magnitude around the metal-insulator transition temperature in CMR oxides. The noise normally peaks slightly lower in temperature than resistance. An applied magnetic field of a few tesla has been shown to effectively suppress the noise peak. Hence, we can infer that the low frequency noise in this case is mainly of magnetic origin [127, 128, 129].

Low frequency noise has been utilised as a dynamic probe of the phase percolation nature of the manganese perovskites. It has been suggested by various studies that there is an extended temperature range around T_C, where ferromagnetic metal clusters exist in a matrix of paramagnetic semiconductor [130, 131]. The material in this temperature range is actually largely inhomogeneous. Raquet et al. [123] measured alternatively large

non-Gaussian noise and giant RTN with resistance steps as high as 0.01 % to 0.2 % between 4 and 180 K in LCMO films deposited on $LaAlO_3$ substrates. This is quite surprising for such a large, macroscopic sample. These fluctuators are very sensitive to temperature change and at certain temperatures only a single fluctuator dominates. The measured average lifetimes of the up and down states can be explained within the two-level fluctuator model, by including a field-dependent energy barrier $E_i(H) = E_i(0) + \Delta m_i \cdot H$, in which E_i is the barrier height to escape from state i and Δm_i is the moment difference between two states. Fitting of the data gives a Δm_i of 550 μ_B, with μ_B the Bohr magnetron. This corresponds to a sample volume of only a few nm^3. Weissman and co-workers also carried out low frequency noise and resistance susceptibility measurement on $La_{0.7}Ca_{0.3}MnO_3$ film grown on NGO (001) substrates [131]. They observed that the in-phase susceptibility appears close to the Curie Temperature, where dR/dT is a maximum. This can be directly related to the fluctuation-dissipation theorem (see Appendix A.2). The out-of-phase susceptibility follows the in-phase counterpart for most of the temperature range but deviates from it near T_C. They also show a slow fluctuation of the low frequency noise magnitude close to T_C. These lead the authors to believe that there exists another phase, namely antiferromagnetic insulator (AFI), together with the other two well-known phases (ferromagnetic metal and paramagnetic insulator), in a temperature range not far from T_C.

Low frequency noise in CMR manganese single grain boundary junctions has also been studied by different authors. These films are epitaxially grown on bicrystalline $SrTiO_3$ or $LaAlO_3$ substrates and show large tunneling magnetoresistance effect under reasonably low field of 20 - 100 mT [132]. Mathieu et al. measured low frequency noise in pulsed-laser deposited

$La_{0.7}Sr_{0.3}MnO_3$ grain boundary junctions on $LaAlO_3$ bicrystal substrates [133]. They found both conventional $1/f$ noise and two-level fluctuations in these junctions, which could be suppressed by applying a magnetic field of 1 T. They attributed it to the modification of domain structure under applied magnetic field around the grain boundary area. Gross and co-workers measured $La_{2/3}Ca_{1/3}MnO_{3-\delta}$ junctions deposited on $SrTiO_3$ bicrystal substrates. These samples show tunneling magnetoresistance as high as 300 % under low temperature. They showed a dependence of the low frequency noise level on the current density in the film. There is a decrease of average octave noise power when the applied current is increased from 10 μA to 1000 μA. Applying a magnetic field can also suppress the low frequency noise, however the magnetic field required is much larger ($\backsim$ 12 T). Some two-level fluctuators are not effectively suppressed even under a magnetic field of 500 mT. This leads them to suggest that the main mechanism of low frequency fluctuations in their samples is the inelastic tunneling through interacting local magnetic states in the grain boundary, which are spin glass like. Their noise data can be at least qualitatively explained by a modified model first suggested by Glazman and Matveev [134], which takes account both the elastic direct or resonant tunneling and inelastic tunnelling involving more impurity states.

During noise measurement on magnetic oxides, special care has to be taken to eliminate the contribution of contact noise to the measured spectrum due to the large resistance of these samples. In Weissman and co-workers' experiment [131], they chose to pattern the sample into a bridge structure, in which current fluctuations generated by poor contacts through the bridge can be roughly cancelled out. The remaining current fluctuation was then measured separately and eliminated from the noise voltage

across the sample bridge. A more complicated technique was introduced by C. Barone et al. [135]. They used series measurements to independently measure the bias source current noise $i_n^{I_B}$, the bias resistor voltage noise $e_n^{R_s}$, and the preamplifier equivalent input voltage noise e_n^A, the four-porbe, two-probe and zero bias noise of the system S_4^{exp}, S_2^{exp}, and S_0^{exp}. The real sample noise $e_n^{R_M}$ is then recovered by a linear combination of the measured quantities from solving the circuit analytically when the noise sources are not correlated. In another paper from the same group, they also showed that failing to effectively eliminate the contact noise from the measurement on oxides samples can lead to false interpretation of the results [136].

Our literature review shows that there have already been a great number of publications in relation to low frequency noise in magnetic materials and micro-structures, especially in systems exhibiting large magnetoresistance (GMR, TMR and CMR) effects, which is closely related to sensor applications. However, there is a lack of studies on simple ferromagnetic materials and the mechanism which leads to the observed noise is still not very well understood. The work presented in this thesis is hoping to move a step further in the above directions.

References

[1] A. Ambrózy. *Electronic noise.* McGraw-Hill, New York; London, 1982.

[2] B. Raquet. *Spin Electronics*, chapter 11, page 232. Springer-Verlag, 2001.

[3] Philippe Réfrégier. *Noise Theory and Application to Physics: From Fluctuations to Information.* Springer-Verlag, New York, 2004.

[4] J. B. Johnson. *Phys. Rev.*, 29:367, 1927.

[5] H. Nyquist. *Phys. Rev.*, 32:110, 1928.

[6] N. F. Mott. *Proc. Phys. Soc.*, 47:571, 1935.

[7] N. F. Mott. *Proc. roy. Soc. A*, 153:699, 1936.

[8] W. Schottky. *Ann. Physik*, 57:541, 1918.

[9] A. van der Ziel. *Noise: sources, characterization measurement.* Englewood Cliffs, London, 1970.

[10] C. Beenakker and C. Schönenberger. *Phys. Today*, 56:37, 2003.

[11] R. Guerrero, F. G. Aliev, Y. Tserkovnyak, T. S. Santos, and J. S. Moodera. *Phys. Rev. Lett.*, 97:266602, 2006.

[12] F. Lefloch, C. Hoffmann, M. Sanquer, and D. Quirion. *Phys. Rev. Lett.*, 90:067002, 2003.

[13] L. Jiang, J. F. Skovholt, E. R. Nowak, and J. M. Slaughter. *Proc. of SPIE*, 5469:13, 2004.

[14] R. Landauer. *IBM J. Res. Develop.*, 1:233, 1957.

[15] S. Datta. *Quantum Transport: Atom to Transistor.* Cambridge University Press, Cambridge, 2005.

[16] M. Reznikov, M. Heiblum, H. Shtrikman, and D. Mahalu. *Phys. Rev. Lett.*, 75:3340, 1995.

[17] A. Kumar, L. Saminadayar, D. C. Glattli, Y. Jin, and B. Etienne. *Phys. Rev. Lett.*, 76:2778, 1996.

[18] Y. Yuzhelevski, M. Yuzhelevski, and G. Jung. *Rev. Sci. Instrum.*, 71:1681, 2000.

[19] S. Machlup. *J. Appl. Phys.*, 25:341, 1954.

[20] K. S. Ralls and R. A. Buhrman. *Phys. Rev. Lett.*, 60:2434, 1988.

[21] R. T. Wakai and D. J. Van Harlingen. *Phys. Rev. Lett.*, 58:1687, 1987.

[22] J. Eroms, L. C. van Schaarenburg, E. F. C. Driessen, J. H. Plantenberg, C. M. Huizinga, R. N. Schouten, A. H Verbruggen, C. J. P. M. Harmans, and J. E. Mooij. *Appl. Phys. Lett.*, 89:122516, 2006.

[23] R. T. Wakai and D. J. Van Harlingen. *Appl. Phys. Lett.*, 49:593, 1986.

[24] P. D. Dresselhaus, L. Ji, S. Y. Han, J. E. Lukens, and K. K. Likharev. *Phys. Rev. Lett.*, 72:3226, 1994.

[25] M. B. Weissman. *Rev. Mod. Phys.*, 60:537, 1988.

[26] E. Milotti. *arXiv:physics/0204033v1.*

[27] J. B. Johnson. *Phys. Rev.*, 26:71, 1925.

[28] W. Schottky. *Phys. Rev.*, 28:74, 1926.

[29] J. L. Tandon and H. R. Bilger. *J. Appl. Phys.*, 47:1697, 1976.

[30] R. F. Voss and J. Clarke. *Nature*, 258:317, 1975.

[31] M. A. Caloyannides. *J. Appl. Phys.*, 45:307, 1974.

[32] R. A. Dukelow. PhD thesis, California Institute of Technology, 1974.

[33] P. Dutta and P. M. Horn. *Rev. Mod. Phys.*, 53:497, 1981.

[34] A. L. McWhorter. *Semiconductor Surface Physics*, page 207. Uniersity of Pennsylvania, Philadelphia, 1957.

[35] F. N. Hooge. *Phys. Lett. A*, 29:139, 1969.

[36] F. M. Fleetwood and N. Giordano. *Phys. Rev. B*, 27:667, 1983.

[37] R. F. Voss and J. Clarke. *Phys. Rev. B*, 13:556, 1976.

[38] J. Clarke and G. Hawkins. *Phys. Rev. B*, 14:1976, 2826.

[39] J. H. Scofield, D. H. Darling, and W. W. Webb. *Phys. Rev. B*, 24:7450, 1981.

[40] R. D. Black, M. B. Weissman, and F. M. Fliegel. *Phys. Rev. B*, 24:7454, 1981.

[41] J. W. Eberhard and P. M. Horn. *Phys. Rev. Lett.*, 39:643, 1977.

[42] J. W. Eberhard and P. M. Horn. *Phys. Rev. B*, 18:6681, 1978.

[43] D. M. Fleetwood and N. Giordano. *Phys. Rev. B*, 25:1427, 1982.

[44] D. M. Fleetwood and N. Giordano. *Phys. Rev. B*, 28:3625, 1983.

[45] F. K. du Pré. *Phys. Rev.*, 78:615, 1950.

[46] C. T. Rogers and R. A. Buhrman. *Phys. Rev. Lett.*, 53:1272, 1984.

[47] P. Dutta, P. Dimon, and P. M. Horn. *Phys. Rev. Lett.*, 43:646, 1979.

[48] D. M. Fleetwood, T. Postel, and N. Giordano. *J. Appl. Phys.*, 56:3256, 1984.

[49] N. Giordano. *Phys. Rev. B*, 53:14937, 1996.

[50] B. Alessandro, C. Beatrice, G. Bertotti, and A. Montorsi. *J. Appl. Phys.*, 68:2908, 1990.

[51] J. R. Petta, M. B. Weissman, and K. P. O'Brien. *Phys. Rev. E*, 54:R1029, 1996.

[52] H. Barkhausen. *Z. Phys.*, 20:401, 1919.

[53] D. M. Stewart, K. J. Stevens, and A. B. Kaiser. *Curr. Appl. Phys.*, 4:308, 2004.

[54] E. Puppin. *Phys. Rev. Lett.*, 84:5415, 2000.

[55] D. H. Kim, S. B. Choe, and S. C. Shin. *Phys. Rev. Lett.*, 90:087203, 2003.

[56] M. A. M. Gijs, J. B. Giesbers, J. W. van Est, J. Briaire, L. K. J. Vandamme, and P. Beliën. *J. Appl. Phys.*, 80:2539, 1996.

[57] J. H. Scofield, J. V. Mantese, and W. W. Webb. *Phys. Rev. B*, 32:736, 1985.

[58] A. H. Verbruggen, R. H. Koch, and C. P. Umbach. *Phys. Rev. B*, 35:5864, 1987.

[59] M. J. C. van Homberg, A. H. Verbruggen, P. F. A. Alkemade, S. Radelaar, E. Ochs, K. Armbruster-Dagge, A. Seeger, and H. Stoll. *Phys. Rev. B*, 57:53, 1998.

[60] T. R. McGuire and R. I. Potter. *IEEE Trans. Magn.*, 11:1018, 1975.

[61] C. H. Marrows. *Adv. Phys.*, 54:585, 2005.

[62] G. G. Cabrera and L. M. Falicov. *Phys. Stat. Sol. (b)*, 61:539, 1974.

[63] G. G. Cabrera and L. M. Falicov. *Phys. Stat. Sol. (b)*, 62:217, 1974.

[64] M. Viret, D. Vignoles, D. Cole, J. M. D. Coey, W. Allen, D. S. Daniel, and J. F. Gregg. *Phys. Rev. B*, 53:8464, 1996.

[65] P. M. Levy and S. Zhang. *Phys. Rev. Lett.*, 79:5110, 1997.

[66] J. F. Gregg, W. Allen, K. Ounadjela, M. Viret, M. Hehn, S. M. Thompson, and J. M. D. Coey. *Phys. Rev. Lett.*, 77:1580, 1996.

[67] U. Rüdiger, J. Yu, S. Zhang, A. D. Kent, and S. S. P. Parkin. *Phys. Rev. Lett.*, 80:5639, 1998.

[68] A. D. Kent, U. Rüdiger, J. Yu, L. Thomas, and S. S. P. Parkin. *J. Appl. Phys.*, 85:5243, 1999.

[69] T. Taniyama, I. Nakatani, T. Namikawa, and Y. Yamazaki. *Phys. Rev. Lett.*, 82:2780, 1999.

[70] D. Ravelosona, A. Cebollada, F. Briones, C. Diaz-Paniagua, M. A. Hidalgo, and F. Batallan. *Phys. Rev. B*, 59:4322, 1999.

[71] R. Danneau, P. Warin, J. P. Attané, I. Petej, C. Beigné, C. Fermon, O. Klein, A. Marty, F. Ott, Y. Samson, and M. Viret. *Phys. Rev. Lett.*, 88:157201, 2002.

[72] C. H. Marrows and B. C. Dalton. *Phys. Rev. Lett.*, 92:097206, 2004.

[73] C. Hassel, M. Brands, F. Y. Lo, A. D. Wieck, and G. Dumpich. *Phys. Rev. Lett.*, 97:226805, 2006.

[74] J. Briaire. *1/f Noise in Permalloy.* PhD thesis, Technische Universiteit Eindhoven, 2000.

[75] L. Jiang, A. Gokce, F. C. S. da Silva, and E. R. Nowak. *Proc. of SPIE*, 5846:156, 2005.

[76] B. Raquet. *J. Magn. Magn. Mater.*, 258-259:119, 2003.

[77] M. Viret, S. Berger, M. Gabureac, F. Ott, D. Olligs, I. Petej, J. F. Gregg, C. Fermon, G. Francinet, and G. Le Goff. *Phys. Rev. B*, 66:220401, 2002.

[78] O. Céspedes, G. Jan, M. Viret, M. Bari, and J. M. D. Coey. *J. Appl. Phys.*, 93:8433, 2003.

[79] P. Bruno. *Phys. Rev. Lett.*, 83:2425, 1999.

[80] J. M. D. Coey, L. Berger, and Y. Labaye. *Phys. Rev. B*, 64:020407, 2001.

[81] S. Samanta, M. V. Kamalakar, and A. K. Raychaudhuri. *J. Nanosci. Nanotechnol.*, 9:5243, 2009.

[82] A. Singh, D. Chowdhary, and A. Ghosh. *arXiv:0908.0136v1.*

[83] N. E. Israeloff, M. B. Weissman, G. A. Garfunkel, D. J. Van Harlingen, J. H. Scofield, and A. J. Lucero. *Phys. Rev. Lett.*, 60:152, 1988.

[84] M. N. Baiblich, J. M. Broto, A. Fert, F. Nguyen Van Dau, F. Petroff, D. Etienne, G. Greuzet, A. Frederick, and J. Cjazelas. *Phys. Rev. Lett.*, 61:2472, 1988.

[85] G. Binash, P. Grünberg, F. Saurenbach, and W. Zinn. *Phys. Rev. B*, 39:4828, 1989.

[86] J. Mathon. *Spin Electronics*, chapter 4, page 71. Springer-Verlag, 2001.

[87] H. T. Hardner, M. B. Weissman, M. B. Salamon, and S. S. P. Parkin. *Phys. Rev. B*, 48:16156, 1993.

[88] H. T. Hardner, S. S. P. Parkin, M. B. Weissman, M. B. Salamon, and E. Kita. *J. Appl. Phys.*, 75:6531, 1994.

[89] L. S. Kirschenbaum, C. T. Rogers, S. E. Russek, and S. C. Sanders. *IEEE Trans. Magn.*, 31:3943, 1995.

[90] D. Herranz, R. Guerrero, R. Villar, F. G. Aliev, A. C. Swaving, R. A. Duine, C. van Haesendonck, and I. Vavra. *Phys. Rev. B*, 79:134423, 2009.

[91] E. Kerr. PhD thesis, University of Dublin, 2006.

[92] R. J. M. van de Veerdonk, P. J. L. Beliën, K. M. Schep, J. C. S. Kools, M. C. de Nooijer, M. A. M. Gijs, R. Coehoom, and W. J. M. de Jonge. *J. Appl. Phys.*, 82:6152, 1997.

[93] Y. Bei and E. W. Hill. *J. Appl. Phys.*, 93:8391, 2003.

[94] Y. Bei and E. W. Hill. *Sens. Actuators, A*, 129:260, 129.

[95] L. S. Kirschenbaum, C. T. Rogers, S. E. Russek, and Y. K. Kim. *IEEE Trans. Magn.*, 33:3586, 1997.

[96] N. A. Stutzke, S. E. Russek, D. P. Pappas, and T. Tondra. *J. Appl. Phys.*, 97:10Q107, 2005.

[97] A. Ozbay, A. Gokce, T. Flanagan, R. A. Stearrett, E. R. Nowak, and C. Nordman. *Appl. Phys. Lett.*, 94:202506, 2009.

[98] F. Gen. PhD thesis, University of Dublin, 2007.

[99] Y. M. Lee, J. Hayakawa, S. Ikeda, F. Matsukura, and H. Ohno. *Appl. Phys. Lett.*, 90:212507, 2007.

[100] E. R. Nowak, R. D. Merithew, M. B. Weissman, I. Bloom, and S. S. P. Parkin. *J. Appl. Phys.*, 84:6195, 1998.

[101] E. R. Nowak, M. B. Weissman, and S. S. P. Parkin. *Appl. Phys. Lett.*, 74:600, 1999.

[102] L. Jiang, E. R. Nowak, P. E. Scott, J. Johnson, J. M. Slaughter, J. J. Sun, and R. W. Dave. *Phys. Rev. B*, 69:054407, 2004.

[103] S. Ingvarsson, G. Xiao, R. A. Wanner, P. Trouilloud, Y. Lu, W. J. Gallagher, A. Marley, K. P. Roche, and S. S. P. Parkin. *J. Appl. Phys.*, 85:5270, 1999.

[104] S. Ingvarsson, G. Xiao, S. S. P. Parkin, W. J. Gallagher, G. Grinstein, and R. H. Koch. *Phys. Rev. Lett.*, 85:3289, 2000.

[105] C. Ren, X. Y. Liu, B. D. Schrag, and G. Xiao. *Phys. Rev. B*, 69:104405, 2004.

[106] W. K. Park, J. S. Moodera, J. Taylor, M. Tondra, J. M. Daughton, A. Thomas, and H. Brückl. *J. Appl. Phys.*, 93:7020, 2003.

[107] D. S. Reed, C. Nordman, and J. M. Daughton. *IEEE Trans. Magn.*, 37:2028, 2001.

[108] K. S. Kim, H. J. Shim, I. J. Hwang, B. K. Cho, J. H. Seok, and J. T. Kim. *J. Appl. Phys.*, 91:8804, 2002.

[109] A. Gokce, E. R. Nowak, S. H. Yang, and S. S. P. Parkin. *J. Appl. Phys.*, 99:08A906, 2006.

[110] J. Scola, H. Polovy, C. Fermon, M. Pannetier-Lecoeur, G. Feng, K. Fahy, and J. M. D. Coey. *Appl. Phys. Lett.*, 90:252501, 2007.

[111] S. H. Liou, R. Zhang, S. E. Russek, L. Yuan, S. T. Halloran, and D. P. Pappas. *J. Appl. Phys.*, 103:07E920, 2008.

[112] R. Guerrero, M. Pannetier-Lecoeur, C. Fermon, S. Cardoso, R. Ferreira, and P. P. Freitas. *J. Appl. Phys.*, 105:113922, 2009.

[113] R. Guerrero, F. G. Aliev, R. Villar, J. Hauch, M. Fraune, G. Güntherodt, K. Rott, H. Brückl, and G. Reiss. *Appl. Phys. Lett.*, 87:042501, 2005.

[114] A. S. Edelstein, G. A. Fischer, M. Pedersen, E. R. Nowak, S. F. Cheng, and C. A. Nordman. *J. Appl. Phys.*, 99:08B317, 2006.

[115] J. Lenz and A. S. Edelstein. *IEEE Sensors J.*, 6:631, 2006.

[116] A. Guedes, S. B. Patil, S. Cardoso, V. Chu, J. P. Conde, and P. P. Freitas. *J. Appl. Phys.*, 103:07E924, 2008.

[117] A. Guedes, S. B. Patil, P. Wisniowski, V. Chu, J. P. Conde, and P. P. Freitas. *IEEE Trans. Magn.*, 44:2554, 2008.

[118] J. E. Bumette, A. S. Edelstein, G. A. Fischer, E. Nowak, W. Bernard, S. F. Cheng, C. Nordman, and W. F. Egelhoff. *J. Appl. Phys.*, 103:07E930, 2008.

[119] M. Pannetier, C. Fermon, G. Le Goff, J. Simola, and E. Kerr. *Science*, 304:1648, 2004.

[120] M. Pannetier, C. Fermon, G. Le Goff, J. Simola, E. Kerr, and J. M. D. Coey. *J. Magn. Magn. Mater.*, 290-291:1158, 2005.

[121] B. Raquet, J. M. D. Coey, S. Wirth, and S. von Molnár. *Phys. Rev. B*, 59:12435, 1999.

[122] J. M. D. Coey, M. Viret, and S. von Molnár. *Adv. Phys.*, 48:167, 1999.

[123] B. Raquet, A. Anane, S. Wirth, P. Xiong, and S. von Molnár. *Phys. Rev. Lett.*, 84:4485, 2000.

[124] L. Méchin, J. M. Routoure, S. Mercone, F. Yang, S. Flament, and R. A. Chakalov. *J. Appl. Phys.*, 103:083709, 2008.

[125] A. K. Raychaudhuri. *Curr. Opin. Solid State Mater. Sci.*, 6:67, 2002.

[126] P. Reutler, A. Bensaid, F. Herbstritt, C. Höfener, A. Marx, and R. Gross. *Phys. Rev. B*, 62:11619, 2000.

[127] G. B. Alers, A. P. Ramirez, and S. Jin. *Appl. Phys. Lett.*, 68:3644, 1996.

[128] H. T. Hardner, M. B. Weissman, M. Jaime, R. E. Treece, P. C. Dorsey, J. S. Horwitz, and D. B. Chrisey. *J. Appl. Phys.*, 81:272, 1997.

[129] V. Podzorov, M. Uehara, M. E. Gershenson, T. Y. Koo, and S. W. Cheong. *Phys. Rev. B*, 61:R3784, 2000.

[130] S. Wirth, A. Anane, B. Raquet, and S. von Molnár. *J. Magn. Magn. Mater.*, 290-291:1168, 2005.

[131] A. Palanisami, M. B. Weissman, and N. D. Mathur. *Phys. Rev. B*, 71:014423, 2005.

[132] C. Höfener, J. B. Philipp, J. Klein, L. Alff, A. Marx, B. Büchener, and R. Gross. *Europhys. Lett.*, 50:681, 2000.

[133] R. Mathieu, P. Svedlindh, R. Gunnarsson, and Z. G. Ivanov. *Phys. Rev. B*, 63:132407, 2001.

[134] L. I. Glazman and K. A. Matveev. *Sov. Phys. JETP*, 67:1276, 1988.

[135] C. Barone, A. Galdi, S. Pagano, O. Quaranta, L. Méchin, J. M. Routoure, and P. Perna. *Rev. Sci. Instrum.*, 78:093905, 2007.

[136] C. Barone, S. Pagano, L. Méchin, J. M. Routoure, P. Orgiani, and L. Maritato. *Rev. Sci. Instrum.*, 79:053908, 2008.

Chapter 3

Experiment Methods

3.1 Sample Fabrication

In this work samples are microfabricated by lithography.[1] Lithographic processes are widely used in the modern semiconductor industries. A lithographic process consists of two different aspects, one is to delineate the desired pattern onto a resist layer, usually a polymer that is spin-coated on the sample surface; the other is to transfer this pattern to the sample. Photolithography and electron beam lithography are used for the first step, whereas argon ion milling and lift-off are used for the second.

3.1.1 Photolithography

Photolithography is the process in which patterns are exposed on photoresists using ultraviolet light (200 - 450 nm). The conventional technique is called contact or shadow printing, in which a flood-exposure of a wafer coated with photoresist are carried out through a mask directly placed on

[1]The metallization process was carried out by several colleagues of the candidate, Gen Feng, Jiafeng Feng, Ciáran Fowley, Byong-Sun Chun, and Junyang Chen on the Shamrock sputtering tool.

top of the substrate. The photomask containing clear and opaque features of the designed pattern, is usually prepared by an electron beam lithography process, due to its much higher resolution. This was the mainstream microfabrication process in the semiconductor industry up to the mid-1970s. The resolution of shadow printing is limited by the diffraction of light at the edge of the opaque feature on the mask as light passes through adjacent clear areas. Diffraction makes the intensity of light on the resist non-uniform and the image edge looks blurred and diffuse [1]. The theoretical resolution of shadow printing for a mask with equal lines and spacings of width b is given by

$$2b_{min} = 3\sqrt{\lambda(s + \frac{1}{2}z)} \tag{3.1}$$

with 2b the grating period, s the gap width between the mask and the photoresist surface, λ the wavelength of the exposing UV light, and z the thickness of the photoresist. This gives a maximum resolution slightly less than 1 μm for hard contact exposure (s=0) [1]. From Eqn.(3.1) we can see that better resolution is achieved by either reducing the distance between the mask and the photoresist, or by thinning the photoresist. However, the second method is not always possible, since the pattern transfer process requires a certain resist thickness. Hence, trying to reduce s in the soft contact exposure or switching to hard contact exposure is the main strategy to achieve higher resolution in photolithography.

In this work, photolithography is routinely used to fabricate either designed micromagnetic structures, e.g. Hall bars or micron-scale electrical contacts to them. The photolithography process was performed in the SNI-AMS Class-100 cleanroom with a Karl Suss MJB-3 UV400 mask-aligner. A 350 W multi-wavelength mercury arc lamp was attached as the light source. Two different photoresists are used for the processing, S1813 from Shipley

as positive resist and AZ nLof 2070 from MicroChemicals as negative resist. Their detailed processing parameters can be found in Appendix B.

3.1.2 Electron Beam Lithography

Electron beam lithography is the microfabrication process which uses beams of electrons to expose the resist. It was first developed in the 1970s for fabricating high density integrated circuits. In the present day semiconductor industry, nearly all integrated circuits processing are carried out with sophisticated deviations of the optical techniques mentioned above. However, electron beam lithography still serves two main roles. First, it is used to write masks for photolithography, for which high resolution and precision is required. Second, it is used in prototyping low volume high precision devices for research and development [2].

Like photons, electrons also possess particle/wave duality. The wavelength of electrons accelerated to a few tens of kV is normally 4 to 5 orders of magnitude shorter than the wavelength of UV photon. So the resolution of electron beam lithography is not limited by diffraction issues. However, the resolution of electron beam lithography is limited by electron forward scattering in the resist, backscattering from the substrate and the resolution of resists used. The scattering process significantly broadens the beam and worsens the resolution of the written pattern. The backscattered electrons also create the so-called 'proximity effect', which is a variable background on which the patterns sit during the exposure. For high-resolution electron beam lithography, minimizing the proximity effect by optimized pattern design and dose variation is of crucial consideration.

An electron beam lithography system normally consists of an electron source, beam control hardware, and related software to edit and process

patterns. In this work, three different electron beam lithography systems were used, namely an FEI Strata Dualbeam 235, a Zeiss EVO 50 and a Zeiss Supra 40. They are all conventional scanning electron microscopes modified with Raith lithography modules [3]. In general, these are scanning beam systems that use Gaussian beams and can carry out either raster or vector scans. Fig. 3.1 shows a simplified diagram of a scanning electron microscopy system with lithography add-ons. Electrons are emitted from the electron gun, whose crossover is focused onto the surface of the workpiece by electromagnetic lenses. An aperture between the first lens and the beam blanking system is called the beam shaping aperture, which also sets the numerical aperture of the system. The beam blanker is used to move the electron beam off the sample surface during writing, which is normally done electrostatically due to the speed requirement of the writing process. A beam position deflector at the end of the electron beam optics is used to shift the electron beams on the workpiece.

The required charge density to be delivered to the workpiece, usually called 'dose' Q is calculated as

$$Q = \frac{IT}{A} \tag{3.2}$$

with I the beam current, T the exposure time and A the workpiece area. The Raith electron beam writing modules we use have two independent 2.5 MHz 16 bit digital-to-analogue converters (DAC), hence, the minimum exposure time (also commonly called 'dwell time') is 0.004 ms.

Electron guns are the defining factor for the resolution of an electron beam lithography system. Normally, two different types of guns are utilized. The first type is thermionic guns, which are simple in design and reliable. It is formed by heating either a bent tungsten wire or a lanthanum hexaboride

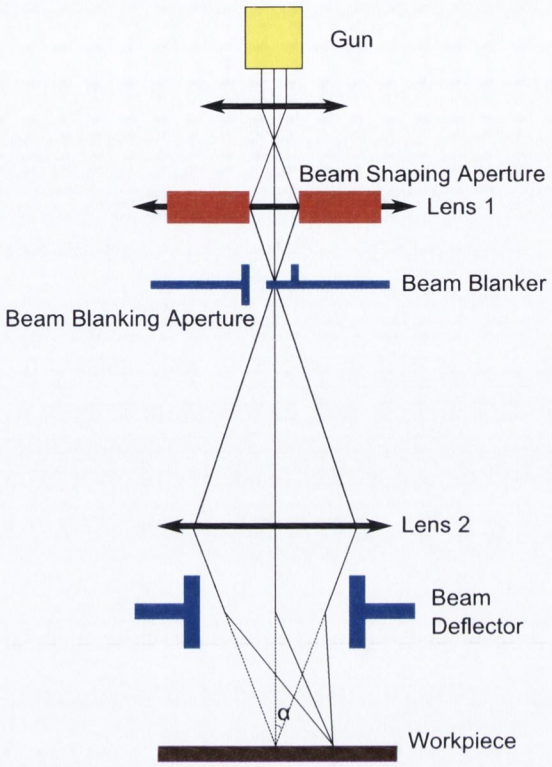


Fig. 3.1: Simplied diagram of a scanning electron beam writing system (reproduced from [2]).

(LaB_6) crytal. The latter is nowadays widely used on thermionic electron beam systems because of its long lifetime (a few thousand hours) and better brightness (more than 10^5 $Acm^{-2}sr^{-1}$). The lanthanum hexaboride tip is heated up to about 1600 ^{0}C. This requires an electron gun vacuum of about 10^{-6} torr to avoid corrosion by gas molecules. The Zeiss EVO 50 system used in this study is of this type. It has a quoted resolution of 50 nm for lithography. The second type is thermionic field emission gun (FEG). In this type of electron gun, an etched sharp tungsten tip with a radius of curvature about 1μm serving as the cathode, is placed in front of a coaxial flat disk serving as the anode. A high voltage of a few kV to a few tens of kV is applied in between which generates an electric field of 10^8 V m^{-1}. The

tungsten tip is heated up to about 1000 - 1500 ^0C, and electrons are emitted from the tip due to a reduction of the work funtion under high electric field. Very high brightness (at least 10^7 $Acm^{-2}sr^{-1}$) can be achieved with thermionic field emission guns and a high vacuum (10^{-9} torr) is required. The FEI Strata Dualbeam 235 and Zeiss Supra 40 are both thermionic field emission systems which give a resolution of 3 - 10 nm.

The major requirement of an electron beam resist compared to its optical counterpart is its resolution. Presently, electron beam resists with resolution down to 5 - 10 nm, are widely used. In this work, most patterning has been carried out on three different electron beam resist systems, namely poly(methyl methacrylate) (PMMA), ma-N 2403 and hydrogen silsesquioxane (HSQ). Their processing conditions are documented in Appendix B and detailed fabrication routines are described in the corresponding chapters.

3.1.3 Lift-off

'Lift-off' is a simple and widely used lithography method for transferring pre-defined patterns on the resist to the sample. A thin metallic film is deposited by evaporation or sputtering on prepatterned photoresist. During the lift-off process, the resist under the film is removed by solvent, taking away the metal films on top, and leaving films only on those parts of the substrate on which films were directly deposited.

Primary considerations of a lift-off process are the resist thickness and cut. It is generally accepted that the deposited metal layer has to be thinner than 1/3 - 1/2 of the photoresist thickness, otherwise the lift-off process may become difficult. An undercut resist profile, with more resist removed from the bottom than the top in a cross-sectional view, is also of help to the lift-off process. This innovates the introduction of the so-called 'lift-off

resist', which is a polymer precoated on the substrate before applying the photoresist, and is able to give higher cuts than the photoresist itself. The most common defects caused by a lift-off process are retention and ears.

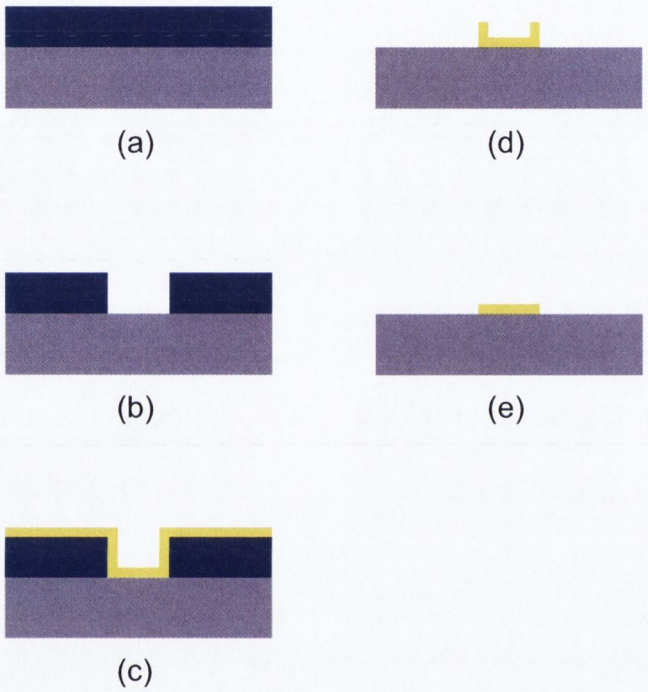


Fig. 3.2: A schematic diagram of the lift-off process. (a) substrate coated with resist; (b) following exposure and resist development; (c) following metallization; (d) following lift-off; (e) after ultrasonication to remove ears.

In this work, lift-off is performed using either acetone or 1165 microresist remover (Shipley). The later contains N-Methyl-2-pyrrolidone (NMP), which is an organic base commonly used as paint stripper. The use of 1165 microresist remover requires an elevated temperature above 80 ^{0}C. Normally, an ultrasonically assisted lift-off process is adopted, except when ultrasonication is likely to damage the pattern. During the metalization process, a thin tantalum layer of 5 - 10 nm is deposited before other metals. This improves the adhesion between the metallic layer and the silicon

substrate, which minimizes accidental remove of the pattern during lift-off. Fig. 3.2 is a schematic of the lift-off process with a conventional resist, with which very little undercut is expected. Fig. 3.3 shows the undercut created by using lift-off resist.

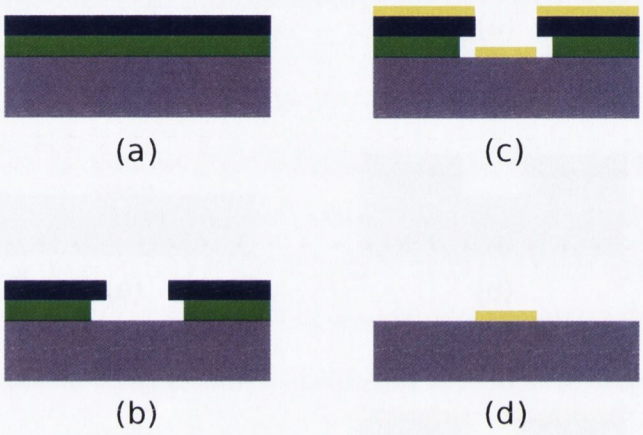


Fig. 3.3: A schematic diagram of the lift-off process with lift-off resist creating the undercut. The lift-off resist is depicted in green.

3.1.4 Argon Ion Milling

Argon ion milling on a Millatron tool was used in this work to transfer the resist pattern to magnetic layers underneath. The Millatron is a broad beam ion milling tool which uses an argon plasma to etch samples located on a rotating stage. Argon ions are produced in a cavity and then accelerated to produce a relatively intense and homogeneous beam using RF source. It is a physical etching process, in which ions sputter away materials which are not protected by the resist. The system has a base pressure of 2×10^{-7}

Torr and a typical working pressure of about 5×10^{-5} Torr when argon gas is used in. A Hiden Analytical secondary ion mass spectrometer (SIMS) is attached to the system, for monitoring ions milled away from the sample. Fig. 3.4 shows the SIMS readout during the milling process of a spin-valve stack.

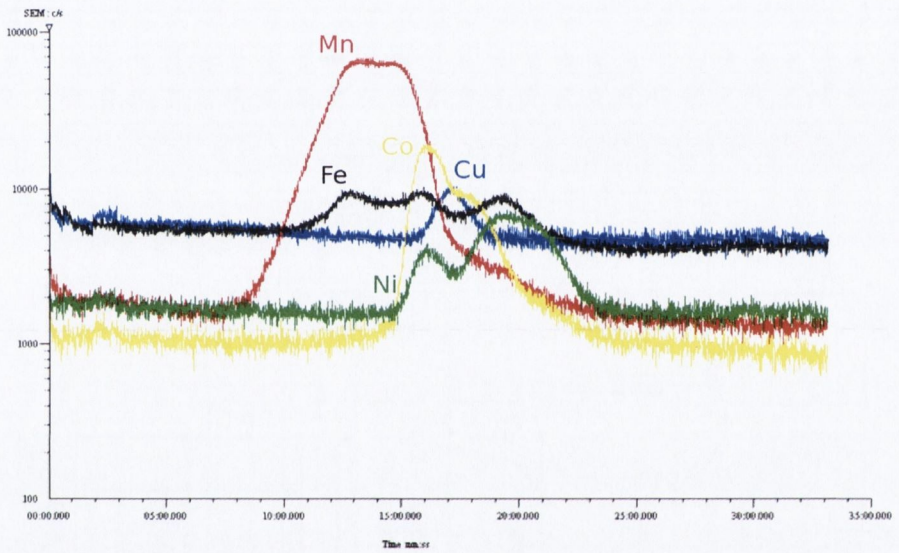


Fig. 3.4: SIMS readout during argon ion milling of a SiO_2/Ta(5)/NiFe(3.5)/CoFe(1.5)/Cu(2.9)/CoFe(2.5)/IrMn(10)/Ta(5) spin-valve stack on the Millatron (numbers in nm). The fact that the SIMS signal does not always follow the stack can be possibly explained by the cross-talk between adjacent mass channels.

3.2 Sample Characterization

3.2.1 Transport and Noise Measurement Set-up

In this work, a transport and noise measurement set-up has been adapted from Prof. Edmund Nowak's laboratory in University of Delaware to ours.

This is a conventional DC noise measurement set-up, which can also monitor the sample resistance through a buffer amplifier circuit while noise data are taken. It is composed of a soft iron shielded box housing the power source, protection circuits, a buffer amplifier and two low noise AC coupled amplifiers. Noise from two voltage channels across the sample can be measured at the same time with the two low noise amplifiers. Their cross-correlation can also be utilized to further reduce the noise background [4]. Fig. 3.5 shows a diagram of the noise and transport measurement circuit.

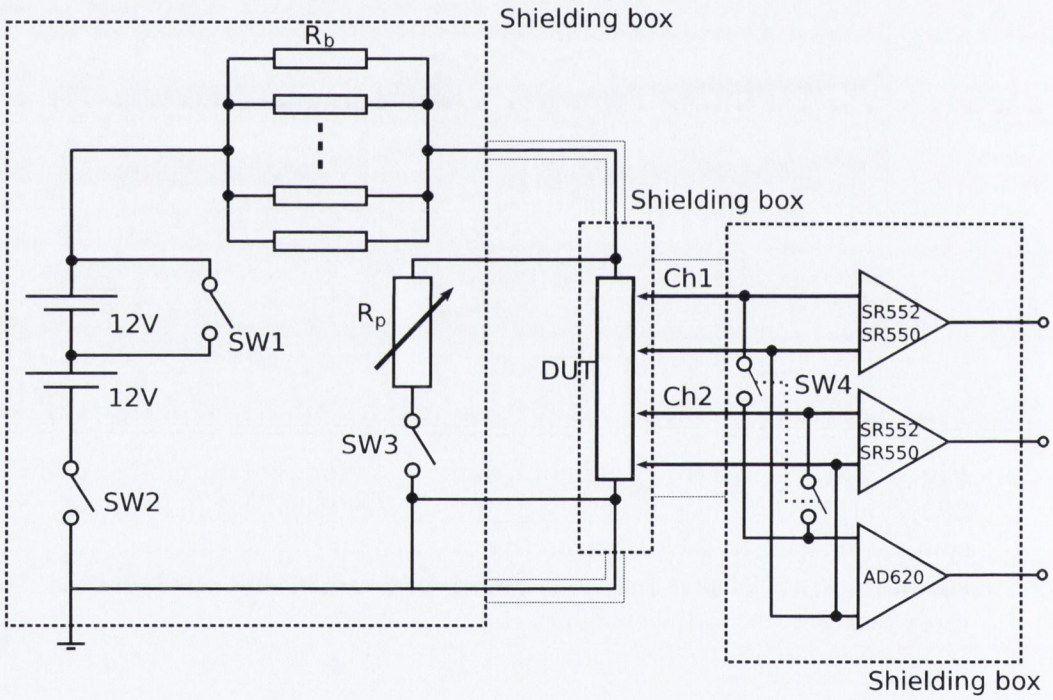


Fig. 3.5: Circuit diagram of the noise and transport measurement set-up.

The power source is made of two 12 V lead acid battery packs in series with a group of low noise current limiting resistors from 2 kΩ to 10 MΩ. This gives discreet current outputs between 2.4 μA and 12 mA. A potentiometer, connected in parallel with the sample, is used to give protection to the device under test (DUT) against voltage spikes when the current is first applied.

The potentiometer is at its resistance minimum, when SW2 is first closed, so current runs through the potentiometer but not the sample. The current through the sample can be slowly brought up by increasing the resistance of the potentiometer. SW3 is used to cut the potentiometer out of the circuit when the current through the sample has reached its set point. This avoids the potentiometer creating leak current path and extra impedance during the noise measurement.

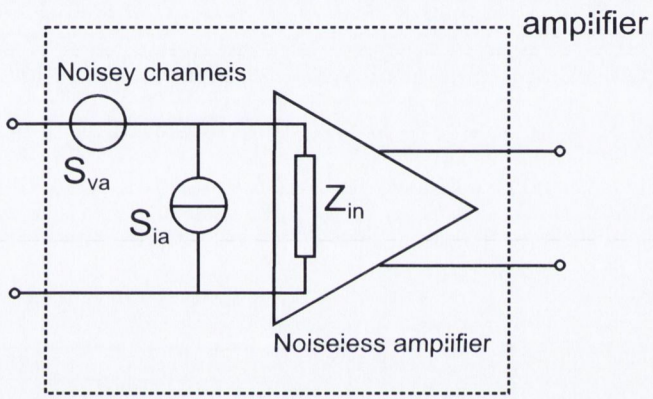


Fig. 3.6: The input noise equivalent circuit diagram of an amplifier.

Fig. 3.6 shows the noise equivalent circuit of an amplifier. In general, the noise channels for an amplifier can be fully characterized in terms of two noise generators, the input equivalent voltage noise S_{va} and the input current noise S_{ia}. The rest of the amplifier can be treated as a noise-free circuit [5]. Depending on the input, amplifiers can be normally divided as bipolar-transistor input amplifiers and junction field effect transistor (JFET) input amplifiers, with the former having lower voltage noise, but likely to suffer from high current noise when a high impedance sample is connected, and the later having lower current noise but higher voltage noise. Data sheets of amplifiers usually specify the input voltage noise at 1 kHz but input current noise might not always be listed.

The buffer amplifier is made of an AD 620 instrumentation amplifier. It has a low input offset drift ($< 0.6\ \mu V/^0C$) and a bias current below 1 nA. The equivalent input voltage noise of the instrumentation amplifier is about 9 $nV/\sqrt{Hz}$ at 1 kHz, which is acceptable for our purpose. Three different gain setting resistors were connected with the IC chip through a multiple switch, hence, totally four different gains, namely 1×, 2×, 11.5×, and 106× can be set for the MR measurement. The instrumentation amplifier has been tested to bring no effect to the noise measurement circuit.

We use two sets of commercially available AC coupled low noise preamplifiers for the set-up, namely SR552 and SR550 from Stanford Research Systems. They match reasonably well with low and intermediate impedance samples, respectively. Table 3.1 is a list of key specifications of the two preamplifiers.

	SR552	SR550
Input	Bipolar junction transistors	Field-effect transistors
Input Impedance:	100 kΩ + 25 pF	100 MΩ + 25 pF
Noise:	1.4 $nV\sqrt{Hz}$ (1000 Hz) 2.5 $nV\sqrt{Hz}$ (10 Hz)	3.6 $nV\sqrt{Hz}$ (1000 Hz) 13 $nV\sqrt{Hz}$ (10 Hz)
Frequency Range:	0.016 Hz - 1 MHz	0.016 Hz - 100 kHz
Maximum inputs:	70 mV_{RMS} (overload) 20 V_{AC} and 50 V_{DC} damage	250 mV_{RMS} (overload) 10 V_{AC} and 100 V_{DC} damage
Common Mode:	1 V peak (Range) 100 dB at 100 Hz (Rejection)	1 V peak (Range) 90 dB at 100 Hz (Rejection)
Gain:	10, 20, 50, 100	1, 2, 5, 10
Gain accuracy:	2% (2 Hz - 100 kHz)	2% (2 Hz - 100 kHz)
Gain stability:	200 $ppm/^0C$	100 $ppm/^0C$
Output impedance:	600 Ω	600 Ω

Table 3.1: Specifications of SR552 and SR550 preamplifiers.

Both the AD 620 circuit and the two sets of preamplifiers can be powered up by either an Agilent E3631A triple output DC power supply or by a home-made battery pack using two laptop backup batteries. Measurement has been carried out with each, and no significant difference in the power

line pickup has been found between them. In the context of this work, we do not specify in which way the amplifiers were powered up during the measurement. Power line pick-up was sometimes present in the measured spectra, they do not alter the conclusion of the work and are removed during signal processing.

The booster amplifier used is a SR640 wide-band voltage amplifier (Stanford Research Systems). It is normally set to give a second stage gain between 10× - 1000×. The amplified noise voltage is then either fed to an HP35660A Fast Fourier Transform Spectrum Analyser or through a Krohn-Hite 3362 Dual channel filter, as anti-aliasing filter, then sampled by a PCI 6250M data acquisition card (DAQ) from National Instruments (NI).

Magnetic field is generated by an electromagnet with an adjustable distance between the two pole pieces, powered up by a 20 A power supply from Bouhnik. The maximum field that can be generated with our sample box fixed in between the electromagnet pole pieces is about 1.2 T. The low frequency noise profile of the electromagnet has been characterized, by measuring inductive pick-up from a 200-turn test coil placed in the centre of the electromagnet using the HP35660A spectrum analyser. No feature which might potentially affect the noise measurement has been found (Fig. 3.7)[2]. The output of the electromagnet can be controlled by setting the current or magnetic field level with the DAQ card's analogue output channels.

The whole measurement system is controlled by a personal computer running LabView (NI). Several LabView programs are either coded or adapted from Prof. Nowak's laboratory for automatic measurements, for example, MR measurement, single spectrum capture, noise and sample voltage against field, coherence measurement, long-time sampling. Many other pro-

[2]The measurement was carried out together with Dr. Plamen Stamenov.

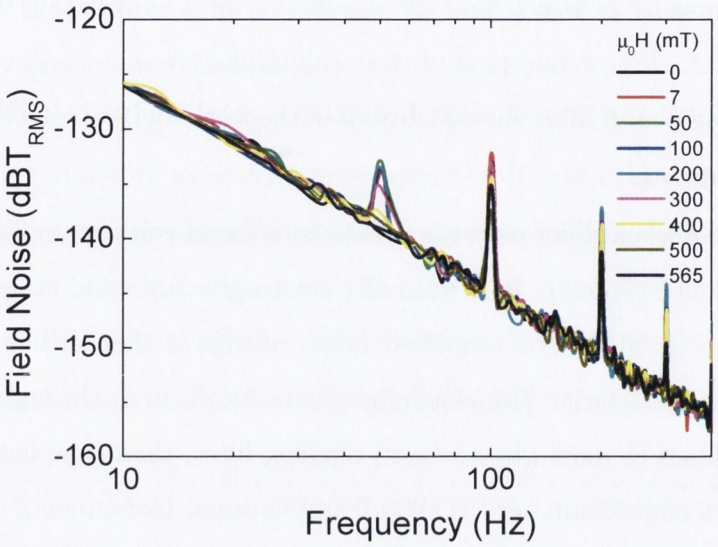


Fig. 3.7: Power spectral density of magnetic field generated by the electromagnet in our set-up. The slope is due to the increase of the impedance of the pickup coil at low frequencies.

grams were also coded for data analysis.

The performance of the set-up was tested by measuring the thermal noise of different metal film resistors. The results are shown in Fig. 3.8 together with the short and open input noise level of the preamplifier (SR552). The short input noise gives the input voltage noise of the amplifier, since the current noise source is effectively shorted from the circuit, whereas the open input noise can be seen as the voltage fluctuation due to the current noise on the input impedance of the amplifier, so it can be converted to the input current noise. It can be seen clearly from the graph that the short input noise of our set-up is very close to the quoted input voltage noise of the SR552 preamplifier at 1 kHz. For the 100 Ω and 1 kΩ resistors, their measured noise spectra can be well predicted by the amplifier input

voltage noise plus their thermal noise $S(f) = 4kTR$, while for the 10 kΩ resistor, the amplifier's input current noise has to be taken into account to correctly predict the measured spectrum. This follows the above discussion, that the bipolar-transistor input SR552 preamplifier is better at measuring low impedance samples. For samples of a few kΩ impedance, the background becomes higher due to the input current noise of the amplifier, and the signal-to-noise ratio (SNR) goes down. Hence, for samples having impedance larger than a few kΩ, the JFET input SR550 preamplifier is desired.

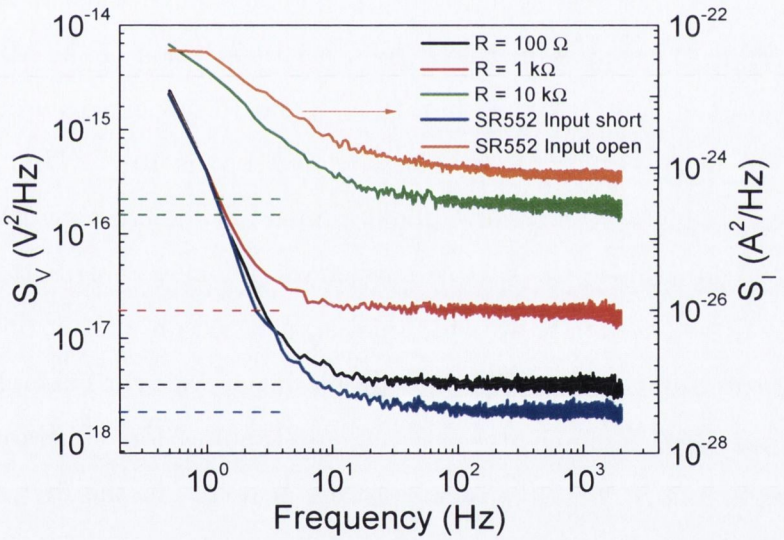


Fig. 3.8: Power spectral density measured on three thin film resistors of 100 Ω, 1 kΩ, and 10 kΩ using SR552 preamplifier with our set-up. Also shown is the amplifier input equivalent voltage and current noise. The blue dashed line is the voltage noise level of SR552 quoted in the specifications. Dashed lines in other colours indicate the respective theoretical estimate of the noise level for each resistor. The lower of the two green dashed lines is a theoretical estimate without taking account of the input current noise, whereas the higher one also has it counted.

3.2.2 Magnetic Force Microscopy

Magnetic force microscopy (MFM) has been widely used in characterizing the domain structure in magnetic samples since its invention 20 years ago [6]. It is an extension of the conventional scanning force microscopy (SFM), which moves a microfabricated flexible cantilever with a sharp tip across a sample surface using piezoelectric scanners. A force image is produced by the deflection of the cantilever due to the interaction between the tip and the sample surface. An MFM tip is either made of a magnetic material, or coated with a thin layer (tens of nm) magnetic material, and can sense the magnetic stray field emerging from a magnetic sample when it is in close proximity to the sample surface. The spatial resolution of the MFM technique is of the order 10 - 100 nm, though sub-10 nm images are achieved in several studies. The force sensitivity of MFM is 10^{-13} N/m, which is considerably higher than conventional atomic force microscopy (AFM) [7]. In order to minimise the sample surface morphology contribution to the MFM contrast, normally an additional scan based on another interaction is used to acquire the sample topographic image [8]. For example, in the widely adopted Veeco-Digital Instruments TappingMode/LiftMode^{TM} interleave technique [9], a two-scan process is used. In the first scan, the magnetic tip traces the sample surface and a surface morphology image is obtained. Then the tip is lifted on the same scan line to a predefined height above the sample surface and another scan is carried out with the feedback switched off. This gives an image to which the main contribution is the magnetic interaction. The great advantage of MFM, compared with other domain imaging techniques, e.g. Lorentz Microscopy and SEM with polarized analysis, is its high resolution and minimal requirement for sample preparation.

The interpretation of magnetic force microscopy images is not trivial due to the complex nature of the interaction between the magnetic tip and the sample. It can be generally treated as a mapping of the stray field from the magnetic surface by a localized point magnetic dipole [10]. Here we use the theoretical work by Hubert et al [11] to interpret the mechanism of MFM image forming because of its simplicity and applicability to a wide range of domain structures. For a magnetic tip in the stray field of a sample, the magnetostatic interaction energy in the weak interaction limit, in which both the sample magnetization and the tip can be considered as rigid, is defined as

$$E_i = -\int_{tip} \mathbf{J}_{tip} \cdot \mathbf{H}_{sample}\, dV \tag{3.3}$$

in which $\mathbf{J}_{tip} = \mu_0 \mathbf{M}_{tip}$ is the tip magnetic polarization.

Due to the reciprocity relation, the interaction energy can also be expressed as the sample magnetization in the stray field of the MFM tip

$$E_i = -\int_{sample} \mathbf{J}_{sample} \cdot \mathbf{H}_{tip}\, dV = \int_{sample} \mathbf{J}_{sample} \cdot \nabla \Phi_{tip}\, dV \tag{3.4}$$

in which Φ_{tip} is the scalar potential of the stray field ($\mathbf{H}_{tip} = -\nabla \Phi_{tip}$). Integrating Eqn. (3.4) by parts, we have

$$E_i = \int_{sample} \sigma_{sample} \Phi_{tip}\, dS + \int_{sample} \rho_{sample} \Phi_{tip}\, dV \tag{3.5}$$

with

$$\rho_{sample} = -\nabla \cdot \mathbf{J}_{sample} \text{ and } \sigma_{sample} = \mathbf{J}_{sample} \cdot \mathbf{n} \tag{3.6}$$

in which ρ_{sample} and σ_{sample} are the magnetic volume and surface charges, respectively. From Eqn.(3.6) we see that, in the weak interaction limit,

an MFM can be considered as a sample magnetic charge mapping tool. The MFM images are formed by the convolution of the sample magnetic charge and the tip scalar potential. In reality, for an MFM running at the amplitude modulation mode, the force gradient between the tip and the sample is measured. In this case, images are the convolution of the sample magnetic charge and the force gradient.

For the MFM measurement presented in this work, a special technique, active Q-control, is used in order to achieve better signal-to-noise ratio for the images. An additional feedback loop consisting of a phase shifter and an amplifier is utilised to actively modify the cantilever damping by a controlled increase or decrease in the 'effective' quality factor (Q-factor) of the system (Fig. 3.9). The theory of this operation is documented in the pioneering paper by Mertz et al [12], and further developed by a few other authors [13, 14, 15].

In an MFM working with phase detection mode, the sensitivity $\Delta\varphi$ is proportional to the Q-factor of the cantilever, described by the equation below [17].

$$\Delta\varphi = \frac{Q}{k} \cdot \frac{\partial F(t)}{\partial z(t)} \tag{3.7}$$

in which $\Delta\varphi$ is the phase shift of the cantilever, Q is the quality factor, k is the spring constant, $F(t)$ is the driving force, and $z(t)$ is the cantilever's deflection. The general equation describing the cantilever motion under amplitude modulation with a self-excitation gain and without any tip-sample interaction is as follows [14]:

$$z''(t) + \frac{\omega_0}{Q} z'(t) + \omega_0^2 z(t) + \omega_0^2 G z(t - \frac{\varphi}{\omega}) = \frac{F_0}{m} \cos(\omega t) \tag{3.8}$$

where ω_0 is the free resonance frequency of the system, G is the gain factor

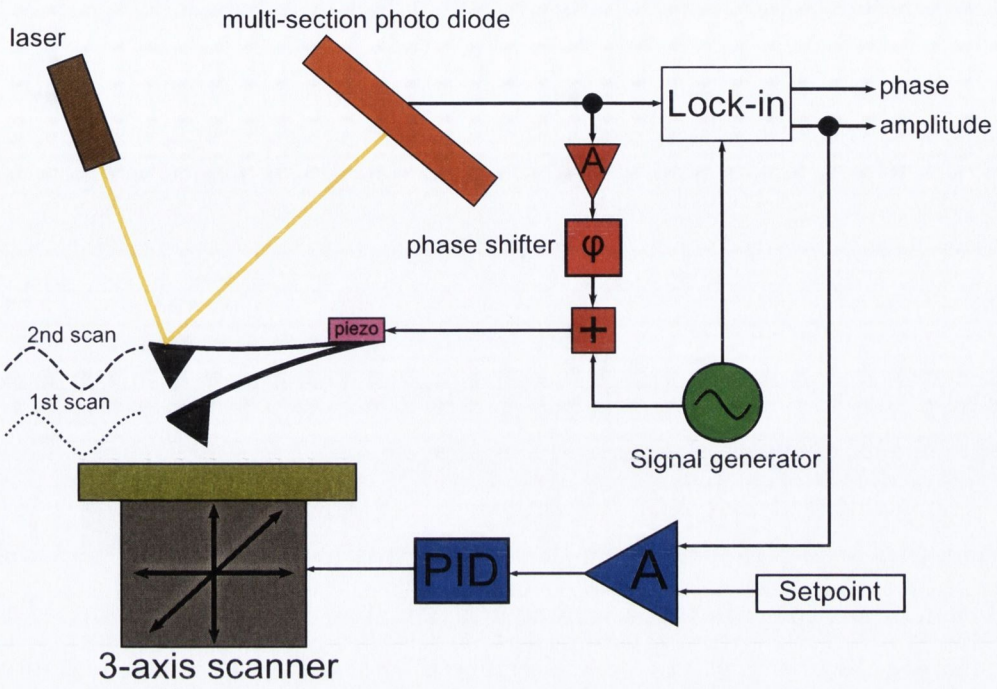


Fig. 3.9: A diagram showing a magnetic force microscopy system with active Q-control feedback loop (adapted from [16]).

without units, and $m{=}k/\omega_0^2$ is the effective mass.

We approximate the cantilever deflection to a sinusoidal function $z(t) \approx A \cdot \sin(\omega t)$, which is not too far from the realistic situation, and choose the phase shift used in the feedback $\varphi{=}{\pm}\pi/2$, we have [18]

$$z(t - \frac{\varphi}{\omega}) = \pm\frac{1}{\omega}z'(t) \tag{3.9}$$

Hence, the equation of motion 3.8 can be recast into the following format.

$$z''(t) + (\frac{\omega_0}{Q} \pm \frac{kG}{m\omega})z'(t) + \omega_0^2 z(t) = \frac{F_0}{m}\cos(\omega t) \tag{3.10}$$

in which we can define

$$\frac{\omega_0}{Q_{eff}} = \frac{\omega_0}{Q} \pm \frac{kG}{m\omega} \tag{3.11}$$

Then we have the effective quality factor Q_{eff} [14] defined as follows.

$$\frac{1}{Q_{eff}} = \frac{1}{Q} \pm \frac{kG}{m\omega\omega_0} \tag{3.12}$$

An enhancement of the Q-factor leads to a higher sensitivity in the phase detection mode.

The magnetic force microscopy measurement was carried out on an Asylum Research MFP-3D system with Ni coated low magnetic moment tips (SmartTip B.V.) in order to minimize the stray field from the tip. The active Q-factor control loop was achieved by its DSP controller, and integrated into the control programme. The height of the tip was 30 - 50 nm from the sample surface, where the stray field from the sample was sensed. This gives a lateral resolution of 30 - 50 nm (As a rule of thumb, the spatial resolution of an MFM is roughly the same as the tip lift height above the sample surface). A typical phase change of 3^0 was observed from one domain to the next, compared to a reported phase resolution of $\sim 0.1^0$ for a home-built AFM [19]. The combination of active Q-control and low moment tips ensure good quality MFM images with minimum distortion of the sample magnetization state due to the tip stray field.

References

[1] M. J. Bowden. *Introduction to Microlithography (Acs Professional Reference Book)*, chapter 2. American Chemical Society, 2nd edition, 1994.

[2] G. Owen and J. R. Sheats. *Microlithography: Science and Technology*, chapter 6. CRC, 1st edition, 1998.

[3] Raith GmbH. *ELPHY Quantum product info.* Raith GmbH, Hauert 18, 44227 Dortmund, Germany, Jan 2008.

[4] S. Demolder, M. Vandendriessche, and A. Van Calster. *J. Phys. E: Sci. Instrum.*, 13:1323, 1980.

[5] A. F. P. van Putten. *Electronic Measurement Systems: Theory and Practice.* Institute of Physics Publishing, Bristol and Philadelphia, 2nd edition, 1996.

[6] Y. Martin and H. K. Wickramasinghe. *Appl. Phys. Lett.*, 50:1455, 1987.

[7] A. K. Petford-Long. *Spin Electronics*, chapter 14, page 316. Springer-Verlag, 2001.

[8] S. Porthun, L. Abelmann, and C. Lodder. *J. Magn. Magn. Mater.*, 182:238, 1998.

[9] Digital Instruments. *Magnetic Force Microscopy (MFM) - Applicable to Dimention Series and Multimode Systems.* Support Note No. 299, Rev. B, 1996.

[10] U. Hartmann. *Phys. Lett. A*, 137:475, 1989.

[11] A. Hubert, W. Rave, and S. L. Tomlinson. *Phys. Stat. Sol. (b)*, 204:817, 1997.

[12] J. Mertz, O. Marti, and J. Mlynek. *Appl. Phys. Lett.*, 62:2344, 1993.

[13] D. Rugar and P. Grütter. *Phys. Rev. Lett.*, 67:699, 1991.

[14] T. R. Rodríguez and R. García. *Appl. Phys. Lett.*, 82:4821, 2003.

[15] J. Kokavecz, Z. L. Horváth, and Á. Mechler. *Appl. Phys. Lett.*, 85:3232, 2004.

[16] H. Hölscher, D. Ebeling, and U.D. Schwarz. *J. Appl. Phys.*, 99:084311, 2006.

[17] T. Yamaoka, K. Watanabe, Y. Shirakawabe, K. Chinone, E. Saitoh, and H. Miyajima. *Jpn. J. Appl. Phys.*, 45:2230, 2006.

[18] nanoAnalytics. *Q-Contorl Information Booklet.* nanoAnalytics, Gievenbecker Weg 11, 48149 Münster, Germany.

[19] R. Nishi, I. Houda, T. Aramata, Y. Sugawara, and S. Morita. *Appl. Surf. Sci.*, 157:332, 2000.

Chapter 4

Magnetization Switching and Fluctuations in $(CoFe/Pt)_n$ Multilayers with Perpendicular Magnetic Anisotropy

Thin films with perpendicular magnetic anisotropy (PMA) have been under intensive investigation in the last few decades. Magnetization switching in PMA media is very often more complicated than for films with only in-plane anisotropy. The existence of the out-of-plane anisotropy constant creates a delicate balance among different energy terms, in competition with the in-plane magnetic shape anisotropy term. Magnetic fluctuations in PMA magnetic films are of great importance for magnetic recording applications, but have not been addressed previously. In this chapter, we show how the magnetic noise due to fluctuations in the magnetization of a small sample volume of a PMA magnetic material changes as we go around the hysteresis loop. The fluctuations are measured using the anomalous Hall

effect, which gives a much higher sensitivity than microscopic magnetometers. First order reversal curves (FORCs) were also used to characterize the magnetization switching process, and an account of the results was based on the classical Preisach model, which treats the magnetic hysteresis as a superposition of elementary square hysteresis loops — 'hysterons'.

4.1 Introduction

4.1.1 Perpendicular Magnetic Anisotropy Media

In micromagnetics, the discrete nature of matter is neglected. The shape anisotropy due to dipolar interactions of a uniformaly-magnetized ellipsoid can then be expressed by the demagnetizing field $\boldsymbol{H}_d$

$$\boldsymbol{H}_d = -N \cdot \boldsymbol{M} \tag{4.1}$$

where N is the demagnetizing factor, which is dependent on the ratio of the three axes of the ellipsoid, a, b, and c [1]. Numerical values of N have been tabulated by Osborn [2].

The demagnetizing factor for a thin magnetic film is simple. It is 1 for the magnetization direction perpendicular to the layer, while zero for any in-plane magnetization direction. This leads to the shape anisotropy of magnetic thin films, defined as the magnetostatic energy due to dipolar interactions per unit volume

$$\varepsilon_d = \frac{1}{2}\mu_0 \boldsymbol{M}_s^2 \cos^2\theta \tag{4.2}$$

in which θ is the angle between the magnetization and the film normal [3].

This shape anisotropy energy favours an in-plane magnetization direction, and it is the reason that an in-plane direction is always the easy magnetization direction in conventional magnetic thin films.

However, there exist a few magnetic thin film systems and superlattice structures, in which the preferred magnetization orientation lies perpendicular to the film plane, due to other anisotropy energy contributions. In general, the effective magnetic anisotropy energy K_{eff} in J/m^3 can be expressed by a volume term K_V and an interface term K_s

$$K_{\text{eff}} = K_V + 2K_s/t \tag{4.3}$$

with t the thickness of the magnetic layer [1].

The main contribution to the first term in Eqn. (4.3) is very often the magnetostatic energy described by Eqn. (4.2). However, in certain magnetic materials, for example, well-oriented chemically ordered $L1_0$ FePt [4] and FePd alloys [5], or hcp cobalt thin films with its c-axis perpendicular to the film plane [6], the magnetocrystalline anisotropy can play a very important part in the volume anisotropy term, even changing the easy magnetization axis from in-plane to out-of-plane.

The second term in Eqn. (4.3), K_s, can normally also be divided into two parts. The first part is usually named as interface anisotropy, first discussed by Louis Néel [7], which also originates from the spin-orbit coupling, as in the case of the magnetocrystalline anisotropy. The difference between the interface anisotropy and the magnetocrystalline anisotropy is due to the breaking of lattice symmetry at the interface [1]. Hence, in magnetic multilayers, having a very high interface to volume ratio, it is possible to obtain an interface anisotropy term favouring the thin film normal direction, e.g. in Co/Pt and Co/Pd multilayers [8, 9, 10, 11]. The second part is often

called 'magneto-elastic anisotropy', which can be seen as the inverse effect of magnetostriction – the change of sample dimension due to its magnetization change[1]. This anisotropy K_{me} can be expressed as

$$K_{\text{me}} = -\frac{3}{2}\lambda\sigma = -\frac{3}{2}\lambda E\epsilon \tag{4.4}$$

with λ the magnetostriction constant, σ the stress, ϵ the strain, and E the elastic modulus given by $\sigma = E\epsilon$ [1]. For thin film multilayers, the most important magneto-elastic anisotropy comes from the mismatch of the lattice parameters of two materials. It has been shown experimentally that the perpendicular anisotropy in Co/Pt and Co/Pd multilayers is partly from this magneto-elastic anisotropy and partly from the interface contribution [12, 13].

One important parameter characterizing a magnetic thin film with perpendicular anisotropy is its 'quality factor' Q defined as [14]

$$Q = \frac{2K_u}{\mu_0 M_s^2} \tag{4.5}$$

It can be seen as the ratio of the out-of-plane uniaxial magnetic anisotropy K_u to the shape anisotropy created by dipolar interactions, with the former consisting of possible contributions from magnetocrystalline, interface, and magneto-elastic anisotropies. Uniformly-magnetized films of a few nanometers thick having spontaneous magnetization M_s and perpendicular anisotropy K_u exhibit perpendicular magnetization when the quality factor Q is greater than 1. The hysteresis may then be a simple square loop like that of a Stoner-Wohlfarth particle (Appendix A.6), with an abrupt switch

[1]Strictly speaking, magneto-elastic anisotropy might not be a pure interface anisotropy. For details see [1].

from magnetization $+M_s$ to $-M_s$ at the coercive field H_c, when the applied field is along the easy axis. Perpendicular magnetization remains possible when $Q < 1$, but in a multidomain state, which is stabilized by the stray field created by a maze of stripe domains. In that case, the magnetization switches from a uniformly-magnetized state in a positive applied field to a maze domain state, which is then progressively demagnetized by domain wall motion. The reverse stripes broaden and the normal stripes narrow before breaking up into segments and bubbles, eventually disappearing as the sample reaches saturation in the reverse direction. This process is depicted in Fig. 4.1. If Q becomes even smaller, the out-of-plane uniaxial anisotropy is not enough to sustain this perpendicular magnetization, and magnetization of the thin film turns in-plane.

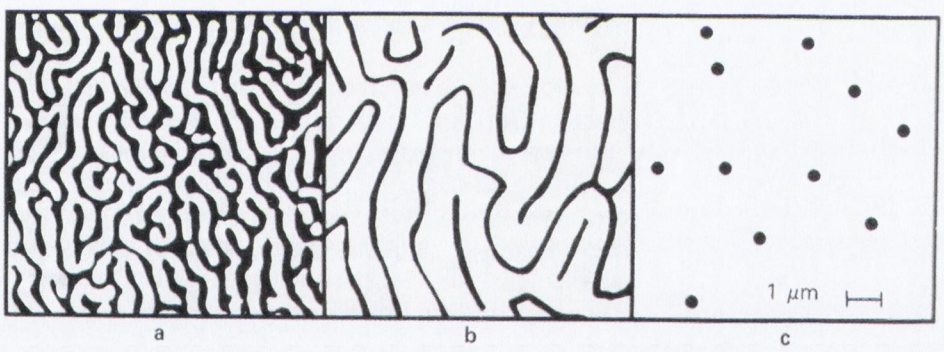


Fig. 4.1: Domains patterns observed in a typical magnetic thin film with $Q \sim 1$ during magnetization switching. (a) Stripe domains, (b) reverse stripes broadening while the normal stripes narrowing, (c) bubble domains (reproduced from [15]).

From the application point of view, magnetic thin films with perpendicular anisotropy were first developed as potential magneto-optical recording media [9], and are still of great interest for the perpendicular magnetic storage industry [16, 17]. It also finds new applications in the spintronics

community [18, 19]. Hence, understanding the physics, especially the magnetization switching process in these materials, is important for addressing these application issues. Cobalt or iron by itself normally does not have enough anisotropy to sustain perpendicular magnetization in unstructured films, but when it is prepared in thin film form and interleaved with layers of Pt or Pd, the interfacial anisotropy and the reduced magnetization of the stack ensure that $Q \sim 1$. They form stripe domains when the applied magnetic field is decreased from positive saturation, which have been used in determining the domain-wall resistance in wires patterned from the stacks [20]. The system we investigate in this chapter, the $(CoFe/Pt)_n$ multilayers with 10 atomic percent iron doping in the cobalt layer, is expected to have a similar magnetic behaviour as the well studied Co/Pt multilayers, possibly with a higher moment due to iron doping.

4.1.2 Anomalous Hall Effect

In magnetic materials in a perpendicular magnetic field, it has been observed that a much larger Hall voltage develops in the transverse direction of the current flow than can by explained by the ordinary Hall effect. Phenomenologically, it can be described by the following equation.

$$\rho_H = R_0 B + R_s \mu_0 M \tag{4.6}$$

with ρ_H the Hall resistivity, R_0 the ordinary Hall coefficient, and R_s the anomalous Hall coefficient [21]. The ordinary Hall voltage changes linearly with the applied magnetic field, while the anomalous Hall coefficient is proportional to the magnetization of the sample. In a ferromagnetic material, it has been suggested that the second term R_s is normally the dominant

contribution [22]. Hence, it can be used to characterize the magnetization switching in a ferromagnet via a simple electrical measurement.

The origin of the anomalous Hall effect is still under an intense debate. It is generally agreed that spin-orbit scattering and the asymmetry in spin-up and spin-down electrons in a ferromagnetic material are the key factors in any model for AHE. Two models have always been mentioned in this context. The first is the 'skew scattering' mechanism, which is the broken left-right symmetry in a scattering event. The second is called 'side-jump' mechanism, which is a quantum mechanical effect causing finite lateral displacement upon scattering, and it is the most significant effect in ferromagnets with short mean free paths. The former model gives a R_s proportional to the longitudinal resistivity of a homogeneous sample, $R_s \propto \rho_{xx}$, whereas the latter model predicts the scaling of R_s as the square of the longitudinal resistivity $R_s \propto \rho_{xx}^2$.

In a magnetic/non-magnetic multilayer system, such as $(\mathrm{CoFe/Pt})_n$ which we studied, it is not clear what the scaling rules should be. Theoretical studies have shown that the scaling rules in superlattice multilayers are to be modified [23], and it was partly supported by subsequent experimental works [13]. For this reason, we use the so-called 'black box' approach to treat our anomalous Hall effect data [24], in which samples are only characterized by the phenomenological parameters without further discussion on the origin of the effect. Hence, for our $(\mathrm{CoFe/Pt})_n$ multilayers

$$\rho_H = \frac{V_H}{I} t \tag{4.7}$$

where V_H is the Hall voltage, I is the longitudinal current through the sample, and t is the total thickness of the multilayers. Assuming the paramagnetic layer (Pt) is not polarized by the ferromagnetic cobalt layer (which

is not exactly true in reality [25]), we have

$$R_s = \frac{R_H t^2}{\mu_0 m_{FM} t_{FM}} \tag{4.8}$$

where R_H is the measured anomalous Hall resistance, m_{FM} and t_{FM} are the magnetic moment and the thickness of cobalt layers, respectively [24].

4.1.3 Preisach Model and First Order Reversal Curves

The hysteresis behaviour of magnetization switching is usually characterized by the major hysteresis loop, which starts from a large positive magnetic field under which the material is saturated, and goes to a large negative magnetic field to saturate the material in the opposite direction, then comes back. This process can be stopped at some point of the major hysteresis loop, and the applied field switched to the opposite direction, driving the material back to saturation. This is called a first-order reversal curve (FORC), and the point at which the field is reversed is called a turning point [26]. A FORC is a minor hysteresis loop with only a single turning point. The magnetic field at this point is denoted H_R, the reversal field. If we measure a series of first-order reversal curves across a range of reversal fields, they will fill the interior of the major hysteresis loop. We denote the magnetization under applied field H on the first-order reversal curve with a reversal field of H_R as $M(H_R, H)$. The FORC distribution parameter $\rho(H_R, H)$ is then defined by a mixed second-order derivative [27, 26, 28],

$$\rho(H_R, H) = -\frac{\partial^2 M(H_R, H)}{\partial H_R \partial H} \tag{4.9}$$

It can be seen that the definition of $\rho(H_R, H)$ eliminates the pure reversible part of the magnetization [29], since in this case the magnetization

$M(H_R, H)$ does not change from one reversal curve to another, and the successive FORCs overlap. Hence, the magnetization is a single variable function against applied magnetic field H. This leads to a zero value of the FORC distribution parameter $\rho(H_R, H)$. A plot of the FORC distribution parameter $\rho(H_R, H)$ against H and H_R is called a FORC diagram.

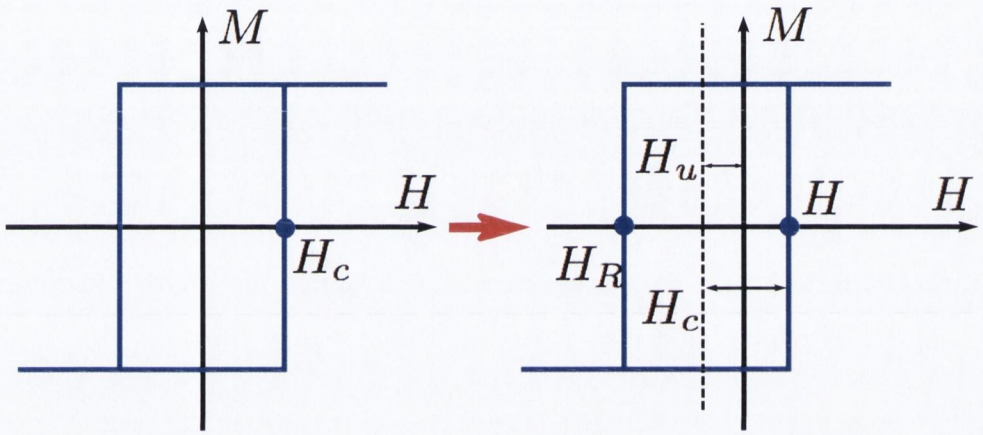


Fig. 4.2: A diagram showing a non-interacting hysteron (left) and a hysteron with an interaction field H_u.

The Preisach model is a mathematical tool for describing the hysteresis behaviour [30]. It considers the material having a large collection of square hysteresis loops – hysterons, each with a normalized magnetization m, but different coercive fields H_c and interaction fields H_u (Fig. 4.2). The interaction field shifts the centre of a hysteron from the origin. A positively saturated hysteron reverses when a magnetic field of $H_R = -H_c + H_u$ is applied, whereas a negatively saturated hysteron reverses at an applied magnetic field of $H = H_c + H_u$ [26]. From the view of Preisach model, the event of a hysteron switching is lodged by the mixed second-order derivative $\rho(H_R, H)$. Hence, a diagram of the FORC distribution parameter against

H_R and H, is effectively a diagram of hysteron switching events. The critical field and interaction field of a hysteron are related to H_R and H by [31, 32]

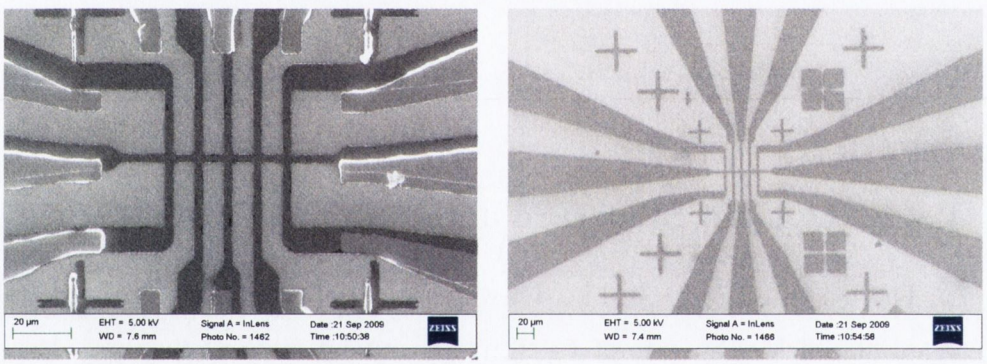
$$H_c = \frac{H - H_R}{2}, \; H_u = \frac{H + H_R}{2} \tag{4.10}$$

Hence, we can also build FORC diagrams on the H_c-H_u plane, namely the Preisach plane. Previously, FORC diagrams have been intensively investigated in magnetic nanoparticles [33, 34, 35, 36]. A FORC diagram of $[Co(0.4\ nm)/Pt(0.7\ nm)]_{50}$ multilayers was also reported [29], together with a few more studies on multilayer thin films [37, 38]. However, no systematic studies on the FORC diagrams in relation to the multilayer repetition was carried out. Moreover, the authors only looked at the FORC diagram on the H_R-H plane, but not on the real Preisach plane.

4.2 Materials and Methods

Our samples of $(CoFe/Pt)_n$ were deposited by DC sputtering in an SFI Shamrock industrial sputter tool on Si/SiO_2 substrates. Layer thicknesses were 0.5 nm and 1.0 nm for the $Co_{90}Fe_{10}$ (numbers are in atomic percent) and Pt, respectively, with a 2 nm Pt cap and seed layer. The number of repeats were 10, 20 and 50. The stacks were patterned into Hall bars by photolithography. Gold pads were fabricated by a second optical lithography process to further reduce the two point resistance of the low repetition samples. Fig. 4.3 shows selected SEM images of the Hall crosses. The wires have a width w = 3 μm, and their thickness t varies from 19 nm for n = 10 to 79 nm for n = 50 (including the Pt seed and capping layers). For the Hall noise measurement, the Hall resistance is measured by passing a current, I = 1 - 3 mA along the wire, and sensing the Hall voltage V ($\sim$ 1

mV) across the transverse contacts on the transport and noise measurement set-up described in Chapter 3. In our case, the anomalous Hall voltage is proportional to the perpendicular magnetization M averaged over the active volume in the Hall bar, which is approximately w^2t. Small incremental changes in field were used to sweep between magnetic states. Noise measurements were started a few seconds after attaining the field setpoint and typically consisted of acquiring 50 - 100 averages of the power spectrum. The averaged power spectrum was binned into 7 consecutive octaves and their values were recorded.



(a) (b)

Fig. 4.3: SEM images of $(CoFe/Pt)_n$ Hall crosses fabricated by photolithography. (a) Hall crosses of a $(CoFe/Pt)_{10}$ sample with additional Au contacts; (b) Hall crosses of a $(CoFe/Pt)_{50}$ sample without additional Au contacts.

Magnetic force microscopy was performed on thin films of the same stack under virgin state of the sample, or else after an AC demagnetization process. No significant difference in domain structure was observed between these two states. This suggests that the stray field of the sputtering gun in our deposition system is too weak to exert any perceptible effect on the domain structure. The MFM images were used to characterize the domain size of the samples. Selected Hall crosses were also imaged under MFM,

and no distinguishable difference in the domain structure was observed in comparison to their thin film counterparts.

Unpatterned samples were also measured in a commercial superconducting quantum interference device (SQUID) magnetometer, with a magnetic field of 5 T for determining their saturation magnetization.

FORCs of the same samples were measured in a magnetotransport set-up on a GMW electromagnet. The current sourcing and voltage readout are both performed by a Keithley 2400 SourceMeter. The whole measurement set-up was connected via GPIB bus, and controlled by a computer running LabView.

4.3 Results

4.3.1 Domain Structure and Anomalous Hall Effect

The hysteresis loops in Fig. 4.4 were deduced from the anomalous Hall signal at a field scan rate of 1 - 2 $\mathrm{mT{\cdot}s^{-1}}$. A hysteretic behaviour closely resembling that for perpendicular anisotropy films with $Q \sim 1$ as described in Section 4.1.1 is evident. On the left, are illustrations of the domain structure in the virgin, unmagnetized state, determined by magnetic force microscopy. The domain structures for the $n = 20$ and $n = 50$ stacks in zero field, after saturation, resemble those in the virgin state. The domain width is 100 - 150 nm. Samples with lower n have a slightly larger domain width, which can be well described by the Kooy-Enz model [39], or a modified model taking the multilayer nature of the sample into account [40] (see Appendix A.7). The comparison with the magnetization loop measured on an unpatterned film ($n = 20$) using a SQUID magnetometer is shown by the dotted line in Fig. 4.4(b). Evidently, the magnetization averaged over

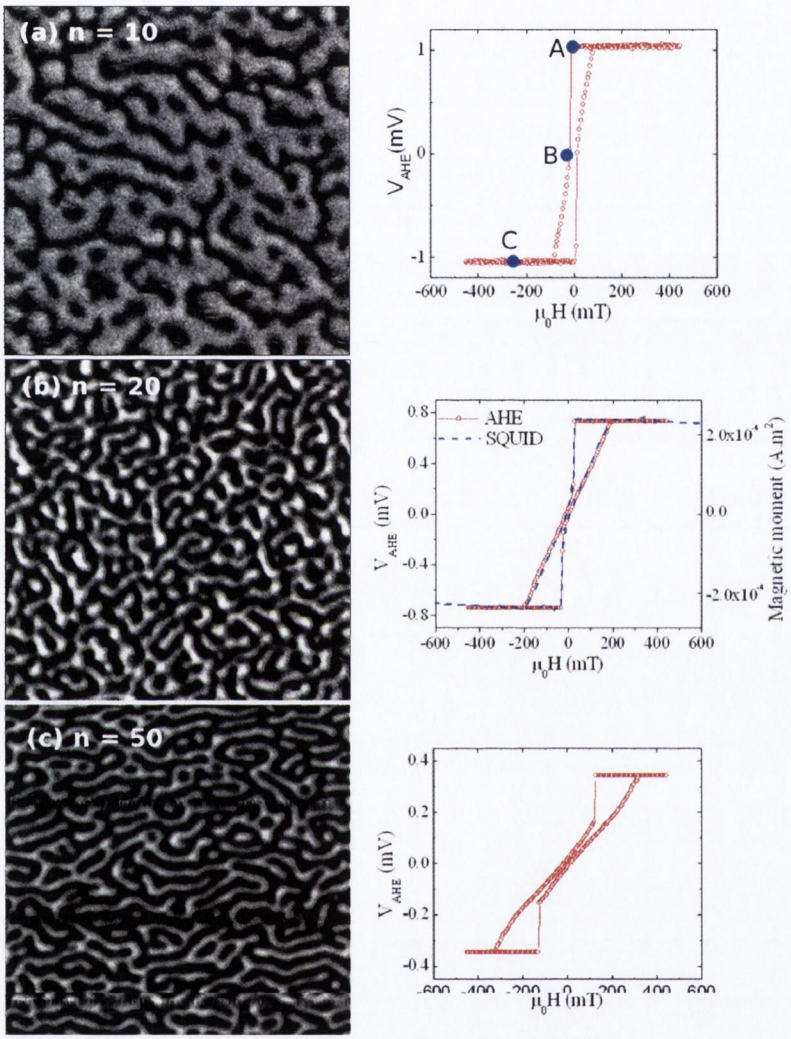


Fig. 4.4: Magnetic hysteresis loops of three ($Co_{90}Fe_{10}$/Pt) multilayer stacks, with different numbers n of bilayer repeats. Hysteresis loops are deduced from the anomalous Hall effect. MFM images (5 μm $\times$ 5 μm) show the domain structure in the virgin state of each sample. In the $n = 20$ case, the magnetization curve is compared with one determined by SQUID magnetometry on an unpatterned film.

the small active Hall volume is representative of the magnetization of the whole film. The reversal in the quasi-linear slanted sections of the hysteresis loops occurs in the maze domain state, as described in detail in Refs. [29] and [41]. Comparisons with loops calculated by Clarke et al. [42] can be used to associate Q numbers of 1.06, 0.94 and 0.69, respectively, with the three samples.

The magnetization of the unpatterned stacks was determined as $M = 500$ kAm^{-1} from SQUID measurements. The magnetic moment in the active volume of the Hall bar is only of order 10^{-13} Am^2, or about 10^{10} Bohr magnetons. This is far beyond the sensitivity of the SQUID. Greater sensitivity to magnetic fluctuations may be achieved by measuring the stray field of a tiny magnet placed on an microsquid, at cryogenic temperatures [43], or by passing an electron beam through the specimen, in Lorentz microscopy [44]. However, the present method provides a measure of the perpendicular magnetization as well. The anomalous Hall resistance can be used to determine both the relative magnetization in a submicron volume, and its temporal fluctuations, quickly and accurately over a range of temperatures.

It is also known that $(Co/Pt)_n$ multilayer systems normally have complicated rate-dependent magnetization processes. In order to confirm that the measured anomalous Hall effect loops in Fig. 4.4 are not greatly affected by the field sweep rate, we measured the AHE voltage while 'boosting' the electromagnet from positive saturation to negative saturation. In this case, the field ramping rate is only limited by the internal current-limiting capacitor of the electromagnet power supply, and a field ramp from +400 mT to -400 mT takes only 5 - 6 s. The resulted half-loop is shown in Fig. 4.5 and compared to that measured by sweeping the field in a normal rate of 1 - 2 mT·s^{-1}, as for Fig. 4.4. No significant difference is observed between these

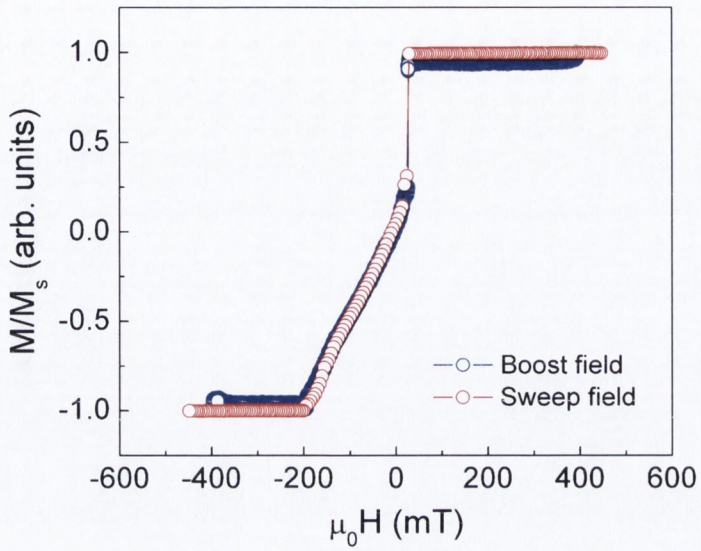


Fig. 4.5: Magnetization curves measured by sweeping the applied magnetic field step by step with a rate of 1 - 2 mT·s^{-1}, and measured by boosting the magnetic field between positive and negative saturation within 5 s.

two cases (much of the difference observed in the figure can be attributed to the oscillation of the current limiting feedback control of the power supply), which suggests that the AHE loops we measured are representative for quite a wide range of field ramping rates.

4.3.2 Anomalous Hall Voltage Noise

Figure 4.6 shows half hysteresis loops on n = 10, 20, 50 stacks, and the Hall voltage noise in an octave centred at 4.8 Hz as a function of field. The noise-field profile on the three stacks show similar behaviours for the lowest three octaves (extending up to $\sim$ 50 Hz) on all the stacks measured. Profiles of the higher octaves show progressively higher field-independent background levels outside the magnetization reversal region. This is due to

the thermal noise of the lead resistance, R_l, in series with the Hall segment. R_l is about 500 Ω, much larger than $R_s \sim 1\ \Omega$, and its thermal noise dominates the power spectrum at high frequencies (see Fig. 4.10). This can be seen more clearly when noise voltage across different octaves are plotted, as in Fig. 4.7. The noise power in each octave is expected to be the same for pure $1/f$ noise ($P = A\ln 2$, with A being a constant), but doubles among consecutive octaves for white noise. It describes exactly what is observed in Fig. 4.7, where $1/f$ noise only exists during the magnetization switching.

Taking Fig. 4.6(b), for example, the magnetic noise behavior can be summarized as follows. When the magnetic field is at positive saturation (450 mT), no low-frequency noise above the thermal background level is observed. Spikes in the low frequency noise power, more than an order of magnitude above the background level, are observed when the magnetic field is swept back to the domain nucleation field, where a sudden switch in Hall voltage occurs. The Hall voltage then crosses over into a regime that is linear in field, which is characteristic of the widening of the reversed stripe domains. Concurrently, the magnetic noise is considerably lower, but remains well above the background. At a more negative field (-150 mT), close to reverse saturation, huge noise spikes reappear together with changes in the slope of the Hall voltage ($dV_H/d\mu_0 H$). The occurrence of noise spikes persists over a magnetic field range of about 50 mT, and disappears when the magnetic layer reaches negative saturation.

Minor loops studies have been carried out to verify the appearance of magnetic noise in relation to the sample magnetization states (Fig. 4.8). It has been shown that magnetic noise only appears in the region of applied field where magnetization reversal occurs. No excess noise was observed when the sample is fully saturated independent of the magnetic history.

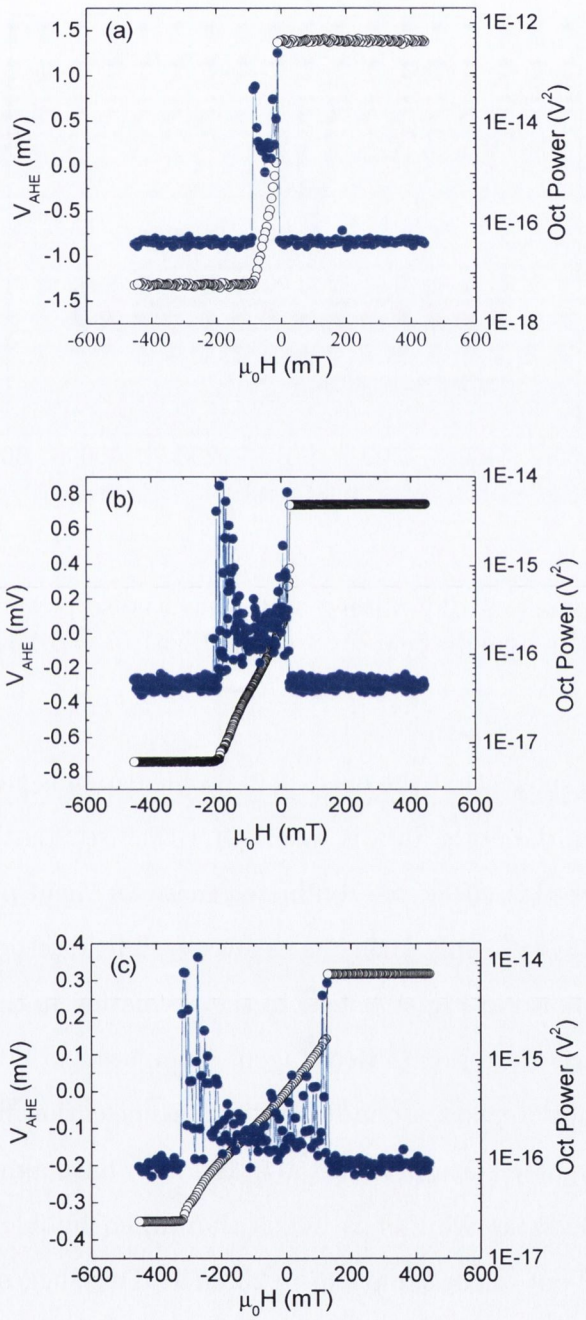


Fig. 4.6: Anomalous Hall voltage and octave noise power (centred at 4.8 Hz) against magnetic field for three samples with different n. The bias current for AHE has been normalized to 1.2 mA.

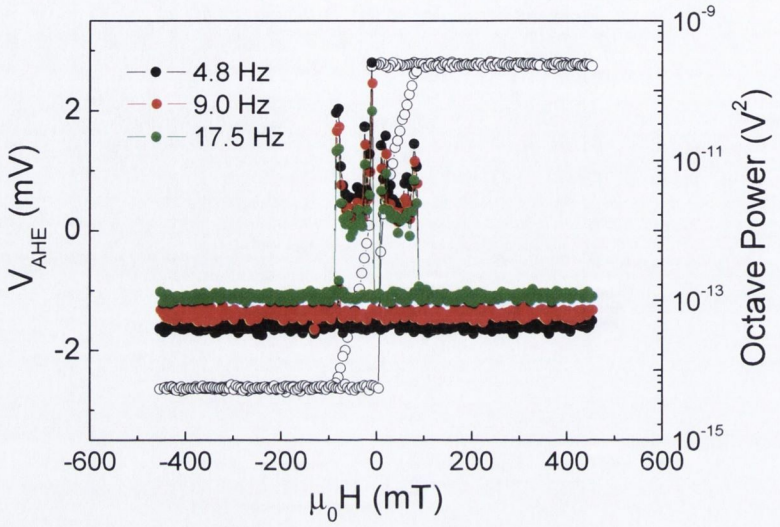


Fig. 4.7: Anomalous Hall votage and octave noise power in the lowest 3 octaves against magnetic field for a sample with $n = 10$. The bias current is 2.4 mA

It has been shown that the noise-field profile depends partly on the waiting time before the noise data is taken after each setpoint field is reached. To characterize this effect, we conducted noise vs. field measurements, in which noise data were only taken 5 min after each field setpoint was reached. The result is shown in Fig. 4.9. Due to the restriction in the total measurement time, fewer data points were taken. Compared to Fig. 4.6(b), we can see that the noise spikes around the domain nucleation field (0 mT) and close to the negative saturation (-150 - -200 mT) have almost disappeared. The only noise spike which has left is that when bubble domains are finally squeezed out of the sample at $\sim$ 200 mT. This suggests that the noise spikes during the above two situations are not due to stationary processes. However, excess noise power of $1/f$ nature, appearing during the continuous expansion of stripe domains, is hardly affected by the length of waiting time

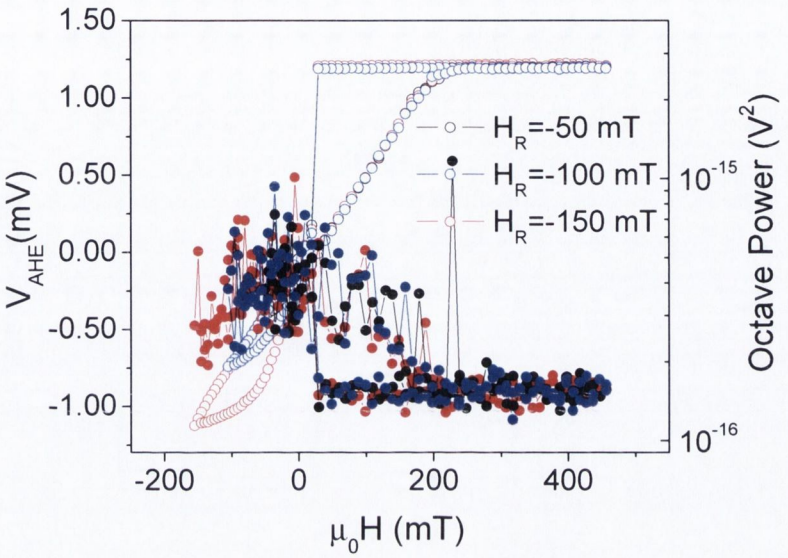


Fig. 4.8: Three minor hysteresis loops of anomalous Hall voltage and octave noise power (centred at 4.8 Hz) against magnetic field measured on a $n = 20$ sample. The reversal field H_R are -50 mT, -100 mT and -150 mT, respectively. The bias current is 1.2 mA.

before which noise data were taken. It is stationary noise.

In order to better understand how the noise is related to the magnetization switching process, we recorded noise spectra at several representative magnetic field levels on the $n = 20$ sample (Fig. 4.10). The magnetic field was swept at a rate of 2 mT·s^{-1} from positive saturation to the field setpoint. At each field, an average power spectrum was determined from 64 consecutive power spectra computed from 5 s time records of the Hall voltage, sampled at 400 Hz. The total data acquisition time at each field setpoint was about 5 min.

The spectra are characterized by excess low-frequency noise scaling inversely with frequency and crossing over to a white (frequency-independent) noise level above 50 Hz. The white noise level is the expected thermal noise,

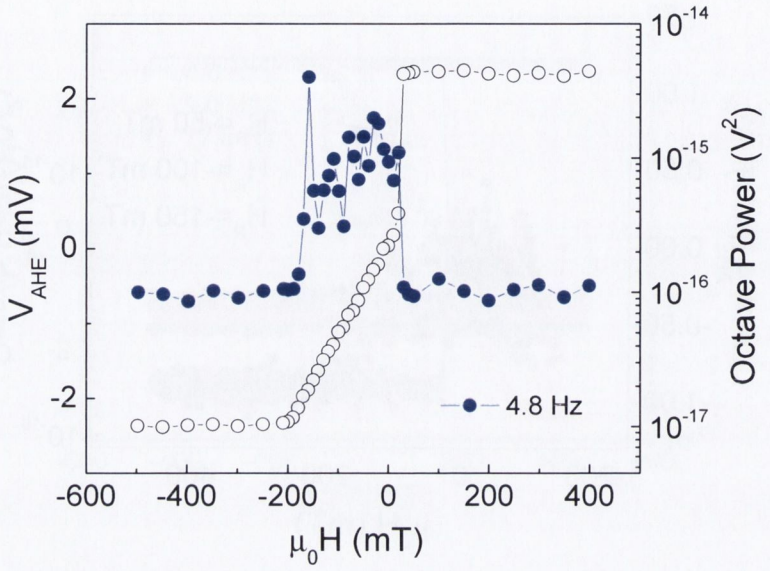


Fig. 4.9: Anomalous Hall voltage and octave noise power (centred at 4.8 Hz) against magnetic field on a sample with $n = 20$. Noise data were taken 5 min after each field setpoint was reached. The bias current is ~ 3.2 mA.

$S_V = 4k_BTR$, coming from the lead resistance. The two noise spectra in Fig. 4.10 having the highest slopes (denoted by the solid symbols • and ▲) were obtained at 25 mT (just before the magnetization switch) and at -175 mT (just before negative saturation). Their low frequency dependences can be fitted by a power-law curve, $S_V = 1/f^\alpha$, with $\alpha \sim 1.7$.

The large noise spikes that occur around the magnetization switching and just before negative saturation are due to step-like magnetic relaxation events that occur during the timescale of our measurements. The relaxation process gives rise to nonstationary noise spectra as illustrated by two other spectra shown in Fig. 4.10 (◯ and △). These spectra were taken during a 5 minute time interval starting 5 min after the setpoint fields were reached. They show very different characteristics compared to their earlier

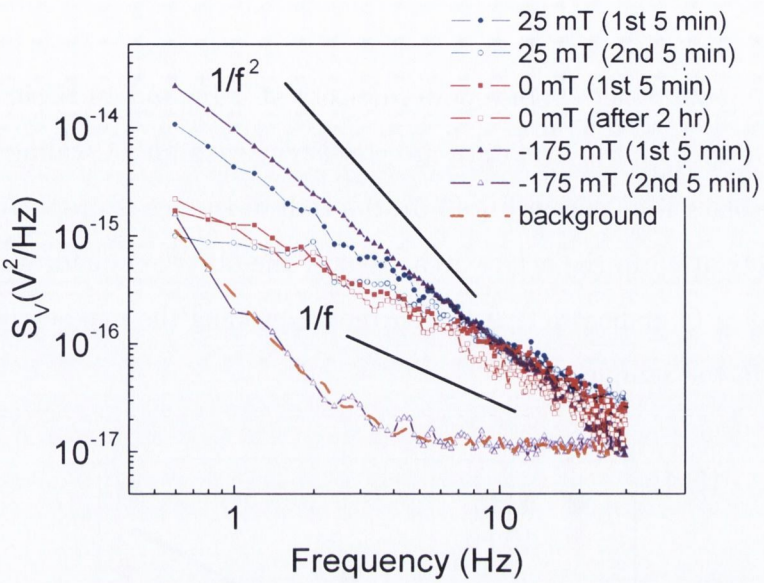


Fig. 4.10: Noise spectra at three different magnetic fields for the sample of Fig. 4.6. The field was swept from positive saturation to the setpoint at a rate of 2 mT·s^{-1}. The background has been subtracted from the spectra except for the one taken in the second 5 min at -175 mT. The dashed line is the background, consisting of the amplifier noise and the thermal background noise of the sample.

counterparts. The spectrum denoted by open circles was measured 5 min after reaching a setpoint field of 25 mT. It closely resembles the $1/f$ spectra measured at 0 mT (■ and □). This can be understood because after the magnetization switch at 25 mT is complete, the sample is in a maze domain state where the magnetic noise has a $1/f$ spectrum. The open triangles denote the spectrum at -175 mT taken after 5 min. It is nearly equivalent to the spectrum of the amplifier plus thermal resistance noise (dashed line) because the relaxation process has driven the system to negative saturation. On the other hand, magnetic noise spectra obtained at a setpoint field of 0 mT were stationary, and of $1/f$ character. There was little or no change

of the spectra within a time frame of a few hours (□ in Fig. 4.10), or even days.

In Fig. 4.11, we plot the noise power density at 4 Hz and 10 Hz in zero field against current bias. The data are consistent with an I^2 scaling (denoted by the black line). From Eq. (4.6), the Hall resistance is proportional to the magnetization in the active area. Hence, the observed quadratic dependence, $S_V \sim I^2$, indicates that the current is probing the magnetization fluctuations in the sample.

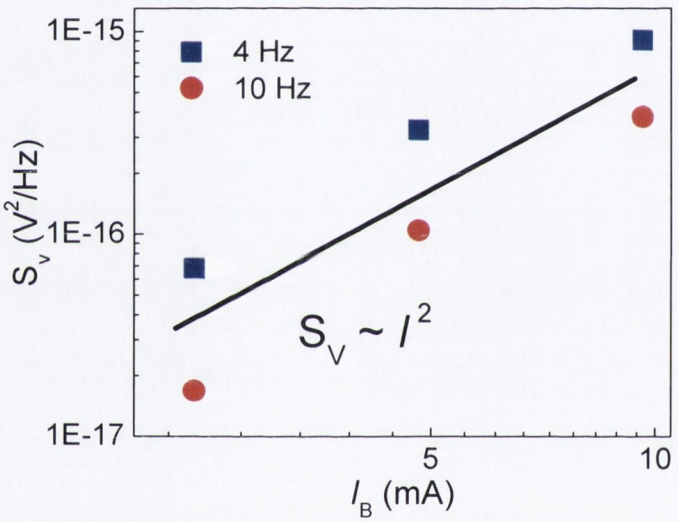


Fig. 4.11: Power spectrum density at 4 Hz and 10 Hz for a $n = 20$ sample with different current biases.

The time evolution of the magnetization can be used to further characterize the magnetic noise spectra. Figure 4.12 shows three time records of the Hall voltage which were started shortly ($\sim$ 1 s) after the setpoint field was reached upon sweeping the field down from positive saturation. Substantial magnetic relaxation is observed at short times for setpoint fields near the magnetization switching field (Fig. 4.12(a)) and there is also

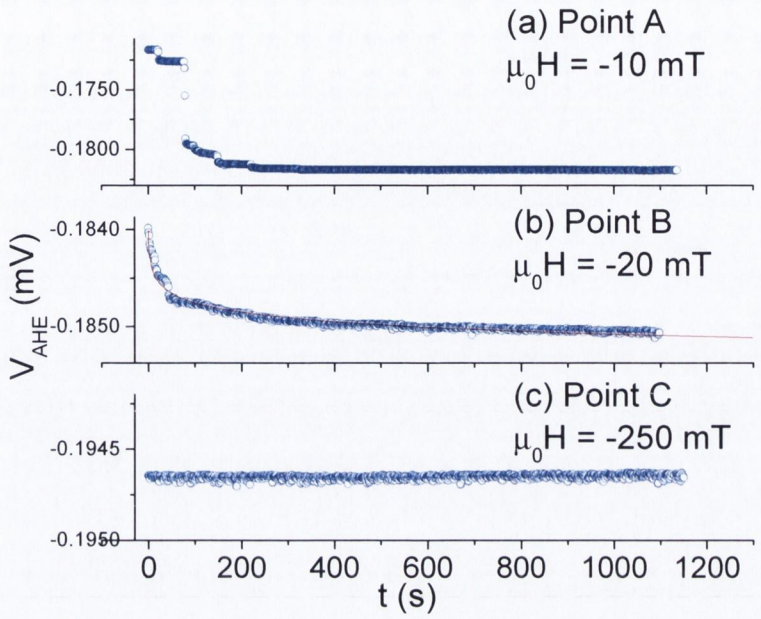


Fig. 4.12: Time sequence measured on a n =10 sample with different setpoint fields. (a) -10 mT, (b) -20 mT, and (c) -250 mT. Points A, B and C refer to those labelled in Fig. 4.4a. The bias current is 1.2 mA.

some relaxation in the quasi-linear V_H vs. $\mu_0 H$ region (Fig. 4.12(b)). No relaxation is observed when the sample is driven to negative saturation (Fig. 4.12(c)). For setpoint fields just before magnetization switching, the relaxation is characterized by a series of Barkhausen jumps such as those shown in Fig. 4.12(a). In the quasi-linear V_H vs. $\mu_0 H$ region, the relaxation is continuous and is related to the magnetic after-effect. Also known as magnetic viscosity, this is the sluggish time response of the magnetization to a change in applied field, within the hysteresis loop. At times which are neither very short, nor very long, the change of magnetization varies as

$$\Delta M = S \ln(t/t_0) \tag{4.11}$$

where S is the magnetic viscosity which is related to a fluctuation field by $H_f = S/\chi_{irr}$, in which χ_{irr} is the irreversible susceptibility [45, 46]. The magnetization relaxation for the $n = 10$ sample at -20 mT can be fitted to Eq. (4.11), with $S \approx 50$ A·m^{-1} and $t_0 \approx 1$ s.

4.3.3 First Order Reversal Curves

The results of the first order reversal curves measurement are summarized in Figs. 4.13 - 4.15 [2]. Due to the sharp transition in the $n = 10$ sample at the switching field, significantly fewer FORCs were recorded. There is a drift of the Hall voltage signal in some of the measurements, which is attributed to the very long time it takes to acquire the full set of FORC loops (in the range of a few tens of hours).

The FORC diagrams of the three samples, plotted on the Preisach plane, with H_c and H_u as the two axes, are summarized in Fig. 4.16.

Some key observations from the FORCs diagrams can be summarized as follows. There are two clearly distinguishable peaks in all the three diagrams, one of which has a positive interaction field H_u, while the interaction field of the other one is negative. The coercive fields for both peaks increase with the number of repetitions, n, from 10 to 50. The coercive field for the peak with negative interaction field is always larger. There is also a trend that the peaks become broader as n increases. When the number of repetitions grows from 10 to 50, the distance between these two peaks becomes larger. The area between the two peaks is considerably quiet, with a very small FORC distribution parameter $\rho(H_u, H_c)$. A slightly larger ρ

[2]The results were obtained in a summer student project for Nicolas Decorde, from INSA Toulouse, set up by the candidate, and coordinated with Dr. Karsten Rode and Dr. Plamen Stamenov. The FORCs diagrams were calculated with the help of Dr. Plamen Stamenov.

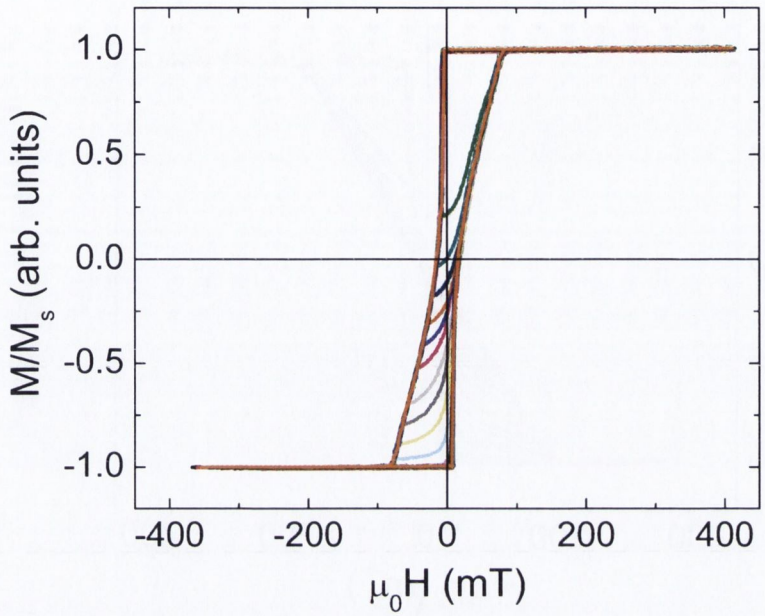


Fig. 4.13: FORCs measured on a $(CoFe/Pt)_{10}$ sample.

for the 50 repetition sample is observed compared to samples with 10 and 20 repetitions. Another noticeable feature is that there exists a small peak with a very small coercive field in the FORCs diagram for the 50 repetition sample besides the other two peaks mentioned above. This peak also has a positive interaction field and is connected to the other positive interaction field peak with an area having non-zero $\rho(H_u, H_c)$ values.

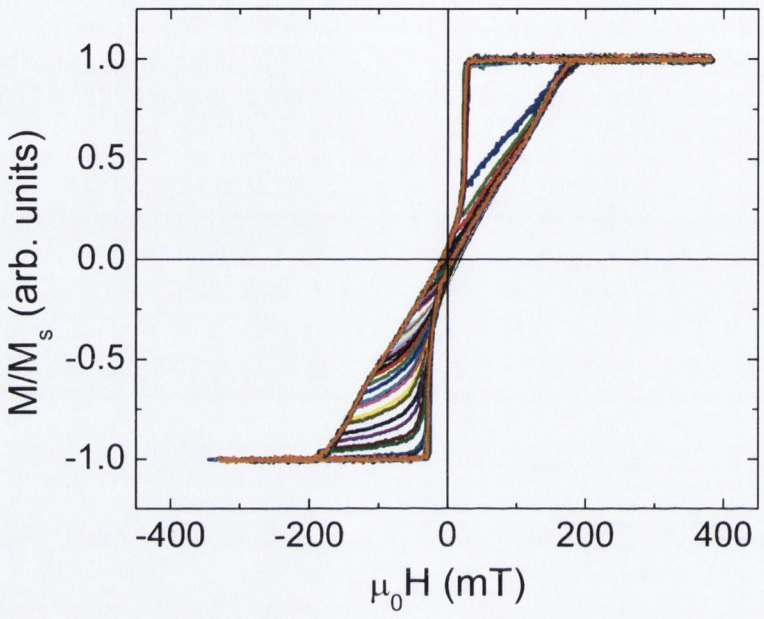


Fig. 4.14: FORCs measured on a $(CoFe/Pt)_{20}$ sample.

4.4 Discussion

4.4.1 Anomalous Hall Voltage Noise

We first consider the $1/f^{1.7}$ noise spectrum at the switching field and before negative saturation. A number of physical processes can lead to a $1/f^{\alpha}$ spectrum with α close to 2, including a drift or stepwise change of resistance [47, 48], a growth-coalescence process [49, 50], and two-level fluctuations having a characteristic transition rate [51, 52]. In the case of electromigration, resistance drift leads to a spectrum with higher spectral density at low frequencies. In previous work, Koch [53] studied the power

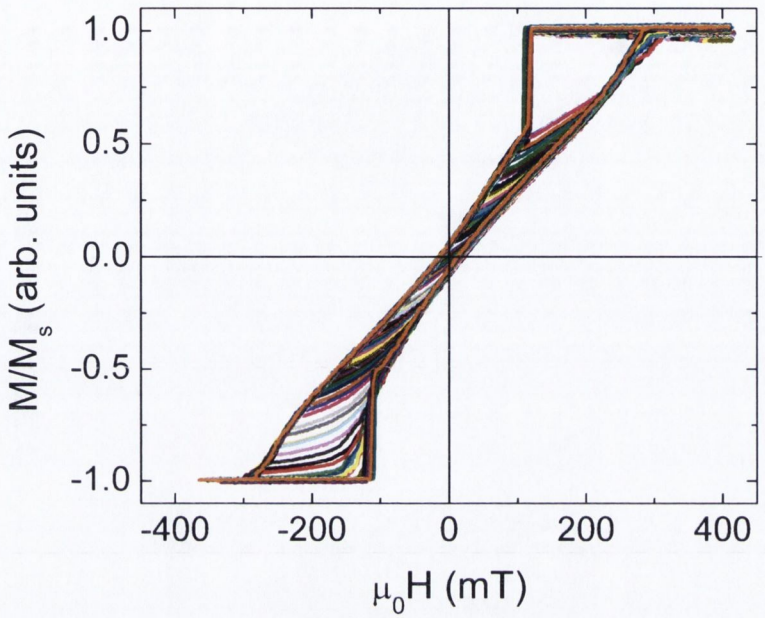


Fig. 4.15: FORCs measured on a $(CoFe/Pt)_{50}$ sample.

spectrum from a resistor whose resistance varies with time

$$R(t) = R_0 + \alpha t \tag{4.12}$$

He showed that its power spectrum could be expressed as

$$S(f) = \frac{\alpha^2 T}{2\pi^2 f^2} \tag{4.13}$$

where T is the measurement time. Similarly, if the resistance of a resistor takes step-like drift, the power spectrum is

$$S(f) = \frac{N^2 \Delta R^2}{2T\pi^2 f^2} \tag{4.14}$$

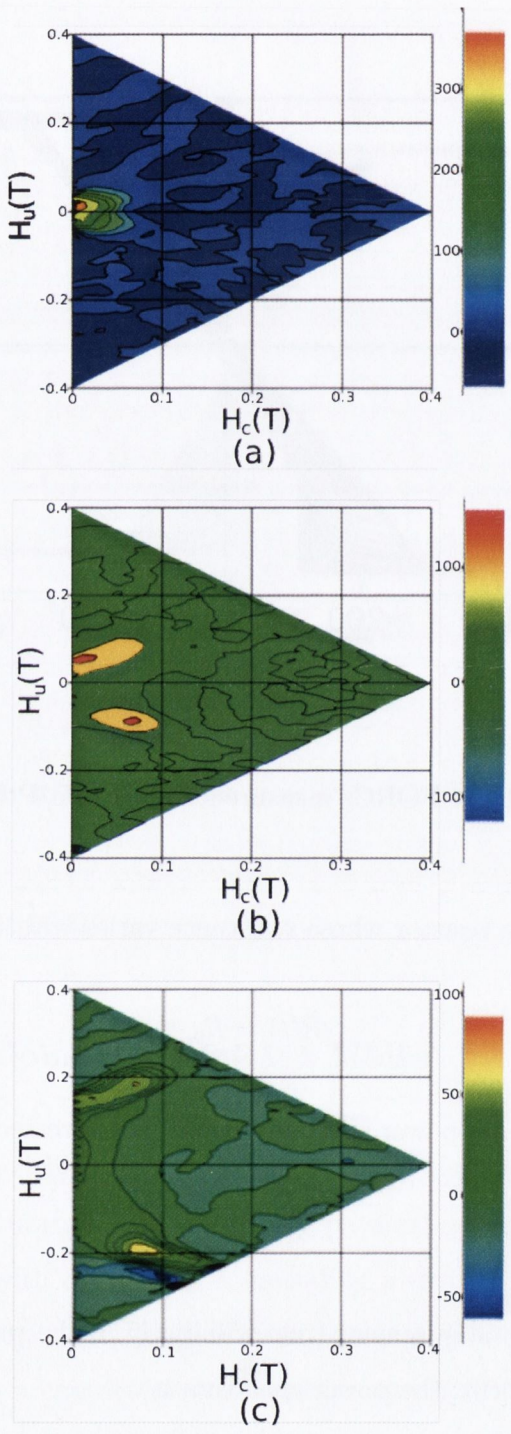


Fig. 4.16: FORCs diagrams for samples with n = (a) 10, (b) 20, and (c) 50.

where N is the number of independent positive resistance jumps in the measurement time T, and ΔR is the size of each resistance step. As a matter of fact, these are both $1/f^2$ spectra. In general, a superposition of both $1/f^2$ and ordinary $1/f$ noise [54] is likely, and thus α values between 1 and 2 can be evident over some range of frequencies. In our case, we attribute the noise spikes and the $1/f^{1.7}$ spectrum to the magnetization relaxation process happening at the switching field and immediately before negative saturation, as already mentioned in the results section.

We now try to understand the nearly $1/f$ noise within the stripe domain state. Two plausible explanations of this magnetic noise are:

— Spontaneous reversals of an activation volume (nucleus), which are not followed by growth of the reverse domain. The activation volume in a hard magnet is approximately δ_B^3, where δ_B is the Bloch wall width $\pi(A/K_u)^{1/2}$, where A is the exchange stiffness. Using values of $A = 10$ pJ m^{-1} [38] and $K_u = 1.5 \times 10^5$ J m^{-3} (corresponding to $Q = 0.94$) for our $n = 20$ sample, we estimate that δ_B is 25 nm and δ_B^3 is 1.5×10^4 nm^3.

— Fluctuations of the position of the domain walls (Fig. 4.17). Walls are expected to be strongly pinned at defect sites. If the average distance between these is d, then the fluctuating volume will be approximately $0.1d^2t$. The value of d ($\sim$ 300 nm) corresponds to the length of the straight segments of domain wall shown in Fig. 4.4b. The reversal volume is then $\approx$ 2.7×10^5 nm^3. These domain wall reconfigurations can be modelled as a fluctuating two-level system, characterized by an activation barrier between two, nearly equivalent energy levels. A superposition of a large number two-level systems with a broad distribution of activation energies is known to give rise to a $1/f$ spectrum (see Chapter 2) [55, 56].

The amplitude of the fluctuations by integrating the 0 mT spectrum

shown in Fig. 4.10 indicates that the fluctuating magnetic volumes are of order 3.0×10^5 nm^3. This volume is similar to the reversal volume due to a moving domain wall, but significantly greater than the activation volume (1.5×10^4 nm^3). Furthermore, a new wall with finite area ($\approx \pi\delta_B t$) must be created to form the activation volume. The energy cost is expensive – $\sigma_w = 4\sqrt{AK} = 5$ mJ per square meter of domain wall, or ≈ 3300 k_BT per nucleus in the $n = 20$ sample. By contrast, there is no need to create new wall area to accommodate the reversal in the second model because the walls themselves are not straight. Therefore, we conclude that the magnetic fluctuations that give rise to stationary $1/f$ noise are related to domain wall movements, rather than a spontaneous nucleation process.

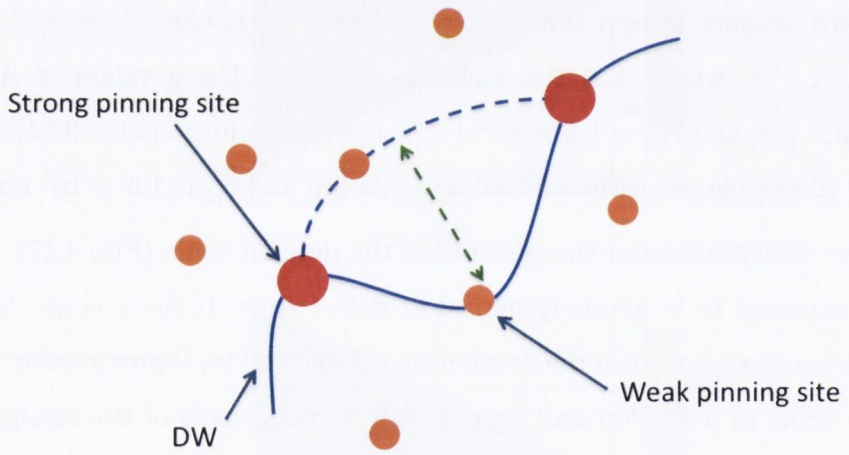


Fig. 4.17: A diagram showing the proposed domain wall fluctuation mechanism as the $1/f$ noise source.

Next, we examine whether the magnetization fluctuations responsible for the stationary $1/f$ noise can be characterized as reversible domain reconfigurations in thermal equilibrium. The fluctuation-dissipation theorem

(FDT) relates the magnetization fluctuations and the susceptibility (see Appendix A.2). A recent study of spin-valve structures reported a linear correlation between the magnetic noise power and the resistance susceptibility that was in quantitative agreement with FDT predictions [57]. A similar trend is evident in our samples; that is, the noise magnitude between saturation states is roughly correlated with the slope of the Hall voltage ($dV_H/d\mu_0 H$).

For a sample in thermal equilibrium and exhibiting a linear response, the power spectrum of the magnetic moment $S_m(f)$ is given by [58]

$$S_m(f) = \frac{2k_B T}{\pi \mu_0 f} \chi_m^{''}(f) \tag{4.15}$$

where μ_0 is the permeability of free space, k_B is Boltzmann's constant, and $\chi_m^{"}(f)$ is the out-of-phase magnetic susceptibility. We then use the Kramers-Kronig relation between the in-phase and out-of-phase susceptibility [59] (see also Appendix A.5), to give

$$\chi_m^{'}(f=0) = \frac{2}{\pi} \int_0^{+\infty} \frac{\chi_m^{''}(f)}{f} df \tag{4.16}$$

in which $\chi_m^{'}$ is the in-phase susceptibility. In our samples, we have

$$S_V(f) = (\frac{\partial V_H}{\partial m})^2 S_m(f) = (1/\Omega)^2 (\frac{\partial V_H}{\partial M})^2 S_m(f) \tag{4.17}$$

where $\Omega = w^2 t$ is the active volume of the sample, and $(\partial V_H/\partial M)$ can be worked out from Eqn. (4.6). Using Eqn. (4.15 - 4.17), we arrive at the total fluctuation relation for anomalous Hall effect

$$\frac{\partial V_H}{(\partial \mu_0 H)} = \frac{\Omega}{\mu_0 I R_s k_B T} \int_0^{+\infty} S_V(f) df \tag{4.18}$$

where I is the bias current. The left hand side of Eqn. (4.18) is given by the slope of the V_H vs $\mu_0 H$ curve in Fig. 4.6, which leads to a DC Hall voltage susceptibility of 3.5×10^{-3} V/T. This value is close to that obtained from the right hand side of the equation, by integrating the $S_V(f)$ curve at zero field in Fig. 4.10 across our measurement window, which is 2.5×10^{-3} V/T. The upper limit of integration in Eqn. (4.18) is made finite because the magnetic noise power is observed to fall below the thermal background above 100 Hz; hence, it can no longer be distinguished. If we assume the magnetic $1/f$ noise extends out to 1 GHz then the predicted Hall voltage susceptibility is still only 3 - 4 times larger than the measured one. Given this uncertainty, the two sides of Eqn. (4.18) are in fair quantitative agreement and this can be regarded as reasonable evidence that in an applied magnetic field between 0 mT and -150 mT, the sample is in a quasi-equilibrium condition.

4.4.2 First Order Reversal Curves

The explanation of FORC diagrams is never simple. Without proper simulation work, most of the conclusions would not be of hundred percent certainty. However, some distinguishing features can be well spotted from our FORC diagrams, which lead to valuable insight into the magnetization switching process in the system.

The two peaks distinguished in each sample, can be associated with two different sets of hysterons, each of which have a similar coercive field H_c and interaction field H_u, respectively. The distance between these two peaks shows how different these two sets of hysterons are. The enlarged distance when n goes from 10 to 50 means that these two sets of hysterons are more different when the number of repetitions goes up. The spread of each peak defines how similarly the hysterons in each set behave. It can

be seen that the similarity among hysterons belonging to the same set also decreases when the repetition number increases. Using Eqn. (4.10), we can work out the reversal field $H_R = H_u - H_c$, for the two peaks. It is shown that the peak with positive interaction field is related to the nucleation field (in the second quadrant for the $n = 10$ sample, and in the first quadrant for samples with $n = 20$ and 50), while the other peak can be attributed to the negative saturation field in the third quadrant. The part of the FORCs diagram in between these two peaks is very quiet, which suggests a highly reversible process. This can be readily seen from a close observation of the first-order reversal curves. The adjacent FORCs between the nucleation and saturation field all have segments, which are nearly parallel to each other. This leads to a negligible mixed second derivative, since the slope of M against H does not depend on the change of H_R. This observation is consistent with our previous analysis on the anomalous Hall voltage noise data, which shows that the nucleation field and the saturation field are the majority of irreversible magnetization events happen. These events lead to a noise spectrum with a slope α close to 2, whereas the area in between nucleation and saturation is dominated by highly reversible magnetization processes, giving a $1/f$ spectrum.

It is worth noting that there is a small peak in the FORC diagram of the $n = 50$ sample, which has a positive interaction field but a very low coercive field. This feature can be associated with the nucleation of reverse bubble domains, before the macroscopic sample magnetization actually undergoes switching due to the avalanche of these reversed nuclei. The macroscopic nucleation field is, in fact, the field at which there is an avalanche from the nuclei into stripe domains. This was previously observed by Davies et al. in FORC measurements on a $[\mathrm{Co}(0.4)/\mathrm{Pt}(0.7)]_{50}$ sample, probed by an

alternating gradient magnetometer, and transmission x-ray microscopy [29]. However, our data show the evolution of this side peak with the increase of layer repetitions — this small peak is very close to and indistinguishable from the main peak with positive interaction field when the number of repetitions is small, but it can be clearly identified in the $n = 50$ sample.

One further step is to understand the origin of different signs in the interaction field for the two sets of hysterons. In the classical Preisach model, the interaction field is given by the shift of the elementary hysteresis loop in response to other surrounding hysterons. Different signs in the interaction field clearly suggests different interactions between neighbouring hysterons in our samples. Since 'hysterons' are not real physical entities, it is not necessary that a homogeneous magnetic material has to be described by a single set of hysterons in the Preisach model. However, the existence of two sets of hysterons can be seen as an indication of the presence of a magnetic component with in-plane easy axis in our samples, along with the out-of-plane magnetic component we have studied so far.

4.4.3 The Existence of In-plane Magnetic Components

There is always the debatable question whether there exists a component of the magnetization in magnetic thin films with $Q \sim 1$ undergoing in-plane reversal, and how much this component contributes to the magnetization process. This is related to the interpretation of the slanted region in the hysteresis loop. While some authors attribute it to domain wall motion across a large number of pinning sites [25], others suggest that magnetization rotation contributes to some or most of the observed magnetization switching events [60, 61]. Due to the fact that most of the techniques probing the hysteresis loop are only sensitive to the component of magnetization in a

single direction. Most of the time, only certain indications to an in-plane component can be given, which does not necessarily lead to a conclusive answer. To the best of the candidate's knowledge, there is only one study so far which gives convincing and definite conclusion concerning this problem [62]. The authors there measured exchange-biased $(Co/Pt)_5$ multilayers in a vector vibrating sample magnetometer, and showed that no in-plane component appeared when the applied magnetic field is aligned exactly along the thin film normal. However, as the perpendicular magnetic anisotropy K_u and sample quality depend strongly on the deposition condition and multilayer repetitions, it is hard to believe that this is a general statement for any (Co/Pt) multilayers.

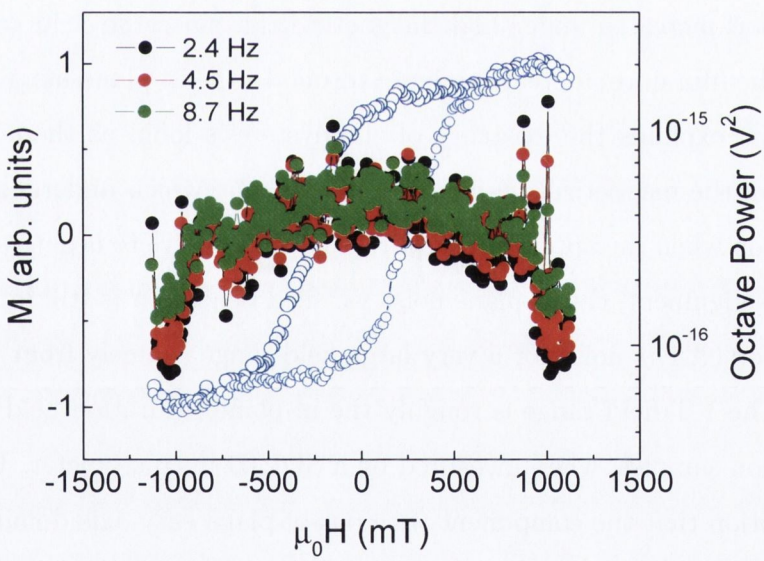


Fig. 4.18: Anomalous Hall voltage and octave noise power for 3 consecutive octaves measured with the magnetic field in-plane for an $n = 20$ sample.

In order to give more insight into this question, we also measured the anomalous Hall voltage noise, with the applied magnetic field in-plane and

perpendicular to the bias current. In the ideal case, the active volume can be seen as a Stoner-Wohlfarth particle (see Appendix. A.6), and the magnetization undergoes a coherent rotation when the applied magnetic field is along the hard axis. Hence, this measurement is expected to give a bell-shaped AHE curve, without any hysteresis, as the anomalous Hall voltage is only proportional to the out-of-plane magnetization. However, the measured Hall voltage vs. field relation is quite different (Fig. 4.18). There is a clearly identifiable hysteresis loop, the magnetization also does not go to saturation under high applied fields. The behaviour we observed can be understood by the fact that perfect alignment of the applied magnetic field and the sample is normally impossible, so the magnetic field actually has a small angle out of the film plane. In this situation, the perpendicular magnetization increases under high magnetic field, since the field component along the film normal creates a large torque to the in-plane magnetization. This also explains the existence of the hysteresis loop, as there is always a part of the magnetization aligned out-of-plane, which undergoes a sharp transition when the applied field switches from positive to negative. Despite this misalignment, the in-plane noise vs. field behaviour is still informative. We observed $1/f$ noise for a very large field range (namely from -1 T to + 1 T). The 1 T field range is roughly the in-plane saturation field of our 20 repetition samples, when measured by a SQUID magnetometer. Under the assumption that the component with out-of-plane easy-axis dominates, the field range of -1 T to + 1 T corresponds to the rotation of this magnetization into plane. Hence, it is possible to observe a $1/f$ spectrum of similar magnitudes to what we observe in the slanted part of the out-of-plane hysteresis curve, when the magnetization undergoes a rotation process.

In our case, there are certain indications that there exists a component

in the film, having an in-plane magnetic easy-axis. For example, the hysteresis looks similar to those in some two-phase systems, and the FORC diagrams have to be described by two sets of 'hysterons'. Concerning the deposition condition (sputtering is normally believed to lead to less homogeneous interfaces between Co and Pt than for example evaporation), and the large number of multilayers in our samples, this is not a surprise. In the following, we use an approach suggested by Stinson et al. [63] to show the existence of this in-plane component. Our previous discussion omitted the contribution of planar Hall effect (PHE) to the measured Hall voltage. PHE is an effect closely related to magnetoresistance. In presence of anisotropic magnetoresistance, the equipotential plane in a magnetic sample might not be perpendicular to the current. This creates a transverse voltage, which is similar to Hall effect. With PHE taken into consideration, the Hall voltage can be expressed as [64]

$$V_H = \frac{R_s I}{t} M\cos\theta + \frac{kI}{d} M^2 \sin^2\theta \sin 2\phi \tag{4.19}$$

in which k is the planar Hall coefficient, θ is the angle between the magnetization and the film normal, and ϕ is the angle between the in-plane magnetization and the bias current direction. The specific point of this relation is that the anomalous Hall voltage (first term in the equation) is an odd function of magnetization, whereas the second term, the planar Hall effect is an even function of magnetization. Hence, if the hysteresis loop with $\mu_0 H < 0$ is subtracted from that with $\mu_0 H > 0$, we will obtain the odd part of the function, which is the AHE, which depends on the perpendicular component of magnetization M. Similarly, by adding the two parts of a hysteresis loop together, the even part is left, which is related to the in-plane magnetization by PHE.

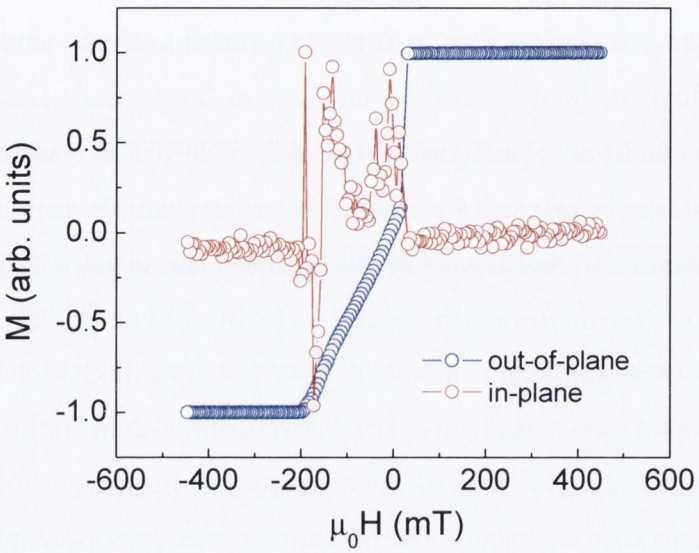


Fig. 4.19: Out-of-plane and in-plane magnetization curves obtained by Hall effect measurement. Units in the figure do not represent the real ratio between the out-of-plane and in-plane magnetization.

Fig. 4.19 shows the result obtained following this approach. While the out-of-plane hysteresis curve hardly changed, its in-plane counter part shows a significant deviation from zero exactly along the slanted part of the out-of-plane hysteresis curve, from about zero field to -200 mT (We assume no in-plane magnetization exists when the sample is saturated). The amount of in-plane magnetization during the magnetization switching cannot be deduced independently, since this would require a separate measurements defining both R_s and k.

However, the key question is probably what role this in-plane component plays in the magnetization switching. We have to admit at this stage that there is not enough evidence for us to give a conclusive answer in relation to how much magnetization in the sample in fact has in-plane easy-axis,

and how much it contributes to our perpendicular-to-plane noise spectra. We point out here that even if the magnetization has an in-plane component during magnetization switching, this does not automatically exclude the perpendicular domain wall motion as the most important effect in the slanted part of the magnetization curve. It is also possible that the in-plane magnetization we observed is related to the spins inside the domain walls, as suggested by some other authors [60]. The out-of-plane anisotropy is still very large, at least for the $n = 10$ and 20 samples (close to 1), compared with some other systems studied in the literature [65, 11, 66]. And the domain size of our samples is about 100 - 150 nm, as given by MFM studies. With these two factors, an out-of-plane easy-axis is expected to be sustained in the majority of the sample area by forming stripe domains. The fact that the out-of-plane hysteresis curve shown in Fig. 4.19 closely resembles that without subtracting PHE signal, also suggests that the in-plane component might be rather small[3]. Hence, we tentatively conclude that the existence of some magnetization with in-plane easy axis, which undergoes a coherent rotation during the out-of-plane magnetization process, should not largely change the discussion we have made in the last two sections.

The other way is probably to treat the system as a whole but with a more complicated magnetization switching behaviour, neither pure nucleation - propagation for thin films with very large perpendicular anisotropy, nor coherent rotation for in-plane anisotropic films, when a magnetic field perpendicular to the film normal is applied. For the former, no $1/f$ spectrum would be expected, as the magnetization switches directly from positive saturation to negative saturation, while for the latter, no sharp transitions associated with Barkhausen jumps would exist.

[3]It is certain that the small PHE signal can be related to a low k or small $\sin 2\phi$. However, without further evidence, our argument should still be the more plausible case.

4.5 Conclusion

In conclusion, we have shown in this chapter that both the magnetization, and the magnetization fluctuations of $(CoFe/Pt)_n$ multilayers can be conveniently measured in patterned Hall bars with micron-scale dimensions, using the anomalous Hall effect. The patterned samples have relatively few walls in the active volume. Magnetic noise, observed only in the unsaturated sections of the hysteresis loop, provides direct information about the magnetization fluctuations in the sample. In regions where domains are created or annihilated a $\sim 1/f^{1.7}$ spectrum appears due to irreversible Barkhausen jumps and magnetization drift. After a time the magnetization in the centre of the loop reaches a steady state, where a $1/f$ spectrum was observed. This arises from a broad distribution of elementary magnetic fluctuations, which are identified as reversible excursions of roughly hundred-nanometer segments of domain wall.

FORC diagrams show the existence of two sets of hysterons in all our $(CoFe/Pt)_n$ samples on the Preisach plane, which can be attributed to the macroscopic nucleation field, and the negative saturation field in a hysteresis loop, respectively. A small set of hysterons, with nearly zero coercive field H_c was also observed in the n =50 sample. This corresponds to the formation of bubble domains in the largely homogeneous sample before the macroscopic magnetization switching takes place, as suggested by other authors [29]. However, these hysterons were largely convoluted with the magnetization switching peak in the other two samples having fewer multilayer repetitions.

References

[1] M. T. Johnson, P. J. H. Bloemen, F. J. A den Broeder, and J. J. de Vries. *Rep. Prog. Phys.*, 59:1409, 1996.

[2] J. A. Osborn. *Phys. Rev.*, 67:351, 1945.

[3] R. Skomski and J. M. D. Coey. *Permanent Magnetism.* Institute of Physics Publishing, 1999.

[4] K. M. Seemann, V. Baltz, M. MacKenzie, J. N. Chapman, B. J. Hickey, and C. H. Marrows. *Phys. Rev. B*, 76:174435, 2007.

[5] D. Ravelosona, A. Cebollada, F. Briones, C. Diaz-Paniagua, M. A. Hidalgo, and F. Batallan. *Phys. Rev. B*, 59:4322, 1999.

[6] M. Hehn, K. Ounadjela, J. P. Bucher, F. Rousseaux, D. Decanini, B. Bartenlian, and C. Chappert. *Science*, 272:1782, 1996.

[7] L. Néel. *J. Physique Rad.*, 15:225, 1954.

[8] F. J. A. den Broeder, H. C. Donkersloot, H. J. G. Draaisma, and W. J. M. de Jonge. *J. Appl. Phys.*, 61:4317, 1987.

[9] W. B. Zeper, F. J. A. M. Greidanus, P. F. Carcia, and C. R. Fincher. *J. Appl. Phys.*, 65:4971, 1989.

[10] W. B. Zeper, H. W. van Kesteren, B. A. J. Jacobs, J. H. M. Spruit, and P. F. Carcia. *J. Appl. Phys.*, 70:2264, 1991.

[11] A. W. Rushforth, P. C. Main, B. L. Gallagher, C. H. Marrows, B. J. Hickey, E. D. Dahlberg, and P. Earnes. *J. Appl. Phys.*, 89:7534, 2001.

[12] H. J. G. Draaisma, W. J. M. de Jonge, and F. J. A. den Broeder. *J. Magn. Magn. Mater.*, 66:351, 1987.

[13] C. L. Canedy, X. W. Li, and G. Xiao. *Phys. Rev. B*, 62:508, 2000.

[14] A. Hubert and R. Schäfer. *Magnetic Domains: The Analysis of Magnetic Microstructures.* Springer-Verlag, 1st edition, 1998.

[15] K. Moorjani and J.M.D. Coey. *Magnetic Glasses.* North Holland, 1984.

[16] O. Donzelli, D. Palmeri, L. Musa, F. Casoli, F. Albertini, L. Pareti, and G. Turilli. *J. Appl. Phys.*, 93:9908, 2003.

[17] P. M. Leufke, S. Riedel, M. S. Lee, J. Li, H. Rohrmann, T. Eimüller, P. Leiderer, J. Boneberg, G. Schatz, and M. Albrecht. *J. Appl. Phys.*, 105:113915, 2009.

[18] B. Rodmacq, V. Baltz, and B. Dieny. *Phys. Rev. B*, 73:092405, 2006.

[19] J. M. Shaw, S. E. Russek, T. Thomson, M. J. Donahue, B. D. Terris, O. Hellwig, E. Dobisz, and M. L. Schneider. *Phys. Rev. B*, 78:024414, 2008.

[20] R. Danneau, P. Warin, J. P. Attané, I. Petej, C. Beigné, C. Fermon, O. Klein, A. Marty, F. Ott, Y. Samson, and M. Viret. *Phys. Rev. Lett.*, 88:157201, 2002.

[21] C. M. Hurd. *The Hall Effect in Metals and Alloys.* Plenum Press, New York, 1972.

[22] J. Moritz, B. Rodmacq, S. Auffret, and B. Dieny. *J. Phys. D: Appl. Phys.*, 41:135001, 2008.

[23] S. F. Zhang. *Phys. Rev. B*, 51:3632, 1995.

[24] O. Shaya, M. Karpovski, and A. Gerber. *J. Appl. Phys.*, 102:043910, 2007.

[25] J. R. Barnes, S. J. O'Shea, M. E. Welland, J. Y. Kim, J. E. Evetts, and R. E. Somekh. *J. Appl. Phys.*, 76:2974, 1994.

[26] E. D. Torre. *Magnetic Hysteresis.* IEEE Press, New York, 1999.

[27] C. R. Pike, A. P. Roberts, and K. L. Verosub. *J. Appl. Phys.*, 85:6660, 1999.

[28] C. R. Pike. *Phys. Rev. B*, 68:104424, 2003.

[29] J. E. Davies, O. Hellwig, E. E. Fullerton, G. Denbeaux, J. B. Kortright, and K. Liu. *Phys. Rev. B*, 70:224434, 2004.

[30] I. D. Mayergoyz. *Mathematical Models of Hysteresis and Their Applications.* Elsevier, 2nd edition, 2003.

[31] F. Béron, L. Clime, M. Ciureanu, D. Ménard, R. W. Cochrane, and A. Yelon. *J. Nanosci. Nanotechnol.*, 8:2944, 2008.

[32] F. Béron, D. Ménard, and A. Yelon. *J. Appl. Phys.*, 103:07D908, 2008.

[33] C. Pike and A. Fernandez. *J. Appl. Phys.*, 85:6668, 1999.

[34] L. Spinu, A. Stancu, C. Radu, F. Li, and J. B. Wiley. *IEEE Trans. Magn.*, 40:2116, 2004.

[35] M. Ciureanu, F. Béron, P. Ciureanu, R. W. Cochrane D. Ménard, A. Sklyuyev, and A. Yelon. *J. Nanosci. Nanotechnol.*, 8:5725, 2008.

[36] J. Wong, P. Greene, R. K. Dumas, and K. Liu. *Appl. Phys. Lett.*, 94:032504, 2009.

[37] J. E. Davies, O. Hellwig, E. E. Fullerton, J. S. Jiang, S. D. Bader, G. T. Zimányi, and K. Liu. *Appl. Phys. Lett.*, 86:262503, 2005.

[38] J. E. Davies, O. Hellwig, E. E. Fullerton, and K. Liu. *Phys. Rev. B*, 77:2008, 014421.

[39] C. Kooy and U. Enz. *Philips Res. Rep.*, 15:7, 1960.

[40] H. J. G. Draaisma and W. J. M. de Jonge. *J. Appl. Phys.*, 62:3318, 1987.

[41] O. Hellwig, G. P. Denbeaux, J. B. Kortright, and E. E. Fullerton. *Physica B*, 336:136, 2003.

[42] D. Clarke, O. A. Tretiakov, and O. Tchernyshyov. *Phys. Rev. B*, 75:174433, 2007.

[43] W. Wernsdorfer, E. Bonet Orozco, K. Hasselbach, A. Benoit, B. Barbara, N. Demoncy, A. Loiseau, D. Doivin, H. Pascard, and D. Mailly. *Phys. Rev. Lett.*, 78:1791, 1997.

[44] K. J. Kirk, J. N. Chapman, and C. D. W. Wilkinson. *J. Appl. Phys.*, 85:5237, 1999.

[45] E. P. Wohlfarth. *J. Phys. F: Met. Phys.*, 14:L155, 1984.

[46] D. Givord and M. F. Rossignol. *Rare-Earth Iron Permanent Magnets.* Oxford University Press, Oxford, 1996.

[47] B. Neri, C. Ciofi, and V. Dattilo. *IEEE Trans. Electron Dev.*, 44:1454, 1997.

[48] S. Kar and A. K. Raychaudhuri. *Appl. Phys. Lett.*, 81:5165, 2002.

[49] A. Steyer, P. Guenoun, and D. Beysens. *Phys. Rev. Lett.*, 68:1869, 1992.

[50] Z. Diao, P. A. Dunne, G. Zangari, and J. M. D. Coey. *Electrochem. Commun.*, 11:703, 2009.

[51] C. T. Rogers and R. A. Buhrman. *Phys. Rev. Lett.*, 53:1272, 1984.

[52] Y. Yuzhelevski, M. Yuzhelevski, and G. Jung. *Rev. Sci. Instrum.*, 71:1681, 2000.

[53] R. H. Koch. *Phys. Rev. B*, 48:12217, 1993.

[54] M. B. Weissman. *Rev. Mod. Phys.*, 60:537, 1988.

[55] F. K. du Pré. *Phys. Rev.*, 78:615, 1950.

[56] P. Dutta and P. M. Horn. *Rev. Mod. Phys.*, 53:497, 1981.

[57] A. Ozbay, A. Gokce, T. Flanagan, R. A. Stearrett, E. R. Nowak, and C. Nordman. *Appl. Phys. Lett.*, 94:202506, 2009.

[58] H. T. Hardner, M. B. Weissman, M. B. Salamon, and S. S. P. Parkin. *Phys. Rev. B*, 48:16156, 1993.

[59] G. B. Arfken and H. J. Weber. *Mathematical Methods for Physicists.* Academic Press, San Diego, 5th edition, 2001.

[60] M. Hehn, S. Padovani, K. Ounadjela, and J. P. Bucher. *Phys. Rev. B*, 54:3428, 1996.

[61] P. Stamenov. *(Private Communications).*

[62] Y. Nie, W. W. Lin, M. Huang, K. X. Xie, J. Du, H. Sang, and G. Xiao. *J. Appl. Phys.*, 103:07C110, 2008.

[63] D. G. Stinson, A. C. Palumbo, B. Brandt, and M. Berger. *J. Appl. Phys.*, 61:3816, 1987.

[64] K. Okamoto. *J. Magn. Magn. Mater.*, 35:353, 1983.

[65] U. Ebels, P. E. Wigen, and K. Ounadjela. *Europhys. Lett.*, 46:94, 1999.

[66] O. Kohmoto, N. Mineji, Y. Isagawa, F. Ono, and O. Kubo. *J. Magn. Magn. Mater.*, 239:36, 2002.

Chapter 5

Spatial Correlation and Statistics of 1/f Noise in Yoke-Shaped Spin Valves

GMR and TMR based magnetic sensors are well known to possess excess low frequency electrical noise, mainly of $1/f$ nature [1, 2]. In this chapter, we investigate low frequency noise in magnetic spin-valve structures. $1/f$ noise due to magnetic fluctuations is usually understood to be a superposition of a large number of fundamental fluctuating magnetic entities. Although many reports on $1/f$ noise in spin-valve structures have been published in the last decade, few give a clear picture on what these magnetic 'fluctuators' are. A second closely related question concerns the correlation length scale of these 'fluctuators'. It has long been accepted that conventional $1/f$ noise is a local effect and scales with the inverse of the sample volume. Hence, no spatial correlation in the $1/f$ noise is expected. However, in ferromagnetic materials and heterostructures, such as spin-valves, the electrical noise is usually of magnetic origin. One obvious magnetic length scale is the domain size,

which extends to several micrometers or larger in soft magnetic thin films. It is interesting to investigate, whether this long range ordering creates any spatial correlation for $1/f$ noise in magnetic layers.

5.1 Introduction

The time and spatial autocorrelation function $C(\tau, d)$ of a fluctuating signal $X(t, r)$ characterizes the correlation of the signal in two different time points $t_1 - t_2 = \tau$, and two different positions $r_1 - r_2 = d$ [3]. The correlation between two signals $X_1(t)$ and $X_2(t)$ can be characterized by the coherence function [4]

$$\eta_{12}^2(f) = \frac{\mid S_{12}(f) \mid^2}{S_1(f)S_2(f)} \tag{5.1}$$

in which $S_{12}(f)$ is the cross-power spectral density of the two signals. $S_1(f)$ and $S_2(f)$ are the individual power spectra. It can be shown that for two signals with spectra $S_1(f)$ and $S_2(f)$ obtained by a single discrete Fourier transform (DFT), the above definition for the coherence function always gives a value of 1. For two signals, each having N independent Fourier transformed spectra, the ensemble averaged coherence function can be defined as

$$\langle \eta_{12}^2(f) \rangle = \frac{\mid \langle S_{12}(f) \rangle \mid^2}{\langle S_1(f) \rangle \langle S_2(f) \rangle} \tag{5.2}$$

in which $\langle S_{12}(f) \rangle$, $\langle S_1(f) \rangle$, and $\langle S_2(f) \rangle$ are the averaged cross-spectrum, the averaged spectrum for $X_1(t)$ and $X_2(t)$, respectively, which are defined as

$$\langle S_{12}(f) \rangle = \frac{1}{N} \sum_{k=1}^{N} X_{1,k}^*(f) X_{2,k}(f) \tag{5.3}$$

$$\langle S_1(f) \rangle = \frac{1}{N} \sum_{k=1}^{N} X_{1,k}^*(f) X_{1,k}(f) \tag{5.4}$$

$$\langle S_2(f) \rangle = \frac{1}{N} \sum_{k=1}^{N} X^*_{2,k}(f) X_{2,k}(f) \tag{5.5}$$

The idea behind the averaged coherence function is that the non-correlated part of the two signals creates a random phase in the cross-spectrum. This is averaged out when $\langle S_{12}(f) \rangle$ is calculated, assuming that a sufficient number of spectra, N, are taken. From the above definition, the statistical error for the averaged coherence function is simply $1/N$.

The above strategy in averaging the coherence function might sometimes prevent an existing coherence between two input signals from being detected, in case of a non-stationary phase situation [5]. Despite its drawbacks, this method is widely used in different signal processing applications, and gives good insight into the magnitude of correlation between two signals [6, 4, 7]. For our highly metallic spin-valve samples, if fluctuations in two parts in the sample are due to the same fluctuator, we would at least expect a steady phase shift, assuming the nature of the fluctuator not changing during our measurement window. Hence, the above defined averaged coherence function can in general be used to characterize the spatial correlation in our spin-valves.

Spatial correlation measurements played an important role in $1/f$ noise studies in the last two decades [3]. This is partly due to the intensively investigated Voss-Clarke (VC) model [8], in which the $1/f$ noise was explained by a temperature fluctuation coupled to the sample resistance by the material's resistance-temperature coefficient (See Chapter 2). The VC model infers a spatial correlation length of the $1/f$ noise, which is related to the sample's thermal diffusion coefficient. As already discussed, the spatial correlation given by the VC model was not observed in various systems, e.g. two electrically isolated Au films [4], adjacent regions of a thin metal film

[9], transistors a few tens of μm apart in an integrated circuit [10], which largely rule out the VC model as a general explanation for electrical $1/f$ noise. Up to now, to our knowledge, spatial correlation studies on magnetic systems have only been previously carried out by Raquet et al. [11] on two adjacent Hall bars, approximately 600 nm apart, patterned on nickel thin films. But a comprehensive report is still lacking.

Statistics has long been accepted as a tool to characterize $1/f$ noise in different materials systems [3, 12, 13, 14, 15, 16, 17]. When the fluctuating quantity is composed of a large number of non-correlated, and identically distributed 'fluctuators', the resultant noise is Gaussian. Gaussian noise is characterized by a Gaussian distribution function and the property that all high-order statistics of it can be expressed in terms of second-order statistics. A deviation from Gaussian noise normally suggests the existence of a small number of fluctuating entities, or correlation among different 'fluctuators'. However, it is challenging to test the Gaussian nature of a noise process. Theoretically, measurement up to an arbitrarily high moment of the fluctuating quantity should be measured in order to prove its Gaussian nature. Practically, representative high moments are selected with the aim of observing the non-Gaussian component of the noise. One of the techniques which is widely used is the covariance matrix [18].

The covariance matrix of a noise spectrum is defined as [19, 20]

$$\rho_{mn} = \frac{\langle \delta O_m \delta O_n \rangle}{\sqrt{\langle \delta O_m^2 \rangle \langle \delta O_n^2 \rangle}} \quad (m \neq n) \tag{5.6}$$

and

$$\rho_{nn} = \langle \delta O_n^2 \rangle / \sum_{f \in O_n} \langle S_1(f) \rangle^2 \tag{5.7}$$

in which the octave sum of a spectrum is defined as

$$O_n = \sum_{f=2^n f_0}^{(2^{n+1}-1)f_0} S_1(f) \tag{5.8}$$

with $S_1(f)$ the power spectral density, or what is called the first spectrum of the fluctuating process $X(t)$. The covariance matrix characterizes how the fluctuations in different octaves are correlated. The diagonal terms ρ_{nn} in the covariance matrix are 1 for Gaussian noise, and deviate from one if non-Gaussianity exists. The other terms should be zero for Gaussian noise, and non-zero for non-Gaussian behaviour. The covariance matrix method has been previously utilized to characterize non-Gaussian noise in semiconductors [21, 22, 23, 24]. There was a single report, in which it was used to study 2 μm wide by 30 μm long spin-valve sensors built into a bridge configuration [25].

Spatial correlation and noise statistics are the techniques we use in this chapter, for revealing fundamental properties and correlation length scales of magnetic 'fluctuators' in spin-valve stacks.

5.2 Sample Preparations

In spin-valves and magnetic tunnel junctions, there are two general approaches to obtain a linear portion in the MR curve for sensing applications. The first is to hard bias the free layer by applying a magnetic field perpendicular to the sample's easy axis [26]. The sensing field is then applied along the easy axis, so the biased free layer rotates from a direction perpendicular to the easy axis back to it, which gives a linear response of the MR curve near zero field. The second is to use shape anisotropy of the free layer, to

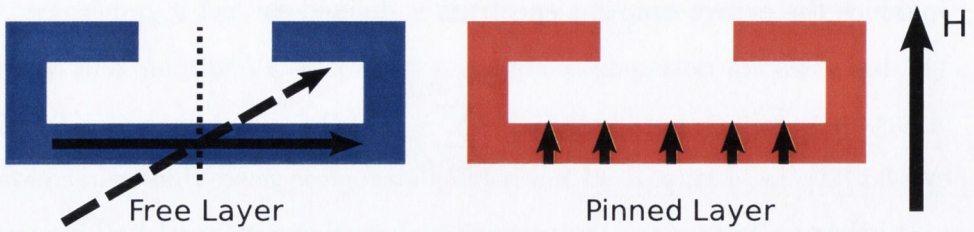
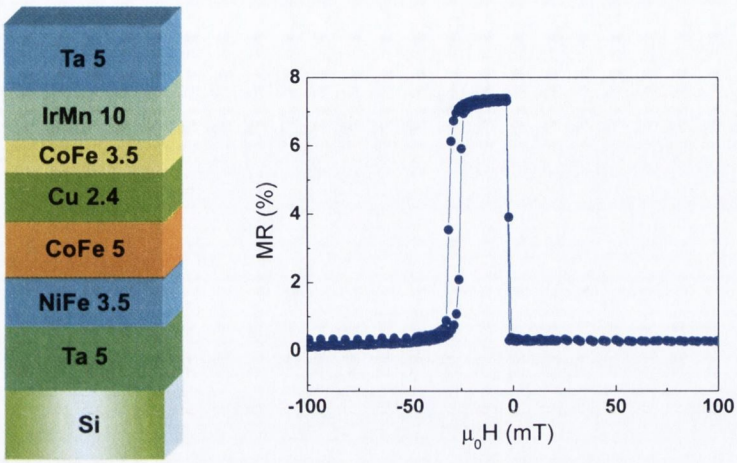


Fig. 5.1: A diagram showing the free layer and the pinned layer magnetization on the arm of the yoke. The applied magnetic field is perpendicular to the arm.

achieve a cross-anisotropy geometry, in which the free layer magnetization is aligned perpendicular to the pinning direction under zero field [27]. When a magnetic field is applied along the pinning direction, a coherent rotation of the free layer also gives a linear response.

In this work, the second approach is adopted. The samples are patterned into yoke-shaped structures (Fig. 5.1). Yoke-shaped design has long been used in the magnetic read head industry, in order to concentrate the magnetic field flux, and achieve a more stable domain structure, reducing 'burst' noise associated with macroscopic domain wall motions [28, 29]. Yoke spin-valve sensors, in the present context, were first introduced by Fermon and co-workers in CEA Saclay, for the spin-valve element in a mixed sensor [30, 31, 32]. The pinned layer easy axis is set by the exchange bias, and is perpendicular to the arm longitudinal, while the free layer easy axis is along the arm. Hence, this design utilizes the cross-anisotropy geometry. Magnetic field is applied perpendicular to the yoke arm. Ideally, no domain exists in the free layer arm of the yoke at zero field after positive saturation. It undergoes a coherent rotation when an external magnetic field is applied. This gives a linear, low hysteresis part in the MR curve around zero field for sensor applications.



(a) (b)

Fig. 5.2: (a) Spin-valve stacks from which the yoke sensors are patterned; and (b) its MR curve (courtesy of B.-S. Chun).

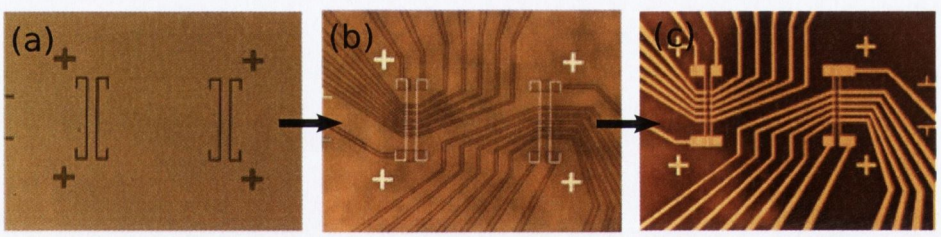


Fig. 5.3: Optical microscope images showing the lithographic steps in patterning the yoke sensor. (a) Defining the yoke sensor; (b) UV lithography to define the contacts; (c) After contact lift-off (coutesy of B.-S. Chun).

Three different sets of spin-valve samples have been fabricated and measured here. Table 5.1 gives a summary of all the yoke samples.

a) Spin-valve stacks patterned into micrometer-size yokes by photolithography with copper electrical contacts. These samples were originally prepared by Dr. B.-S. Chun for the EU BIOMAGSENS project, as mag-

Sample set	Spin-valve stack	Contacts	w	l	m	e1e2	e2e3	e3e4	e4e5	e5e6	e6e7	comments
(a)	NiFe/CoFe/Cu/CoFe/	Cu	5.0	400.0	50.0	5.0	5.0	5.0	5.0	5.0	5.0	micrometer-scale yoke sensors
(b)	$Co_{40}Fe_{40}B_{20}$/Cu/$Co_{40}Fe_{40}B_{20}$	Cu	2.0	16.0	6.0	2.0	1.0	0.5	0.5	0.5	n/a	high $1/f$ noise
			0.6	15.6	3.6	2.0	1.0	0.5	0.5	0.5	n/a	excluded from the results
(c)	NiFe/CoFe/Cu/CoFe	spin-valve	2.0	16.0	6.0	2.0	1.0	0.5	0.5	0.5	n/a	type I
			0.6	15.6	3.6	2.0	1.0	0.5	0.5	0.5	n/a	type I
			0.6	15.6	3.6	2.0	0.8	0.3	0.3	0.3	n/a	type II

Table 5.1: List of spin-valve samples measured in Chapter 5. For spin-valve stacks, only the two ferromagnetic layers together with the spacers from the bottom of the stack to the top, are listed for simplicity. The exchange-bias is obtained by depositing 10 nm IrMn directly on the top ferromagnetic layer for all the samples (top-pinned structure). Yoke structures are always patterned with their arms perpendicular to the pinned direction to achieve the cross-anisotropy unless otherwise specified. w denotes the width of the yoke arm, l is the length of the whole yoke structure, and m is the transverse dimension of the yoke. The electrodes in the micrometer-scale yoke sensors are labelled from e1 to e7, in which e1 and e7 are used to pass the bias current, while e2 - e5 are used to probe the voltage. The current contacts in sample set (b) are (c) are not labelled. Hence, the six voltage contacts are labelled e1 to e6. The spacings between adjacent electrical contacts are given in μm.

netic sensors for detecting biomolecules attached to functionalized magnetic nanoparticles. The spin-valve stack used is SiO_2/Ta (5)/NiFe (3.5)/CoFe (5)/Cu (2.4)/CoFe (3.5)/IrMn (10)/Ta (5), with bracketed numbers in nanometers. An optimized GMR ratio of 7 - 8% is observed (Fig. 5.2). There are four individual yoke-shaped sensors, each of 400 μm length and 5 μm width per chip. There are seven electrical contacts on each yoke. The outer two contacts are for passing the current, while the inner five contacts with a spacing of 5 μm between each, are used to sense the voltage output of the sensor. The exchange bias was set by a 20 mT magnetic field applied perpendicular to the longitudinal direction of the yoke during sample growth. The lithographic process to pattern the yoke sensor is depicted in Fig. 5.3.

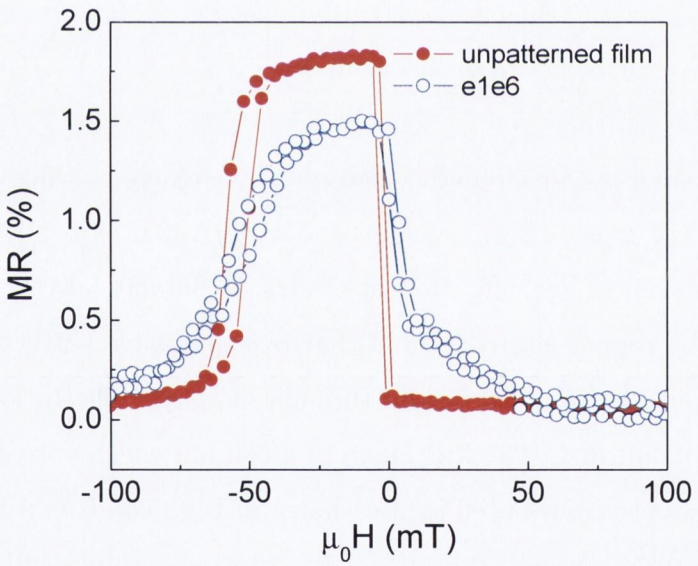


Fig. 5.4: MR curves of the unpatterned spin-valve stack with $Co_{40}Fe_{40}B_{20}$ as ferromagnetic electrodes, and a yoke sample with $w = 600$ nm patterned from the same spin-valve stack, measured across e1e6.

b) Spin-valves patterned by electron beam lithography into sub-micro-

meter size yokes with seven copper electrical contacts. Samples of two different widths were fabricated, namely 2 μm and 600 nm. Spin-valve stacks of SiO_2/Ta (5)/$Co_{40}Fe_{40}B_{20}$ (3)/Cu (2.8)/$Co_{40}Fe_{40}B_{20}$ (3)/IrMn (10)/Ta (5) were first grown in the Shamrock sputtering tool (numbers in nanometers). The MR ratio of an unpatterned stack is about 1.75%, as shown in Fig. 5.4. Its relatively low MR ratio may be related to the amorphous nature of $Co_{40}Fe_{40}B_{20}$. A yoke pattern together with alignment marks was then defined by EBL using ma-N 2403 negative tone resist and argon ion milling. A second EBL step was used to define the copper electrical contacts, using single layer PMMA and a lift-off process. The spacings between adjacent voltage contacts are designed to be 2 μm, 1 μm, 500 nm, 500 nm, and 500 nm. Fig. 5.5 depicts the labelling of the electrodes and the designed electrode - electrode spacings for a $w = 2$ μm yoke structure. Proximity effect, during the electron beam exposure, has significantly reduced the spacings between the last three copper contacts to be 350 - 400 nm. Finally, the pattern was contacted with photolithography, by aligning the alignment marks against a UV mask. SEM images of a 2 μm width and a 600 nm width yoke are shown in Fig. 5.6. Robust electrical contacts have been obtained between the copper electrodes and the yoke spin-valve pattern. A current of more than 120 μA could be sent through samples while the low frequency noise was monitored. The MR curve of a 600 nm width yoke sample measured across electrodes e1e6 is also shown in Fig. 5.4. It can be seen that the MR ratio decreases slightly to 1.5% after patterning, and the magnetization switching is less well defined. This may be explained by a slight mis-alignment against the pinned direction in the EBL patterning, and the argon ion beam damage to the spin-valve stack in the ion milling process.

The major challenge for these samples when noise spatial correlation

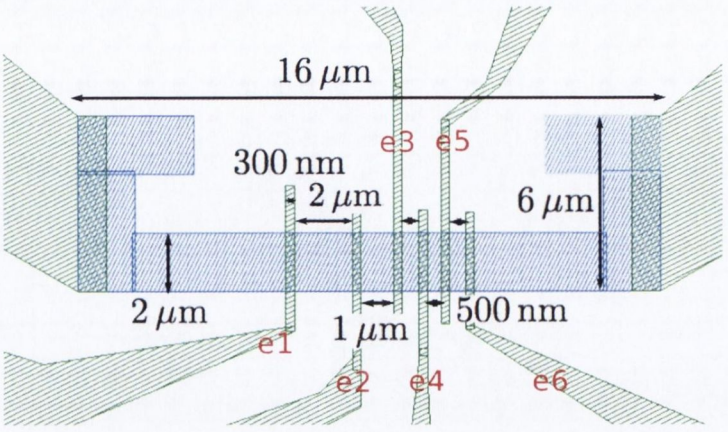
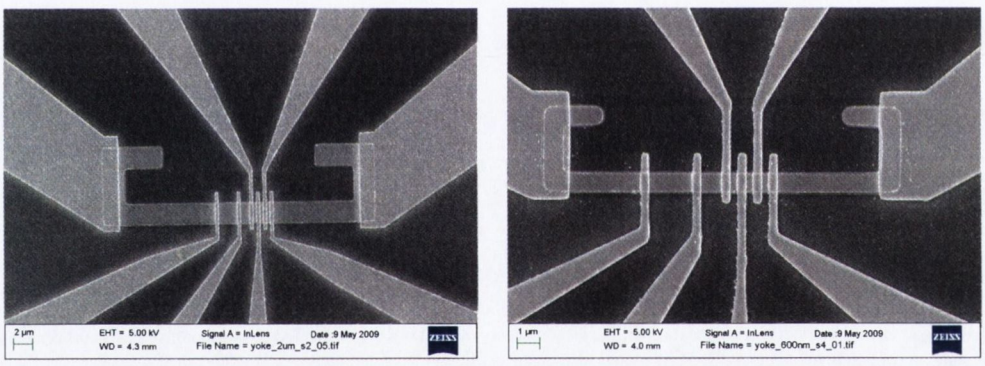


Fig. 5.5: Pattern design for a $w = 2$ μm yoke sample with corresponding dimensions and labels for electrodes.



(a) (b)

Fig. 5.6: SEM images of (a) a 2 μm width yoke sample, (b) a 600 nm width yoke sample with copper contacts.

measurement is concerned is their large contact $1/f$ noise. The contact-$1/f$ noise was measured to be about an order of magnitude larger than the intrinsic $1/f$ noise from the patterned spin-valve. We attributed the contact noise mainly to the current electrical leads, as cross-correlation measurement always gave a unity coherence, no matter which electrode pairs were probed. The AC coupled amplifiers (SR552) exert a tiny sensing current through the voltage leads, compared to the bias current through the sample.

Hence, a much larger contact noise contribution from the current leads is not a surprise. Due to the large contact $1/f$ noise, the results on this group of samples are excluded from our following discussions.

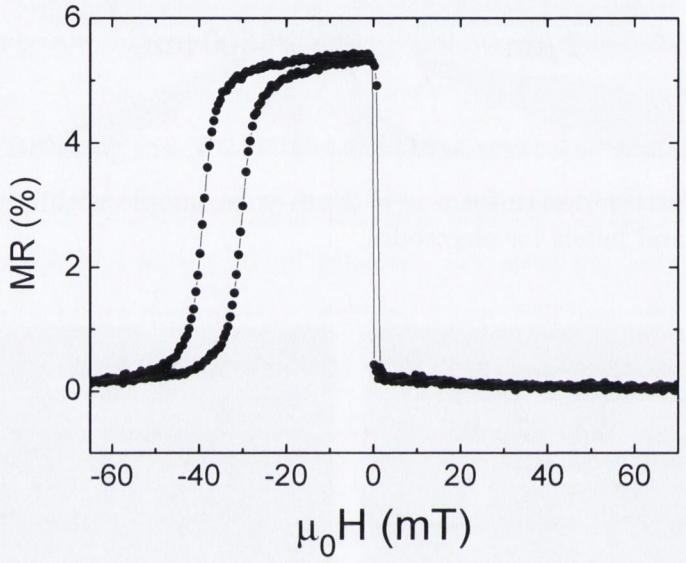
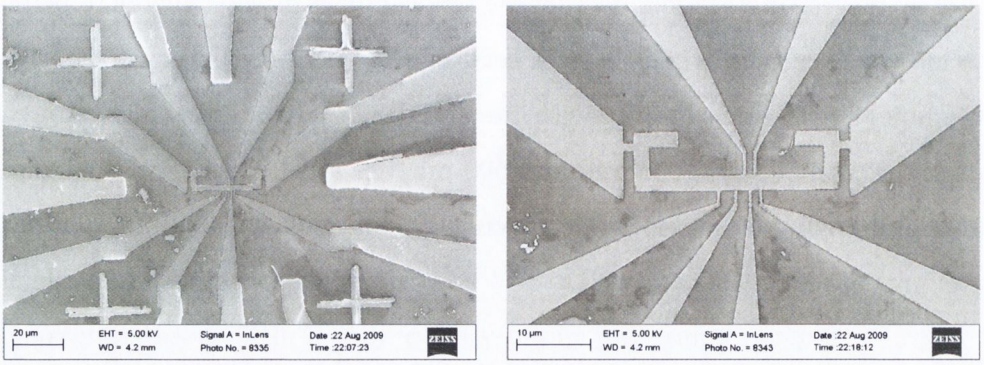


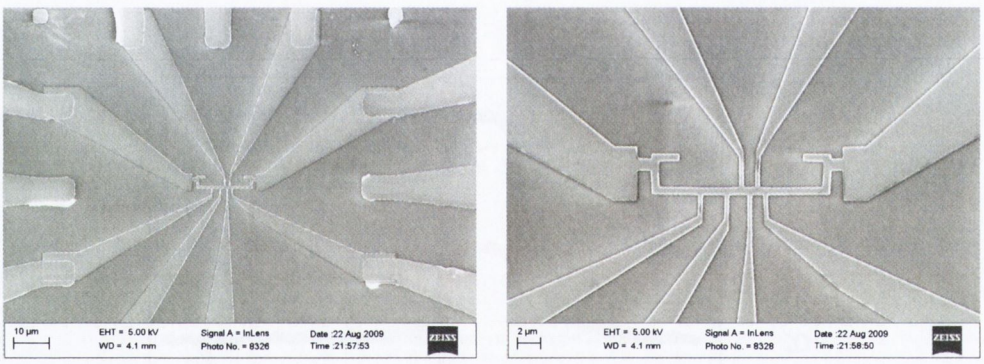
Fig. 5.7: GMR vs. applied field for an unpatterned spin-valve stack used to pattern the yokes in sample set c).

c) Spin-valves patterned into yokes plus seven electrical contacts by a single EBL process. The stacks used were SiO_2/Ta (5)/NiFe (3.5)/CoFe (1.5)/Cu (2.9)/CoFe (2.5)/IrMn (10)/Ta (5), with the numbers in nanometers. Unpatterned thin films show a GMR ratio of 5 - 6 % (Fig. 5.7). There is good coupling between magnetic states of the ferromagnetic layers and the resistance of the sample due to the large MR ratio. The spacings of adjacent voltage contacts were designed to be the same as set b). Besides, another set of samples were fabricated with even closer spacings between adjacent voltage contacts, e.g. 2 μ, 800 nm, 300 nm, 300 nm, and 300 nm.



(a) (b)

Fig. 5.8: SEM images of a yoke spin-valve structure with 2 μm width patterned by single step EBL.



(a) (b)

Fig. 5.9: SEM images of a yoke spin-valve structure with 600 nm width patterned by single step EBL.

A photolithography process was used to contact these yokes to micro-scale copper electrodes. The micromagnetics of these yokes is slightly modified as the contacts are also made of spin-valve stacks. The contacts are noise free (checked by the protocol described in Appendix A.8), and a large current of 1 - 2 mA can be sent through these samples, in order to have a much larger $1/f$ response at low frequency. Fig. 5.8 and Fig. 5.9 show several scanning electron microscopy images of the fabricated yoke samples.

In the results section, we denote the samples in set (a) 'micrometer-scale yoke sensors', while those in set (c) 'sub-micron-scale yoke patterns'. Samples in the latter group, with the standard electrode spacings, namely 2 μm, 1 μm, 500 nm, 500 nm, and 500 nm, are labelled as type I, whereas samples having closer electrode spacings (2 μm, 0.8 μm, 300 nm, 300 nm, 300nm) are labelled as type II.

5.3 Results and Discussion

5.3.1 Micrometer-scale Yoke Sensors

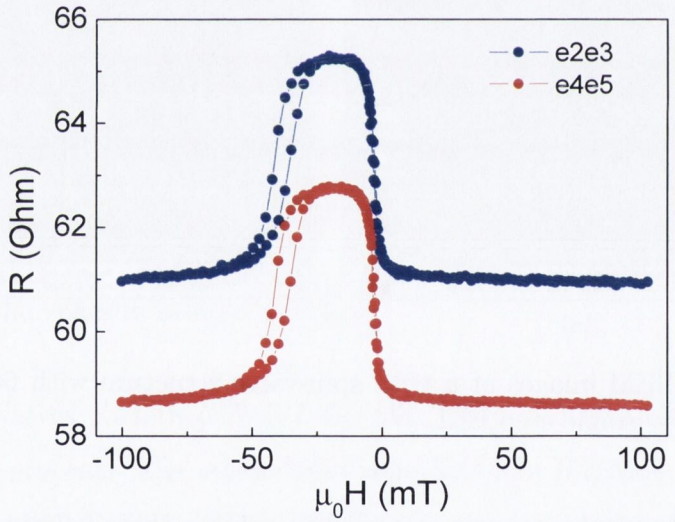


Fig. 5.10: Two MR curves measured across different electrode pairs on a yoke spin-valve biomagsensor.

Fig. 5.10 shows two MR curves measured on two adjacent pairs of electrodes on a micrometer-scale yoke sensor [1]. The MR ratio is slightly lower

[1]Results on the micrometer-scale yoke sensors were measured together with Prof.

than 8 %, which is close to the MR ratio of unpatterned spin-valve stack. There is a linear and non-hysteretic R-H region close to zero field due to the free layer switching, whereas the pinned layer switches between an applied magnetic field of -25 and -50 mT. A difference in the resistance R between these two electrode pairs, having nominally the same distance in between, is about 2.5 Ohm, which is less than 5 % of the total resistance. MR curve characteristics confirm a good quality of our patterning process.

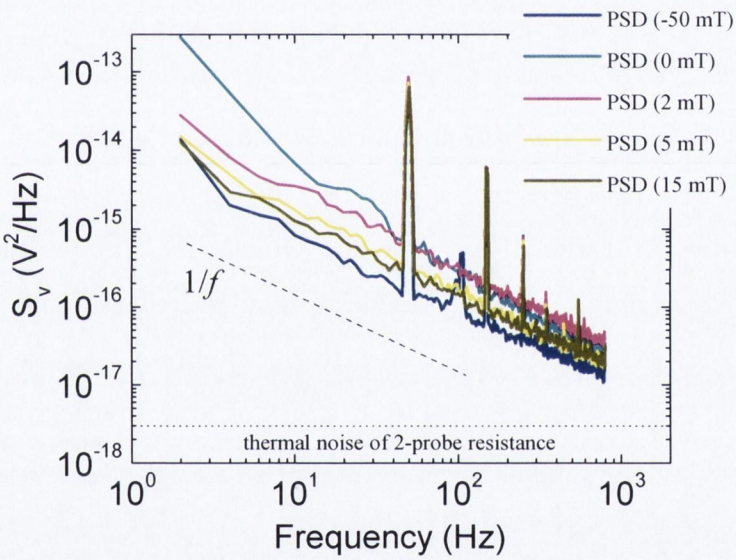


Fig. 5.11: PSD measured across e2e3 on a micro-scale yoke sensor.

In Fig. 5.11, we show noise spectra measured between e2 and e3 on the same yoke sensor during magnetization switching. They are all of $1/f$ nature and well above the thermal plus amplifier noise floor in the frequency range of our measurement (up to 800 Hz). Fig. 5.12 shows selected values of $fS_V(f)/V^2$ against an applied magnetic field. We analyse the data by

Edmund Nowak during his sabbatical stay in Trinity College, Dublin.

a modified Hooge formula, in which instead of averaging against the total number of charge carriers N_c (Eqn. (2.14)), noise spectra are averaged against the sample volume Ω [2].

$$\frac{S_V(f)}{V^2} = \frac{\gamma}{\Omega f^\alpha} \tag{5.9}$$

In Eqn. (5.9), we assume that the sample obeys Ohm's law, $R = V/I$, hence, the power spectral density is proportional to V^2. This is well justified for spin-valves. In contrast to Eqn. (2.14), the Hooge parameter, γ, defined in this way has a dimension of volume. It is normally quoted in μm^3. According to Eqn. (5.9), $fS_V(f)/V^2$ is equal to γ/Ω, for pure $1/f$ noise ($\alpha = 1$). Since the sample volume always stays the same, the normalized noise power characterizes the increase of γ during magnetization switching. Using the width of the yoke sensor, $w = 5$ μm, the spacing between two adjacent electrodes, $d = 5$ μm, the thickness of the free layer and the pinned layer, $t = 8.5$ nm and 3.5 nm, respectively, we obtain a Hooge parameter γ between 4×10^{-13} and 2×10^{-12} μm^3. The γ value we observed is comparable to that reported in previous studies on spin-valve stacks of similar dimension (10^{-13} to 10^{-11} μm^3) [2].

Fig. 5.13 shows the values of the averaged coherence function at different applied magnetic fields measured across three different pairs of electrodes. The result shown is an average of 100 consecutive spectra taken by the HP 35660A spectrum analyser. We summarize the result by further averaging the frequency dependent coherence function between 18 and 46 Hz, well within the low frequency $1/f$ noise range, also eliminating any power line pick-ups. The error bars are the standard deviation of the coherence function across this frequency span. When the same electrode pairs are used (e2e3 - e2e3), the coherence is 1, which is expected for two totally correlated

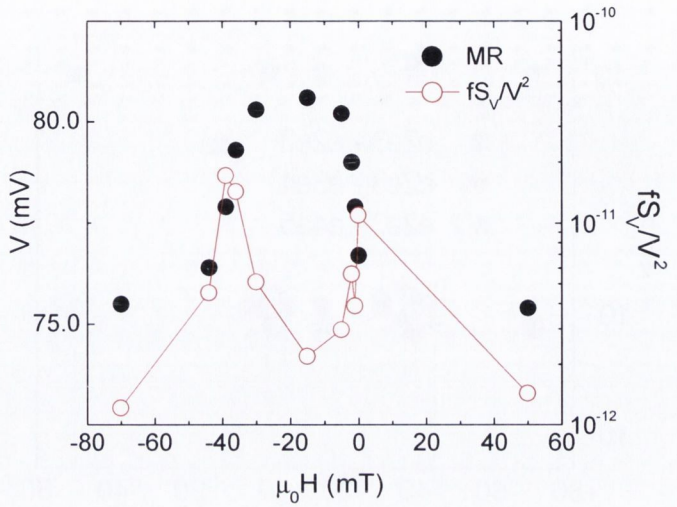


Fig. 5.12: $fS_V(f)/V^2$ against applied magnetic field for a yoke biomagsensor measured across e2e3. $fS_V(f)/V^2$ has been averaged between 18 - 22 Hz.

signals. Non-correlated amplifier noise contributes little to the observed coherence function, due to the much larger $1/f$ noise in our frequency window. A close look at the coherence function up to the highest measurement frequency, shows a decrease of the coherence above 100 Hz, which is related to the amplifier noise contribution at high frequencies, where the $1/f$ noise power is significantly lower (Fig. 5.14). The averaged coherence is 0.01 for both of the other two electrode pairs, e2e3 - e3e4 and e2e3 - e4e5. This is the statistical error from averaging 100 DFT spectra. There is no coherence in the low frequency noise between the different electrode pairs for this sample. We thus suggest that the coherence length for $1/f$ noise in our spin-valve sensors is below 5 μm, which is the distance between two adjacent electrode pairs (For e2e3 - e3e4, the two electrode pairs contain a common electrode. Still no coherence was measured in this case. If we take this into account,

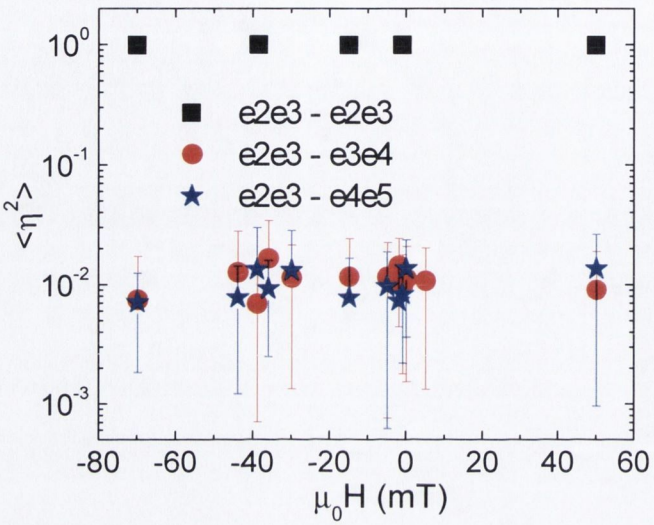


Fig. 5.13: Coherence data between different electrode pairs on a yoke spin-valve sensor. The coherence between a frequency range of 18 to 46 Hz was averaged to avoid power line pick-up and the error bars are the standard deviations.

the coherence length is expected to be even less).

To explain the $1/f$ noise in spin-valve structures, models based on a micro-spin approximation have been suggested [33, 34, 35]. These models assume single domain ferromagnetic layers with infinite intralayer exchange energy. The fluctuation is induced by a small deviation in the magnetization angle in relation to its equilibrium value. Micro-spin models can normally qualitatively reproduce the noise-field relation (Fig. 5.11 and Fig. 5.12) during magnetization switching in spin-valve samples.

However, despite the fact that it is always puzzling how the micro-spin approximation leads to a low frequency $1/f$ noise spectrum, our measurement suggests that there are origins to the $1/f$ noise, which these models

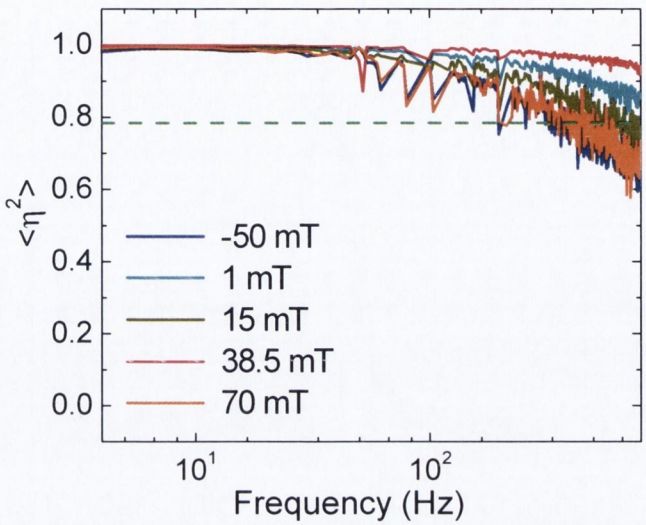


Fig. 5.14: Averaged coherence function $\langle \eta^2(f) \rangle$ for e2e3 on a micrometer-scale yoke sensor. The green dashed line shows the predicted coherence function for a 1 kohm resistor (which is similar to the two-probe resistance of the sample) connected in both channels. Voltage noise from the amplifiers significantly decreases the coherence function at high frequencies. Some spurious power line pick-ups are removed during data processing.

do not account for. In one of the works, it was suggested that the effective volume for the micro-spin is about 10^{-17} m^3 [35]. This is slightly larger than the volume between our adjacent electrode pairs. Assuming an auto-correlation function $C(\tau, d) \sim 1$ inside this volume — magnetization in the whole volume switches together, it is expected to lead to an increase in the coherence between the two adjacent electrode pairs. Our null result on micrometer-scale yoke sensors then indicates that any micro-spin model can only be an approximated approach in explaining low frequency noise in spin-valve samples, or at least the above estimated effective volume is too large.

5.3.2 Sub-micron-scale Yoke Patterns

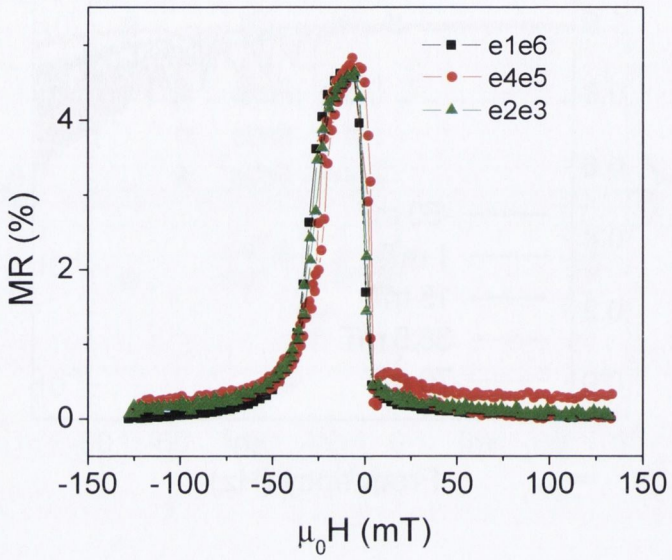


Fig. 5.15: MR curves of a $w = 2$ μm yoke (type I) measured across different electrode pairs.

Fig. 5.15 shows MR curves measured on different electrode pairs on a w = 2 μm yoke. Slightly lower MR ($\sim$ 5%), compared to the spin-valve stack without patterning (Fig. 5.7) is observed in this sample. This is probably due to the argon beam damage to the spin-valve stack during the milling process. The free layer switches at around zero field, while the pinned layer starts switching at -7 mT. The hysteresis during the free layer switching is small. This is as expected for a spin-valve sensor with cross anisotropy geometry, in which the free layer rotates coherently in a narrow field range around zero, giving a linear output. It suggests that the contact pads, which are also made of spin-valve multilayers do not greatly complicate the micromagnetics or the sample spin structure, most likely due to the pinning of domain walls at the corners of the electrodes. Hence, the longitudinal

part of the yoke is assumed to undergo a rotation-like process during the magnetization switching. The four-probe resistance of different electrode pairs are between 5 ohm for the electrodes with closest spacing (d = 400 nm), and 60 ohm for the outermost two electrodes (e1e6, d = 4.2 μm).

Fig. 5.16(a) shows the noise vs. magnetic field behaviour in a half loop for the same yoke, summed across three different octaves. Our observation is very similar to results of different authors on several spin-valve samples larger in size [1, 2]. When the sample is at positive saturation, only thermal background noise is measured. There is a sudden increase of the noise power during the free layer switching. The noise power then decreases significantly when the two ferromagnetic layers are in antiparallel configuration. Another more pronounced peak in noise power shows up during the pinned layer switching. And it finally goes down to the same thermal background level when the sample reaches negative saturation. The observed octave noise power in Fig. 5.16(a) suggests that during magnetization switching, the measured low frequency noise is mainly of $1/f$ nature, with the noise power from three consecutive octaves roughly on top of each other.

It has been shown by several authors that the low frequency noise in spin-valve sensors scales with dR/dH. This relation was previously summarized by Nowak and co-workers in Eqn. (2.23), and explained in a framework utilizing the fluctuation-dissipation theorem (see Appendix A.2) [2]. We also verified the relation in our w = 2 μm sample, by plotting the Hooge parameter γ against $dR/d\mu_0 H$ (Fig. 5.16). Eqn. (2.23) says that the Hooge parameter α should scale with $1/R(dR/dH)$. While in spin-valve samples, the total MR ratio is less than 10 %, hence, the scaling is simplified to follow only dR/dH.

The Hooge parameter of this w = 2 μm yoke, between 10^{-13} and 10^{-11}

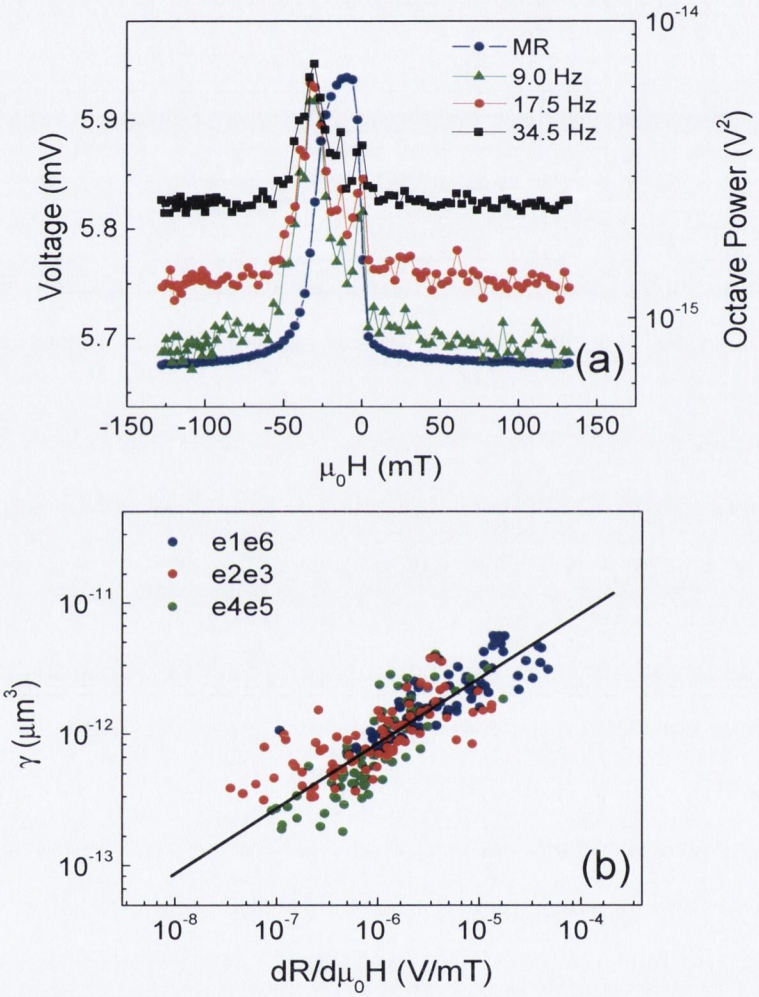


Fig. 5.16: (a) Noise summed across three consecutive octaves against magnetic field in a $w = 2\ \mu$m yoke sample (type I); (b) Hooge parameter γ during magnetization switching in the same sample plotted against $dR/d\mu_0 H$. The black line is a guide to the eyes.

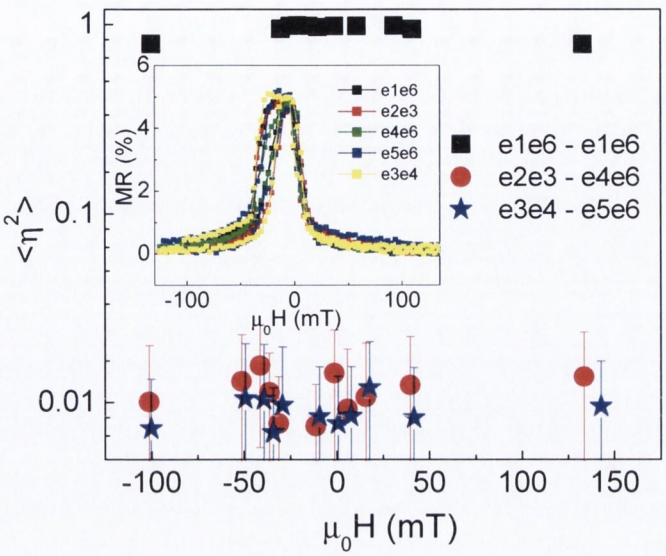


Fig. 5.17: Ensemble averaged coherence function $\langle \eta^2 \rangle$ for a $w = 600$ nm yoke pattern and its MR curves measured across corresponding electrode pairs.

μm^3, is also comparable to values given by other authors [2]. Hooge parameters from three different electrode pairs fall on top of each other. This indicates that there is no difference in the Hooge parameter when different sizes of the sample volume are probed. Hence, the Hooge formula (Eqn. (5.9)) is still valid for this $w = 2$ μm yoke spin-valve, with an active free layer volume of 5×10^{-15} cm^3 between the nearest adjacent electrodes (e4e5). Our observation proves that the volume scaling described in the Hooge formula is still valid in spin-valve structures down to this sample size.

With the micromagnetics and the noise - field behaviour verified on our samples, we started the measurement of the coherence between different electrode pairs. The averaged coherence function data together with its MR curves for a $w = 600$ nm yoke sample (type I) are summarized in Fig. 5.17.

The MR curves are less uniform than what was observed in the $w = 2$ μm sample (Fig. 5.15), suggesting the possible existence of a few domains in the sample active volume. It is still possible to have a linear and low hysteretic part in the MR curve due to the free layer switching close to zero field. The averaged coherence function shows a similar behaviour compared to that observed in micrometer-scale yoke sensors. A coherence close to 1 was observed when the two AC coupled amplifiers (SR552) are connected across the same electrode pair, whereas no coherence above the statistical error (0.01) was observed on adjacent electrode pairs. In our sub-micron-scale yokes, the spacing between adjacent electrode pairs is significantly reduced compared with that for the micrometer-scale yokes (e2e3 - e4e6 and e3e4 - e5e6 both have a spacing of 400 nm apart). We thus further reduce the correlation length of $1/f$ in spin-valves to hundreds of nanometers.

For electrode pairs e1e6 - e1e6, there is a slight decrease in $\langle \eta^2 \rangle$ to about 0.8 for large applied magnetic fields, when the sample is fully saturated. This can be understood by the contribution from uncorrelated voltage noise of the amplifiers. To correct this, the following formula can be utilized [4].

$$\langle \eta_c^2(f) \rangle = \frac{\langle \eta_{12}^2(f) \rangle}{[1 + \langle S_{A1}(f) \rangle / \langle S_1(f) \rangle][1 + \langle S_{A2}(f) \rangle / \langle S_2(f) \rangle]} \tag{5.10}$$

in which $\langle S_{A1}(f) \rangle$ and $\langle S_{A2}(f) \rangle$ are the averaged amplifier voltage noise spectra for the two amplifiers, respectively. Taking the measured background noise across e1e6 ($\sim 1.7 \times 10^{-17}$ V^2/Hz), and the measured voltage noise from the amplifiers ($\sim 2.6 \times 10^{-17}$ V^2/Hz), the corrected coherence function $\langle \eta_c^2 \rangle \simeq 1$ at 133 mT applied field, as expected.

It is important to note that electrical noise due to magnetic fluctuations in the contacts (also made of spin-valve stack for the submicron-scale yokes), together with the excess noise due to the contact resistance between

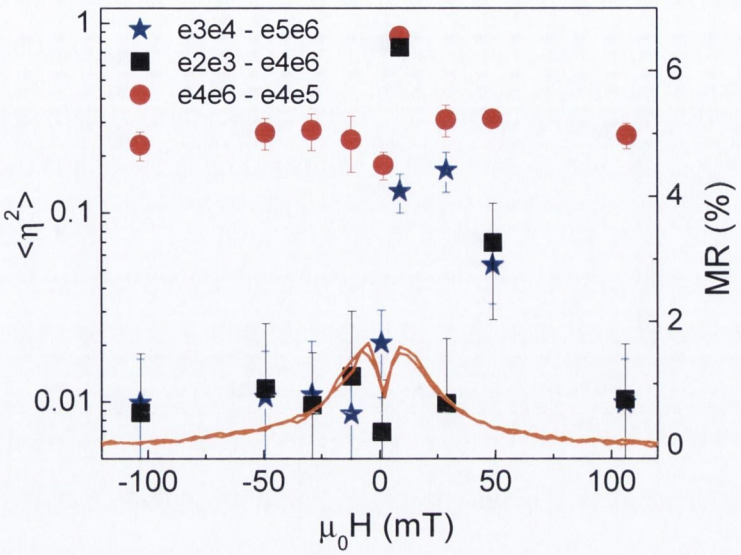


Fig. 5.18: Ensemble averaged coherence function against applied magnetic field, and a MR curve measured between electrode 1 and 2, on a $w = 2$ μm yoke sample, with the easy-axis of the free layer and the pinned layer both along the yoke arm.

photolithographically patterned copper electrodes and the spin-valve stack, contributes very little to the measured low frequency noise. According to the Hooge formula (Eqn. 5.9), $1/f$ noise scales inversely with the sample volume Ω. In our samples, the contact pads are much larger than the yoke pattern, hence, a much lower normalized $1/f$ noise $S_V(f)/V^2$ from contact pads is expected. Furthermore, the input current of the AC coupled amplifiers is tiny compared with the bias current of the sample. So $1/f$ noise from voltage contacts is negligible. If any noise originated from contact magnetic fluctuations is present, it is with the current contacts, and leads to a higher coherence value than expected. Occasionally, this was indeed observed on some samples (normally with a $\langle \eta^2 \rangle$ between 0.02 - 0.05 for two widely spaced electrode pairs under sample magnetic saturation). These

samples are excluded from our data analysis.

However, some non-trivial coherence between different electrode pairs, sometimes much larger than expected values for non-correlated signals, was also observed in our samples. For example, Fig. 5.18 shows the averaged coherence function and a representative MR curve (e1e2, right axis) for a $w = 2$ μm yoke, in which the yoke arm was patterned to be along the exchange-bias pinned direction. This sample does not have the above described cross-anisotropy. Under zero field, the free layer and the pinned layer are nearly aligned to the same direction, with a very small angle between their respective magnetization caused by misalignment during the patterning process. When a magnetic field is applied perpendicular to the yoke arm, both the free layer and the pinned layer turn towards the field direction, with the free layer leading the trend. Hence, the MR first goes up, as the angle between the free layer and pinned layer increases. After the free layer magnetization is aligned with the applied field, further increase in the magnetic field can only reduce the angle between the pinned layer and the free layer, due to the pinned layer magnetization further turning towards the applied field direction. Hence, the resistance of the sample goes down and then saturates when the magnetization in the two ferromagnetic layers are well aligned. Although not applicable as a sensing unit, this complex magnetization process gives us a good system to test the influence of macroscopic domain wall motion, on low frequency noise and its spatial coherence function.

From Fig. 5.18, we can clearly see that the coherence function for all the three electrode pairs, under positive or negative saturation, is as expected for a system without any spatial correlation. For electrode pairs e4e6 - e4e5, since e4e6 contains e4e5, and its volume is twice of the latter, we

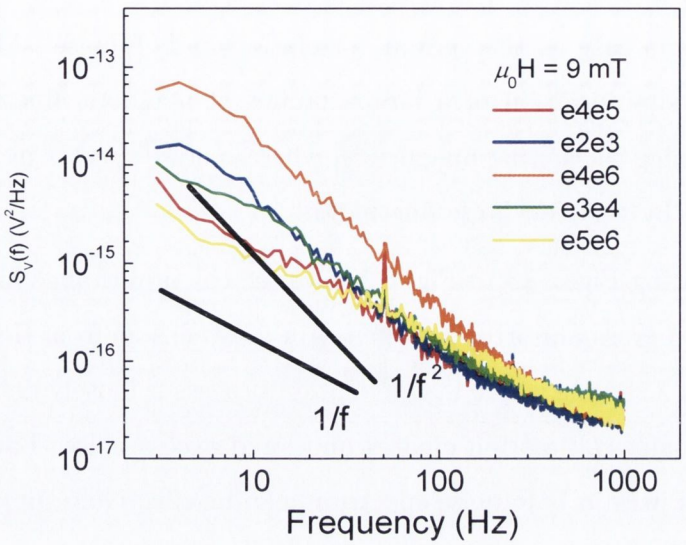


Fig. 5.19: Noise spectra across five electrode pairs at 9 mT, where the coherence function increases significantly. The black line depicts the $1/f^2$ slope. For the lower two spectra (e4e5 and e5e6), bumps and deviations from pure $1/f$ slope are clearly visible. The sample is the same as that shown in Fig. 5.18.

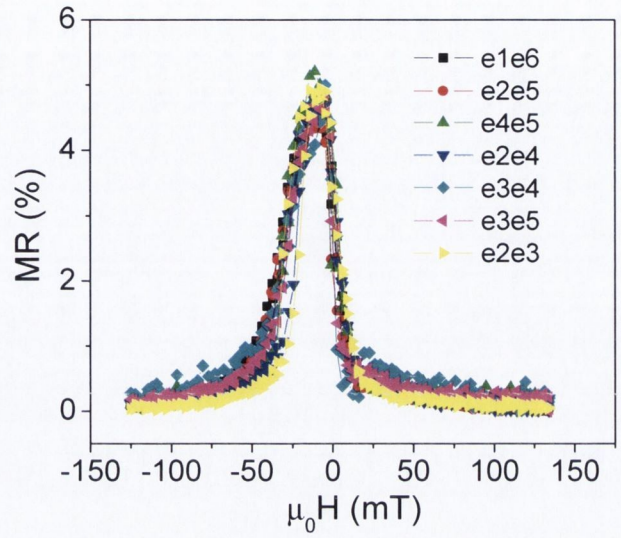
expect an ensemble averaged coherence function of 0.25, which is close to what was observed. However, during magnetization switching, there is an increase, different in its magnitude, in the coherence function for all the three electrode pairs. Fig. 5.19 shows representative noise spectra taken at the magnetic field setpoint, where the coherence function significantly increases compared to its saturation value. The upper three spectra (e4e6, e2e3 and e3e4) reveal a clear $1/f^2$ nature, whereas the lower two (e4e5 and e5e6) show significant deviations from the featureless $1/f$ slope. Both kinds of spectra can be attributed to macroscopic domain wall movement. This suggests that domain wall propagation through the sample, or a domain wall hopping between two or multiple pinning sites, introduce a large spatial

correlation in the measured low frequency noise spectra. However, this is not the same case as the spatial correlation in $1/f$ noise. Magnetic $1/f$ noise is a superposition of a large number of magnetic fluctuators, each having similar fluctuating magnitude, whereas noise spectra in Fig. 5.19 are dominated by very few large fluctuators.

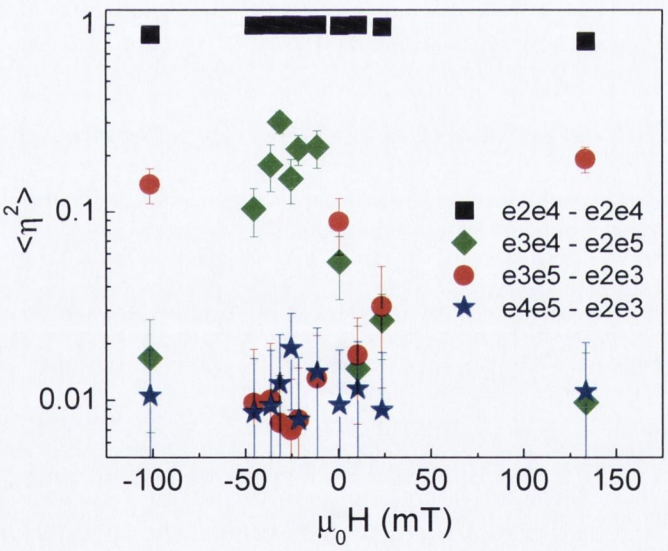
Comparing Fig. 5.18 to Fig. 5.17, we see the importance in achieving a well-defined cross-anisotropy geometry in yoke sensors from the noise point of view. In a sample where magnetization process is loosely defined, macroscopic domain wall motion creates undesired excess noise. Large two-level fluctuators, with a $1/f^2$ noise spectrum, can be effectively suppressed when the magnetization process is mainly rotation, as what is expected for a Stoner-Wohlfarth particle under an applied magnetic field perpendicular to its easy-axis (see Appendix A.6). Hence, domain structure engineering should always play an important role in magnetic sensor designs, though those magnetic fluctuators which dominate in the low frequency range in a spin-valve stack, have been shown not to be individual domains.

Fig. 5.20 shows the MR curves (a), and coherence function measured (b) across four selected electrode pairs at different magnetic field for a $w = 600$ nm yoke sample with closer electrodes spacings (type II). The MR curves, measured across different electrode pairs, show similar switching fields for both the free layer and the pinned layer. The linear and low hysterestic portion around zero field is also clearly identifiable. An interesting observation from Fig. 5.20(b) is that the averaged coherence function increases during magnetization switching for electrode pairs e3e4 - e2e5 and decreases for e3e5 - e2e3. In the following, we try to find an explanation to the observed change in the coherence function.

To exclude large scale domain wall motion, similar to what has been



(a)



(b)

Fig. 5.20: MR curves, and coherence function recorded at different magnetic field for four electrode pairs on a $w = 600$ nm yoke sample (type II).

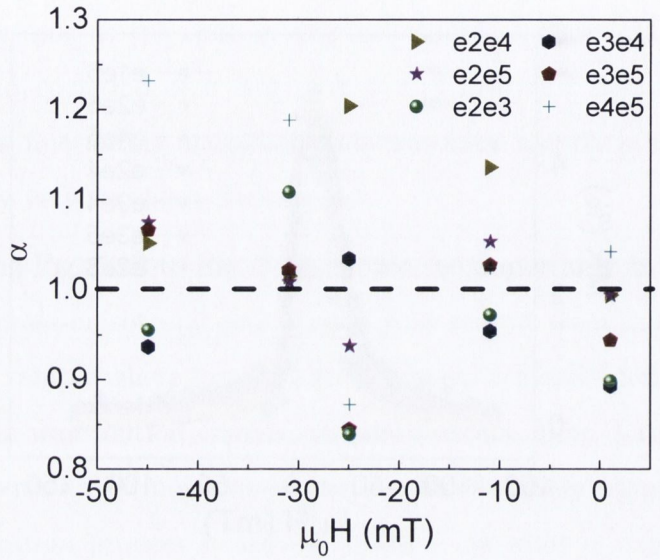


Fig. 5.21: α parameter obtained by fitting measured noise spectra at different magnetic field values with a $1/f^{\alpha}$ function. Sample is a $w = 600$ nm sub-micron-scale yoke pattern (type II).

observed in Fig. 5.18 and Fig. 5.19, as the reason for the observed change in the coherence function, we plot the slope of the $1/f^{\alpha}$ spectra α at a few magnetic field setpoints during magnetization switching (Fig. 5.21). The α parameter is always within 0.8 and 1.2, during the whole magnetization switching process. This means that all the observed noise spectra can be generally treated as $1/f$ noise (see Chapter 2). No bump or deviation from the $1/f$ slope was observed by inspecting the obtained noise spectra directly (Fig. 5.22), except the fact that some of the spectra join the thermal noise background at a high enough frequency [2]. This largely eliminates macroscopic domain wall motion as the reason for the observed change in

[2]For the spectra shown in Fig. 5.22, it might be argued that the black line (e2e4) shows a small bump at about 20 Hz. However, it is hardly evident compared with those in Fig. 5.19.

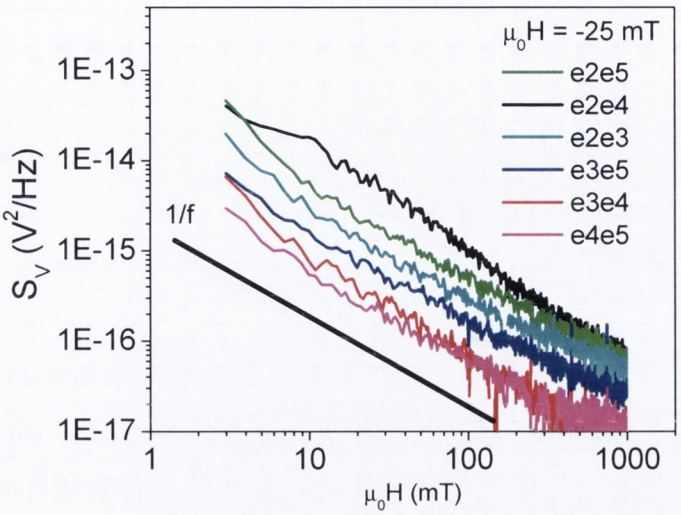


Fig. 5.22: Power spectral density measured across different electrode pairs at -25 mT on a $w = 600$ nm yoke sample (type II). The background thermal plus amplifier noise has been subtracted.

the coherence function.

A better view of the problem can be gained by investigating the volume scaling of $fS_V(f)/V^2$. As discussed before, the volume scaling of $1/f$ noise holds in our $w = 2$ μm yoke sample. In this $w = 600$ nm yoke pattern, the smallest active volume is further reduced from 5×10^{-15} cm^3 for the $w = 2$ μm yoke sample (Fig. 5.16) to less than 10^{-15} cm^3. Fig. 5.23 shows this relation at -25 mT, where the coherence function either peaks (for e3e4 - e2e5), or it is largely suppressed (for e3e5 - e2e3). The normalized $1/f$ noise magnitude, $fS_V(f)/V^2$, is plotted against the distance between electrode pairs d. d was estimated by measuring the spacing between two furthest separated electrode pairs (e1e6), and using the relation that the voltage measured across an electrode pair is proportional to the spacing between the two electrodes. This method gives a spacing of 280 nm between the

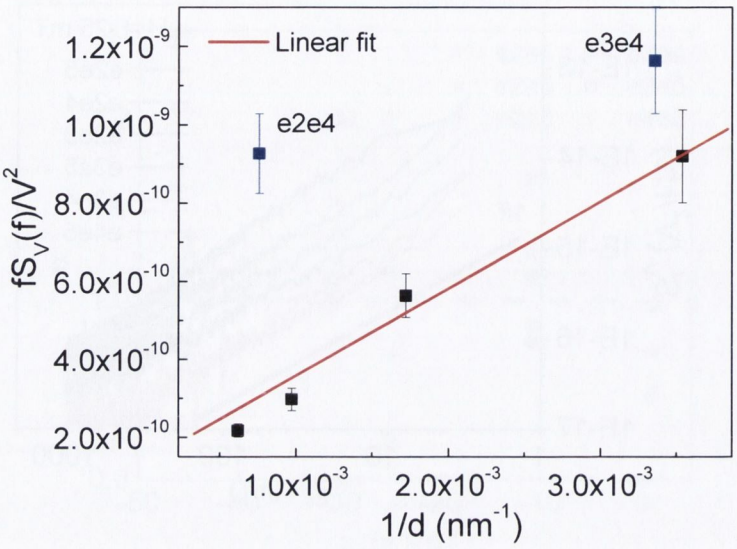


Fig. 5.23: $fS_V(f)/V^2$ plotted against $1/d$ for different electrode pairs at -25 mT, for a $w = 600$ nm yoke sample (type II), with d the spacing between two electrodes. $fS_V(f)/V^2$ is averaged between 18 - 42 Hz.

closest electrode pair (e4e5), which is close to that measured directly on the SEM (320 nm). Two electrode pairs do not fall on the line for a linear scaling between $fS_V(f)/V^2$ and $1/\Omega$, as predicted by the Hooge formula (Eqn. (5.9)). They are e3e4 and e2e4 (which also contains e3e4 as a segment). The noise from these two electrode pairs is significantly higher than the others. Hence, if we take the volume between e3 and e4 being noisier than the rest of the sample, the observed coherence function change in Fig. 5.20(b) can then be understood. Noise between e3 and e5 is dominated by the volume e3e4, hence, an increase in the coherence function was observed during magnetization switching between e3e4 and e2e5. Similarly, as e2e3 does not contain e3e4 but e3e5 does, the coherence function between these two electrode pairs drops. Noise in e2e3 and e4e5 are not spatially correlated, because they are separated by the noisier block — e3e4.

The above observation suggests that the local structure and magnetic inhomogeneity in a spin-valve sample can introduce significant deviations from the widely accepted volume scaling relation described in the Hooge formula. The length scale to observe this deviation in our samples is below 300 nm laterally, or in a volume of roughly 4.5×10^{-16} cm^3. However, the noise spectrum associated with this small volume still has a nominally $1/f$ slope, which indicates that fundamental magnetic fluctuators are at least an order of magnitude smaller in size (as a rule of thumb, if a $1/f$ noise spectrum is formed by superposition the spectra of more than 10 two-level fluctuators, it is impossible to identify its elementary components).

	OCT1	OCT2	OCT3	OCT4	OCT5	OCT6	OCT7
OCT1	1.505	0.000	0.000	0.000	0.000	-0.001	0.001
OCT2	0.000	1.836	0.000	0.000	0.000	-0.001	0.000
OCT3	0.000	0.000	1.692	0.000	0.000	0.000	0.001
OCT4	0.000	0.000	0.000	1.975	0.000	-0.001	0.000
OCT5	0.000	0.000	0.000	0.000	0.882	0.000	0.000
OCT6	-0.001	-0.001	0.000	-0.001	0.000	1.850	0.011
OCT7	0.001	0.000	0.001	0.000	0.000	0.011	2.107

Table 5.2: Covariance matrix of octave noise power measured on electrode pair e3e4 at -102 mT. The sample probed is a $w = 600$ nm yoke pattern (type II).

	OCT1	OCT2	OCT3	OCT4	OCT5	OCT6	OCT7
OCT1	2.652	4.207	0.891	0.985	0.278	0.324	0.211
OCT2	4.207	6.027	2.462	2.573	0.893	0.821	0.447
OCT3	0.891	2.462	4.579	0.698	0.232	0.253	0.147
OCT4	0.985	2.573	0.698	4.649	0.326	0.355	0.224
OCT5	0.278	0.893	0.232	0.326	2.772	0.182	0.125
OCT6	0.324	0.821	0.253	0.355	0.182	6.090	0.289
OCT7	0.211	0.447	0.147	0.224	0.125	0.289	11.882

Table 5.3: Covariance matrix of octave noise power measured on electrode pair e3e4 at -25 mT. The sample probed is a $w = 600$ nm yoke pattern (type II).

To further characterize the volume between e3e4, we measure the co-

	OCT1	OCT2	OCT3	OCT4	OCT5	OCT6	OCT7
OCT1	1.612	0.628	0.040	0.007	0.061	0.024	0.075
OCT2	0.628	2.021	0.192	0.039	0.051	0.059	0.003
OCT3	0.040	0.192	1.966	0.065	0.066	0.091	0.057
OCT4	0.007	0.039	0.065	2.152	0.056	0.089	0.144
OCT5	0.061	0.051	0.066	0.056	2.117	0.097	0.149
OCT6	0.024	0.059	0.091	0.089	0.097	3.118	0.263
OCT7	0.075	0.003	0.057	0.144	0.149	0.263	4.933

Table 5.4: Covariance matrix of octave noise power measured on electrode pair e2e5 at -25 mT. The sample probed is a $w = 600$ nm yoke pattern (type II).

variance matrices for e3e4 and e2e5 under different applied magnetic fields. The data were taken by a sampling programme running at 2048 Hz for 1024 sec at each field setpoint. Samples within 1 sec were discrete Fourier transformed to obtain the power spectral density without averaging. The power spectra were then binned into 7 consecutive octaves, centred from 4.8 Hz to 272 Hz. The covariance matrices were then worked out by a LabView programme. Table 5.2 shows the covariance matrix for e3e4 at negative saturation (-102 mT). The off-diagonal terms are nearly all zero, as expected for the thermal noise, which is Gaussian. The diagonal terms are more than the Gaussian expectation value 1. The reason of this is not clear. It may be attributed to power line pick-ups, which introduces additional correlation in the noise power within a single octave, especially for higher octaves.

The covariance matrix for the same electrode pair under -25 mT applied magnetic field is significantly different (Table 5.3). The off-diagonal terms are much larger than the Gaussian expectation, so are the diagonal terms (even compared with those in Table 5.2). It has been further checked out that this increase in the variance between octaves is not due to other common non-Gaussian effects, for example so-called 'spectral wandering' [21, 20]. Hence, we attribute the observed non-Gaussian noise to the fact

that only very few fluctuators exist in the active volume. In comparison, the covariance matrix for a significantly larger sample volume (e2e5), at the same applied magnetic field, was shown in Table 5.4. The non-Gaussian off-diagonal terms are still clearly identifiable, however, these are much less than those obtained with e3e4. Thus, we believe that though the spacing between e3e4 is larger than the lateral dimension of a single fluctuator, the number of fluctuators in e3e4 is not large. It suggests that the spacing between the closest spaced electrodes ($\sim$ 300 nm), should not be more than two orders of magnitude larger than the typical spatial correlation length for $1/f$ noise in spin-valves.

Using a rough estimation, Weissman and co-workers reported an upper limit of fluctuating magnetic volume of 6×10^{-16} cm^3 in spin-valves, by measuring the low frequency electrical noise and its non-Gaussianity on a bridged spin-valve sensor [25]. Our attempt to measure the spatial coherence length directly gives surprisingly consistent results compared with theirs. The only difference is that our results suggest that this volume is probably about ten times less, hence, in the 10^{-17} cm^3 range.

We now return to the question given at the beginning of this chapter — what are the elementary magnetic fluctuators in a spin-valve stack? As we already have a rough estimate of the fluctuating volume and an upper limit for the spatial correlation length, the question can be stated in another way — what known structure or magnetic length scale is close to the characteristic length given by our measurement? Magnetic domains have already been excluded from the picture, due to their large size in soft ferromagnetic materials. And the exchange length of a few nanometers is too small. This

leaves us only a few options in between. The first is probably the domain wall width (see Chapter 1). It has been reported to be 30 nm - 50 nm for permalloy and CoFe ferromagnetic thin films [36, 37, 38], right in the sub-hundred nanometer scale [3]. However, in our samples, at least between adjacent electrodes, the yoke arm is assumed to be in a single domain state. Even in a less ideal case, if 2 - 3 domain walls are present, it will be highly unlikely for them to generate a $1/f$ noise spectrum rather than a $1/f^2$ spectrum. There is also no well-known mechanism, in which domain wall width plays the role as the spatial correlation length for magnetic noise. The other is the grain size in magnetic thin films. In sputtered soft magnetic films, e.g. permalloy and CoFe, this value was normally reported to be between 10 nm and 120 nm [39, 40]. Grain boundaries create a barrier which weakens the exchange interaction between adjacent spins, while inside a single grain, strong exchange interaction leads to a uniform magnetization. In a macroscopic single domain state, the direction of magnetization in each grain can fluctuate within a small angle around its equilibrium value. The magnetization fluctuation is coupled to the sample resistance through the GMR effect. Hence, superposition of a large number of grain magnetization fluctuations in a spin-valve sample, gives the observed $1/f$ noise. The fluctuating volume in this case, is about 6×10^{-18} cm^3 to 1×10^{-17} cm^3, and the spatial coherence length is in sub-hundred nanometers, which are both close to the values estimated from our experiment. It is important to note here that several authors recently suggested magnetic ripple states as another possible candidate for fundamental magnetic fluctuators [41, 42].

It has been well established in the literature that a multi-domain state

[3]Domain wall width depends strongly on geometric factors of micromagnetic structures, e.g. thin film thickness and the lateral dimension of the pattern. However, in a soft magnet, it is normally not less than a few nm and not more than 200 nm, still within the possible range.

normally shows higher low frequency noise than the same structure in a single domain state [32]. Assuming magnetic grains as individual magnetic fluctuators does not violate this statement. The first reason is that a loosely defined, complex multi-domain state is highly likely to associate with large range domain wall motion during magnetization switching. This is a potential source for excess random telegraph noise. The second reason is that the nature of the fluctuators that can be observed in the measurement window and their number are in close relation to the magnetic structure of the sample. The fluctuating amplitude and characteristic frequency of a magnetic grain, depend strongly on the depth and the shape of the potential well it sits in. The depth and the shape of the potential well are functions of the sample magnetic structure. A uniformly magnetized state leads to deep and sharp potential wells. This may reduce the fluctuating amplitude of the fluctuators, and push many fluctuators out of the measurement window.

5.4 Conclusion

Spatial correlation measurement has been carried out on spin-valve samples patterned into yoke-shapes, in order to determine the spatial correlation length of magnetic $1/f$ noise. It has been shown that this length scale is below the closest spacing between our electrodes, which is about 300 nm. Sometimes, a noisier region in a similar length range can be identified in the sample, whose noise spectrum is above the volume scaling relation defined in the Hooge formula, and highly non-Gaussian. This suggests that though we have not yet obtained measurable spatial correlation, the spatial coherence length of $1/f$ noise should not be much less than the closest electrode spacing in our samples, which is about 300 nm. This leads us to suggest that

the individual fluctuating entities in a spin-valve are ferromagnetic grains created in the thin film deposition process.

Spatial correlation attributed to large range domain wall motion was occasionally observed in samples where magnetization states are loosely defined. This suggests that optimising the magnetic sensor design, to largely suppress random domain wall hopping, plays an important role in achieving low noise magnetic sensors based on spin-valve stacks.

References

[1] Y. Bei and E. W. Hill. *J. Appl. Phys.*, 93:8391, 2003.

[2] A. Ozbay, A. Gokce, T. Flanagan, R. A. Stearrett, E. R. Nowak, and C. Nordman. *Appl. Phys. Lett.*, 94:202506, 2009.

[3] Sh. Kogan. *Electronic Noise and Fluctuations in Solids.* Cambridge University Press, 1996.

[4] J. H. Scofield, D. H. Darling, and W. W. Webb. *Phys. Rev. B*, 24:7450, 1981.

[5] G. D. Brushe and J. R. Waller. *Digital Signal Process.*, 1:110, 2001.

[6] G. C. Carter, C. H. Knapp, and A. H. Nuttall. *IEEE Trans. Audio Electroacoust.*, AU-21:337, 1973.

[7] J. S. Bendat and A. G. Piersol. *Random Data: Analysis and Measurement Procedures.* Wiley-Interscience, 2nd edition, 1986.

[8] R. F. Voss and J. Clarke. *Phys. Rev. B*, 13:556, 1976.

[9] R. D. Black, M. B. Weissman, and F. M. Fliegel. *Phys. Rev. B*, 24:7454, 1981.

[10] J. Kilmer, E. K. Chenette, C. M. van Vliet, and P. H. Handel. *Phys. Status Solidi A*, 70:287, 1982.

[11] B. Raquet. *J. Magn. Magn. Mater.*, 258-259:119, 2003.

[12] W. E. Purcell. *J. Appl. Phys.*, 43:2890, 1972.

[13] U. J. Strasilla and M. J. O. Strutt. *J. Appl. Phys.*, 45:1423, 1974.

[14] R. F. Voss. *Phys. Rev. Lett.*, 40:913, 1978.

[15] H. G. E. Beck and W. P. Spruit. *J. Appl. Phys.*, 49:3384, 1978.

[16] T. G. M. Kleinpenning and A. H. de Kuijper. *J. Appl. Phys.*, 63:43, 1987.

[17] M. B. Weissman. *Rev. Mod. Phys.*, 60:537, 1988.

[18] P. J. Restle, M. B. Weissman, and R. D. Black. *J. Appl. Phys.*, 54:5844, 1983.

[19] G. A. Garfunkel, G. B. Alers, and M. B. Weissman. *Phys. Rev. B*, 41:4901, 1990.

[20] K. M. Abkemeier. *Phys. Rev. B*, 55:7005, 1997.

[21] P. J. Restle, R. J. Hamilton, M. B. Weissman, and M. S. Love. *Phys. Rev. B*, 31:2254, 1985.

[22] P. J. Restle, M. B. Weissman, G. A. Garfunkel, P. Pearah, and H. Morkoç. *Phys. Rev. B*, 34:4419, 1986.

[23] B. D. Nevins and M. B. Weissman. *Phys. Rev. B*, 41:1301, 1990.

[24] G. B. Alers, S. Martin, R. A. Hamm, A. Feygenson, and R. D. Yadvish. *Appl. Phys. Lett.*, 66:198, 1995.

[25] J. R. Petta, T. Ladd, and M. B. Weissman. *IEEE Trans. Magn.*, 36:2057, 2000.

[26] M. Tondra, J. M. Daughton, D. X. Wang, R. S. Beech, A. Fink, and J. A. Taylor. *J. Appl. Phys.*, 83:6688, 1998.

[27] Y. Lu, R. A. Altman, A. Marley, S. A. Rishton, P. L. Trouilloud, G. Xiao, W. J. Gallagher, and S. S. P. Parkin. *Appl. Phys. Lett.*, 70:2610, 1997.

[28] W. Yi, R. E. Jones, and M. H. Kryder. *J. Appl. Phys.*, 81:4918, 1997.

[29] G. N. Phillips, M. Eisenberg, N. Persat, E. A. Draaisma, L. Abelmann, and J. C. Lodder. *Sens. Actuators, A*, 91:34, 2001.

[30] M. Pannetier, C. Fermon, G. Le Goff, J. Simola, and E. Kerr. *Science*, 304:1648, 2004.

[31] M. Pannetier, C. Fermon, G. Le Goff, J. Simola, E. Kerr, and J. M. D. Coey. *J. Magn. Magn. Mater.*, 290-291:1158, 2005.

[32] C. Fermon, M. Pannetier-Lecoeur, N. Biziere, and B. Cousin. *Sens. Actuators, A*, 129:203, 2006.

[33] R. J. M. van de Veerdonk, P. J. L. Beliën, K. M. Schep, J. C. S. Kools, M. C. de Nooijer, M. A. M. Gijs, R. Coehoom, and W. J. M. de Jonge. *J. Appl. Phys.*, 82:6152, 1997.

[34] E. W. Hill. *IEEE Trans. Magn.*, 36:2785, 2000.

[35] E. W. Hill and A. F. Nor. *IEEE Trans. Magn.*, 37:2031, 2001.

[36] U. Rüdiger, J. Yu, S. Zhang, A. D. Kent, and S. S. P. Parkin. *Phys. Rev. Lett.*, 80:5639, 1998.

[37] Y. P. Zhao, R. M. Gamache, G. C. Wang, T. M. Lu, G. Palasantzas, and J. Th. M. De Hosson. *J. Appl. Phys.*, 89:1325, 2001.

[38] C. Yu, S. F. Lee, Y. D. Yao, Y. R. Ma, J. L. Tsai, and C. R. Chang. *MIcrosc. Microanal.*, 8:1370, 2002.

[39] J. W. Freeland, K. Bussmann, and Y. U. Idzerda. *Appl. Phys. Lett.*, 76:2603, 2000.

[40] Y. C. Wang, J. Ding, J. B. Yi, B. H. Liu, T. Yu, and Z. X. Shen. *J. Magn. Magn. Mater.*, 282:211, 2004.

[41] W. F. Egelhoff Jr., P. W. T. Pong, J. Unguris, R. D. McMichael, E. R. Nowak, A. S. Edelstein, J. E. Burnette, and G. A. Fischer. *Sens. Actuators, A*, in press.

[42] E. R. Nowak. pirvate communications.

Chapter 6

Electrochemical Noise Analysis of Hydrogen Bubble Evolution on Platinum Cathode

In this chapter, we utilise the above developed low frequency noise measurement technique to investigate the magnetic field effect on an electrochemical system, hydrogen evolution reaction during water electrolysis.

6.1 Introduction

Magnetoelectrochemistry is a multidisciplinary research field consisting of two distinct aspects. One is to use electrodeposition and related microfabrication techniques to fabricate magnetic thin films [1, 2, 3], multilayers [4, 5, 6], nanowires [7, 8, 9], and devices [10, 11, 12]. The other is to use magnetic fields to modify the electrochemical process occurring in an electrochemical cell.

In this respect, magnetic fields often show unexpected influences on elec-

trochemical processes. Many of the effects are traceable to the action of the Lorentz force on mass transport [13, 14]. Strong magnetic field gradients may also play a role when there are paramagnetic species in solution [15]. Evidence for an influence of magnetic field on reaction kinetics is more scattered and controversial [16, 17, 18, 19].

There are reports of magnetic field modification of cyclic voltammograms at high overpotentials, where hydrogen is liberated at the cathode from an aqueous electrolyte. In the case of copper in acidified copper sulphate, for example, the hydrogen current increased with applied field for overpotentials between -0.8 mV and -1.5 V with respect to a Ag/AgCl reference electrode, but decreased at higher overpotentials [20]. In some more recent experiments, Koza et al [21] and Krause et al [22] also showed that desorption of hydrogen is enhanced in a perpendicular magnetic field during both iron and cobalt deposition.

Electrochemical noise analysis [23, 24, 25, 26, 27] provides a quantitative overview of the electrolytic gas-evolution process. A cell operating galvanostatically will exhibit potential fluctuations over a wide range of frequency due to the time-varying occlusion of part of the cathode surface by growing gas bubbles, with consequent fluctuations in the concentration of dissolved gas and electrolyte impedance.

Gas-evolving electrodes are widely used in electrochemical processes [28, 29], among which the hydrogen evolution reaction during electrolysis of water attracts great attention [30, 31, 32]. It is the main industrial process for producing hydrogen using hydropower, wind turbines, or sunlight as green energy [33], and also the side reaction in chlorine production. In many electrodeposition processes carried out in aqueous solution, hydrogen evolution is an unavoidable side reaction [34, 35]. Hence, it is worthwhile to

investigate how a magnetic field may be used to influence or control hydrogen gas evolution. Here with hydrogen evolution during water electrolysis as a model system, we investigate the applicability of electrochemical noise analysis as a quantitative method to characterize the magnetic field effect on electrochemical systems.

6.2 Materials and Methods

Following the original reports by Gabrielli et al [23, 24, 25, 26] in the absence of a magnetic field, we chose a simple electrochemical system with small platinum electrodes and an aqueous solution of 0.5 M Na_2SO_4 as the electrolyte. The working electrode and counter electrode were made of 0.5 mm diameter platinum wire sealed in glass tubes and polished[1]. Potentials are measured with respect to a Ag/AgCl reference electrode with saturated KCl. The experiments were carried out galvanostatically with a Solatron SI1280B electrochemical workstation. The polarity of the current follows the corrosion convention, in which a positive (negative) current is anodic (cathodic). Most data were collected at -10 mA, corresponding to a current density of -51 mA/mm^2. The high current density and small working electrode area were chosen to obtain significant fluctuations in the cathode potential. A large electromagnet with pole sizes 200 mm was used to apply up to 1.5 T magnetic field either parallel or perpendicular to the working electrode surface.

The noise spectra were determined by one of the following two methods.

a) The analog voltage output of the electrochemical unit was fed unfiltered via a 10:1 voltage divider to the input of a Hewlett Packard HP35660A

[1]Platinum electrodes used in this study were prepared by fellow PhD student Peter Dunne.

spectrum analyser. The spectra were captured in six or seven different frequency spans between 12.8 Hz and 12.8 kHz. Data were then assembled to give the power spectral densities. Spectra shown in this work are the averages of ten data sets.

b) The analog voltage output of the electrochemical unit was fed to a SR560 low noise preamplifier which was differentially input with a potentiometer and dry batteries. This was done to null the DC component of the signal, thereby reducing the digital noise level, while preserving the low-frequency part of the signal. This technique is better than using a high-pass filter, which significantly corrupts the low frequency spectrum. Data points were sampled at 100 kHz by a National Instruments PCI-6250 16-bit data acquisition (DAQ) card, whose A/D converter goes up to 1 MHz, for 10 minutes. The preamplifer also serves as an anti-aliasing filter in this set-up. The power spectral densities were then obtained using a discrete fourier transform programme written in LabView.

In Fig. 6.1, we show the schematic diagram of our measurement set-up.

6.3 Results and Discussion

We observed two different types of noise spectra in our experiments (Fig. 6.2), similar to those previously described by Gabrielli et al. [24].

This was explained by a model developed in the same work. They considered a sequence of time x_j, between two successive bubble departures. This sequence can be treated as a sequence of independent random variables with the same distribution function $u(x) = dP(x_j < x)/dx$, with $P(x_j < x)$ the possibility of finding x_j of a value less than x. For type I spectra, they assumed that the distribution function was exponential, $u(x) = \lambda exp(\lambda x)$,

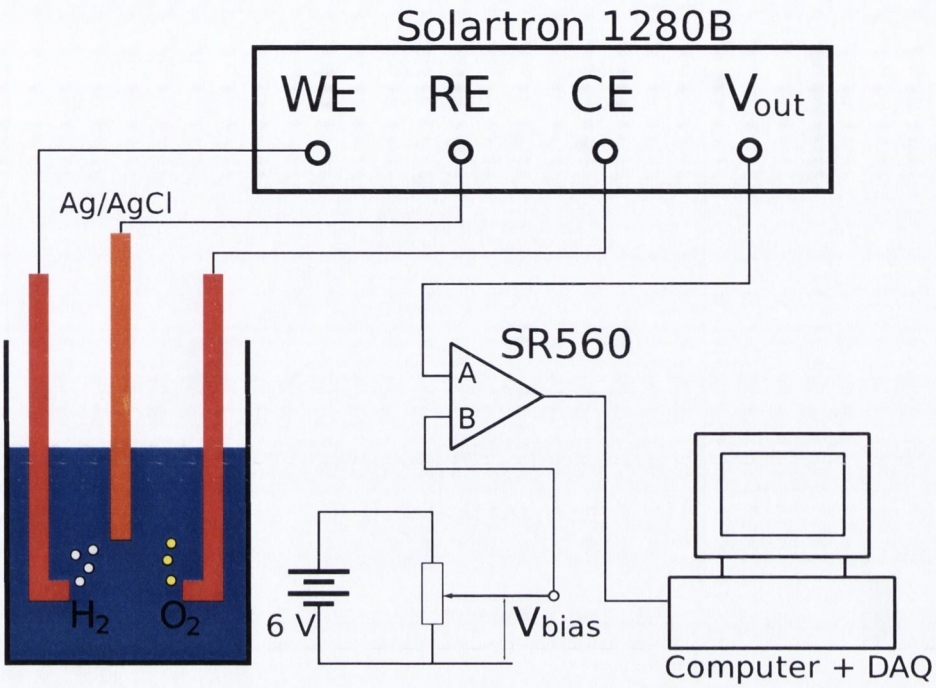


Fig. 6.1: Schematic diagram of the electrochemical noise analysis set-up.

with $1/\lambda$ the mean time between two consecutive jumps. It is characterized by the fact that there are more short time intervals than long time ones. The PSD of the potential fluctuations can be given by [24]

$$S_V(f) = \frac{2\lambda < \Delta\eta^2 >}{\lambda^2 + 4\pi^2 f^2} \tag{6.1}$$

with the mean value of the potential jump amplitude $< \Delta\eta >= k/\lambda$, in which k is the slope of the linear potential increase when a bubble grows. This is a Debye-Lorentzian spectrum which has a low frequency plateau and a high frequency decrease following $1/f^2$.

Type II spectra are modelled by a pseudoperiodical distribution func-

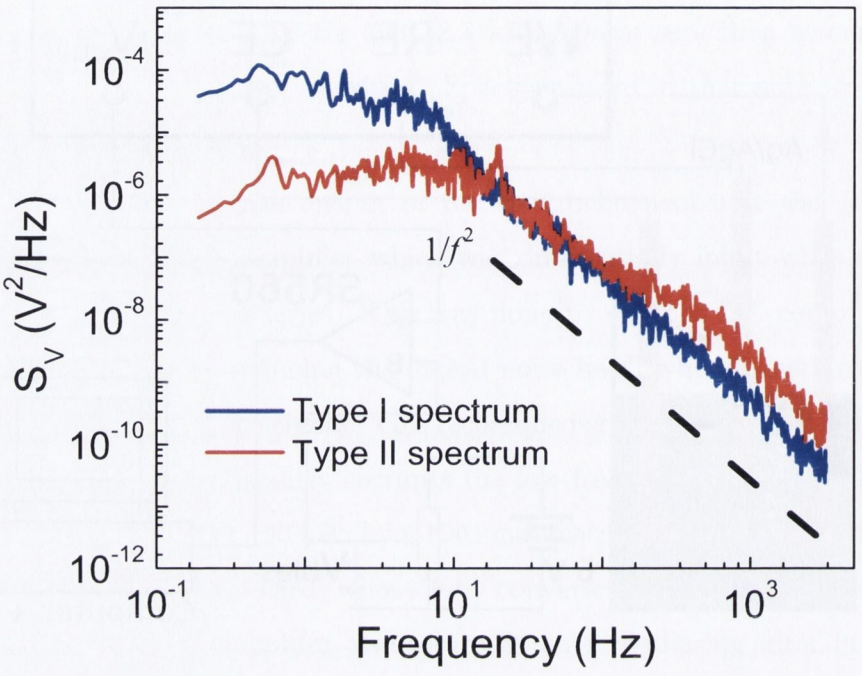


Fig. 6.2: Examples of noise spectra obtained using the spectrum analyser in the absence of an applied field. The black line shows the $1/f^2$ power spectrum.

tion.

$$u_1(x) = \frac{\nu}{2 - exp(-\nu x_0)} \exp(-\nu \mid x - x_0 \mid) \tag{6.2}$$

in which x_0 is the time pseudoperiod and ν in s^{-1} represents the pronounced character of this pseudoperiodicity. This is the case when the bubbles are released from the electrode surface in a quasi-periodic way. The PSD has a pronounced peak at f_p, above which the spectrum also decrease as $1/f^2$, but with several harmonics of f_p sitting on top of the $1/f^2$ slope. The peak frequency f_p is related to the average bubbles evolved per unit time $f_p = \lambda$.

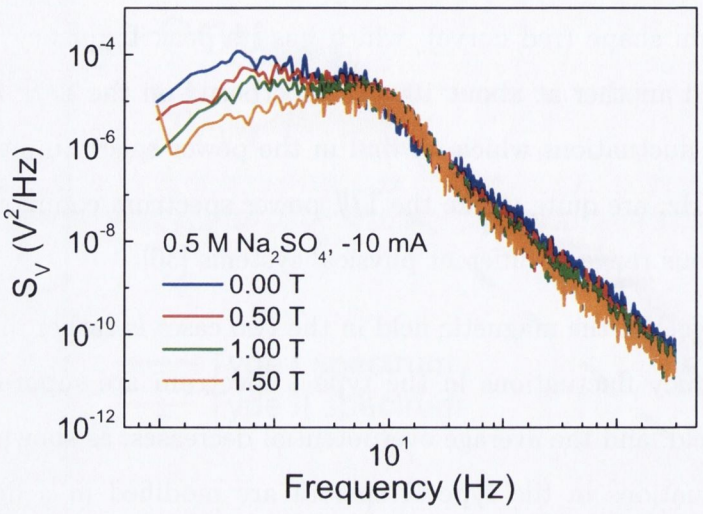
For the type I spectrum (blue curve), we observed a corner frequency

(above which the power spectral density falls in a nearly $1/f^2$ slope) of about 10 Hz, above which it falls according to $1/f^2$. More common is the type II spectrum shape (red curve), which has its peak frequency f_p at about 20 Hz, and another at about 100 Hz superposed on the $1/f^2$ background. The $1/f^2$ fluctuations which we find in the power spectrum at frequencies above 10 Hz, are quite unlike the $1/f$ power spectrum commonly found in an enormous range of different physical systems [36].

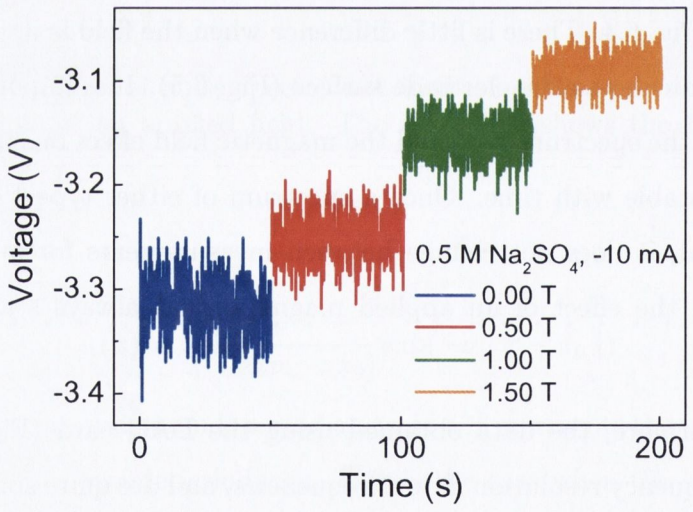
The effect of the magnetic field in the two cases is rather different. The low-frequency fluctuations in the type I spectrum are suppressed by the applied field, and the average overpotential decreases, as shown in Fig. 6.3. The fluctuations in the type II spectra are modified in a different way. Fields of up to 0.5 T have little effect. Then, in higher fields, there is a clear and rather abrupt increase in the low-frequency fluctuations, as shown in Fig. 6.4. There is little difference when the field is applied parallel or perpendicular to the electrode surface (Fig. 6.5). It is important to note that both the spectrum type and the magnetic field effect on each spectrum type are stable with time. Once a spectrum of either type I or type II is established, it does not change between measurements for at least a few days, and the effect of an applied magnetic field always stays the same (Fig. 6.6).

Furthermore, the data obtained using the DAQ card (Fig. 6.7) gives better frequency resolution at low frequencies, and are quite similar to those obtained with the spectrum analyser (Fig. 6.4). In Fig 6.8, we show the threshold effect of the applied field on the low frequency plateau (data average across 0.1 - 1 Hz) summarized from Fig. 6.7. The dashed red line is a guide to the eye.

Atomic hydrogen is the primary product of electrolysis at the platinum

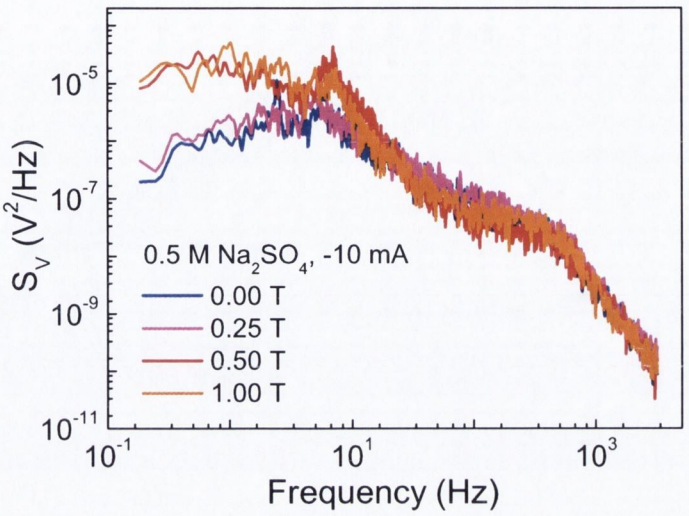


(a)

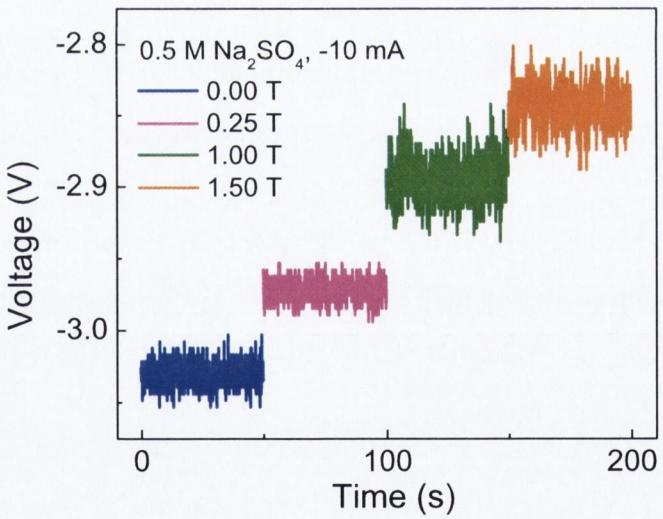


(b)

Fig. 6.3: (a) Power spectral density of type I spectra and (b) corresponding time sequence under applied magnetic field. Note how the amplitude of the voltage fluctuations and the overpotential decrease with applied field.



(a)



(b)

Fig. 6.4: (a) Power spectral density of type II spectra and (b) corresponding time sequence (b) under applied magnetic field. Note that how the noise amplitude increases above a threshold field < 1 T.

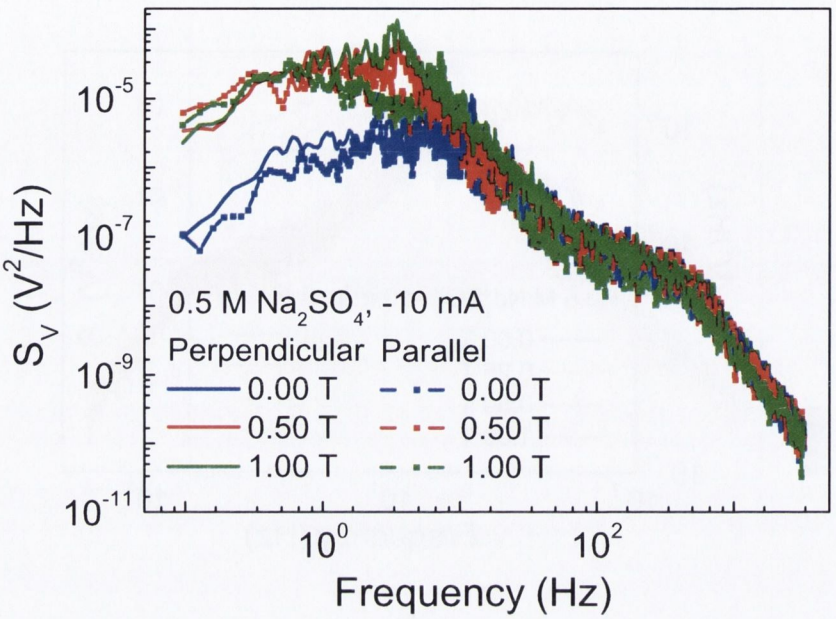


Fig. 6.5: Power spectral density of type II spectra measured with the applied magnetic field parallel and perpendicular to the electrochemical current.

cathode surface. Schematically, it diffuses across the surface or enters solution to form molecular hydrogen H_2. The surface concentration of a dissolved gas can be estimated from the concentration-related overpotential η_{cs} at the electrode interface

$$C_g = C_{sg}\exp[-(\frac{nF}{RT})\eta_{cs}] \tag{6.3}$$

with n the number of electrons participating in the electrode reaction, R the universal gas constant, F the Faraday constant equal to 96,487 C mol^{-1}, η_{cs} the concentration overpotential due to the product gas supersaturating the electrolyte near the electrode surface, and C_{sg} the saturated concentration of

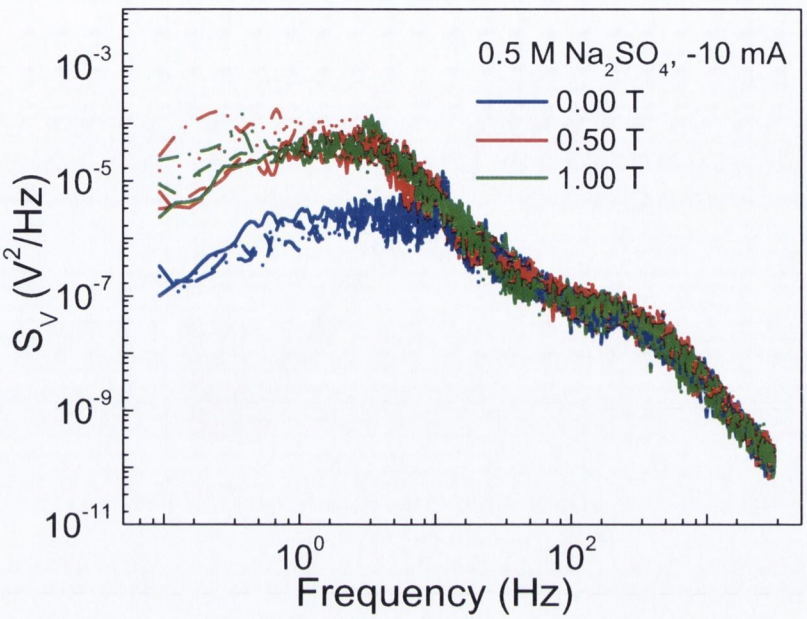


Fig. 6.6: Power spectral density of type II spectra measured within 3 days. For each applied magnetic field level, 4 spectra were recorded at different times, twice on the 1st day (straight line and dashed line), once the 2nd day (dotted line) and once the 3rd day (dashed dotted line), respectively. The spectra, and the magnetic field effect are stable and reproducible in time.

dissolved gas at 273 K and under 1 atm gas pressure [37]. For hydrogen gas, this value is $C_{sg} = 7.24 \times 10^{-4}$ mol/L [38]. At the high current densities used in our experiments (-51 mA/mm^2), the electrolyte has reached its limiting supersaturation in molecular hydrogen, which is about 100 times greater than C_{sg}. Eventually, gas nuclei will form spontaneously at some nucleation sites on the surface of the platinum cathode, where they begin to grow and coalesce. More H_2 gas diffuses into the bubble from the surrounding electrolyte, and H_2 formed at the platinum surface also diffuses into the growing bubble.

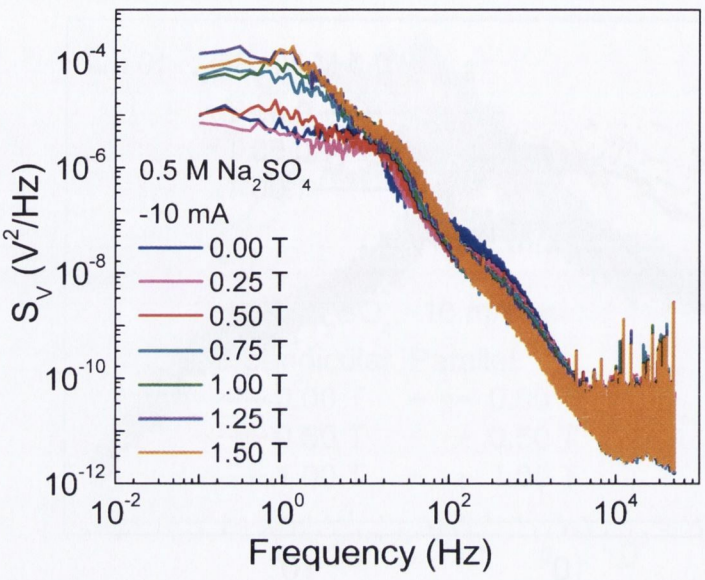


Fig. 6.7: Magnetic field effect on the type II spectra measured by a DAQ board.

We relate our experimentally observed $1/f^2$ noise spectrum to a growth-coalescence model suggested by Steyer et al. [39]. Unlike Gabrielli et al. [24], the authors consider the growth of spherical droplets randomly seeded on a two dimensional surface growing as $R(t) = R_0 t^{\alpha}$, with R the radius of the droplet, and R_0 its initial value. They obtained a surface coverage function changing against time t which is very similar to the time sequence of overpotential fluctuation we observed (Fig. 6.9). The PSD in their model was shown to have a linear $1/f^2$ dependence down to the lowest frequency. We attribute the difference between the spectra we observed and their model — the existence of a low frequency plateau in our case, to the fact that hydrogen bubbles leave the electrode surface in a real experiment, while only the growth of the droplets was considered in their model. They also show that the $1/f^2$ spectrum is a direct result of the growth-coalescence

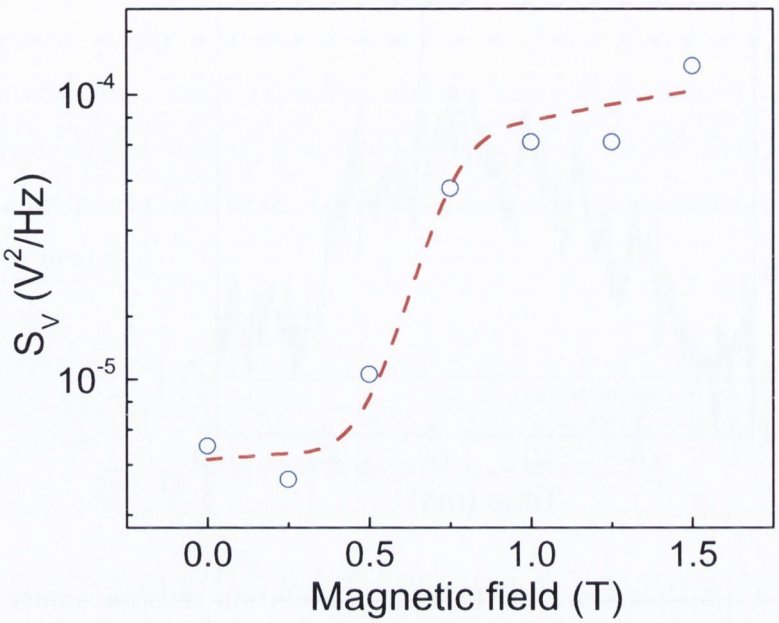


Fig. 6.8: The threshold effect of the applied magnetic field on the low frequency plateau of type II spectrum. Each data point is averaged across the PSD in Fig. 6.7 between 0.1 Hz and 1 Hz. The dashed red line is a guide to the eyes.

process and does not depend on the growth exponent α.

The potential of the gas-evolving working electrode can be expressed by

$$E_w = E_{IR} + \eta_s + \eta_{ci} + \eta_{cs} \tag{6.4}$$

in which E_{IR} is the potential drop due to the ohmic resistance between the working and the reference electrodes, which can be modified by bubbles covering the working electrode surface, η_s is the surface overpotential for charge transfer reaction, η_{ci} is the concentration overpotential created by the consuming of reactive ions, and η_{cs} is the same surface concentration-related overpotential as in Eqn. (6.3) [40]. The second term in Eq. (6.4) η_s,

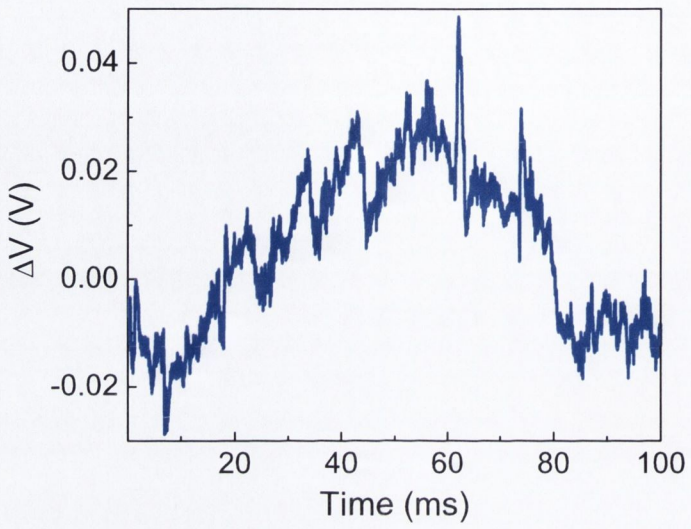


Fig. 6.9: A time sequence of the bubble evolution reaction under zero magnetic field. Applied current is -10 mA.

is a kinetic term and can be decomposed into two terms, η_{s0} and η_a, with the first term representing the surface overpotential when no bubble is present on the electrode surface, and the second term corresponds to a secondary current distribution effect around the bubbles when they form. The value of η_a has been estimated to be small in many gas-evolving electrochemical reactions [40, 38].

Under the present experimental conditions (high current density), a local pH increase close to the cathode surface is expected. This effect induces a possible change of the third term η_{ci} in Eq. (6.4), and shifts the overpotential. It may also happen that the agitation due to the Lorentz force when a magnetic field is applied will increase the mixing with the bulk solution, and contribute partly to the overpotential decrease we observed. However, this effect is normally believed to be less significant [40] and is omitted in magnetoelectrochemistry studies [38].

This leaves us with the first term E_{IR} and the fourth term η_{cs} in the equation. In the following discussions, we first consider the effect of the first term, since several previous studies have suggested that under a large applied current density, it is the dominant effect [24, 41, 37]. We then add the fourth term back at the end of the discussion, to see how it might change in our analysis.

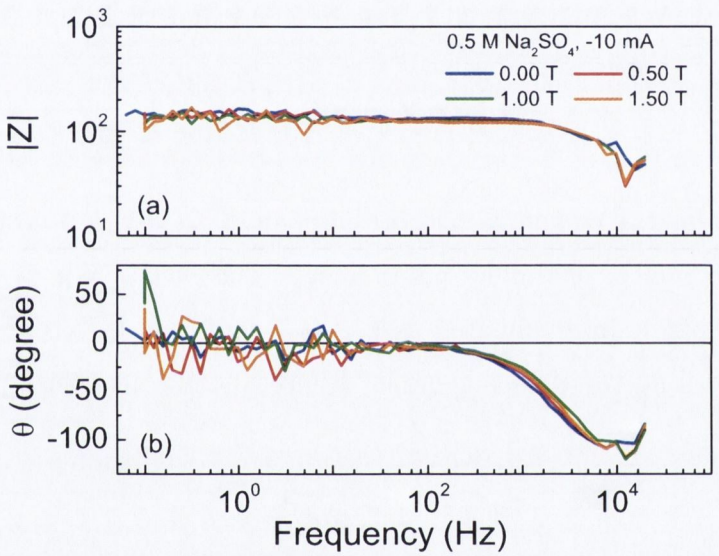


Fig. 6.10: Electrochemical impedance spectra of 0.5 M Na_2SO_4 under different applied magnetic fields. The applied current is -10 mA.

We first try to exclude two possible spurious effects which might influence the observed spectra under magnetic field. The first one is the change of the complex electrochemical impedance under an applied magnetic field. We used electrochemical impedance spectroscopy to further characterize our electrochemical system (Fig. 6.10). Although the low frequency parts of the spectra are normally noisy due to the creation and departure of hydrogen bubbles, there is very little change either in the absolute value of the so-

lution impedance $\mid Z \mid$ or the phase angle θ up to at least a few thousand Hertz. Hence, we are confident that the alteration of the electrochemical noise spectra under magnetic fields, especially the change of the low frequency plateau, is not related to an impedance change of the system. The second consideration is the influence of the Zeeman energy under an applied magnetic field. Normally any magnetic field effects on chemical reactions are negligible because the tiny energy involved. For paramagnetic ions, their magnetization is proportional to the applied magnetic field.

$$\boldsymbol{M} = \chi \cdot \boldsymbol{H} = \frac{C}{T}\boldsymbol{H} \tag{6.5}$$

in which χ is the magnetic susceptibility, and C is the Curie constant. The Curie constant of one molar paramagnetic ions, each having one unpaired electron can be approximated as $(N_A/k_B)\mu_0\mu_B^2$, with N_A the Avogadro's number and μ_B the Bohr magneton. Hence, the magnetic susceptibility can be expressed as

$$\chi = \frac{N_A\mu_0\mu_B^2}{k_BT} \tag{6.6}$$

The magnetic energy is $E_B = -(1/2)MB = -\chi B^2/2\mu_0$, where B is the applied field [42]. Using Eqn. (6.6) for χ, we have

$$E_B = \frac{1}{2}N_A\mu_B^2B^2/k_BT \tag{6.7}$$

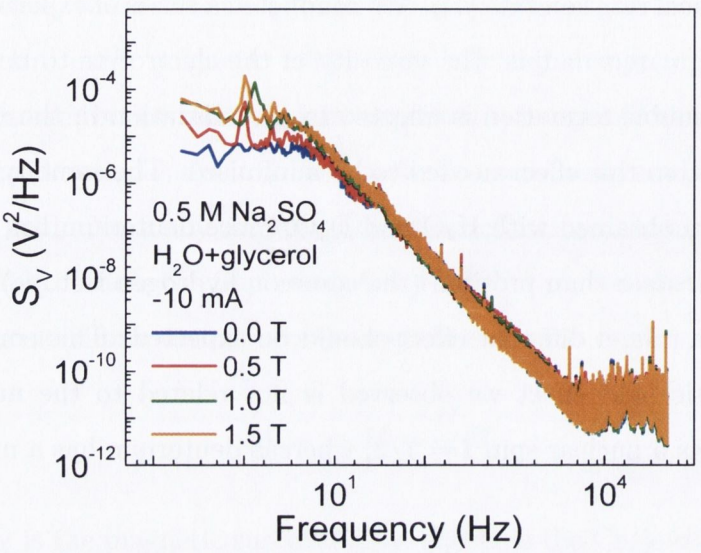
This leads to an energy of only 6.25 mJ/mol at 300 K, while the energy required to move one mole electrons across a potential difference of 1 V is more than 6×10^4 J. However, in some circumstances, large magnetic field effects on some chemical reactions can be traced back to the nuclear spins [43]. It is conceivable that the coupling of the nuclear spins in the hydrogen

molecules to the nearby paramagnetic moment (Pt) might induce a change of the chemical reaction rate [44]. We conducted a series of experiments with D_2O, taking care to adjust the viscosity of the electrolyte to be the same. Hydrogen bubble formation is affected by any variation in the viscosity of the solution, so this effect needed to be minimised. The same type II noise spectra were obtained with H_2O and D_2O. Since deuterium has a different nuclear spin state than protium (the common hydrogen isotope), if nuclear spins play a role, a different effect should be expected. This confirms that the magnetic field effect we observed is not related to the nuclear spin (protium has a nuclear spin $I = 1/2$, whereas deuterium has a nuclear spin $I = 1$).

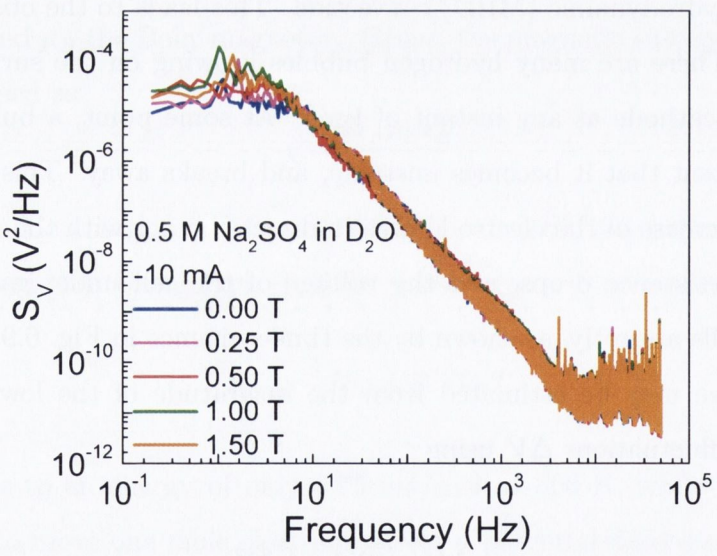
With the above two possible explanations excluded, we attribute the observed magnetic field effect a change in hydrogen bubble size due to the magnetohydrodynamic (MHD) convection. This leads to the observed E_{IR} change. There are many hydrogen bubbles growing on the surface of the platinum cathode at any instant of time. At some point, a bubble grows to the extent that it becomes unstable, and breaks away. This leads to a sudden increase of the electrode area in direct contact with the electrolyte; the cell resistance drops, and the voltage of the cell under galvanostatic control falls abruptly, as shown by the time-sequence in Fig. 6.9. A typical bubble size may be estimated from the magnitude of the low frequency potential fluctuations ΔV using

$$\Delta V = R_e I \alpha_e (\frac{r_d}{r_e})^2 \tag{6.8}$$

where $R_e I$ is the average overpotential (~ 3.1 V), α_e is a numerical constant equal to 0.4 and r_d/r_e is the ratio of the bubble radius to the cathode radius (250 μm) [24]. The result is around 40 μm, which is consistent with



(a)



(b)

Fig. 6.11: Power spectra of hydrogen and deuteron evolution in H_2O and D_2O under applied magnetic field.

the bubble size seen by visual inspection.

The observed influences of magnetic fields on the voltage noise fluctuations can be understood in the framework of mechanical agitation created by the Lorentz force

$$\boldsymbol{F}_L = \boldsymbol{j} \times \boldsymbol{B} \tag{6.9}$$

Here $\boldsymbol{j}$ is the current density and $\boldsymbol{B}$ is the magnetic field. The current lines around a bubble on the surface will tend to have a radial as well as a transverse component. A torque is therefore exerted on the bubble which is proportional to the product of $\boldsymbol{B}_\perp$ and $\boldsymbol{j}_r$, where $\boldsymbol{B}_\perp$ is the component field normal to the electrode surface and $\boldsymbol{j}_r$ is the radial component of the current density around the bubble. This twist-off effect is expected to contribute to the premature departure of gas bubbles, when the field has a component normal to the electrode surface [21]. Normally the mechanical effect of the Lorentz force, whether it is to sweep the surface or apply torque to the bubbles, will tend to dislodge the bubbles sooner than would otherwise be the case. The average bubble size should be reduced by the field, and potential fluctuations reduced correspondingly. The data in Fig. 6.3 show a progressive reduction in the amplitude of the low-frequency fluctuations and a decrease in overpotential with applied field for type I spectra. Estimating the size of the larger bubbles from the low-frequency potential fluctuations using Eqn. (6.8) gives that the size of the large bubbles in the plateau below 10 Hz is reduced progressively as a function of field, from 46 μm in 0 T to 36 μm in 1.5 T. This corresponds to a halving of the bubble volume.

However, there may be a secondary effect of sweeping bubbles across the cathode. During growth, small bubbles nucleated at adjacent spots tend to coalesce. When they are swept across the cathode surface by the

Lorentz-force-induced flow, they will tend to coalesce with other bubbles they encounter, and grow larger before they are released. The more characteristic type II behaviour illustrated in Fig. 6.4 and Fig. 6.7 shows this effect. There the low-frequency fluctuations increase with field, beyond a threshold of 0.5 T. The average bubble radius deduced from Eqn. (6.8) at 10 Hz increases by about a factor 1.5 from 0 T to 1.5 T. The edge of the electrode is where largest bubbles are likely to be found, and the small ones tend to merge with the larger ones growing there, leaving a larger voltage drop when they are released. This can probably also explain why we observe two different types of spectra in the study. The edges of micro-polished Pt electrodes are normally less well controlled than the centre area. A rough edge might be able to accommodate more large bubbles, which enhance the low frequency fluctuation. The reason of this correlation between spectra type and magnetic field effect still requires further investigation.

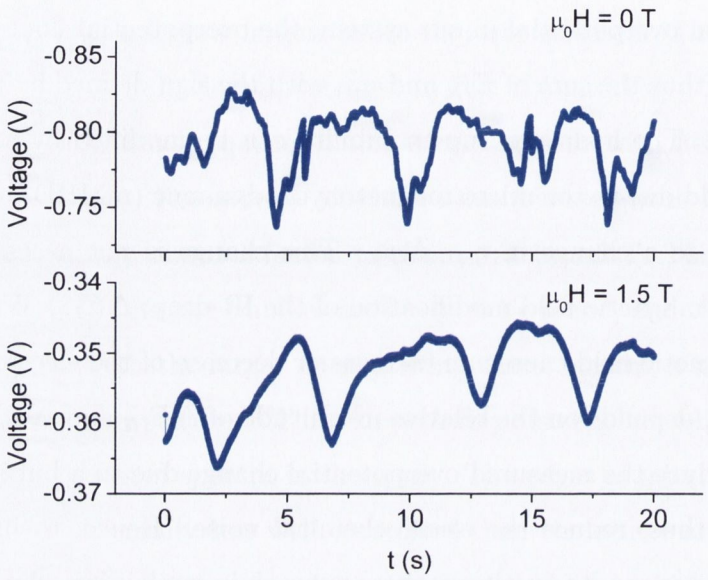
Now we look at the influence of the fourth term in Eqn. (6.4), η_{cs} on the overpotential fluctuation. It was first predicted by Dukovic and Tobias [45], then experimentally verified by Gabrielli and co-workers [37] that the supersaturation effect η_{cs} associated with bubble evolution has an opposite sign to the resistance change E_{IR}. This can be understood in the following way. The growth of bubbles is mainly due to the diffusion of dissolved hydrogen gas from the surrounding electrolyte. Hence, the concentration of dissolved hydrogen gas is lower around the bubbles than further away. This effect will locally lower the concentration overpotential and attract current lines to the regions where bubbles are attached, which is the exact opposite to the IR-drop E_{IR}. As we have seen above, the dominant effect under our high current density, is highly likely to be the IR-drop. However, inclusion of the fourth term in Eqn. (6.4) makes it possible to see the two types of spectra

in a different light. Assuming the existence of a smaller but comparable concentration overpotential in our system, the overpotential fluctuation we measured is thus the sum of E_{IR} and η_{cs}, with the sign defined by the larger term – E_{IR}. The hydrogen supersolubility can be modified by an applied magnetic field due to the micro magnetohydrodynamic (mMHD) effect [38], which leads to a change in η_{cs}, $\Delta\eta_{cs}$. This change is not necessarily the same as the magnetic field modification of the IR-drop, ΔE_{IR}. Whether an applied magnetic field causes an increase or decrease of the electrochemical noise power, depends on the relative magnitude of ΔE_{IR} and $\Delta\eta_{cs}$. A large $\Delta\eta_{cs}$ can reduce the measured overpotential change due to a bubble departure event, thus, reduce the electrochemical noise. Hence, to include η_{cs} into the picture can be an alternative approach in explaining why magnetic field has different effects on different type of spectra.

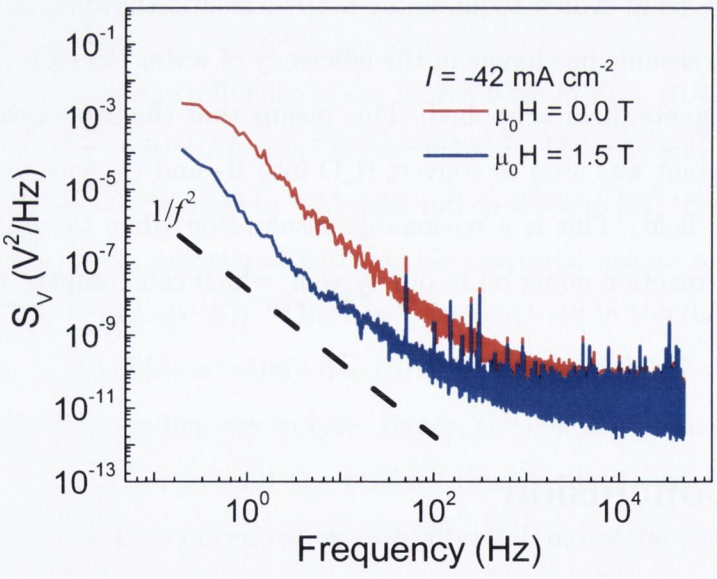
Another point which requires further clarification is that in the above analysis we assume no change in the efficiency of water electrolysis reaction when a magnetic field is applied. This means that the same proportion of applied current was used to convert H_2O into H_2 and O_2 with and without a magnetic field. This is a reasonable assumption when there is no other major side reaction going on in our system, which can compete with water electrolysis.

6.4 Conclusion

The influence of the magnetic field on hydrogen production at a small platinum electrode is understood in terms of the influence of the Lorentz force on the size distribution of the bubbles produced. The $1/f^2$ power spectrum above 10 Hz is typical of a droplet coalescence process. The field



(a)



(b)

Fig. 6.12: Time sequences and power spectra of hydrogen evolution during copper electrodeposition under zero and 1.5 T applied magnetic field.

deceases the overpotential for hydrogen formation by 10 % for 1.5 T, similar to that expected by mechanical agitation. Depending on the type of noise spectrum, the Lorentz force generated by the magnetic field can either increase or decrease the low frequency hydrogen evolution noise below 10 Hz, but the reason for the correlation is not understood. An improved measurement scheme, which uses a high frequency sinusoidal signal to directly probe the electrolyte resistance, has been suggested by Gabrielli and co-workers [37], but no magnetic field has yet been applied.

The study shows that electrochemical noise analysis is a useful supplementary tool in characterizing the magnetic field effect on gas evolution electrochemical analysis. More quantitative results are expected from this analysis compared to conventional methods which are mainly based on cyclic voltammetry [20]. Fig. 6.12 shows time sequences and power spectrum density of hydrogen evolution during electrodeposition of copper under a constant current density of -42 mA/cm^2 [46]. The electrodes used were 0.5 mm diameter copper. Large steps due to the departure of hydrogen bubbles from the working electrode is clearly seen. An applied magnetic field of 1.5 T significantly alters the hydrogen evolution process, as shown both from the time sequence and the power spectra. The average bubble size decreases from 0.9 mm in diameter to 0.5 mm, according to an analysis similar to that in the above section. This suggests that this technique may also be used to study hydrogen evolution as competing side reaction during metal electrodeposition.

References

[1] T. Osaka, M. Takai, K. Hayashi, K. Ohashi, M. Saito, and K. Yamada. *Nature*, 392:796, 1998.

[2] X. Xu and G. Zangari. *J. Electrochem. Soc.*, 155:D742, 2008.

[3] F. M. F. Rhen, G. Hinds, C. O'Reilly, and J. M. D. Coey. *IEEE Trans. Magn.*, 39:2699, 2003.

[4] S. K. J. Lenczowski, C. Schönenberger, M. A. M. Gijs, and W. J. M. de Jonge. *J. Magn. Magn. Mater.*, 148:455, 1995.

[5] Y. Jyoko and W. Schwarzacher. *Electrochim. Acta*, 47:371, 2001.

[6] Q. X. Liu, L. Péter, J. Tóth, L. F. Kiss, Á. Cziráki, and I. Bakonyi. *J. Magn. Magn. Mater.*, 280:60, 2004.

[7] A. Fert and L. Piraux. *J. Magn. Magn. Mater.*, 200:338, 1999.

[8] L. Sun, Y. Hao, C. L. Chien, and P. C. Searson. *IBM J. Res. Dev.*, 49:79, 2005.

[9] M. Abid, J. P. Abid, S. Jannin, S. Serrano-Guisan, I. Palaci, and J. Ph. Ansermet. *J. Phys.: Condens. Matter*, 18:6085, 2006.

[10] B. Doudin, G. Redmond, S. E. Gilbert, and J. Ph. Ansermet. *Phys. Rev. Lett.*, 79:933, 1997.

[11] H. Wang, Y. Wu, M. Wang, Y. Zhang, G. Li, and L. Zhang. *Nanotech.*, page 1651, 2006.

[12] C. S. Yang, C. Zhang, J. Redepenning, and B. Doudin. *Appl. Phys. Lett.*, 84:2865, 2004.

[13] R. Aogaki, K. Fueki, and T. Mukaibo. *Denki Kagaku*, 43:509, 1975.

[14] F. M. F. Rhen, G. Hinds, and J. M. D. Coey. *Electrochem. Commun.*, 6:413, 2004.

[15] A. Sugiyama, H. Makoto, R. Morimoto, Y. Nagai, and R. Aogaki. *Electrochim. Acta*, 49:5115, 2004.

[16] T. Weier, K. Eckert, S. Mühlenhoff, C. Cierpka, A. Bund, and M. Uhlemann. *Electrochem. Commun.*, 9:2479, 2007.

[17] M. Waskaas. *J. Phys. Chem. B*, 97:6470, 1993.

[18] J. M. D. Coey. *Europhys. News*, 36:246, 2003.

[19] S. Legeal, M. Chatelut, O. Vittori, J. P. Choppart, and O. Aaboubi. *Electrochim. Acta*, 50:51, 2004.

[20] G. Hinds, F. E. Spada, J. M. D. Coey, T. R. Ní Mhíocháin, and M. E. G. Lyons. *J. Phys. Chem. B*, 105:9487, 2001.

[21] J. A. Koza, M. Uhlemann, A. Gebert, and L. Schultz. *Electrochem. Commun.*, 10:1330, 2008.

[22] A. Krause, M. Uhlemann, A. Gebert, and L. Schultz. *Electrochim. Acta*, 49:4127, 2004.

[23] C. Gabrielli, F. Huet, and M. Keddam. *J. Appl. Electrochem.*, 15:503, 1985.

[24] C. Gabrielli, F. Huet, M. Keddam, and A. Sahar. *J. Appl. Electrochem.*, 19:683, 1989.

[25] C. Gabrielli, F. Huet, and M. Keddam. *J. Electrochem. Soc.*, 138:L82, 1991.

[26] A. Benzaïd, F. Huet, M. Jérôme, F. Wenger, C. Gabrielli, and J. Galland. *Electrochim. Acta*, 47:4315, 2002.

[27] A. Berradja, D. Déforge, R. P. Nogueira, P. Ponthiaux, F. Wenger, and J. P. Celis. *J. Phys. D: Appl. Phys.*, 39:3184, 2006.

[28] M. P. M. G. Weijs, L. J. J. Janssen, and G. J. Visser. *J. Appl. Electrochem.*, 27:371, 1997.

[29] S. A. Guelcher, Y. E. Solomentsev P. J. Sides, and J. L. Anderson. *J. Electrochem. Soc.*, 145:1848, 1998.

[30] H. Cheng, K. Scott, and C. Ramshaw. *J. Electrochem. Soc.*, 149:D172, 2002.

[31] H. Matsushima, T. Nishida, Y. Konishi, Y. Fukunaka, Y. Ito, and K. Kuribayashi. *Electrochim. Acta*, 48:4119, 2003.

[32] T. Iida, H. Matsushima, and Y. Fukunaka. *J. Electrochem. Soc.*, 154:E112, 2007.

[33] G. W. Crabtree, M. S. Dresselhaus, and M. V. Buchanan. *Phys. Today*, 57:39, 1004.

[34] N. D. Nikolić, K. I Popov, Lj. J. Pavlović, and M. G. Pavlović. *J. Electroanal. Chem.*, 588:88, 2006.

[35] J. A. Koza, S. Mühlenhoff, M. Uhlemann, K. Eckert, A. Gebert, and L. Schultz. *Electrochem. Commun.*, 11:425, 2009.

[36] M. B. Weissman. *Rev. Mod. Phys.*, 60:537, 1988.

[37] C. Gabrielli, F. Huet, and R. P. Nogueira. *Electrochim. Acta*, 50:3726, 2005.

[38] H. Matsushima, D. Kiuchi, and Y. Fukunaka. *Electrochim. Acta*, 54:5858, 2009.

[39] A. Steyer, P. Guenoun, and D. Beysens. *Phys. Rev. Lett.*, 68:1869, 1992.

[40] J. A. Leistra and P. J. Sides. *J. Electrochem. Soc.*, 134:2442, 1987.

[41] C. Gabrielli, F. Huet, M. Keddam, A. Macias, and A. Sahar. *J. Appl. Electrochem.*, 19:617, 1989.

[42] G. Hinds, F. M. F. Rhen, and J. M. D. Coey. *IEEE Trans. Magn.*, 38:3216, 2002.

[43] N. J. Turro. *Proc. Natl. Acad. Sci. USA*, 80:609, 1983.

[44] M. Matsumoto and J. H. Espenson. *J. Am. Chem. Soc.*, 127:11447, 2005.

[45] J. Dukovic and C. W. Tobias. *J. Electrochem. Soc.*, 134:331, 1987.

[46] D. Fernández, P. A. Dunne, Z. Diao, and J.M.D. Coey. unpublished.

Chapter 7

Future Work

In this thesis, low frequency fluctuations in three different magnetic systems were investigated. Some possible extensions of the work described in Chapter 4 and 5 are now discussed.

A very natural but highly challenging extension of the work in Chapter 4 is to extend the method to the nanoscale, by patterning smaller Hall bars. This leads to the chance of capturing very few, or even a single domain wall in the Hall cross, and probe the resulting fluctuation. One very obvious obstacle is the increase of lead resistance R_l, which significantly enhances the thermal noise background. However, it is possible to overcome this problem by patterning high conductive contacts to a small Hall cross, or measuring the sample at low temperature (as the thermal noise scales with temperature). The temperature dependence of the low frequency anomalous Hall voltage forms another possible extension of the present work. As expected from our domain wall fluctuation picture, the change of temperature should be able to move fluctuators in or out-of the measurement frequency window, thus reduce or enhance the $1/f$ noise in the slanted part of the hysteresis loop. The verification of this prediction will give strong support to our pro-

posal, in which the $1/f$ noise is generated by a thermally activated process. Concerning the in-plane magnetization component, a systematic measurement of the planar Hall effect and the anisotropic magnetoresistance in the $(CoFe/Pt)_n$ multilayers is a good starting point.

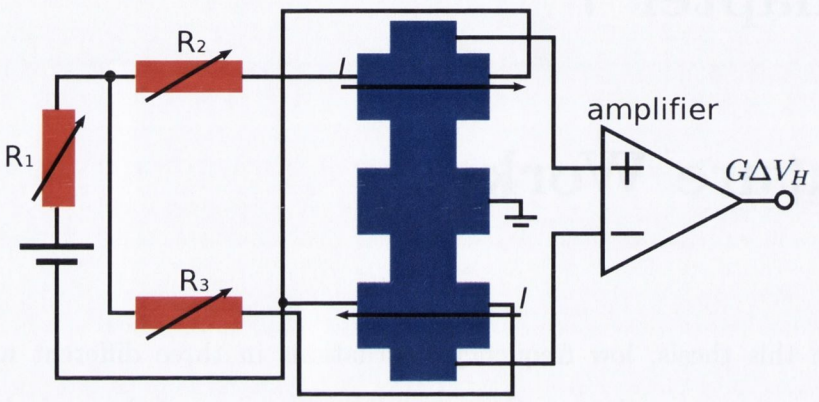


Fig. 7.1: A diagram showing the seven-terminal Hall noise measurement method.

The measurement scheme can also be improved by adopting the seven-terminal Hall noise measurement method first suggested by von Molnár and co-workers [1, 2, 3]. Fig. 7.1 shows a diagram of this approach. It involves passing two currents with the same amplitude but in different directions, through two Hall crosses forming a Hall resistance bridge. This leads to a zero output of the sample Hall voltage, $V_{H1} + V_{H2} = 0$. The bridge is insensitive to spatially correlated fluctuations, such as temperature drift or noise pick-up from applied magnetic fields. An additional Hall cross is patterned in between the bridge for the common ground, this helps to reduce the requirement on the common mode rejection ratio for the amplifiers. It is also possible to connect a buffer amplifier between the common ground and one of the Hall voltage leads for monitoring the Hall voltage during the noise measurement.

In relation to the FORC diagrams, more theoretical work is required to achieve a better interpretation of the large amount of information they contain. One possible protocol will be to simulate the FORC diagrams with the two sets of hysterons described in Chapter 4, plus a few other adjustable parameters to take account of, for example, the highly reversible region. This will at least show us if our understanding is correct, and by comparing the simulation with the experiments, some more feature may be added into the previously discussed magnetization process. It is also worth extending this method to other PMA systems, e.g. Co/Pd multilayers, and exchange-biased PMA films.

Our work in Chapter 5 brings more understanding of the low frequency noise in spin-valve structures. Little or no spatial correlation in the $1/f$ noise was shown within electrode pairs, approximately 250 nm apart. The individual fluctuating entity was found out to be largely below the domain size in soft ferromagnet. However, domain wall movement across the sample can cause highly spatially correlated fluctuations, whose spectra deviate significantly from the usual $1/f$ noise. One very obvious question is how to measure the correlation length of these magnetic fluctuators experimentally. This requires further narrowing the spacing between adjacent electrode pairs. However, the resistance between the electrode pairs will soon become too small to be matched by normal transistor based amplifiers. This will require the use of transformer amplifiers, or more advanced instrumentation. The other interesting direction would be to find direct evidence to support our suggestion in Chapter 5, that grains in the ferromagnetic layer of tens of nanometers in size, with a weakened exchange interaction between them, are the fundamental magnetic fluctuators observed in the low frequency noise spectrum of a spin-valve. A possible experiment is to

further weaken the inter-grain exchange interaction by a low energy argon gas etching of the samples. Grain-boundaries should be more vulnerable to the etching process. If all the other parameters are similar, our picture leads to the prediction that samples after argon treatment would become noisier compared with those measured just after deposition.

Samples we measured in this study normally have more complicated micromagnetics than what was described by a simple coherent rotation process. This makes the interpretation of our results less trivial. One possible solution is to apply an appropriate field sequence before noise measurement to wash out all the possible domian walls from the sample. This would require some intensive micromagnetic simulation work, in order to find the proper magnetic field sequence. It is also worthwhile patterning better EBL yoke samples, with low noise gold contacts, which can be enhanced by a post-fabrication annealing process. Measurement on these samples will make the data much easier to understand, and avoid some possible artefacts. However, a foreseeable problem is that the electrical contacts might serve as strong pinning sites for domain walls, and the magnetization process still deviates from a well-defined coherent rotation in these samples. It is also possible to extend the spatial correlation to some other micromagnetic structures, where the magnetic states are well understood. Ring-shaped spin-valve samples are a good candidate, as the vortex state and onion states in these structures are linked simply by reversing the magnetization in one of the two arms of the ring. It will be interesting to see how the spatial correlation of the low frequency noise changes when the sample changes from an onion state to a vortex state.

References

[1] Y. Q. Li, C. Ren, P. Xiong, S. von Molnár, Y. Ohno, and H. Ohno. *Phys. Rev. Lett.*, 93:246602, 2004.

[2] J. Müller, S. von Molnár, Y. Ohno, and H. Ohno. *Phys. Rev. Lett.*, 96:186601, 2006.

[3] Y. Q. Li. PhD thesis, Florida State University, 2003.

Appendix A

Theoretical Aspects

A.1 Basic Statistical Mechanics

Ideas covered in this section are fundamental statistical mechanics, and can be found in most of the monographs on statistical physics [1, 2]. The discussions here follow that in [1].

Suppose $P(X)$ is the probability of observing the system in the state X with an energy $H(X)$. $P(X)$ and $H(X)$ should satisfy the following relations.

$$\sum P(X) = 1 \tag{A.1}$$

$$\sum P(X)H(X) = \langle H(X) \rangle = U \tag{A.2}$$

with U the internal energy of the system, which is fixed by the thermo bath.

The Shannon entropy of the system is defined as

$$S_S = -\sum P(X) \ln P(X) \tag{A.3}$$

which is at its maximum under thermoequilibrium. To find the probability

$P(X)$ which maximizes S_S, we use the Lagrange function as following.

$$\psi_{\alpha,\beta}(P) = -\sum P(X)\ln P(X) - \alpha\sum P(X) - \beta\sum H(X)P(X) \quad \text{(A.4)}$$

in which α and β are the Lagrange multipliers. By setting $\partial\psi_{\alpha,\beta}(P)/\partial P(X) = 0$, we have

$$P(X) = \exp[-1 - \alpha - \beta H(X)] \quad \text{(A.5)}$$

in which α and β are related by $\sum P(X) = 1$. This gives

$$\exp(-1-\alpha)\sum \exp[-\beta H(x)] = 1 \quad \text{(A.6)}$$

Using Eqn. (A.5), we arrive at

$$P_\beta(X) = \frac{\exp[-\beta H(X)]}{Z_\beta} \quad \text{(A.7)}$$

in which the partition function Z_β is defined as

$$Z_\beta = \sum \exp[-\beta H(X)] \quad \text{(A.8)}$$

It can be proved that $\beta = 1/(k_B T)$. Thermodynamic quantities at equilibrium can be expressed by the partition function. Table A.1 lists some of the important relations.

A.2 Fluctuation-Dissipation Theorem

The fluctuation-dissipation theorem is an important result of thermodynamics. In the case of magnetic fluctuation, it relates the magnetization fluctuations and the susceptibility [3, 4]. We deduce the fluctuation-

Thermodynamic quantities	Expressed by the partition function
Free energy	$F_\beta = -\frac{1}{\beta}\ln Z_\beta = -k_B T \ln Z_\beta$
Internal energy	$U_\beta = -\frac{\partial}{\partial\beta}\ln Z_\beta = \frac{\partial}{\partial\beta}(\beta F_\beta)$
Entropy	$S_\beta = -k_B\beta\frac{\partial}{\partial\beta}(lnZ_\beta) + k_B lnZ_\beta = -\frac{\partial}{\partial T}F_\beta$
Magnetic moment	$m_\beta = \frac{\partial}{\partial h}(\frac{1}{\beta}\ln Z_\beta) = -\frac{\partial}{\partial h}F_\beta$
Susceptibility	$\chi_\beta = \frac{\partial^2}{\partial h^2}(\frac{1}{\beta}lnZ_\beta) = -\frac{\partial^2}{\partial h^2}F_\beta$

Table A.1: Some important relations between the partition function and thermodynamic quantities.

dissipation theorem from the partition function described in Appendix A.1 (for more detailed information, see [1]).

We start with defining the impulse response function $\sigma(t)$ as

$$\sigma(t) = \frac{\partial m_{h_0}(t)}{\partial h_0}|_{h_0=0} \tag{A.9}$$

in which $m_{h_0}(t)$ is the response of the system to an input of the form $h(t) = h_0[1 - s(t)]$ with s(t) the Heaviside step function.

$$s(t) = \begin{cases} 1 & \text{when } t \geq 0 \\ 0 & \text{when } t < 0 \end{cases} \tag{A.10}$$

Here we introduce the term of conjugate intensive and conjugate extensive quantities in thermodynamics. An intensive quantity is independent to the number of particles making up the physical system, whereas the value of an extensive quantity is proportional to the number of particles. Two quantities, arising from different thermodynamical energy functions are defined as a conjugate pair if their product has units of energy, in which the inten-

sive quantity $h(t)$ can be seen as the input signal to the system, whereas its conjugated extensive quantity $m_{h_0}(t)$ is the response of the system. For example, in magnetic systems, h is the applied magnetic field, and m is the magnetic moment.

The general susceptibility $\chi(t)$ is related to the impulse response function $\sigma(t)$ by

$$\chi(t) = -\frac{d\sigma(t)}{dt} \tag{A.11}$$

and its Fourier transform can be expressed as

$$\chi(f) = -\mathrm{i}2\pi f\sigma(f) \tag{A.12}$$

The susceptibility is often decomposed into a real (in-phase) part and an imaginary (out-of-phase) part, $\chi(f) = \chi^{'}(f) - \mathrm{i}\chi^{''}(f)$. Then we have the out-of-phase susceptibility

$$\chi^{''}(f) = \pi f\sigma(f) \tag{A.13}$$

The system is at equilibrium at $t = 0$, since the magnetic field h_0 has been applied for an infinite length of time. Hence, the probability of finding the system in a state Y is

$$P_\beta(Y) = \frac{\exp[-\beta H(Y)]}{Z_\beta} \tag{A.14}$$

in which

$$H(Y) = H_0(Y) - h_0 m(Y) \tag{A.15}$$

is the internal energy under an applied magnetic field.

We further define $P(t, 0, X, Y)$ as the probability of having the system

in state Y at $t = 0$ and state X at t. According to the Bayes' relation, it can also be expressed as $P(t, 0, X|Y)P_\beta(Y)$, with $P(t, 0, X|Y)$ the conditional probability in finding the system in state X at time t, given it is at state Y when $t = 0$. This leads to an expression of $P(t, X)$

$$P(t, X) = \sum_Y P(t, 0, X, Y) = \sum_Y P(t, 0, X|Y)P_\beta(Y) \tag{A.16}$$

The function R_{h_0} can be expressed by the probability of the system in a certain state X at time t, $P(t, X)$.

$$R_{h_0} = \sum m(X)P(t, X) = \sum_X \sum_Y m(X)P(t, 0, X|Y)P_\beta(Y) \tag{A.17}$$

Hence, from Eqn. (A.9) we obtain an expression of $\sigma(t)$ in terms of $m(X)$ and the related probability functions

$$\begin{aligned} \sigma(t) &= \sum_X \sum_Y m(X)[P(t, 0, X|Y)\frac{\partial}{\partial h_0}P_\beta(Y)] && \text{(A.18)} \\ &= \beta\{\sum_X \sum_Y m(X)m(Y)P_\beta(t, 0, X, Y) - [\langle m(X)\rangle]^2\} && \text{(A.19)} \end{aligned}$$

in which $P_\beta(t, 0, X, Y)$ is probability at equilibrium in finding the system in state Y at $t = 0$ and state X at t.

The autocorrelation function of the magnetic moment is

$$\begin{aligned} C(\tau) &= \langle m(t)m(t + \tau) - \langle m(t)\rangle\rangle^2 && \text{(A.20)} \\ &= \sum_X \sum_Y m(X)m(Y)P_\beta(t, 0, X, Y) - [\langle m(X)\rangle]^2 && \text{(A.21)} \end{aligned}$$

From Eqn. (A.19) and Eqn. (A.21) we see that $\sigma(t) = \beta C(\tau)$, which

brings us to the fluctuation-dissipation theorem

$$S_m(f) = \frac{k_B T \chi''(f)}{\pi f} \tag{A.22}$$

Eqn. (A.22) is different by a factor of $\mu_0/2$ compared to Eqn. (4.15), which is the fluctuation-dissipation relation in a real magnetic system. This can be understood in that the magnetostatic energy in a magnetic field $\boldsymbol{H}$ is $-\frac{1}{2}\mu_0 \boldsymbol{m} \cdot \boldsymbol{H}$ instead of $\boldsymbol{m} \cdot \boldsymbol{H}$ as assumed in Eqn. (A.15).

Another important relation as a direct result of the fluctuation-dissipation theorem and the Kramers-Kronig relation (see Appendix A.5) is the total fluctuation theorem.

$$\langle m^2(X) \rangle - \langle m(X) \rangle^2 = k_B T \chi_\beta \tag{A.23}$$

It says that the total fluctuation of the system is proportional to the susceptibility χ_β of the system at equilibrium, and the susceptibility is always a positive quantity. In spin-valves and magnetic tunnel junctions, it also helps understand why according to many measurements, the Hooge parameter γ scales with the resistance susceptibility.

A.3 Parseval's Theorem

The Parseval's theorem relates the integral of $X(t)$ in the time domain to the integral of $S(f)$ in the frequency domain. The Fourier transform of $X(t)$ is defined as[1]

$$T(f) = \int_{-\infty}^{+\infty} X(t) \exp(-2\pi \mathrm{i} f t) dt \tag{A.24}$$

[1]The treatment in this section follows [5].

and its inversion gives

$$X(t) = \int_{-\infty}^{+\infty} T^*(f)\exp(-2\pi \mathrm{i} f t)df \tag{A.25}$$

Hence, we have

$$\begin{aligned}
\int_{-\infty}^{+\infty} S(f)df &= \int_{-\infty}^{+\infty} T^*(f)T(f)df & \text{(A.26)}\\
&= \int_{-\infty}^{+\infty} T^*(f)df \int_{-\infty}^{+\infty} X(t)\exp(-2\pi \mathrm{i} f t)dt & \text{(A.27)}\\
&= \int_{-\infty}^{+\infty} X(t)dt \int_{-\infty}^{+\infty} T^*(f)\exp(-2\pi \mathrm{i} f t)df & \text{(A.28)}\\
&= \int_{-\infty}^{+\infty} X^2(t)dt & \text{(A.29)}
\end{aligned}$$

This gives the Parseval's theorem.

A.4 Wiener-Khintchine Theorem

The Wiener-Khintchine theorem [1, 5] shows that the power spectrum density can be expressed as the Fourier transform of the autocorrelation function. We start from the definition of the power spectrum density[2].

$$S(f) = \lim_{T\to\infty}(\frac{1}{T})\int_{-T/2}^{+T/2}\int_{-T/2}^{+T/2}\langle X(t)X(v)\rangle\exp[-\mathrm{i}2\pi f(t-v)]dtdv \tag{A.30}$$

Substituting $\tau = v - t$ leads to

$$S(f) = \lim_{T\to\infty}(\frac{1}{T})\int_{-T/2}^{+T/2} dt \int_{-T/2-t}^{+T/2-t} X(t)X(t+\tau)\rangle\exp[-\mathrm{i}2\pi f\tau)]d\tau \tag{A.31}$$

Since $\langle X(t)X(t+\tau)\rangle$ does not depend on t for a stationary process and

[2]The treatment in this section follows [5].

approaches zero for very large τ, Eqn. (A.31) can be approximated as

$$S(f) = \int_{-\infty}^{+\infty} \langle X(t)X(t+\tau)\rangle \exp(\mathrm{i}2\pi f\tau)d\tau \tag{A.32}$$

which is the Wiener-Khintchine theorem.

A.5 Kramers-Kronig Relation

The Kramers-Kronig dispersion relation connect the out-of-phase susceptibility $\chi''(f)$ to the in-phase susceptibility $\chi'(0)$ for a causal process. For a more detailed discussion, we refer to [6]. Here we follow a largely simplified version described in [7]. We start from the susceptibility in time domain $\chi(t)$. For a causal process, the susceptibility $\chi(t)$ is zero for $t < 0$. Hence, the following equation holds[3].

$$\chi(t) = \chi(t)s(t) \tag{A.33}$$

with $s(t)$ the Heaviside step function as defined in Appendix A.2. The inverse Fourier transform of $\chi(t)$ is

$$\chi(t) = \int_{-\infty}^{+\infty} \chi(f')\exp(\mathrm{i}2\pi ft)df' \tag{A.34}$$

Inserting Eqn. (A.34) into the right hand side of Eqn. (A.33), and making Fourier transform of both sides gives

$$\chi(f) = \frac{1}{2}\int_{-\infty}^{+\infty} \chi(f')[\frac{1}{\mathrm{i}\pi(f-f')} + \delta(f-f')]df' \tag{A.35}$$

[3]For those who insist on the purity of mathematics, the following equations might seem 'dirty'.

using the Fourier transform of the Heaviside step function being

$$s(f) = \frac{1}{2}[\frac{1}{\mathrm{i}\pi f} + \delta(f)] \tag{A.36}$$

in which $\delta(f)$ is the delta function.

Expanding $\chi(f)$ into its real and imaginary part, and making $f = 0$ gives

$$\chi'(0) = \frac{2}{\pi}\int_0^{+\infty} \frac{\chi''(f)}{f} df \tag{A.37}$$

which is the Kramer-Kronig relation.

A.6 The Stoner-Wohlfarth Model

The Stoner-Wohlfarth model is the simplest and highly instructive model in micromagnetics [8, 9, 10]. Its fundamental assumption is that the exchange energy dominates other interactions, so a constant magnetization exists in the whole sample volume [11]. During the magnetization switching, the exchange energy term always remains the same, given the model its other name — the coherent rotation model. In practice, it describes the magnetization switching in magnetic particles of about 10 nm in size, or less [12]. Under certain condition, it can also be used to analyse the magnetization switching in magnetic thin films.

Assuming an uniaxial ellipsoid ($a = b$) with the applied magnetic field $\boldsymbol{H}$ parallel to its c-axis. Its energy density can be expressed as[4]

$$\varepsilon = K_1 \sin^2\theta + \frac{\mu_0}{4}(1 - 3D)M_s^2 \sin^2\theta - \mu_0 M_s H \cos\theta \tag{A.38}$$

[4] Discussions in this section follow [10]. Some errors in the equations in the original literature are corrected.

in which K_1 is the magnetocrystalline energy constant, D is the demagnetizing factor along c-axis, and θ is the angle between magnetization $\boldsymbol{M}$ and the c-axis. The anisotropy field is defined as

$$H_k = \frac{2K_1}{\mu_0 M_s} \tag{A.39}$$

which is the ratio between the magnetocrystalline energy and the magnetostatic energy when $D = 1$.

It can be easily seen that two minima exist for ε, namely when the magnetization $\boldsymbol{M}$ aligns parallel or antiparallel to the c-axis, with $\theta = 0$ and π, respectively. The transition between these two energy minima happens at the coercivity, which is

$$H_c = \frac{2K_1}{\mu_0 M_s} + \frac{1}{2}(1 - 3D)M_s \tag{A.40}$$

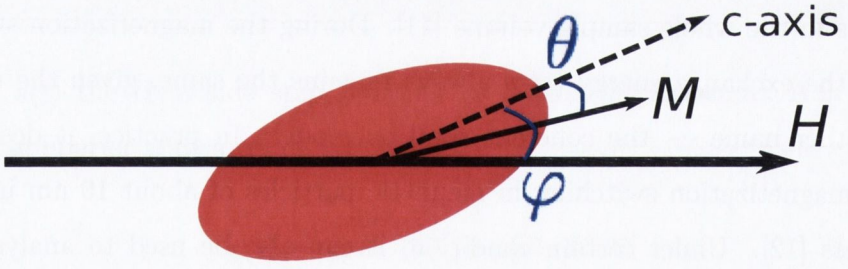


Fig. A.1: A diagram of a Stoner-Wohlfarth particle.

This expression says that the coercivity H_c in a Stoner-Wohlfarth particle is simply the anisotropy field H_k plus the shape-anisotropy field. In case when the applied magnetic field is not along the c-axis (Fig. A.1), we have

$$\varepsilon = K\sin^2\theta - \mu_0 M_s \cos(\theta - \varphi) \tag{A.41}$$

where φ is the direction between the applied magnetic field and the c-axis, and the first term on the right hand side takes account of both the magnetocrystalline energy and the shape-anisotropy energy. Hysteresis loops can be established by analysing $\partial\varepsilon/\partial\theta = 0$ and $\partial^2\varepsilon/\partial\theta^2 = 0$. An important situation is when $\varphi = \pi/2$, in which the applied magnetic field is perpendicular to the c-axis. The hysteresis turns out to be a straight line with zero energy product and a slope of $dM/dH = 2K/\mu_0 M_s^2$. This describes one of the approaches in obtaining linear response in a spin-valve sensor, in which the magnetic field is applied perpendicular to the easy axis of the free layer, and the free layer undergoes a coherent rotation process.

A.7 The Draaisma-de Jonge Model

Draaisma and de Jonge [14] extended the Kooy-Enz model [15] for stripe domains to magnetic-nonmagnetic multilayer structures[5]. They assume that the perpendicular anisotropy is large enough to orient all the stripe domains either up or down. Domain walls are assumed to be infinitely thin and completely mobile. The system they consider is a multilayer structure with N bilayers, having a ferromagnetic layer of thickness t, and a nonmagnetic layer of thickness s. To minimize the magnetostatic energy, the domain walls in all the ferromagnetic layers are at the same positions. The magnetization in each domain is equal to the saturation magnetization M_s. The size of the up stripe domains is d_1, and the size of the down stripe domains is d_2. Fig. A.2 depicts the sample geometry under consideration.

[5]The deduction in this section follows [14] and [16].

The sample magnetization can be expressed as

$$M = \frac{d_1 - d_2}{d_1 + d_2} M_s \tag{A.42}$$

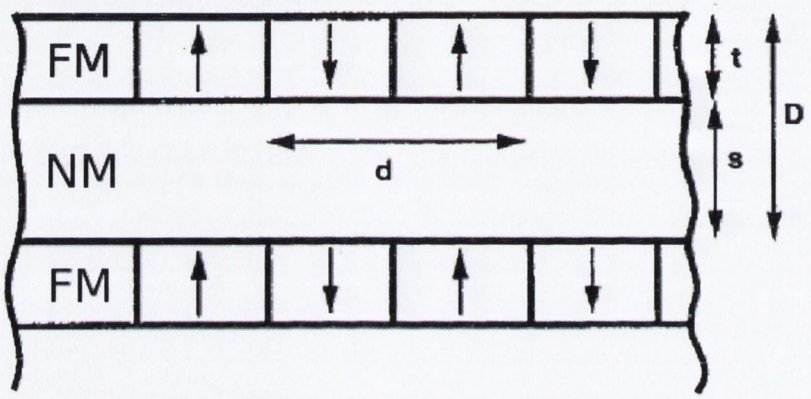


Fig. A.2: A sketch depicts the sample geometry considered in the Draaisma-de Jonge model (adopted from [13]).

The total magnetic energy per volume e_{tot} of the stripe domain structure can be expressed as the sum of three energy terms, all normalized to the magnetostatic energy of a fully magnetized sample, $1/2\mu_0 M_s^2$. They are the magnetostatic energy e_d, the Zeeman energy in an applied magnetic field e_h, and the domain wall energy e_w. The magnetostatic energy can be written as [6]

$$e_d = \frac{E_d}{\frac{1}{2}\mu_0 M_s^2} = m^2 + \sum_{n=1}^{+\infty} \frac{4}{(n\pi)^3} \frac{d}{t} \sin^2[\frac{1}{2} n\pi(m+1)] f_n(d) \tag{A.43}$$

in which m is the reduced magnetization $m = M/M_s$ and $f_n(d)$ is the

[6] For a complete treatment of the magnetostatic energy, please refer to [14].

magnetostatic energy coefficient expressed as

$$f_n(d) = (1 - e^{-2\pi n(t/d)}) + \frac{\sinh^2(\pi nt/d)}{\sinh^2[\pi n(t+s)/d]} \times [\frac{1}{N}(1 - e^{-2\pi nN(t+s)/d}) - (1 - e^{-2\pi n(t+s)/d})] \quad \text{(A.44)}$$

The Zeeman energy can be expressed as

$$e_h = \frac{E_H}{\frac{1}{2}\mu_0 M_s^2} = -2hm \quad \text{(A.45)}$$

in which $h = H/M_s$ is the reduced magnetic field. The third energy term, the domain wall energy is expressed as follows.

$$e_w = \frac{E_w}{\frac{1}{2}\mu_0 M_s^2} = \frac{2\tau}{d} \quad \text{(A.46)}$$

in which $\tau = \sigma_w/\frac{1}{2}\mu_0 M_s^2$ is the ratio between the domain wall energy density and the magnetostatic energy under saturation, $d = d_1 + d_2$ is the domain period. Minimising the total energy $e_{tot} = e_d + eh + ew$ gives

$$d = \sqrt{2\tau/\frac{\partial e_d}{\partial d}} \quad \text{(A.47)}$$

$$h = m + \sum_{n=1}^{+\infty} \frac{1}{(n\pi)^2} \frac{d}{t} \sin[\pi n(m+1)] f_n(d) \quad \text{(A.48)}$$

Eqn. (A.47) and Eqn. (A.48) give can be used to find the domain period d and the reduced magnetization m as different applied magnetic field h numerically.

A.8 Verification of Contact Noise

A complete treatment of this problem can be found in the work of Barone et al. [17]. In this work, we use a simple protocol, utilized by some previous authors to detect the appearance of excess contact noise [18]. This protocol involves measuring the sample noise with the same bias current with different ballast resistors. Due to the contribution of contact noise, total measured noise is larger when a smaller ballast resistor is in the circuit.

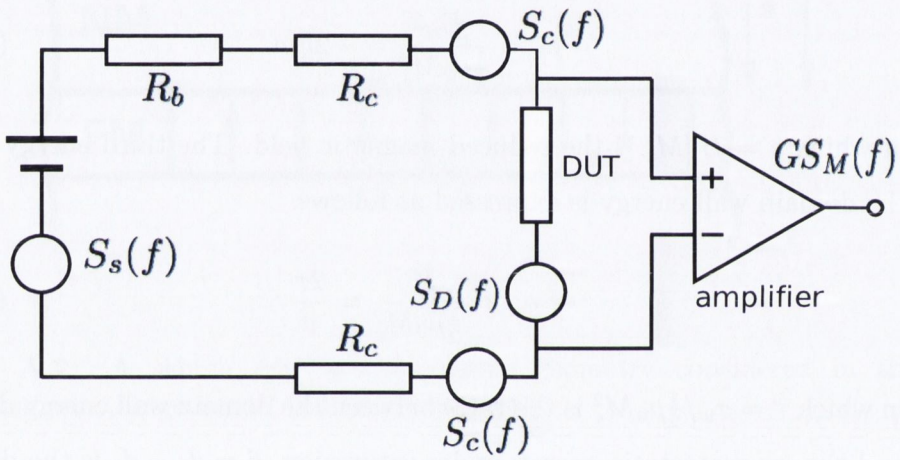


Fig. A.3: Circuit diagram in analysing the effect of contact noise. Other noise sources except those shown in the diagram are omitted for clarity.

The protocol can be verified as followings. Fig. A.3 shows a diagram of the measuring circuit. Assuming different noise sources are not correlated, the voltage noise measured across the sample can be expressed as

$$S_M(f) = A[S_s(f) + S_c(f)] + BS_D(f) \tag{A.49}$$

in which $S_M(f)$, $S_s(f)$, $S_c(f)$, and $S_D(f)$ are the measured noise, voltage equivalent noise of the source, the contacts, and the device under test,

respectively. A and B are two constants which are given as

$$A = (\frac{R_D}{R_b + R_c + R_D})^2 = (\frac{R_D}{R_b})^2 \tag{A.50}$$

$$B = (\frac{R_b + R_c}{R_b + R_c + R_D})^2 \sim 1 \tag{A.51}$$

when the resistance of the ballast resistor is much larger than the sum of the device and contacts resistance, which is the case in our measurement.

If we assume S_s being small compared with other contributions, Eqn. (A.49) has only two terms. The first term is the contribution from the device under test, which is the desired signal. The second term is the contact noise, which we would like to avoid. Consider two different ballast resistors, R_{b1} and R_{b2}. If $R_{b1} > R_{b2}$, we have $A_1 < A_2$. This suggests that the contact noise contributes less to the first case than to the second case, which justifies our method. Fig. A.4 shows an example of this method, measured with two different ballast resistors (10 kohm and 20 kohm) on a 2 μm yoke in sample set (3) in Chapter 5. The contact noise contribution is seen to be negligible.

It has to be admitted that this method is only valid when the contact noise contribution is not too small compared with the noise of the device. However, it is often a better approach than the conventional method, in which the sample noise measured under four-probe geometry is compared with that measured in two-probe geometry, as not all the samples can be routinely measured in both geometries, and the two power spectra are usually not directly comparable. For example, in our yoke samples, the two-probe geometry for sure leads to a much larger $1/f$ noise power spectral density, since the voltage drop is much higher. The above method also does not assume any particular noise - voltage scaling (β in Eqn. (2.14)), which

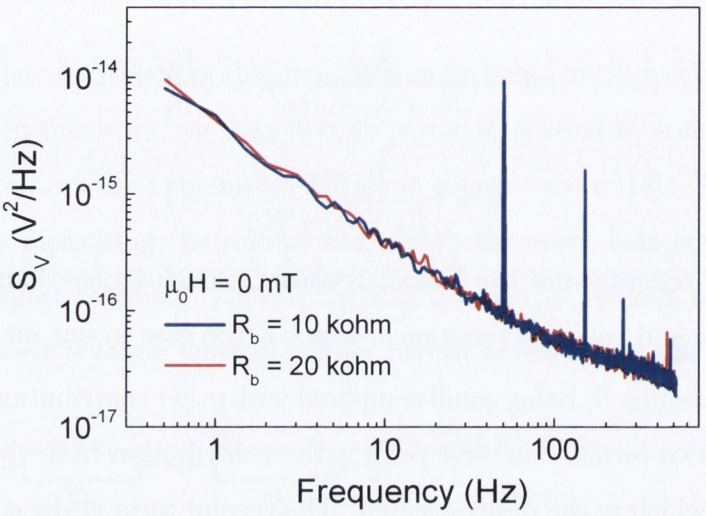


Fig. A.4: Power spectral density across electrode 2 and electrode 3 in a $w = 2$ μm yoke measured with two different ballast resistors. The bias current was 120 μA.

makes it applicable to systems in which the noise properties are not well characterized.

References

[1] Philippe Réfrégier. *Noise Theory and Application to Physics: From Fluctuations to Information.* Springer-Verlag, New York, 2004.

[2] W. Greiner, L. Neise, and H. Stöcker. *Thermodynamik under Statistische Mechanik.* Beijing University Press, (chinese translation) edition, 2001.

[3] H. B. Callen and T. A. Welton. *Phys. Rev.*, 83:34, 1951.

[4] M. Lax. *Rev. Mod. Phys.*, 32:25, 1960.

[5] A. van der Ziel. *Noise: sources, characterization measurement.* Englewood Cliffs, London, 1970.

[6] G. B. Arfken and H. J. Weber. *Mathematical Methods for Physicists.* Academic Press, San Diego, 5th edition, 2001.

[7] J. Briaire. *1/f Noise in Permalloy.* PhD thesis, Technische Universiteit Eindhoven, 2000.

[8] E. D. Torre. *Magnetic Hysteresis.* IEEE Press, New York, 1999.

[9] A. Aharoni. *Introduction to the Theory of Ferromagnetism.* Lanzhou University Press, (chinese translation) edition, 2002.

[10] R. Skomski. *Simple Models of Magnetism.* Oxford University Press, 2008.

[11] E. C. Stoner and E. P. Wohlfarth. *Phil. Trans. R. Soc. London A*, 240:599, 1948.

[12] W. Wernsdorfer, B. Doudin, D. Mailly, K. Hasselbach, A. Benoit, J. Meier, J. Ph. Ansermet, and B. Barbara. *Phys. Rev. Lett.*, 77:1873, 1996.

[13] J. R. Barnes, S. J. O'Shea, M. E. Welland, J. Y. Kim, J. E. Evetts, and R. E. Somekh. *J. Appl. Phys.*, 76:2974, 1994.

[14] H. J. G. Draaisma and W. J. M. de Jonge. *J. Appl. Phys.*, 62:3318, 1987.

[15] C. Kooy and U. Enz. *Philips Res. Rep.*, 15:7, 1960.

[16] O. Donzelli, D. Palmeri, L. Musa, F. Casoli, F. Albertini, L. Pareti, and G. Turilli. *J. Appl. Phys.*, 93:9908, 2003.

[17] C. Barone, A. Galdi, S. Pagano, O. Quaranta, L. Méchin, J. M. Routoure, and P. Perna. *Rev. Sci. Instrum.*, 78:093905, 2007.

[18] C. Leemann, M. J. Skove, and E. P. Stillwell. *Solid State Commun.*, 35:97, 1980.

Appendix B

Lithography Recipes

In relation to this thesis work, several lithography recipes on different resists systems were developed or improved. They are documented in this section.

B.1 Photoresists

B.1.1 Shipley Microposit S1813

Shipley Microposit S1813 is a widely used positive photoresist, for its wide processing window, good reproducibility, and low toxicity [1]. It requires a dose of about 150 mJ/cm^2 for UV exposure. The developer for it is 0.23 N TMAH with trade name MIF-319. The processing conditions are as follows.

- Clean the wafer, and remove water residuals by pre-baking it at 120 ^{0}C on a hotplate for 2 min.
- Spin coating S1813 at 4000 rpm for 1.2 - 1.5 μm thickness.
- Soft bake the resist at 115 ^{0}C for 90 sec.

- UV exposure for 6 sec.
- Postexposure baking of the resist at 115 ^{0}C for 60 sec.
- Develop in MIF-319 for 17 - 23 sec.
- Wash with running water.

B.1.2 AZ nLOF 2070

AZ nLOF 2070 (Clariant Corporation) is a negative tone chemically amplified resist with comparably large processing window, and suitable for metal lift-off applications [2]. The required dose is between 60 - 180 mJ/cm^2 depending on the resist thickness. We use a dose much higher than the quoted value due to the fact that the resist is strictly i-line sensitive, while our UV light source has a broad spectrum. In this work, a thinned resist was used, which gives resist thickness of about 400 nm after coating at 4000 rpm. This is much thinner than the conventional resist thickness, for improving the resist resolution. The developer is 0.26 N TMAH with trade name AZ 326. A post-exposure baking process is required to activate the deprotection reaction (chemical amplification). Its processing parameters are as follows.

- Clean the wafer, and remove water residuals by pre-baking it at 120 ^{0}C on a hotplate for 2 min.
- Spin coating AZ nLOF 2070 at 4000 rpm for 300 nm - 500 nm thickness.
- Soft bake the resist at 100 ^{0}C for 60 sec.
- UV exposure for 8 - 10 sec.

- Post-exposure baking at 110 ^{0}C for 60 sec.
- Develop in AZ 726 developer for 20 - 45 sec.

B.2 Electron beam resists

B.2.1 Polymethyl Methacrylate (PMMA)

PMMA is the standard positive electron beam resist, and probably the most widely used electron beam resist ever. Nowadays, it is still among the electron beam resists with highest resolution. It normally requires a dose of 150 - 350 μC/cm^2, and has a very wide processing window which leads to unbeaten run-to-run reproducibility. PMMA is normally purchased in two molecular weights, 950 kD and 495 kD, in anisole [3]. In this study, most of the patterns were written with a single layer 950 kD PMMA resist. The processing parameters for single layer 950 kD PMMA are as follows.

- Clean the wafer, and remove water residuals by pre-baking it at 120 ^{0}C on a hotplate for 2 min.
- Spin coating PMMA 950k at 1500 rpm for 45 sec. This gives a thickness of 150 nm - 200 nm.
- Soft bake at 180 ^{0}C for 25 min.
- Expose with a dose of about 90 μC/cm^2 under 10 kV.
- Develop in MIBK:IPA = 1:3 solution for 42 sec.
- Wash in IPA for 15 sec.
- Blow dry or spin dry.

Another approach using double layer PMMA resist to assist 'lift-off' was also improved based on the previous processing parameters. This approach uses a layer of 495 kD PMMA underneath the 950 kD PMMA to create an undercut, since 495 kD PMMA is more vulnerable to the developer after exposure. However, this was not used as a routine procedure for sample preparation in this work, as resist undercut significantly restricts the pattern density.

- Clean the wafer, and remove water residuals by pre-baking it at 120 ^{0}C on a hotplate for 2 min.
- Spin coating PMMA 495k at 3000 rpm for 45 sec.
- Soft bake at 165 ^{0}C for 5 min.
- Spin coating PMMA 950k at 4000 rpm for 45 sec.
- Soft bake at 180 ^{0}C for 20 min.
- Expose with a dose of 60 - 85 μC/cm^2 under 10 kV.
- Develop in MIBK:IPA = 1:3 solution for 35 sec.
- Wash in IPA for 15 sec.
- Blow dry or spin dry.

The above processing parameters might lead to a thick resist layer which increases surface charging during electron beam writing. Attention is required to minimize the effect, e.g. good charge release path for the sample and looped pattern writing.

B.2.2 ma-N 2403

ma-N 2403 (microresist technology) is a deep UV sensitive negative tone photoresist which can also be exposed by electron beam [4]. It is a non-chemically amplified resist with a moderate resolution of about 30 nm. It requires a dose similar to PMMA and has very good etch resistance. The developer is 0.26 N TMAH with trade name AZ 726. In this work, we use a set of processing parameters which are very similar to the standard ones.

- Clean the wafer, and remove water residuals by pre-baking it at 120 ^{0}C on a hotplate for 2 min.
- Spin coating ma-N 2403 at 3000 rpm for 45 sec. This gives a resist thickness of about 300 nm.
- Soft bake at 90 ^{0}C for 60 sec.
- Expose with a dose of 60 - 100 μC/cm^2 under 10 kV.
- Develop in AZ 726 for 60 sec.
- Wash in water for 60 sec.
- Blow dry or spin dry.

B.2.3 Hydrogen Silsesquioxane (HSQ)

Reproducible linewidths in the lower 30 nm range are beyond the limits of conventional organic polymer based negative electron beam resist. It was first reported by Namatsu et al. [5] that HSQ serves as an inorganic polymeric-type negative tone electron beam resist which yields sub-20 nm width lines with good reproducibility, due to its small molecule size. The

electron beam exposure causes the cross-linking via Si-H bond. After exposure, it forms an amorphous structure which is similar to SiO_2, and becomes insoluble in alkaline hydroxide developers. The processing of HSQ was further developed by van Delft and co-workers in the Philips Research Laboratories [6, 7, 8]. Shortly after, sub-10 nm structures were routinely obtained by several research groups and companies, which established HSQ as the negative tone counterpart of PMMA having the ultimate resolution.

However, processing parameters are critical for HSQ exposure. The resist is believed to strongly absorb water under ambient condition, which results in a comparably small processing window. Due to its highly insulating nature, HSQ also causes significant surface charging during electron beam exposure. HSQ is purchased from Dow Coring under trade name FOX-12 [9] or XR-1541 [10]. In this work, the HSQ processing is as follows.

- Clean the wafer, and remove water residuals by pre-baking it at 120 ^{0}C on a hotplate for 2 min.
- Spin coating HSQ resist at 2000 rpm for 45 sec. This leads to a resist thickness of 150 - 200 nm.
- Pre-exposure bake of the resist at 90 ^{0}C for 40 min.
- Expose with a dose of 100 - 300 μC/cm^2 under 10 kV.
- Develop in AZ 326 for 60 sec.
- Wash in water for 5 min.
- Blow dry or spin dry.

References

[1] Shipley, Marlborough, Massachusetts. *Microposit S1800 series photo resists.*

[2] Clariant Corporation, Somerville, New Jersey. *AZ nLOF 2000 Series i-Line Photoresists*, 2002.

[3] MICROCHEM, Newton, Massachusetts. *NANO PMMA and Copolymer*, 2001.

[4] Micro resist technology GmbH, Berlin-Koepenick, Germany. *ma-N 2400 - Negative Tone Photoresist Series.*

[5] H. Namatsu, T. Yamaguchi, M. Nagase, K. Yamazaki, and K. Kurihara. *Microelectron. Eng.*, 41-42:331, 1998.

[6] F. C. M. J. M. van Delft, J. P. Weterings, A. K. van Langen-Suurling, and H. Romijn. *J. Vac. Sci. Technol. B*, 18:3419, 2000.

[7] F. C. M. J. M. van Delft, W. S. M. M. Ketelaars, M. Kroon, and J. Lambregts. *J. Vac. Sci. Technol. b*, 20:2763, 2002.

[8] M. Peuker, M. H. Lim, H. I. Smith, R. Morton, A. K. van Langen-Suurling, J. Romijn, E. W. J. M. van der Drift, and F. C. M. J. M. van Delft. *Microelectron. Eng.*, 61-61:803, 2002.

[9] Dow Corning, Midland, Michigan. *Information About FOx-1x and FOx-2x Flowable Oxides*, 1996.

[10] Dow Corning, Midland, Michigan. *Dow Corning XR-1541 E-Beam Resist*, 2008.

Publications:

1. Z. Diao, E. R. Nowak, G. Feng, and J. M. D. Coey, *Magnetic noise in structured hard magnets*, (submitted).

2. J. Y. Chen, J. F. Feng, Z. Diao, G. Feng, X. F. Han, and J. M. D. Coey, *Tailoring magnetization reversal in exchange-biased* $[Co/Pt]_n$ *multilayer with perpendicular magnetic anisotropy*, (submitted).

3. J. F. Feng, Z. Diao, G. Feng, E.R. Nowak and J. M. D. Coey, *Magnetic noise in MgO-based magnetic tunnel junction rings*, (submitted).

4. J. M. D. Coey, L. Mazza, D. Fernández, and Z. Diao, *Magnetic field effects in Electrochemistry*, (submitted).

5. Z. Diao, J. Y. Chen, G. Feng, and J. M. D. Coey, *Magnetic force microscopy study of domain structures in patterned* $(CoFe/Pt)_n$ *multilayer films with perpendicular anisotropy*, (unpublished).

6. D. Fernández, P. A. Dunne, Z. Diao, and J. M. D. Coey, *Influence of magnetic field on co-reduction of hydrogen in* $Cu/CuSO_4$ *system*, (unpublished).

7. Z. Diao, P. A. Dunne, G. Zangari, and J. M. D. Coey, *Electrochemical noise analysis of the effects of a magnetic field on cathodic hydrogen evolution*, Electrochem. Commun. 11 (2009) 740 - 743.

8. Z. Diao, M. Abid, P. Upadhyaya, M. Venkatesan, and J. M. D. Coey, *Vortex states in soft magnets in two and three dimensions*, J. Magn. Magn. Mater. (in press).

9. A. Prina-Mello, Z. Diao, and J. M. D. Coey, *Internalization of ferromagnetic nanowires by different living cells*, J. Nanobiotechnol. 4 (2006) 9.